Doctoral Dissertation
Doctoral Program in Energy Engineering (35th Cycle)

Laser Micromachining: An Enabling Technology for Functional Surfaces and Materials

By

Devanarayanan Meena Narayana Menon

******

Supervisor:
Prof. Davide Luca Janner

Doctoral Examination Committee:
Prof. Daniel Milanese, Referee, University of Parma
Prof. Jordi Ignés-Mullol, Referee, University of Barcelona

Politecnico di Torino
2023

Declaration

I hereby declare that, the contents and organization of this dissertation constitute my own original work and does not compromise in any way the rights of third parties, including those relating to the security of personal data.

Devanarayanan Meena Narayana Menon

2023

* This dissertation is presented in partial fulfillment of the requirements for **Ph.D. degree** in the Graduate School of Politecnico di Torino (ScuDo).

I would like to dedicate this thesis to my loving parents

Acknowledgment

I would like to express my deepest gratitude to my advisor, Prof. Davide Janner, for his unwavering support, guidance, and mentorship throughout my doctoral journey. His expertise, patience, and encouragement have been instrumental in shaping the direction of this research and pushing me to achieve my best.

I am also indebted to the members of the PHOTONEXT group at LINKS FOUNDATION, especially Dr. Nadia Boetti for her invaluable support at the Laser Lab. Also, I thank the GLANCE group members and my colleagues for their support, through facilities, meetings, celebrations and smiles. I would also like to acknowledge interdepartmental center PHOTONEXT for their scholarship which was crucial to perform this work.

This acknowledgement would be incomplete without the mention of Matteo Giardino, who is highly knowledgeable and has been my constant friend throughout this journey supporting me in every way possible and a pleasure to listen to, especially for Saturday coffee sessions. My friend, Malhar Nagar has also thankfully been a constant presence whether for technical discussions or to share good times. I would also like to thank Dr. Diego Pugliese for his help in glass making and also for the support when needed. Thank you Daniele D'Ambrosio for your wonderful time and all the help you provided at the labs.

My heartfelt thanks to my family, and especially my mother Dr. Meena Saradamma, whose unwavering belief in me and the constant encouragement that kept me motivated during the challenging times of this journey. Their understanding, love, and support have been my pillar of strength throughout my academic pursuit.

A big thanks to the lovely couple Srushti G and Arjun S, at whose place I was the happiest in Turin. The discussions, suggestions and the food were a lovely combination that I always long for. I would also like to thank Aarathy E, who has supported me as a constant friend from the

beginning of this journey. A shoutout to all my Turin friends for the good times that we have cherished together.

I would take this moment to thank my dear friends Varun V and Amar M for their wonderful presence throughout this journey through their calls or get together. Sudarshan S has also been a wonderful friend to catch up with and laugh together on a weekly basis. I would also like to thank Krishna P, Shaurya, Vamshi, Nikhita, and the rest of the Europe group.

Most importantly I would like to offer my gratitude to Prashanti Nilayam, a wonderful place that I have spent my time since childhood, and all the associated educational institutions from primary school to SSSIHL. My pranams and Sai ram to all my teachers since primary school. Cheers to all my classmates and friends from the same. Pranams to my beloved Swami.

Completing this PhD thesis has been a challenging yet rewarding endeavor, and I am thankful to everyone who has played a part, however big or small, in its realization. Their support and belief in my abilities have been invaluable, and I am truly grateful for their presence in my life.

JAI HIND

Abstract

Laser micromachining is a well-established industrial processing technique. Due to the performance attainable with modern lasers, like high power, coherence, and monochromaticity, it has been utilized for cutting, welding, and engraving various materials, including metals, polymers, and composites. However, besides its traditional use, advancement in the laser technology has enabled a new perspective for laser processing towards advanced applications like surface functionalization, precision modification, and chemical alterations at the micro- and nano-scale. The applications for such material modifications include thin film dewetting, microfluidic channels, 3D optical waveguides, cell scaffolds, drug delivery systems, and solar and fuel cell applications.

Many of these advanced applications rely on ultrafast laser systems that use non-linear interactions to modify different materials in bulk with high precision. However, although several such applications have been demonstrated at a research level, an industrial-scale translation of these techniques has been dragging. That is due to the complexity, relatively slow processing, and expensive equipment involved with such ultrafast laser systems. On the contrary, long pulsed nanosecond lasers have been industrially established and could offer solutions to various advanced applications involving large-scale production.

This thesis focuses on the use of an industrial grade fiber nanosecond laser system to push the boundary of laser surface modifications on different materials: from metals to ceramics, from glass to polymers. Leveraging on the flexibility of

this approach and based on extensive research on the laser material interaction conducted during the development of the thesis, different applications are proposed here. Those applications include the fabrication of superhydrophobic/ superamphiphobic surfaces, surface texturing for improved functioning of solid oxide fuel cells, precision modification of microstructures and optics on bioresorbable glass, and ultrahydrophobic high gauge factor strain sensors based on reduced graphene oxide.

This research demonstrates that a high degree of control on the surface texture, like roughness or hierarchical structures, can be obtained by an accurate choice of laser parameters. For example, by appropriately adjusting the laser pulsewidth, aluminum can be made superamphiphobic. In another case, tunable surface roughness is achieved by varying the laser fluence obtaining an improved solid oxide fuel cell interconnect with the oxide glass sealant. Promising results have also been obtained by modifying glasses of biomedical interest like bioresorbable calcium phosphate glass. Indeed, in those glasses, the heat affected zones (HAZ) generally associated with nanosecond lasers can be reduced the resulting inverse Marangoni flow of the locally melted glass can be controlled to obtain microtextures on the glass surface. That enables to obtain e.g. micro-optics structures in the form of hyperbolic and spherical microlenses or diffraction gratings.

In addition, this thesis's work explored combining laser texturing capabilities with chemical surface treatments. Besides obtaining superamphiphobic surface with fluorosilane coatings, an eco-friendly rapid chemical treatment was developed using vegetable oil on the laser treated surfaces to achieve superhydrophobicity.

Finally, even though nanosecond laser micromachining can't reach all the capabilities offered by ultrafast lasers, several applications could use this former

as a powerful tool towards industrial scale processing for advanced applications and novel functional surfaces.

Contents

List of Figures

List of Tables

Chapter 1

Laser Interaction with Materials

1.1 Background

The study of laser micromachining for different material types has its basis in laser-matter interaction. In particular, within the realm of pulsed laser modification, a variety of factors contribute to the resulting surface modifications, such as pulsewidth, wavelength, pulse repetition rate, and pulse energy, to name a few. Before delving into the experimental findings of this thesis, it is essential to provide a concise introduction to laser-matter interaction and its primary mechanisms. Furthermore, it is helpful to review the different pathways for photon-phonon energy transfer, depending on the temporal characteristics of the laser pulse and the target material. This chapter elucidates the dynamics of material interaction with ultrashort and pulsed lasers, specifically nanosecond lasers. Additionally, we outline the crucial laser parameters that govern the material surface modification presented in the following chapters, covering the main aspects of the present research on nanosecond laser micromachining.

1.2 Aim and Objectives

The work discussed in this doctoral study takes advantage of the inherent effects associated with nanosecond pulse interaction with materials. The study uses an industrial grade nanosecond fiber laser for surface modifications on

different materials such as metals, polymers, glass, and ceramics for various applications ranging from surface modification for superhydrophobicity to fabrication of micro-optics and piezoresistive sensors. Apart from the laser modification of the surfaces, the study is also devoted to performing appropriate surface chemical treatments to realize the desired functional properties. According to the applications involved, the complete study could be separated into the following:

(i) Controlled use of appropriate laser parameters and following surface chemical treatment to fabricate either superamphiphobic surfaces or eco-friendly superhydrophobic surfaces. In addition, to the commonly used silanization technique, this study aims to propose an alternative eco-friendly coating procedure that is rapid and inexpensive.

(ii) Precision laser modification of an anti-bacterial bioresorbable glass leveraging the Inverse Marangoni effect. The ability for precise surface modification is to be tested through fabrication of micro-optics on the bioresorbable glass surface, which is interesting for in-vivo optical monitoring.

(iii) Laser texturing of surface to enhance joining strength of similar/dissimilar materials. Controlled modification of surface roughness is to be studied, for the desired applications. Also, in the case of ceramic Si_3N_4, the silica generated during laser processing step is removed through HF etching, which is then to be evaluated for joining strength.

(iv) Laser processing of a polyimide substrate to generate reduced graphene oxide for fabrication of a superhydrophobic strain sensor with a high gauge factor. The stability characterization of rGO and its possible transfer on different materials.

1.3 Introduction

The current section introduces the basics of Light Amplification by Stimulated Emission of Radiation (LASER) through the fundamental working principle, the primary characteristics of a laser beam, and the different types of laser systems. A literature review is then provided on the laser-matter interaction of different materials, mainly using pulsed laser systems, and the evolution of the corresponding material characteristics resulting in structural/chemical modifications. Finally, the various structural modifications resulting from laser-matter interaction are presented. This chapter aims to present a literature review and the state-of-the-art technologies required to introduce laser micromachining, especially using relatively long pulsed nanosecond laser systems in comparison to ultrafast pulses in the pico- and femto-second regimes.

1.4 Laser – A Brief Introduction

A laser system primarily consists of an optical cavity with a gain medium between the reflecting ends, forming a resonating optical cavity, as shown in Figure 1.1. Generally, both ends of the reflecting cavity consist of plane-parallel/spherical mirrors or fiber Bragg gratings, where the latter is commonly used as the optical cavity of fiber lasers [1,2]. Also, one of the cavity end mirrors is partially transparent (output window), while the other end is highly reflective, thereby maintaining the optical resonance of the cavity.

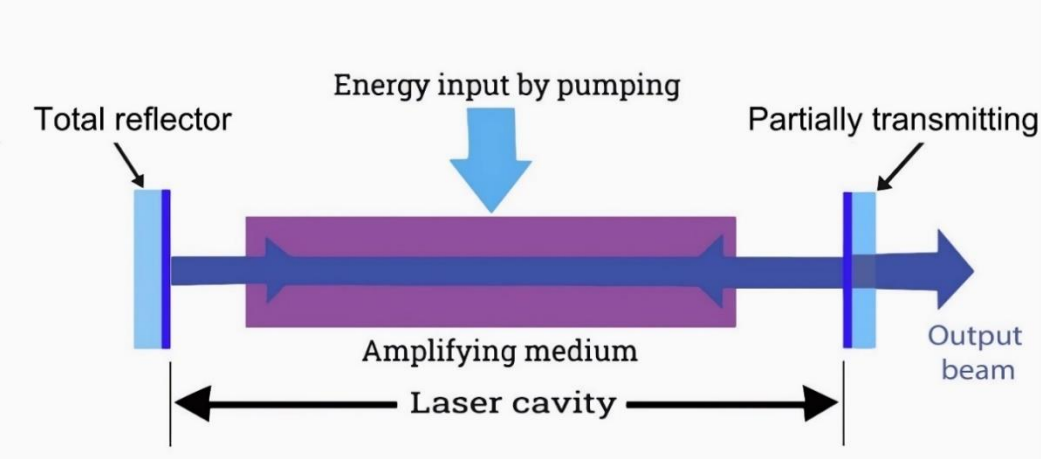

Figure 1.1. Illustration of the primary components of a laser system

The first laser was experimentally realized by Theodore Maiman in 1960, which was based on a ruby crystal with emission at 694.3 nm [3]. Following his invention, different laser systems were realized with gain medium-dependent emissions from ultraviolet to mid-infrared wavelengths. Various materials in different states of matter can act as the gain medium, providing corresponding emission wavelengths [4–6]. Even for a single state of matter, the gain medium can be of different forms, such as ceramic, single crystals, or an optical fiber, as shown in Figure 1.2.

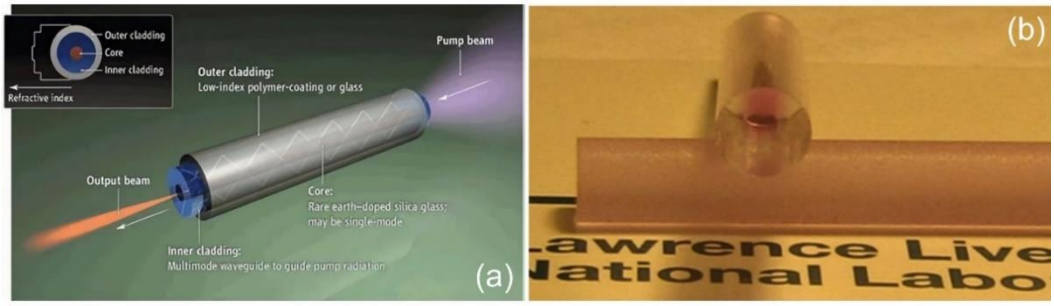

Figure 1.2. (a) Working principle of a fiber laser; **[7]**(b) 3D printed transparent ceramic YAG laser rods with central Neodymium doping **[8]**.

The tabular information about the different laser types, emission wavelength, modes of operation, and their typical applications are shown in Figure 1.3.

1.4.1 Principle of LASER

In an atomic system, the electrons can occupy different energy states. Once the electrons absorb energy from an external source, such as through pumping, the electrons must eventually release energy to regain the lowest stable ground state of the system. The emission of the absorbed energy during the excited-to-ground state transition could occur through two different photon emission pathways, spontaneous and stimulated emissions [9,10].

The former is a quantum mechanical process wherein the excited state of the system transits from excited states to the lower energy levels through photon emission in a stochastic manner without any need for external stimulation [11]. The stimulated emission occurs in a timescale of about 10^{-8} s after excitation [10]. The number of photons in the excited state at time t is given by the following:

$$N_2(t) = N_2(0)\ exp\left(\frac{-t}{\sigma_{21}}\right) \tag{1}$$

Laser Type	Mode of Operation	Wavelength Range	Applications
Gas Lasers			
CO2 Laser	Continuous	9.2 - 10.8 µm	Cutting, engraving, welding, medical procedures
He-Ne Laser	Continuous	632.8 nm	Alignment, holography, spectroscopy
Argon Laser	Continuous	488 - 514.5 nm	Confocal microscopy, flow cytometry, laser light shows
Excimer Laser	Pulsed	Varies (e.g., ArF-193 nm)	Eye surgery, microfabrication, semiconductor manufacturing
Solid-State Lasers			
Nd:YAG Laser	Continuous or Pulsed	1.064 µm	Material processing, laser marking, tattoo removal
Ruby Laser	Pulsed	694.3 nm	Dermatology, research, rangefinding
Titanium-Sapphire Laser	Continuous or Pulsed	650 - 1100 nm	Biomedical imaging, spectroscopy, ultrafast science
Fiber Lasers			
Ytterbium Fiber Laser	Continuous or pulsed	1.06 µm	Material processing, laser cutting, welding
Erbium Fiber Laser	Continuous or pulsed	1.5 µm	Telecommunications, medical procedures
Diode Lasers			
Semiconductor Laser	Continuous	Varies	Data transmission, barcode scanners, laser printers, gain medium pumping
Dye Laser	Pulsed	Varies	Spectroscopy, laser-induced fluorescence, research

Figure 1.3. Different types of lasers with their output characteristics and common application.

On the other hand, when the excited electronic states interact with photons, it becomes possible to relax through an alternative mean, namely stimulated emission. The stimulated decay occurs only when the interacting photon has an energy difference equivalent to the energy difference between the excited and ground state. The above phenomenon results in the amplification of coherent and monochromatic photons. Therefore, if the atomic energy levels could be maintained to support stimulated emission, then it leads to light amplification by stimulated emission of radiation or LASER.

For the stimulated emission to dominate, the gain medium must support population inversion [12,13]. For a material with N_1 atoms in the ground state at energy E_1 and N_2 atoms in the higher energy level E_2, the equilibrium Boltzmann distribution dictates a more significant population in the ground state given by the relation $N_1 > N_2$. These intermediate unique energy levels (E_2) that could accumulate excited electrons are called metastable states, with a relatively long lifetime [14,15]. Therefore, the laser-active medium has to be carefully designed to include metastable states for the accumulation of electrons in the higher energy orbitals, which could result in stimulated emission in the presence of seed photons, as shown in Figure 1.4. The incoming seed photons of appropriate energy modify the probability function of the high-level orbitals, thereby temporarily destroying the metastability and increasing the probability of de-excitation [16,17].

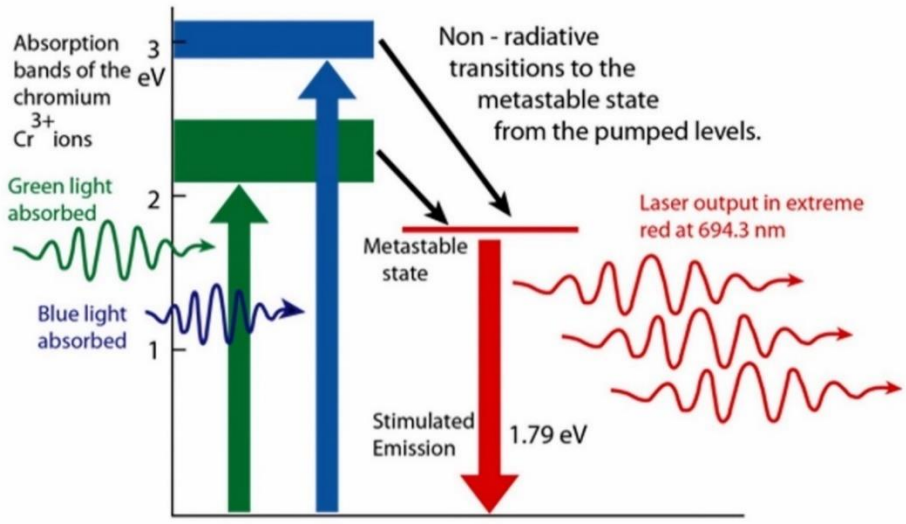

Figure 1.4. Illustration of pumping levels of a Ruby laser demonstrating metastable state **[18]**.

As previously shown in Figure 1.1, the amplified emission of coherent photons is by design situated in the optical cavity, which supports multiple passes through the gain medium. The following relationship gives the positive intensity variation of emitted photons along the laser gain medium,

$$\frac{dI(z)}{dz} = \sigma_{21}\ \Delta N\ I(z) \tag{2}$$

where the intensity variation dI is determined by the stimulated emission cross-section σ_{21} and ΔN, which is the population inversion.

The gain medium with the appropriate metastable energy level is excited (pumped) using an external energy source such as an electric discharge, flash lamp, or another laser source to obtain lasing [19,20]. The gain medium would support population inversion due to the available metastable levels with relatively large decay times [21,22]. Consequently, stimulated emission would be supported, leading to a cascade of photons in the process. This process reaches equilibrium in a resonant optical cavity, providing a stable output from the partially transparent cavity mirror/grating, as shown in Figure 1.5.

To briefly summarise, the three fundamental requirements for the functioning of a laser are the following:

(i) **Pumping Source**: An external source that is necessary to excite the gain medium, which is the primary step for the gain medium to perform lasing.

(ii) **Gain medium**: As the heart of the laser, the gain medium is selected with appropriate metastable energy levels with a greater decay time that supports population inversion of excited energy levels, consequently resulting in stimulated emission. The desired output wavelength is the energy difference between the metastable and ground states.

(iii) **Optical resonator**: An optical cavity arrangement with reflecting mirrors at the ends and the gain medium in between that supports optical gain. The optical setup is designed to support optical feedback so that the overall optical gain exceeds the cavity losses.

Hence, resulting in light amplification by stimulated emission of radiation (LASER).

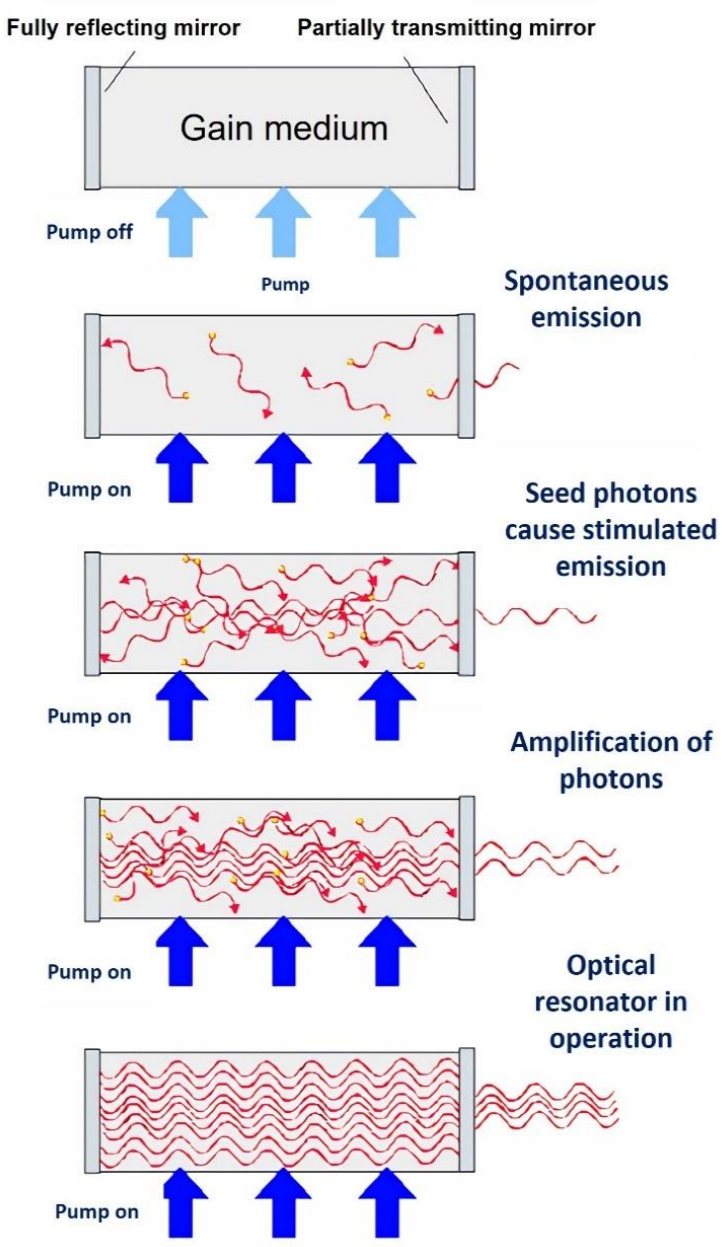

Figure 1.5. Principle of laser action from gain medium pumping to a stable optical output **[23]**.

1.5 Laser Beam Characteristics

Laser technology is of prime importance today, with applications ranging from fundamental studies to daily life appliances. This importance is mainly due to the laser beam's unique characteristics that set it apart from any other light source. The main characteristics of a laser beam are detailed below.

Monochromaticity and Line Broadening

Monochromaticity is related to the fact that only photons matching the energy gap between excited and ground states can be amplified in the cavity. However, monochromaticity is a relative term, and in essence, the bandwidth of laser light is very narrow compared to broadband light sources like LED or solar radiation.

Line broadening corresponds to the spectral linewidth, or the wavelength range emitted by the laser. A variety of factors could contribute to the line broadening. Overall, the broadening effect can be broadly classified into two categories, namely homogeneous and inhomogeneous broadening. They could be further subdivided based on the specific cause.

(i) Homogeneous broadening occurs due to the local environment and interaction of atoms/molecules throughout the laser gain medium. The main causes are the following:

- Natural broadening: Also called Lorentian broadening, it is caused by the uncertainty of atomic energy levels [24]. The broadening linewidth (Γ) is given by $\Gamma=1/T_2$, where T_2 is the radiative lifetime of the excited state.

- Collisional broadening: This occurs as a result of gain medium particle interaction, where the broadening linewidth (Γ) is given by $\Gamma= \gamma \times P$, where γ is the broadening coefficient, and P is gas medium pressure [25].

- Pressure broadening: This occurs due to the pressure variations in the gain medium [26].

(ii) Inhomogeneous broadening occurs due to the variation in the local environment within the gain medium. A common type is Doppler broadening, arising from the random thermal motion of the atoms and molecules. Also, Zeeman and Stark broadening exists due to local magnetic and electric field effects [26].

Coherence (Temporal and spatial)

The coherence of a laser beam is associated with the correlation of its optical phase over the cross-section of the beam (spatial) or at different time intervals (temporal). More detailed definitions can be given as follows:

(i) Temporal Coherence: Also known as longitudinal coherence, it refers to the degree of correlation at different points in the beam's temporal profile (waveform). A high temporally coherent beam would naturally imply consistent frequency or wavelength with minimal phase fluctuation [27]. High temporal coherence makes lasers ideal for interferometric or holographic applications.

(ii) Spatial coherence refers to the consistent and predictable phase correlation between different points in the beam wavefront, characterizing the wavefront stability [28]. Practically, this translates to tightly focused and well-collimated beam properties.

Laser beams are both temporally and spatially coherent. Figure 1.6 illustrates the concepts of spatial and temporal coherence for a laser wavefront.

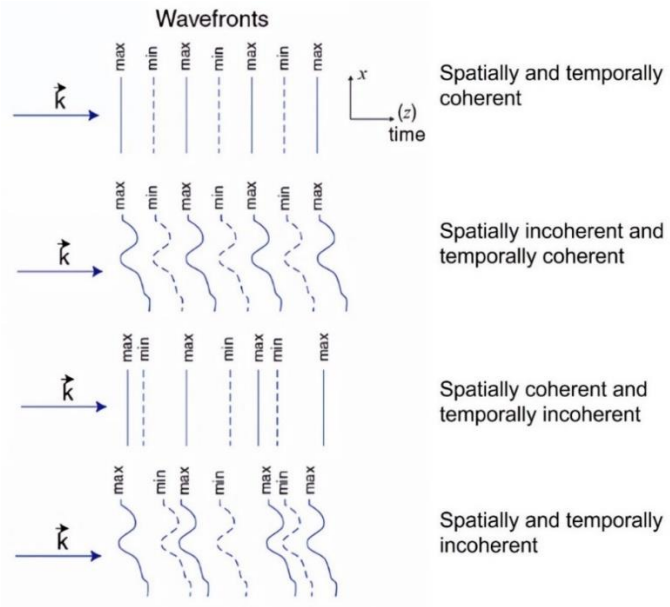

Figure 1.6. Illustration of spatial and temporal coherence of a wavefront **[29]**.

Low divergence

The low divergence of laser beams results in the high directionality of the laser beam. It is a direct consequence of the laser generation inside the resonant cavity, where only the wave propagation along the appropriate optical axis can result in the resonance property [30]. This directionality makes delivering optical energy over relatively long distances along a designed optical path possible.

Radiance (Brightness)

The radiance of the laser is defined as the power emitted per unit surface area per unit solid angle. The radiance of the laser beam is given by

$$B = \frac{4P}{\pi\theta D^{2}} \tag{3}$$

where B represents the brightness or radiance, P is the beam power, D is the diameter of the circular beam cross-section, and θ is the beam divergence angle.

1.6 Modes of Laser Operation

Apart from the materials that constitute the active medium, the configuration of a laser cavity gives different modes of laser operation. In particular, the temporal profile of the laser emission, even at the same wavelength, is paramount since it may determine different outcomes on its interaction with materials. Below, the main modes of laser operation are reported and described in their characteristics and features for materials processing.

1.6.1 Continuous Wave (CW)

In this operation mode, the optical output from the laser cavity is relatively constant in time for a continuously pumped cavity. Since the laser output is continuous, the mode is also known as *free-running mode*. They have wide applications in various fields, such as scientific research, materials processing, additive manufacturing, biomedical applications, communication, and fiber optics. For example, CO_2 lasers are extensively used industrially for cutting, welding, surface heat treatment, and engraving on different material types [31]. Their high average power and long wavelength make them also ideal for medical applications such as dermatology, tumour ablation, dentistry, and surgery [32].

1.6.2 Pulsed Operation

In this operation mode, the optical output is restricted to a specific timescale, generating an optical pulse. These optical pulses are separated spatiotemporally, and a pulse repetition rate defines the number of such optical pulses that cross a fixed point in space per unit of time. The temporal restriction of the pulse can be varied from milliseconds to femtoseconds, depending on the technique used for pulse generation. Due to the relatively short temporal width of the pulse, even microjoules of pulse energy can deliver a peak power of gigawatts range, in the case of femtosecond laser [33,34]. Pulsed laser systems have tremendous applications in micromachining and fundamental scientific research. Two techniques for the generation of short (nanosecond) and ultrashort (femtoseconds) pulses are described in the following:

Mode-locked Operation

This operation takes advantage of multiple longitudinal oscillating modes in the laser cavity. The longitudinal modes are independent of each other and maintain a fixed phase relationship during the cavity round trip. Therefore, destructive/constructive interference amongst the longitudinal modes occurs spatially, as shown in Figure 8. An active (electro-optic) or passive (saturable absorber) modulation element in the cavity amplifies only the constructive interference amongst the modes [35]. The effect resembles an optical pulse performing round trips along the cavity. As a direct consequence of the constructive interference, this technique generates ultrashort pulses of femtosecond to few picosecond timescales [36]. The pulsewidth of the mode-locked laser output is given by the following formula:

$$\Delta t_{pulse} = \frac{(0.44 \ \ \tau)}{\sqrt{N}} \tag{4}$$

where Δt_{pulse} is the pulsewidth, and N is the number of longitudinal laser modes [37]. Figure 1.7 depicts the ultrashort pulse generation through constructive interference of the longitudinal modes.

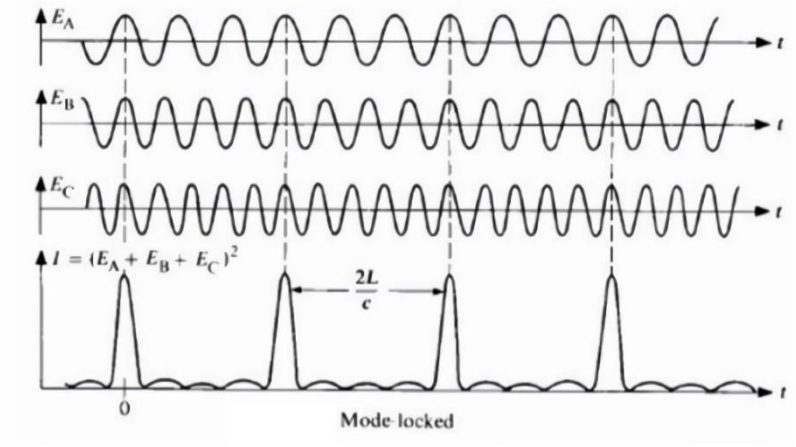

Figure 1.7. Constructive and destructive interference between different longitudinal modes in a laser cavity results in pulse generation **[38]**.

Q-switched Operation

Q-switching is a standard mode used to generate nanosecond and long picosecond pulses. An additional attenuator in the optical cavity controls intracavity loss. Figure 1.8 illustrates the working principle of Q-switching in a schematic diagram.

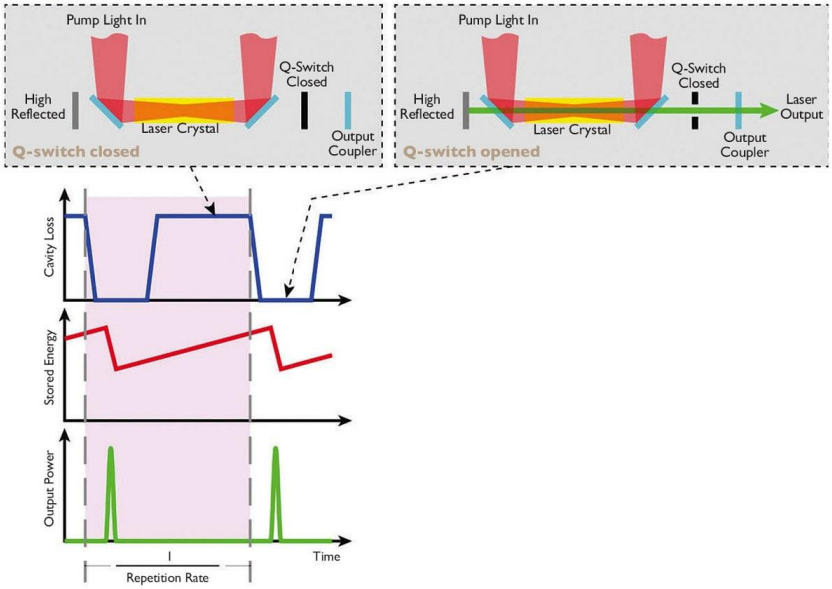

Figure 1.8. Schematic diagram representing the working principle of Q-switching in a laser cavity **[39]**.

The attenuator, while in function, cause resonator loss and reduce the resonator quality (Q) factor. However, upon inhibition, the resonator Q factor increases, resulting in lasing and optical output. Also, when the attenuator is in function, the cavity is simultaneously pumped, resulting in maximum energy stored in excited states of the gain medium [38]. The frequency of active or passive modulation of the attenuator provides optical pulses of the corresponding timescale at the output.

1.7 Laser-Matter Interaction

Depending on the material type, the laser beam interaction with the material would result in reflection, absorption, and transmission. The material property defines the resulting propagation or energy transfer of the incoming beam. During beam propagation within the material, the Beer-Lambert law defines the optical intensity at a specific depth given by,

$$I(z) = I_0 e^{-\alpha z} \tag{5}$$

where I_0 is the incident beam intensity, and α is the material absorption coefficient [40]. The absorption coefficient of a material is a function of the wavelength of the incident light, as shown in Figure 1.9 and, generally, is higher for ultraviolet (UV) wavelengths followed by visible and near-infrared (NIR) wavelengths [41].

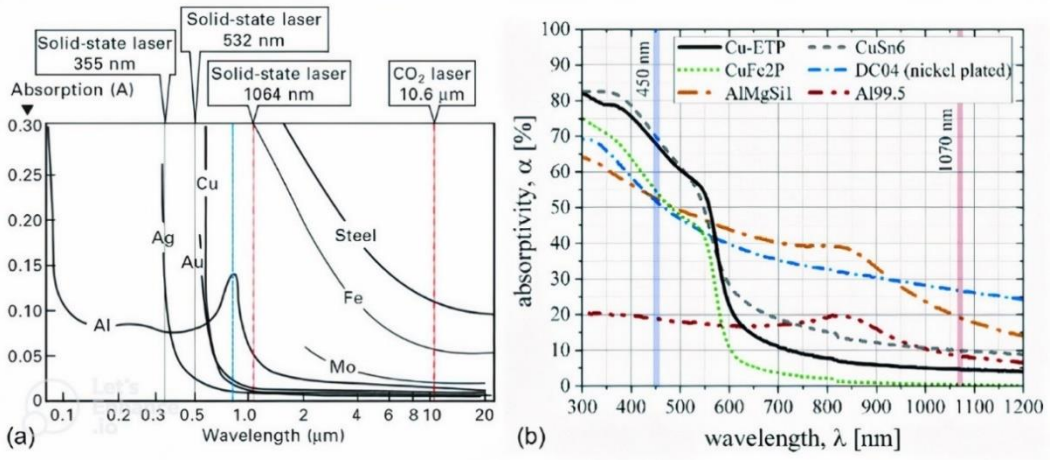

Figure 1.9 The absorption coefficient of different materials in (a) broad spectrum; (b) UV to NIR spectral region **[42]**.

In the case of UV-pulsed laser interaction, the photon energy is relatively high and can cause direct interband energy transitions. This phenomenon facilitates a rather cold ablation of materials compared to infrared wavelengths with predominant thermal effects [43]. In addition, a short wavelength allows to achieve smaller focal spots, which can be of great interest for micromachining applications [44].

During the laser pulse interaction with the material, the first to respond to the intense electric field is the electronic system of the material through excitation from the valence to the conduction bands [45]. This event occurs in a very short timescale of tens to hundreds of femtoseconds, as shown in Figure 1.10.

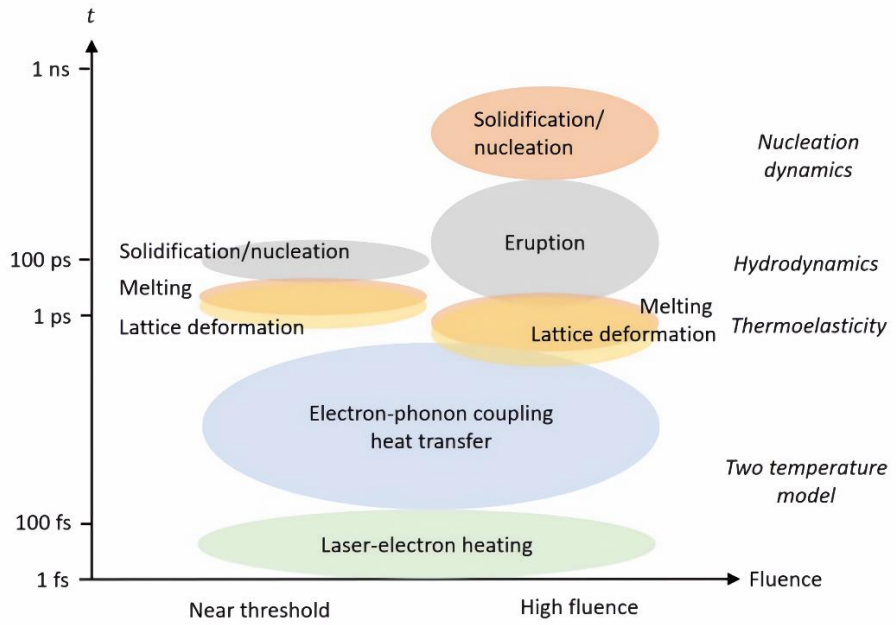

Figure 1.10. Timescale of different phenomena and corresponding physics in volved in femtosecond laser interaction of solids **[46]**.

The rapid transition of valence electrons generate a non-equilibrium state in the material, instantly generating a separate electron and lattice (i.e., ions) systems in terms of energy, where the lattice is still cold as the hot electrons are generated [47]. This non-equilibrium results in a chain of subsequent processes that finally culminate in material ablation or melt-resolidification and is highly influenced by the intensity and temporal characteristics of the interacting pulse. Therefore, based on the temporal width of the interacting pulse, the material interaction dynamics are separately discussed as ultrafast (i.e., femto/picosecond) and long-pulsed (nanosecond) regimes in the following sub-section . The rapid thermalization of the electron sub-system and the eventual energy transfer leading to the thermal evolution of the lattice sub-system can be described by a two-temperature model given below [48]:

$$C_e \frac{\partial T_e}{\partial t} = -\frac{\partial Q\ z}{\partial z} - \gamma\ T_e - T_i\ + S \tag{6}$$

$$C_i \frac{\partial T_i}{\partial t} = \gamma\ T_e - T_i \tag{7}$$

$$Q(z) = -\, k_e\, \partial T_e / \partial z, S = I(t) A e^{\alpha z} \tag{8}$$

where z represents the direction of laser propagation, perpendicular to the target surface, S is the laser source term, $Q(z)$ represents heat flux, C_e and C_i represents the heat capacities of the electron and lattice subsystems, respectively, A is the surface transmittivity, γ is a parameter representing electron-lattice coupling, and α is the absorption coefficient of the material.

1.7.1 Ultrafast Laser Interaction

The advantage of ultrafast laser interaction is the ability to modify even transparent dielectric materials through non-linear photoionization mechanisms [49,50]. In the case of ultrafast optical pulses with photon energy below the material band gap, the non-linear photoionization occurs through multiphoton or tunneling ionization, as shown in the Figure 1.11. The Keldysh parameter defined the dominance of the corresponding ionization mechanism through the following equation [50],

$$\gamma = \frac{\omega}{e}\sqrt{\frac{m_e c n \epsilon_0 E_g}{I}} \qquad \gamma = \begin{cases} > 1.5, & \text{Tunnelling} \\ < 1.5, & \text{Multiphoton} \end{cases} \tag{9}$$

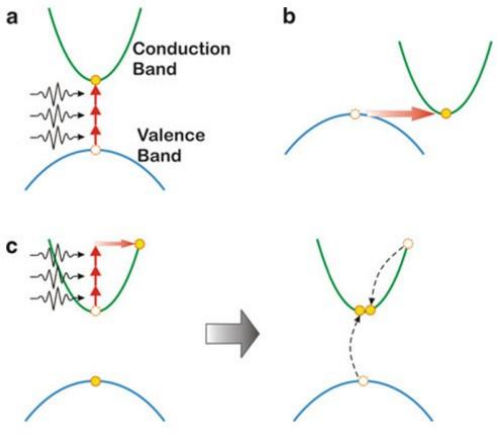

Figure 1.11. Schematic demonstrating the different photoionization processes in ultrafast laser interaction with dielectric materials: (a) Multiphoton ionization; (b) Tunnelling ionization, and (c) Impact ionization **[51,52]**.

where ω represents laser frequency, m_e is the effective electron mass, E_g is the material band gap, n represents the material refractive index, and I is the incident laser beam intensity. In general, tunnelling ionization is dominant for high intensity and low frequency, whereas the multiphoton mechanism dominates for low-intensity and high-frequency laser pulse [53]. Once the conduction band is populated, a third ionization mechanism, avalanche ionization, becomes possible [54]. In this phenomenon, multiple photons are absorbed by the conduction band electrons. When the conduction electrons have energy beyond the band gap, they can impact ionize a valence band electron. As the name suggests, this process continues exponentially, increasing the conduction band's population. Figure 2.2 depicts the three different mechanisms of photoionization in dielectrics.

In the case of metals, due to the presence of conduction band electrons, direct photon absorption occurs through Inverse Brehmstrahlung and impact ionization effects [55]. Following the ionization, the material modification proceeds similarly independent of material type. In terms of temporal scale, following the optical excitation, the *e-e* interaction leads to electron thermalization in the order of a few tens of femtoseconds (fs). The electron thermalization is followed by the electron-phonon interaction up to a few picoseconds (ps), eventually elevating the lattice temperature. In commonly used ultrafast micromachining setups, the pulse duration is of the order of hundred femtoseconds to a few picoseconds. Therefore $\tau_e \ll \tau_L \ll \tau_i$, where τ_e is the electron cooling time, τ_L is the pulse duration and τ_i is the lattice heating time. Under such timescale consideration, the electron temperature can be considered quasi-stationary, while the pulse duration is much lower than the lattice heating time resulting in negligibly low lattice temperatures at the end of pulse interaction [56]. The electron and lattice temperatures are then derived from equations (2.3) and (2.4), resulting in the following equations:

$$T_e \simeq \frac{I\,\alpha}{\gamma} exp(-\alpha z) \tag{10}$$

$$T_i \simeq \frac{F\,\alpha}{C_i} exp(-\alpha z) \tag{11}$$

where I and F represent material absorbed intensity and fluence, respectively. Figure 1.12 shows the electron and lattice temperatures and corresponding

electron-lattice equilibrium time with varying pulsewidth interaction on chromium.

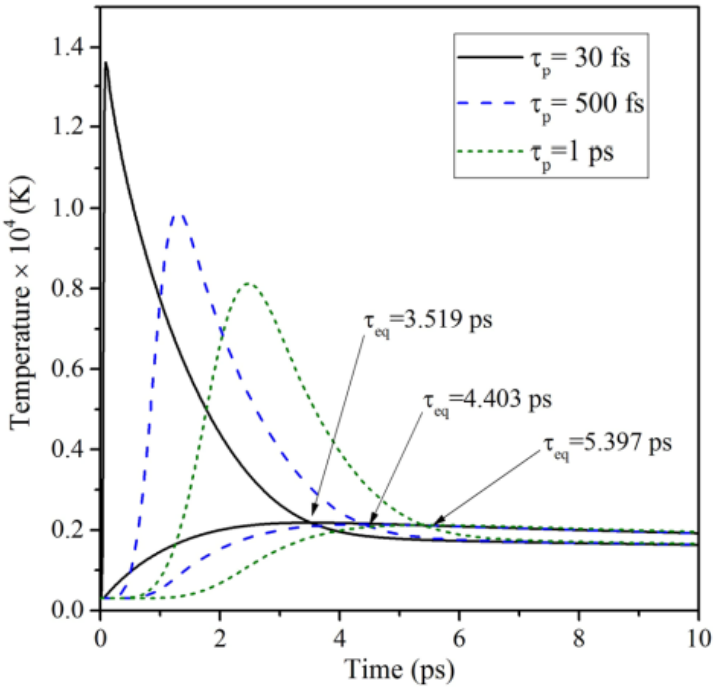

Figure 1.12. Electron and lattice temperature dynamics for different pulsewidth laser interactions on Chromium. The equilibrium time τeq which marks the intersection between the electron and lattice temperature is shown for the different pulsewidths. The lattice temperature is represented by the black curve that begins from below 500 K and rise with a relatively low slope to a maximum of about 2000 K **[57]**.

1.7.2 Nanosecond Laser Interaction

In the case of nanosecond pulses interacting with matter, the condition $\tau_L \gg \tau_i$ is applicable, and equations 6 and 7 reduce to the following equation,

$$C_i \frac{\partial T}{\partial t} = \frac{\partial}{\partial z}\left(k_o \frac{\partial T}{\partial z}\right) + I\alpha\, exp(-\alpha z) \tag{12}$$

In this pulse regime, the electron and lattice systems attain equilibrium early during the laser pulse interaction (tens of picoseconds). In the nanosecond case, the intensity of interaction is of the order of $10^8 - 10^9\ W/cm^2$ and consequently results in minimal ionization [58]. Therefore, unlike the ultrafast regime, transparent materials cannot be modified directly due to the linear photon absorption mechanism.

Due to the long pulsewidth and the linear absorption mechanism, the absorbed optical energy is translated into thermal energy on the interacting surface. The heat penetration depth l_h, defines the extent of thermal diffusion into the target material given by $l_h \sim (D\tau_L)^{1/2}$, where D is the thermal diffusion coefficient [59].

1.8 Dynamic Processes During Nanosecond Laser Interaction

1.8.1 Melt Formation

The energy of the absorbed pulse has a major role in the resulting temperature increase of the surface, due to its ability to deliver greater optical energy that eventually gets transformed to thermal energy. At a specific laser fluence (pulse energy/area), the temperature rise surpasses the material's melting point, resulting in the onset of melt formation. Therefore, fluence above this threshold would induce transient molten material on the surface [60]. Because of this phase transformation, the molten state supports greater mobility of the component species and increased solubility compared to the solid state. Depending on the thermal energy transfer to the surrounding material, radial temperature gradients could develop in the molten region resulting in convection flow. The melt flow generally follows the Marangoni effect, where the liquid surface tension decreases with temperature, resulting in melt flow towards cooler surrounding regions, as shown in Figure 1.13.

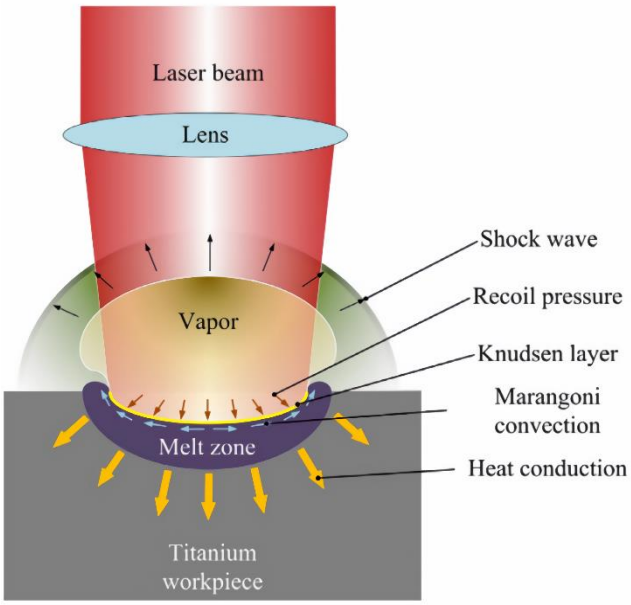

Figure 1.13. Illustration depicting the interaction of nanosecond pulse with a metal (Ti) **[61]**.

1.8.2 Ablation

Ablation refers to the material removal at the surface following laser interaction. Material vaporization initiates the ablation phenomenon above a particular laser fluence threshold [62]. The fluence threshold is material dependent, and in the case of nanosecond pulses, the threshold fluence generally ranges from 1-10 J/cm^2 [63]. With increasing laser fluence, the ablation mechanism could proceed through spallation and phase explosion. Each of these material removal mechanisms is described in the following.

(a) Vaporization

As a first step towards material removal, vaporization occurs when the melt-zone temperature exceeds the material's boiling point. At such a material state, when the surface temperature is below the thermodynamic critical temperature, an intermediate region is formed just above the melt zone called the Knudsen layer [64]. The Knudsen layer is defined by a non-equilibrium distribution of the velocity components, normal to the surface. Above this Knudsen layer, the normal velocity components of vapor molecules possess a uniform distribution. In simulations regarding laser evaporation, the Knudsen layer is treated as a

discontinuity, where the boundary condition provides for coupling between the heat transfer equation of the surface with dynamic gas equations of the vapor phase.

(b) Spallation

This phenomenon is related to the melt dynamics of the target surface. The rapid temperature increase in a confined volume generates compressive stress in the material volume [65]. The propagation of a compressive pressure deeper into the bulk of the interacting surface relaxes the instability wave. Following the compressive wave, an unloading tensile wave is generated [66]. The tensile stress can have sufficient strength to cause solid fracture or sputtering of the molten layer, as shown in Figure 1.14.

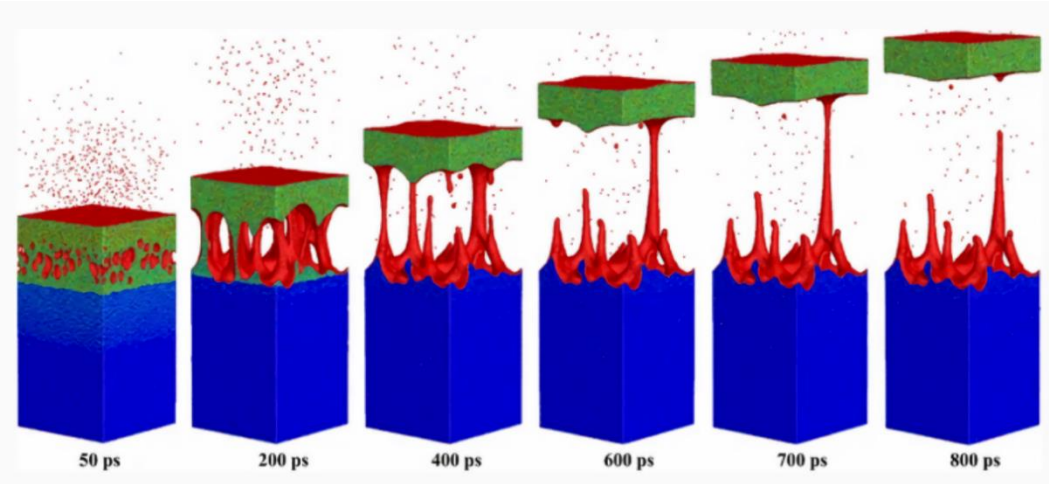

Figure 1.14. Snapshots of material configuration obtained through TTM-MD simulation of 50 fs laser interaction of Cr target. The dark blue region represents the bcc Cr structure, the molten region is shown in green, and the topmost layer and spalled region are represented in red **[67]**.

The ejection of solid particles and liquid droplets due to the stress relaxation dynamics is called spallation or photomechanical ablation [68]. Pulse duration τ_L plays an important role in the case of laser-induced spallation. The spallation effect is dominant for the case where τ_L is lower than the time required for mechanical relaxation of the heated volume (τ_s) [69]. The laser induced melting in a constant volume, thereby resulting in compressive stress build-up, is valid for the following condition,

$$max\{\tau_L, \tau_{e-ph}\} \leq \tau_s \approx \frac{L_v}{C_s} \tag{13}$$

where max is to select the larger amongst the temporal values between pulsewidth and electron-phonon relaxation time.

(c) Phase Explosion

Incident laser fluence above the spallation regime reveals an abrupt change in the ablation behaviour [70]. A homogenous and rapid transition of the heated volume into a liquid-vapor mixture now takes over as the primary mechanism of material ejection. The phase explosion regime is closely correlated and occurs around the thermodynamic critical temperature of the material [71]. In the case of ultrafast pulse interaction, the phase explosion provides greater ablation yield in the region of stress confinement, as shown in Figure 1.15(a).

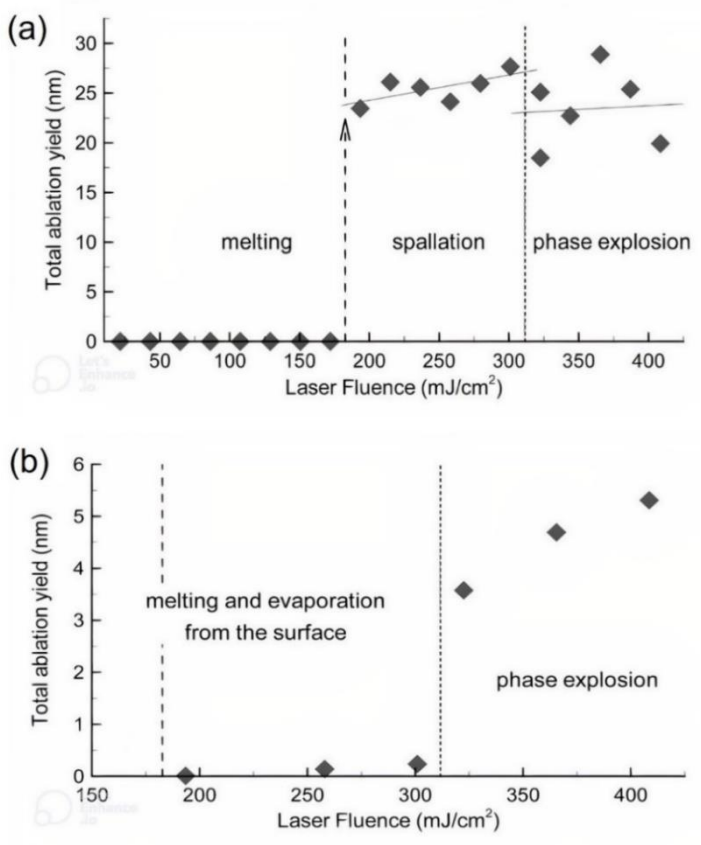

Figure 1.15. Simulation results of total ablation yield on a Ni target as a function of laser fluence for (a) 1ps and (b) 50 ps. The ablation plumes are analyzed at a timescale of 500 ps and 620 ps, respectively **[72]**.

Figure 1.15 demonstrates the difference in ablation characteristics for laser pulses of different temporal widths. However, in the case of long pulse interaction, a direct transition from vaporization to phase explosion at the material's critical temperature is more probable due to the pulse's relatively low-stress confinement ability. This is because the stress build-up in the confined region during initial pulse interaction is not maintained as the material expansion occurs during the later part of the pulse. The continuous heating by the long pulse ensures low-pressure build-up in the confined interaction region [73].

In the case of pulses longer than nanoseconds, the material removal dynamics follow the latter case of direct transition from vaporization to phase explosion. After laser ablation, plasma formation occurs and expands even after the laser pulse ceases.

1.8.3 Laser-Induced Plasma

The rapid energy transfer followed by an electron-phonon interaction results in the generation of neutral and ionic species. Ionized atoms, molecules, ejected metal vapor, and molten particles form the primary plasma above the interaction surface. After the primary plasma formation, the plasma dynamics involve the expansion process. The plasma expansion occurs in two stages: isothermal expansion and adiabatic expansion. In the case of isothermal expansion, the laser pulse interacts with the target surface. Consequently, the neutral/charged species comprising the primary plasma partially absorb the optical energy through inverse Bremsstrahlung and photoionization mechanism. Therefore, simultaneously, the target surface acts as a source for the expanding plasma while the laser absorption acts as the heat source for the expanding plasma. The convection pushes the plume forward because of non-equilibrium in temperature distribution, compressing the air and generating a shockwave. This debris causes a barrier in the case of multi-pulse interaction, where the plume partially absorbs the following pulse, creating a plasma shielding effect. However, once the laser pulse ends, the second stage of plasma expansion, namely adiabatic expansion, sets in. In this stage, due to the more significant plume pressure compared to the surrounding, the plasma front continues to expand with decreased temperature and density. This stage eventually leads to plasma cooling. Figure 1.16 shows the plasma plume evolution upon infrared nanosecond laser interaction with the aluminum target.

Apart from the plasma dynamics, laser parameters also influence the plasma characteristics. A study conducted by Bogaerts et al. reported that the plasma plume expansion increased from $0.1\ mm$ to $0.8\ mm$ at a corresponding irradiance increase from $3 \times 10^9\ W/cm^2$ to $3 \times 10^9\ W/cm^2$ [74]. Also, several researchers have studied the effect of laser wavelength on plasma formation and absorption. The plasma absorption at 1064 nm was found to be lower than at 532 nm and 266 nm, even though the inverse Bremsstrahlung absorption coefficient was significantly higher at IR wavelengths [75]. This effect could be explained by the considerably low density of the plasma due to the low absorption of IR wavelength by the target material.

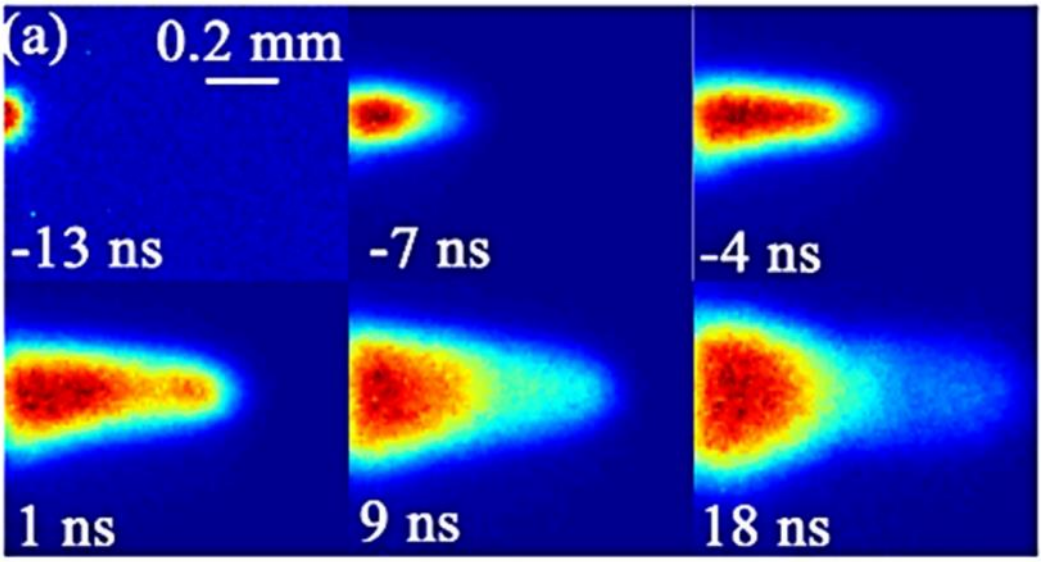

Figure 1.16. Spatio-temporal evolution of plasma plume by nanosecond laser interaction with Al at a fluence of 2.3 J/mm^2 **[76]**.

1.9 Pulsewidth Effect on Precision Machining

Because of the electron-phonon energy transfer dynamics, the surface modification features differ by a large extent between ultrafast and long-pulsed laser interaction. A critical evaluation factor for precision machining is the heat-affected zone (HAZ). The long-pulsed laser modifications display strong evidence of HAZ, thereby generating detrimental effects on desired surface modification. The presence of an interacting laser pulse during lattice energy transfer causes a

temperature increase in the vicinity of the focal spot. This effect generally causes a gradient in surface modification features through the thermalization-induced melting and vaporization of even the surrounding regions to the focal spot. Figure 1.17 shows the electron microscope images of surface modifications generated on a monocrystalline sodium chloride surface by a nanosecond laser (16 ns) and a femtosecond laser (300 fs), respectively. In the case of the nanosecond laser modification, cracks, roughness, recast, and irregular modification boundaries are usually observed.

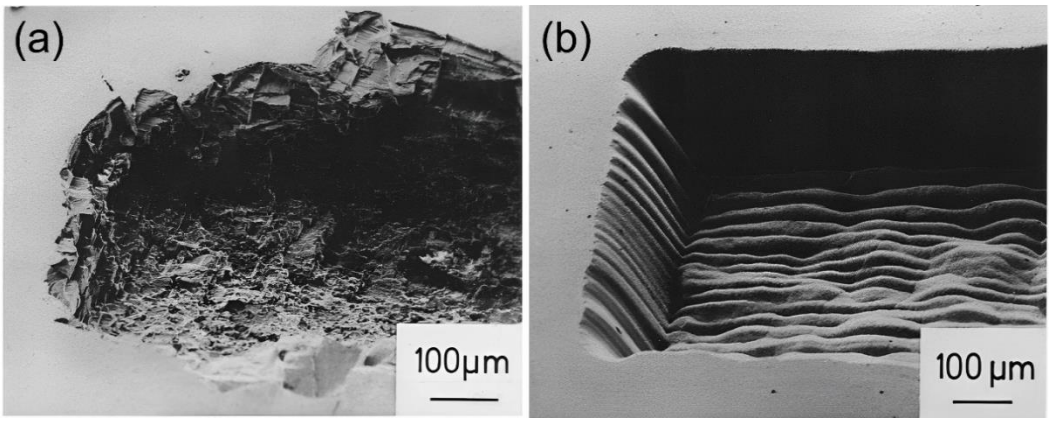

Figure 1.17. Scanning electron micrographs of laser ablation on crystalline sodium chloride (NaCl) using an excimer laser (248 nm) (a) nanosecond pulses (16 ns); (b) femtosecond pulses (300 fs) **[77]**.

In addition to precise surface machining, ultrafast lasers hold the unique ability to process dielectric materials in the material bulk, opening a plethora of applications ranging from waveguide and microfluidic channel writing in glasses to micro-optics generation in bulk polymers. Another interesting ability of the ultrafast laser is the two-photon polymerization (TPP). TPP is a non-linear process that enables the creation of complex 3D architecture on polymer resins. The high intensity at the focal volume initiates the non-linear two photon absorption process. Following the excitation of the lattice system, the polymerization reaction occurs depending on the photoresist used. The interaction region at the laser focal spot is photopolymerized, and the non-polymerized photoresist is removed later. The above-mentioned abilities of the ultrafast laser interaction make this technique suitable for fabricating MEMS for lab-on-chip applications. Gregor Weisgrab et al. developed a special photosensitive resin for TPP to fabricate complex constructs for homogeneous cell invasion and matrix deposition, as shown in Figure 1.18.

Furthermore, the biodegradable scaffold fabrication technique with optimized laser parameters supports large-scale fabrication. Yanlei Hu et al. reported a highly efficient strategy to fabricate an aspheric microlens array using holographic femtosecond laser-induced photopolymerization [78]. In the above study, the characteristics of the spatial light modulator on the pattern reconstruction are analyzed to fabricate closely packed microlens arrays with desired optical properties.

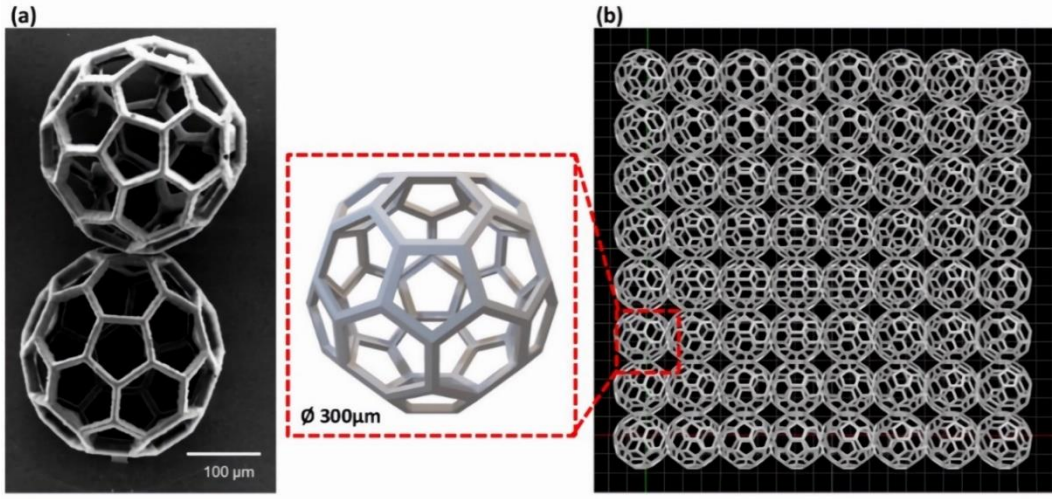

Figure 1.18. Design of a buckyball-based scaffold from poly (trimethylene-carbonate) using TPP. (a) SEM images of buckyball printed at optimum laser parameters; (b) 3D render of the scaffold to be printed in an 8×8×8×3 array **[79]**.

Compared to cleanroom-based complex fabrication techniques such as photolithography, ultrafast laser machining and lithography offer a relatively simple 3D fabrication technique with dimensional accuracy and excellent control of the shape and sizes.

However, when it comes to surface fabrication, a few drawbacks need to be addressed by ultrafast laser machining to realize large-scale fabrication at an industrial scale. Firstly, ultrafast laser systems are still expensive (100s kEUR) when considering large-scale use; however, with the advancement in laser technology, these systems are becoming more and more inexpensive. Secondly, due to the low average power of the output, the processing rate and throughput of these laser systems is very low, which is yet another bottleneck toward large-scale implementation. Especially for generating micro-features, long pulsed laser systems offer an advantage in terms of processing speeds, trading off some

processing quality when compared to femtosecond systems. In this context, nanosecond laser systems provide an excellent alternative for surface processing of materials. These systems are relatively inexpensive (10 kEUR) and are well-established in the industry. Although these systems generate thermal effects such as HAZ, with appropriate control of laser parameters, the modifications could be of desired quality in large-scale fabrication. Secondly, in specific applications, the thermal effects generated by nanosecond laser can be used to advantage for enhanced surface functionalities. The following section describes a few studies that have used nanosecond laser-based modifications for interesting functional materials applications.

1.10 Nanosecond Laser Micromachining: A Viable Alternative

Nanosecond micromachining is generally considered for standard industrial processing requirements such as cutting and marking different materials. However, these systems can be a prominent alternative to ultrafast systems, especially in the domain of functional surface fabrication, such as superhydrophobic and anti-reflective surfaces. In the last decade, with the improvement in fiber laser technology and master oscillator power amplifier systems (MOPA), industrial laser systems with variable pulse width and high repetition rate (i.e., $500\ kHz$) have been realeased in the commercial nanosecond laser segment. This tunability of the laser parameters enables to control the resulting thermal effects on the target substrate up to an appreciable extent, thereby facilitating a relatively precise modification with reduced HAZ.

Broadband near completely absorbing surfaces offers a variety of applications for anti-reflecting surfaces, energy harvesting, and imaging in low light conditions. For example, antireflective surfaces can be useful for the conversion of photoelectric or photothermal conversion efficiency of solar installations, stealth properties of military devices, and low light imaging. The common approach of coating and deposition for anti-reflection on metallic surface face long-term performance challenges due to degradation with time. As an alternative, laser micromachining can be sued to fabricate micro-nano-structured surfaces directly onto the metal surface. Additionally, the natural hierarchical nature of the surface due to the thermal effect provides efficient light-trapping within the structures, as shown in Figure 1.19. Abu Taher et al. used a nanosecond laser $(532nm)$ to generate hierarchical nanostructures consisting of nanorods,

nanoparticles, and nanocavities on a stainless-steel substrate. The hierarchical substrate displayed efficient anti-reflecting properties with less than 0.5% specular reflection in a broadband range of $250 - 1800\,nm$. In another study, nanosecond $(532nm)$ was used to generate optimized surface features on copper with broadband absorption at 98.9% $(220 - 800nm)$ and 91.9% $(220 - 2500nm)$. The laser processed surfaces exhibit high photothermal conversion efficiency at 52% under 15 sun illuminations, which resulted in great improvement of desalination efficiency.

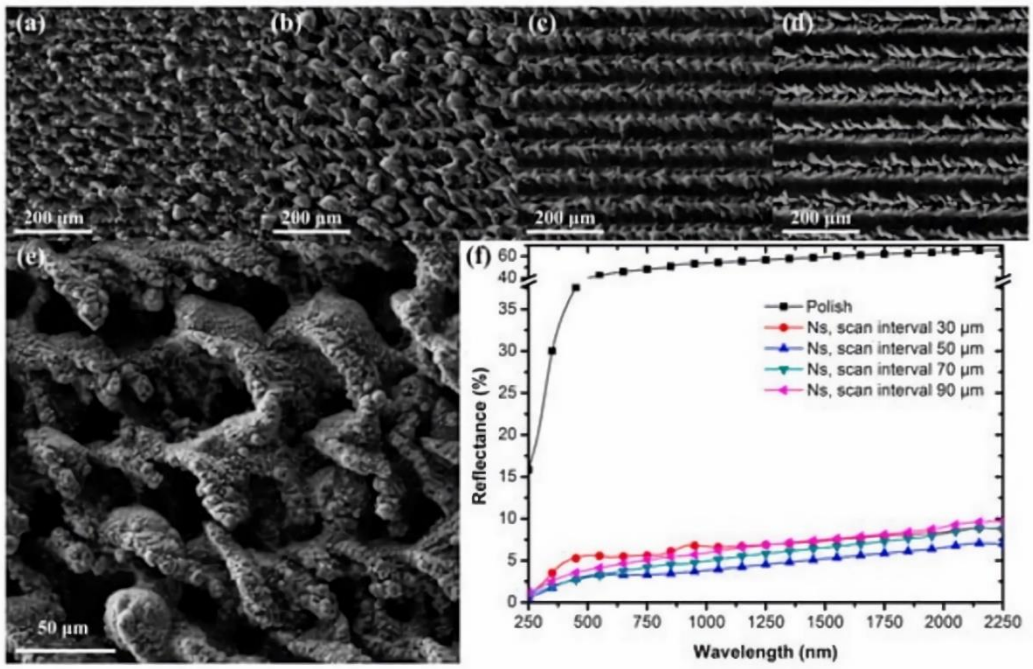

Figure 1.19. SEM images of microstructures generated on a Ti-6Al-4V alloy using a nanosecond laser (532 nm) at different scan intervals; (a) 30 µm; (b) 50 µm; (c) 70 µm; (d) 90 µm; (e) enlarged image of modification corresponding to (b); (f) comparison of the corresponding reflectance values **[80]**.

In the domain of nanostructuring, laser-induced periodic surface structures (LIPSS) have generated tremendous interest for various functional applications ranging from anti-bacterial, improved cell adhesion, anti-icing, and drag reduction. Even though the formation mechanism of LIPSS has not been clearly understood, the surface plasmon polariton model is the widely used explanation for the phenomenon. Most studies involving LIPSS have generally focused on using ultrafast lasers with reduced thermal effects to generate self-arranged uniform surface nano-features.

Interestingly, nanosecond lasers are generally avoided for precision machining, and nanostructuring can generate LIPSS features, as shown in Figure 1.20. However, relatively few studies have reported using nanosecond laser-based LIPSS to fabricate functional surfaces. P Nürnberg et al. generated LIPSS on SiO_2 layers and reported a continuous transition from parallel to perpendicular orientations with increasing oxide thickness [81]. T Karkantonis et al. generated $sub-500\,nm$ LIPSS on the stainless steel surface [82]. The effect of the processing gas environment was also analyzed in the above study, where the argon environment enhanced the LIPSS quality by minimizing laser-induced oxidation.

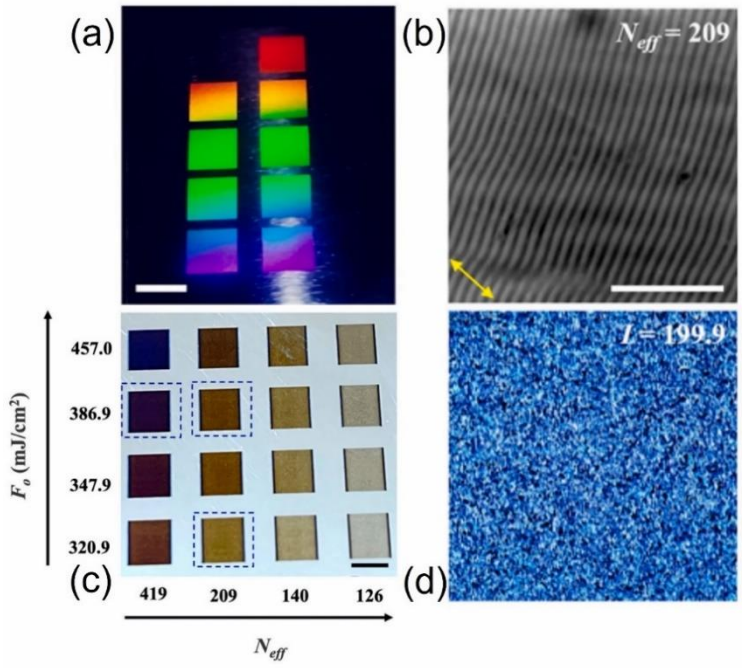

Figure 1.20. (a) Optical image of diffraction colors from the LIPSS surface on stainless steel (SS); (b) SEM image of the LIPSS pattern at an effective pulse number of 209 at a pulse fluence of 17.1 mJ/cm^2; (c) matrix showing color generation due to oxidation on SS at higher pulse fluences; (d) blue light diffraction image corresponding to (b) **[83]**.

Another advantage of a relatively long pulsed nanosecond laser is in stealth dicing of silicon. It is well known that the ultrashort pulse duration is advantageous for bulk processing of dielectrics such as glass; however, the same does not translate well in the case of silicon. The extremely high non-linear coefficient of silicon cause filament formation along with prefocal absorption. This results in the formation of an under-dense plasma with insufficient electron density to cause material modification in the silicon bulk. However, long-pulsed

nanosecond laser does not exhibit such behavior and can be effectively used for wafer dicing, fabrication of microfluidics, waveguides, and holograms in the silicon bulk, as shown in Figure 1.21.

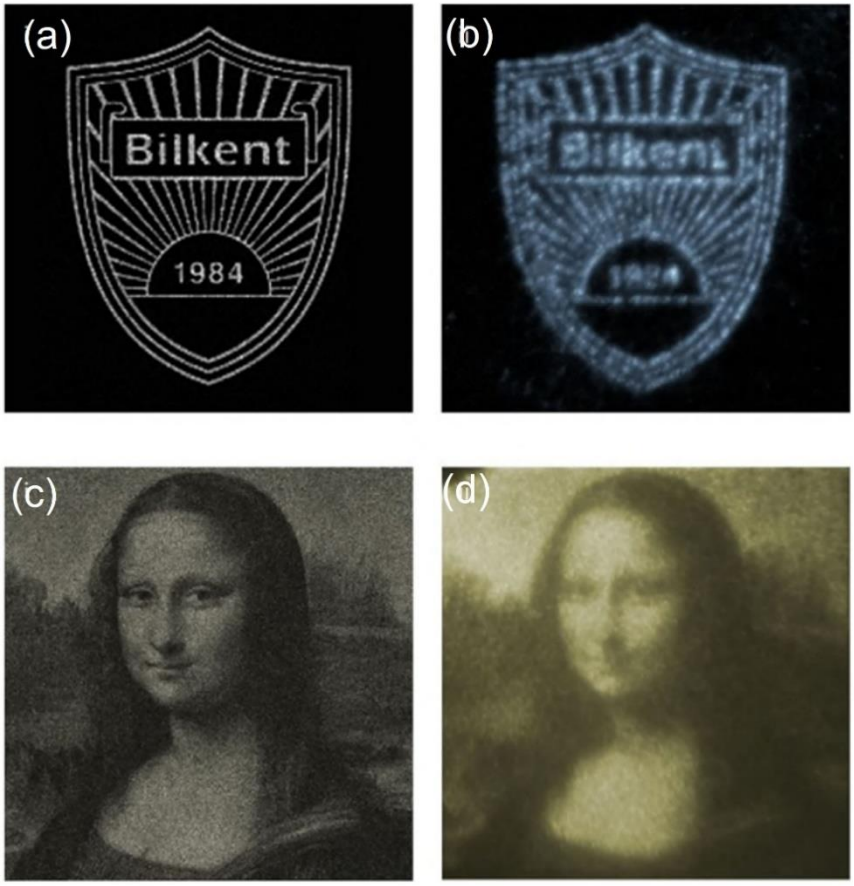

Figure 1.21. Nanosecond laser (1.55 μm, 5ns) based bulk machining in silicon (a,b) Simulation of a binary image with high-frequency spatial components and corresponding holograms written in silicon; (c,d) greyscale image of Mona Lisa by Leonardo da Vinci and the corresponding hologram written in silicon **[84]**.

The work presented in this thesis consists study of laser interaction on different materials such as metals, glass, ceramics, and polymer. Since it would be confusing to have the materials and methods together in a single section, the major processing and analysis instruments and techniques used in this study are outlined in the Appendix section. However, specific materials and techniques are otherwise introduced in the appropriate chapter of description.

References

1. Barré, N.; Romanelli, M.; Lebental, M.; Brunel, M. Waves and Rays in Plano-Concave Laser Cavities: I. Geometric Modes in the Paraxial Approximation. *Eur. J. Phys.* **2017**, *38*, 034010, doi:10.1088/1361-6404/aa6461.
2. Feng, T.; Jiang, M.; Ren, Y.; Wang, M.; Yan, F.; Suo, Y.; Yao, X.S. High Stability Multiwavelength Random Erbium-Doped Fiber Laser with a Reflecting-Filter of Six-Superimposed Fiber-Bragg-Gratings. *OSA Continuum* **2019**, *2*, 2526, doi:10.1364/OSAC.2.002526.
3. Blázquez-Castro, A.; Fernández-Piqueras, J.; Santos, J. Genetic Material Manipulation and Modification by Optical Trapping and Nanosurgery-A Perspective. *Front. Bioeng. Biotechnol.* **2020**, *8*, 580937, doi:10.3389/fbioe.2020.580937.
4. Tian, F.; Ikesue, A.; Li, J. Progress and Perspectives on Composite Laser Ceramics: A Review. *Journal of the European Ceramic Society* **2022**, *42*, 1833–1851, doi:10.1016/j.jeurceramsoc.2021.12.061.
5. Abu Hassan, M.R.; Yu, F.; Wadsworth, W.J.; Knight, J.C. Cavity-Based Mid-IR Fiber Gas Laser Pumped by a Diode Laser. *Optica* **2016**, *3*, 218, doi:10.1364/OPTICA.3.000218.
6. Liu, H.; Sun, S.; Zheng, L.; Wang, G.; Tian, W.; Zhang, D.; Han, H.; Zhu, J.; Wei, Z. Review of Laser-diode Pumped Ti:Sapphire Laser. *Microw Opt Technol Lett* **2021**, *63*, 2135–2144, doi:10.1002/mop.32882.
7. JOHAN NILSSON; DAVID N. PAYNE High-Power Fiber Lasers., doi:: 10.1126/science.1194863.
8. Seeley, Z.; Yee, T.; Cherepy, N.; Drobshoff, A.; Herrera, O.; Ryerson, R.; Payne, S.A. 3D Printed Transparent Ceramic YAG Laser Rods: Matching the Core-Clad Refractive Index. *Optical Materials* **2020**, *107*, 110121, doi:10.1016/j.optmat.2020.110121.
9. Azkargorta, J.; Iparraguirre, I.; Barredo-Zuriarrain, M.; García-Revilla, S.; Balda, R.; Fernández, J. Random Laser Action in Nd:YAG Crystal Powder. *Materials* **2016**, *9*, 369, doi:10.3390/ma9050369.
10. Jeske, J.; Lau, D.W.M.; Vidal, X.; McGuinness, L.P.; Reineck, P.; Johnson, B.C.; Doherty, M.W.; McCallum, J.C.; Onoda, S.; Jelezko, F.; et al. Stimulated Emission from Nitrogen-Vacancy Centres in Diamond. *Nat Commun* **2017**, *8*, 14000, doi:10.1038/ncomms14000.
11. Itoh, T.; Yamamoto, Y.S.; Ozaki, Y. Plasmon-Enhanced Spectroscopy of Absorption and Spontaneous Emissions Explained Using Cavity Quantum Optics. *Chem. Soc. Rev.* **2017**, *46*, 3904–3921, doi:10.1039/C7CS00155J.

12. Wei, G.; Wang, X.; Liao, L. Recent Advances in Organic Whispering-Gallery Mode Lasers. *Laser & Photonics Reviews* **2020**, *14*, 2000257, doi:10.1002/lpor.202000257.

13. Azzam, S.I.; Kildishev, A.V.; Ma, R.-M.; Ning, C.-Z.; Oulton, R.; Shalaev, V.M.; Stockman, M.I.; Xu, J.-L.; Zhang, X. Ten Years of Spasers and Plasmonic Nanolasers. *Light Sci Appl* **2020**, *9*, 90, doi:10.1038/s41377-020-0319-7.

14. Rawlins, W.T.; Galbally-Kinney, K.L.; Davis, S.J.; Hoskinson, A.R.; Hopwood, J.A.; Heaven, M.C. Optically Pumped Microplasma Rare Gas Laser. *Opt. Express* **2015**, *23*, 4804, doi:10.1364/OE.23.004804.

15. Pitz, G.A.; Anderson, M.D. Recent Advances in Optically Pumped Alkali Lasers. *Applied Physics Reviews* **2017**, *4*, 041101, doi:10.1063/1.5006913.

16. Wei, Y.; Liu, S.; Li, X.; Yu, Y.; Su, X.; Li, S.; Shang, X.; Liu, H.; Hao, H.; Ni, H.; et al. Tailoring Solid-State Single-Photon Sources with Stimulated Emissions. *Nat. Nanotechnol.* **2022**, *17*, 470–476, doi:10.1038/s41565-022-01092-6.

17. Gazazyan, E.; Gazazyan, A. Formation and Stimulated Photodissociation of Metastable Molecules with Emission of Photon at the Collision of Two Atoms in a Laser Radiation Field. *Laser Phys.* **2017**, *27*, 045301, doi:10.1088/1555-6611/aa6169.

18. Kusuma, H.H.; Astuti, B.; Ibrahim, Z. Absorption and Emission Properties of Ruby (Cr:Al $_2$ O $_3$) Single Crystal. *J. Phys.: Conf. Ser.* **2019**, *1170*, 012054, doi:10.1088/1742-6596/1170/1/012054.

19. Bogachev, A.V.; Garanin, S.G.; Dudov, A.M.; Eroshenko, V.A.; Kulikov, S.M.; Mikaelian, G.T.; Panarin, V.A.; Pautov, V.O.; Rus, A.V.; Sukharev, S.A. Diode-Pumped Caesium Vapour Laser with Closed-Cycle Laser-Active Medium Circulation. *Quantum Electron.* **2012**, *42*, 95–98, doi:10.1070/QE2012v042n02ABEH014734.

20. Almabouada, F.; Louhibi, D. A SIMMER CIRCUIT FOR FLASH-LAMP PUMPING OF SOLID-STATE LASERS.

21. Wu, S.; Brown, R.C.; Phillips, W.D.; Porto, J.V. Pulsed Sisyphus Scheme for Laser Cooling of Atomic (Anti)Hydrogen. *Phys. Rev. Lett.* **2011**, *106*, 213001, doi:10.1103/PhysRevLett.106.213001.

22. Sun, Z.; Millis, A.J. Transient Trapping into Metastable States in Systems with Competing Orders. *Phys. Rev. X* **2020**, *10*, 021028, doi:10.1103/PhysRevX.10.021028.

23. Kim, J.W.; Moon, D.G. Basic Principles of Laser for Prostate Surgery. *Korean J Androl* **2011**, *29*, 101, doi:10.5534/kja.2011.29.2.101.

24. Bayrakli, I. Electromagnetically Induced Transparency in Natural and Artificial Molecules. *Optics & Laser Technology* **2021**, *141*, 107168, doi:10.1016/j.optlastec.2021.107168.

25. Farooq, A.; Alquaity, A.B.S.; Raza, M.; Nasir, E.F.; Yao, S.; Ren, W. Laser Sensors for Energy Systems and Process Industries: Perspectives and Directions. *Progress in Energy and Combustion Science* **2022**, *91*, 100997, doi:10.1016/j.pecs.2022.100997.

26. Bashir, S.; Farid, N.; Mahmood, K.; Shahid Rafique, M. Influence of Ambient Gas and Its Pressure on the Laser-Induced Breakdown Spectroscopy and the Surface Morphology of Laser-Ablated Cd. *Appl. Phys. A* **2012**, *107*, 203–212, doi:10.1007/s00339-011-6730-4.

27. Cao, H.; Chriki, R.; Bittner, S.; Friesem, A.A.; Davidson, N. Complex Lasers with Controllable Coherence. *Nat Rev Phys* **2019**, *1*, 156–168, doi:10.1038/s42254-018-0010-6.

28. Mosavi, N.; Nelson, C.; Marks, B.S.; Boone, B.G.; Menyuk, C.R. Simulation of Partially Spatially Coherent Laser Beam and Comparison with Field Test Data for Both Terrestrial and Maritime Environments.; Turner, M.D., Kamerman, G.W., Wasiczko Thomas, L.M., Spillar, E.J., Eds.; Baltimore, Maryland, USA, June 9 2014; p. 908015.

29. Grunwald, R.; Elsaesser, T.; Bock, M. Spatio-Temporal Coherence Mapping of Few-Cycle Vortex Pulses. *Sci Rep* **2014**, *4*, 7148, doi:10.1038/srep07148.

30. Laskin, A.; Laskin, V. Imaging Techniques with Refractive Beam Shaping Optics.; Forbes, A., Lizotte, T.E., Eds.; San Diego, California, USA, October 15 2012; p. 84900J.

31. Deepak, J.R.; R.P, A.; Saran Sundar, S. Applications of Lasers in Industries and Laser Welding: A Review. *Materials Today: Proceedings* **2023**, S221478532300620X, doi:10.1016/j.matpr.2023.02.102.

32. Shen, D.; Wei, J.; Chen, L.; Shen, X.; Wang, L. Besides Photothermal Effects, Low-Level CO $_2$ Laser Irradiation Can Potentiate Skin Microcirculation Through Photobiomodulation Mechanisms. *Photobiomodulation, Photomedicine, and Laser Surgery* **2019**, *37*, 151–158, doi:10.1089/photob.2018.4570.

33. Travers, J.C.; Grigorova, T.F.; Brahms, C.; Belli, F. High-Energy Pulse Self-Compression and Ultraviolet Generation through Soliton Dynamics in Hollow Capillary Fibres. *Nat. Photonics* **2019**, *13*, 547–554, doi:10.1038/s41566-019-0416-4.

34. Pronin, O.; Seidel, M.; Lücking, F.; Brons, J.; Fedulova, E.; Trubetskov, M.; Pervak, V.; Apolonski, A.; Udem, Th.; Krausz, F. High-Power Multi-

Megahertz Source of Waveform-Stabilized Few-Cycle Light. *Nat Commun* **2015**, *6*, 6988, doi:10.1038/ncomms7988.

35. Leke, P.A.; Dikandé, A.M. Dynamics of Passively Mode-Locked Lasers with Saturable Absorber and Saturable Nonlinearity. *Appl. Phys. B* **2020**, *126*, 157, doi:10.1007/s00340-020-07510-8.
36. Huo, T.; Qi, L.; Chen, J.J.; Miao, Y.; Chen, Z. Integrated Pulse Scope for Tunable Generation and Intrinsic Characterization of Structured Femtosecond Laser. *Sci Rep* **2021**, *11*, 9670, doi:10.1038/s41598-021-87938-w.
37. Jin, J. Dimensional Metrology Using the Optical Comb of a Mode-Locked Laser. *Meas. Sci. Technol.* **2016**, *27*, 022001, doi:10.1088/0957-0233/27/2/022001.
38. *Current Developments in Optical Fiber Technology*; Harun, S.W., Ed.; InTech, 2013; ISBN 978-953-51-1148-1.
39. Jörg Heller A Primer on Solid-State Lasers 2022.
40. Li, W.; Batteux, F.; Araujo, S.; Delpouve, N.; Saiter, J.-M.; Tan, L.; Negahban, M. Measurement of Beer-Lambert Attenuation Coefficient and Curing Kinetics Power Order: A Method Based on Rapid-Scan FTIR During Laser Curing on an ATR. *Macromol. Symp.* **2016**, *365*, 173–179, doi:10.1002/masy.201650022.
41. Teixidor, D.; Orozco, F.; Thepsonthi, T.; Ciurana, J.; Rodríguez, C.A.; Özel, T. Effect of Process Parameters in Nanosecond Pulsed Laser Micromachining of PMMA-Based Microchannels at near-Infrared and Ultraviolet Wavelengths. *Int J Adv Manuf Technol* **2013**, *67*, 1651–1664, doi:10.1007/s00170-012-4598-x.
42. Bunaziv, I.; Akselsen, O.M.; Ren, X.; Nyhus, B.; Eriksson, M. Laser Beam and Laser-Arc Hybrid Welding of Aluminium Alloys. *Metals* **2021**, *11*, 1150, doi:10.3390/met11081150.
43. Kramer, T.; Remund, S.; Jäggi, B.; Schmid, M.; Neuenschwander, B. Ablation Dynamics – from Absorption to Heat Accumulation/Ultra-Fast Laser Matter Interaction. *Advanced Optical Technologies* **2018**, *7*, 129–144, doi:10.1515/aot-2018-0010.
44. Parry, J.P.; Shephard, J.D.; Hand, D.P.; Moorhouse, C.; Jones, N.; Weston, N. Laser Micromachining of Zirconia (Y-TZP) Ceramics in the Picosecond Regime and the Impact on Material Strength: Laser Micromachining of Zirconia Ceramics. *International Journal of Applied Ceramic Technology* **2011**, *8*, 163–171, doi:10.1111/j.1744-7402.2009.02420.x.
45. Hassan, M.Th.; Luu, T.T.; Moulet, A.; Raskazovskaya, O.; Zhokhov, P.; Garg, M.; Karpowicz, N.; Zheltikov, A.M.; Pervak, V.; Krausz, F.; et al.

Optical Attosecond Pulses and Tracking the Nonlinear Response of Bound Electrons. *Nature* **2016**, *530*, 66–70, doi:10.1038/nature16528.

46. Zhan, N.; Guo, B.; Jiang, L.; Zhang, T.; Chen, M.; Lin, G. Multiphysics Modeling of Femtosecond Laser–Copper Interaction: From Electron Dynamics to Plasma Eruption. *Physics of Fluids* **2023**, *35*, 012003, doi:10.1063/5.0131001.
47. Appavoo, K.; Wang, B.; Brady, N.F.; Seo, M.; Nag, J.; Prasankumar, R.P.; Hilton, D.J.; Pantelides, S.T.; Haglund, R.F. Ultrafast Phase Transition via Catastrophic Phonon Collapse Driven by Plasmonic Hot-Electron Injection. *Nano Lett.* **2014**, *14*, 1127–1133, doi:10.1021/nl4044828.
48. Li, X.; Guan, Y. Theoretical Fundamentals of Short Pulse Laser–Metal Interaction: A Review. *Nanotechnology and Precision Engineering* **2020**, *3*, 105–125, doi:10.1016/j.npe.2020.08.001.
49. Tan, D.; Sharafudeen, K.N.; Yue, Y.; Qiu, J. Femtosecond Laser Induced Phenomena in Transparent Solid Materials: Fundamentals and Applications. *Progress in Materials Science* **2016**, *76*, 154–228, doi:10.1016/j.pmatsci.2015.09.002.
50. Beresna, M.; Gecevičius, M.; Kazansky, P.G. Ultrafast Laser Direct Writing and Nanostructuring in Transparent Materials. *Adv. Opt. Photon.* **2014**, *6*, 293, doi:10.1364/AOP.6.000293.
51. V Popruzhenko, S. Keldysh Theory of Strong Field Ionization: History, Applications, Difficulties and Perspectives. *J. Phys. B: At. Mol. Opt. Phys.* **2014**, *47*, 204001, doi:10.1088/0953-4075/47/20/204001.
52. *Femtosecond Laser Micromachining*; Osellame, R., Cerullo, G., Ramponi, R., Eds.; Topics in Applied Physics; Springer Berlin Heidelberg: Berlin, Heidelberg, 2012; Vol. 123; ISBN 978-3-642-23365-4.
53. Madsen, L.B.; Jensen, F.; Tolstikhin, O.I.; Morishita, T. Structure Factors for Tunneling Ionization Rates of Molecules. *Phys. Rev. A* **2013**, *87*, 013406, doi:10.1103/PhysRevA.87.013406.
54. Shneider, M.N.; Miles, R.B. Laser Induced Avalanche Ionization in Gases or Gas Mixtures with Resonantly Enhanced Multiphoton Ionization or Femtosecond Laser Pulse Pre-Ionization. *Physics of Plasmas* **2012**, *19*, 083508, doi:10.1063/1.4747344.
55. Milder, A.L.; Le, H.P.; Sherlock, M.; Franke, P.; Katz, J.; Ivancic, S.T.; Shaw, J.L.; Palastro, J.P.; Hansen, A.M.; Begishev, I.A.; et al. Evolution of the Electron Distribution Function in the Presence of Inverse Bremsstrahlung Heating and Collisional Ionization. *Phys. Rev. Lett.* **2020**, *124*, 025001, doi:10.1103/PhysRevLett.124.025001.

56. Jiang, L.; Wang, A.-D.; Li, B.; Cui, T.-H.; Lu, Y.-F. Electrons Dynamics Control by Shaping Femtosecond Laser Pulses in Micro/Nanofabrication: Modeling, Method, Measurement and Application. *Light Sci Appl* **2017**, *7*, 17134–17134, doi:10.1038/lsa.2017.134.

57. Saghebfar, M.; Tehrani, M.K.; Darbani, S.M.R.; Majd, A.E. Femtosecond Pulse Laser Ablation of Chromium: Experimental Results and Two-Temperature Model Simulations. *Appl. Phys. A* **2017**, *123*, 28, doi:10.1007/s00339-016-0660-0.

58. Coulomb Explosion Phenomenon Using Gigawatt Intensity Laser Fields: An Exotic Realm of Laser–Cluster Interaction. *CURRENT SCIENCE* **2023**, *100*.

59. Sinha, S. Thermal Model for Nanosecond Laser Ablation of Alumina. *Ceramics International* **2015**, *41*, 6596–6603, doi:10.1016/j.ceramint.2015.01.106.

60. Fang, R.; Vorobyev, A.; Guo, C. Direct Visualization of the Complete Evolution of Femtosecond Laser-Induced Surface Structural Dynamics of Metals. *Light Sci Appl* **2016**, *6*, e16256–e16256, doi:10.1038/lsa.2016.256.

61. Yan, Z.; Mei, X.; Wang, W.; Pan, A.; Lin, Q.; Huang, C. Numerical Simulation on Nanosecond Laser Ablation of Titanium Considering Plasma Shield and Evaporation-Affected Surface Thermocapillary Convection. *Optics Communications* **2019**, *453*, 124384, doi:10.1016/j.optcom.2019.124384.

62. Kalus, M.; Barcikowski, S.; Gökce, B. How the Physicochemical Properties of the Bulk Material Affect the Ablation Crater Profile, Mass Balance, and Bubble Dynamics During Single-Pulse, Nanosecond Laser Ablation in Water. *Chemistry A European J* **2021**, *27*, 5978–5991, doi:10.1002/chem.202005087.

63. Wang, Y.; Zhang, M.; Huang, Y.; Cao, X.; Dong, Y.; Zhao, J.; Li, Y.; Wang, Y. Ablation Threshold Modelling and Validation of Metal Nanosecond Laser Processing. *Optics Communications* **2022**, *523*, 128608, doi:10.1016/j.optcom.2022.128608.

64. Tao, S.; Zhou, Y.; Wu, B.; Gao, Y. Infrared Long Nanosecond Laser Pulse Ablation of Silicon: Integrated Two-Dimensional Modeling and Time-Resolved Experimental Study. *Applied Surface Science* **2012**, *258*, 7766–7773, doi:10.1016/j.apsusc.2012.04.141.

65. Wu, C.; Zhigilei, L.V. Microscopic Mechanisms of Laser Spallation and Ablation of Metal Targets from Large-Scale Molecular Dynamics Simulations. *Appl. Phys. A* **2014**, *114*, 11–32, doi:10.1007/s00339-013-8086-4.

66. Grigoryev, S.Yu.; Lakatosh, B.V.; Krivokorytov, M.S.; Zhakhovsky, V.V.; Dyachkov, S.A.; Ilnitsky, D.K.; Migdal, K.P.; Inogamov, N.A.; Vinokhodov, A.Yu.; Kompanets, V.O.; et al. Expansion and Fragmentation of a Liquid-Metal Droplet by a Short Laser Pulse. *Phys. Rev. Applied* **2018**, *10*, 064009, doi:10.1103/PhysRevApplied.10.064009.

67. Abou-Saleh, A.; Karim, E.T.; Maurice, C.; Reynaud, S.; Pigeon, F.; Garrelie, F.; Zhigilei, L.V.; Colombier, J.P. Spallation-Induced Roughness Promoting High Spatial Frequency Nanostructure Formation on Cr. *Appl. Phys. A* **2018**, *124*, 308, doi:10.1007/s00339-018-1716-0.

68. Shugaev, M.V.; Zhigilei, L.V. Thermodynamic Analysis and Atomistic Modeling of Subsurface Cavitation in Photomechanical Spallation. *Computational Materials Science* **2019**, *166*, 311–317, doi:10.1016/j.commatsci.2019.05.017.

69. Winter, J.; Rapp, S.; Spellauge, M.; Eulenkamp, C.; Schmidt, M.; Huber, H.P. Ultrafast Pump-Probe Ellipsometry and Microscopy Reveal the Surface Dynamics of Femtosecond Laser Ablation of Aluminium and Stainless Steel. *Applied Surface Science* **2020**, *511*, 145514, doi:10.1016/j.apsusc.2020.145514.

70. Zhang, Z.; Yang, Z.; Wang, C.; Zhang, Q.; Zheng, S.; Xu, W. Mechanisms of Femtosecond Laser Ablation of Ni3Al: Molecular Dynamics Study. *Optics & Laser Technology* **2021**, *133*, 106505, doi:10.1016/j.optlastec.2020.106505.

71. Shin, Y. ANALYSIS OF NANOSECOND LASER ABLATION OF ALUMINUM WITH AND WITHOUT PHASE EXPLOSION IN AIR AND WATER.

72. Zhigilei, L.V.; Lin, Z.; Ivanov, D.S. Atomistic Modeling of Short Pulse Laser Ablation of Metals: Connections between Melting, Spallation, and Phase Explosion. *J. Phys. Chem. C* **2009**, *113*, 11892–11906, doi:10.1021/jp902294m.

73. Ehrhardt, M.; Lorenz, P.; Bayer, L.; Han, B.; Zimmer, K. Studies of the Confinement at Laser-Induced Backside Dry Etching Using Infrared Nanosecond Laser Pulses. *Applied Surface Science* **2018**, *427*, 686–692, doi:10.1016/j.apsusc.2017.08.099.

74. Bogaerts, A.; Chen, Z. Effect of Laser Parameters on Laser Ablation and Laser-Induced Plasma Formation: A Numerical Modeling Investigation. *Spectrochimica Acta Part B: Atomic Spectroscopy* **2005**, *60*, 1280–1307, doi:10.1016/j.sab.2005.06.009.

75. Hussein, A.E.; Diwakar, P.K.; Harilal, S.S.; Hassanein, A. The Role of Laser Wavelength on Plasma Generation and Expansion of Ablation Plumes in Air. *Journal of Applied Physics* **2013**, *113*, 143305, doi:10.1063/1.4800925.

76. Wu, J.; Wei, W.; Li, X.; Jia, S.; Qiu, A. Infrared Nanosecond Laser-Metal Ablation in Atmosphere: Initial Plasma during Laser Pulse and Further Expansion. *Appl. Phys. Lett.* **2013**, *102*, 164104, doi:10.1063/1.4803044.

77. S. Küper; M. Stuke Ablation of Uv-Transparent Materials with Femtosecond Uv Excimer Laser Pulses. *Microelectronic Engineering* **1989**, *Volume 9*, Pages 475-480, doi:https://doi.org/10.1016/0167-9317(89)90104-4.

78. Hu, Y.; Chen, Y.; Ma, J.; Li, J.; Huang, W.; Chu, J. High-Efficiency Fabrication of Aspheric Microlens Arrays by Holographic Femtosecond Laser-Induced Photopolymerization. *Appl. Phys. Lett.* **2013**, *103*, 141112, doi:10.1063/1.4824307.

79. Weisgrab, G.; Guillaume, O.; Guo, Z.; Heimel, P.; Slezak, P.; Poot, A.; Grijpma, D.; Ovsianikov, A. 3D Printing of Large-Scale and Highly Porous Biodegradable Tissue Engineering Scaffolds from Poly(Trimethylene-Carbonate) Using Two-Photon-Polymerization. *Biofabrication* **2020**, *12*, 045036, doi:10.1088/1758-5090/abb539.

80. Lou, R.; Zhang, G.; Li, G.; Li, X.; Liu, Q.; Cheng, G. Design and Fabrication of Dual-Scale Broadband Antireflective Structures on Metal Surfaces by Using Nanosecond and Femtosecond Lasers. *Micromachines* **2019**, *11*, 20, doi:10.3390/mi11010020.

81. Nürnberger, P.; Reinhardt, H.M.; Kim, H.-C.; Pfeifer, E.; Kroll, M.; Müller, S.; Yang, F.; Hampp, N.A. Orthogonally Superimposed Laser-Induced Periodic Surface Structures (LIPSS) upon Nanosecond Laser Pulse Irradiation of SiO 2 /Si Layered Systems. *Applied Surface Science* **2017**, *425*, 682–688, doi:10.1016/j.apsusc.2017.06.316.

82. Karkantonis, T.; Gaddam, A.; Sharma, H.; Cummins, G.; See, T.L.; Dimov, S. Laser-Enabled Surface Treatment of Disposable Endoscope Lens with Superior Antifouling and Optical Properties. *Langmuir* **2022**, *38*, 11392–11405, doi:10.1021/acs.langmuir.2c01671.

83. Karkantonis, T.; Gaddam, A.; Tao, X.; See, T.L.; Dimov, S. The Influence of Processing Environment on Laser-Induced Periodic Surface Structures Generated with Green Nanosecond Laser. *Surfaces and Interfaces* **2022**, *31*, 102096, doi:10.1016/j.surfin.2022.102096.

84. Chambonneau, M.; Grojo, D.; Tokel, O.; Ilday, F.Ö.; Tzortzakis, S.; Nolte, S. In-Volume Laser Direct Writing of Silicon—Challenges and Opportunities. *Laser & Photonics Reviews* **2021**, *15*, 2100140, doi:10.1002/lpor.202100140.

Chapter 2

Laser Modification on Metals: Superhydrophobic Surfaces

2.1 Superhydrophobicity: An Introduction

Various modern technologies have been inspired by nature. Nature's ability to generate appropriate functional surfaces pushed by the need for survival has often been mimicked and translated by humans into functional material technologies. A couple of interesting examples of natural functional surfaces would comprise the gradient refractive index of the moth-eye for its anti-reflection property and water collection ability of the desert beetle, where tiny grooves and bumps on its skin condense and collect water to its mouth [1,2]. Another attractive, functional surface property is superhydrophobicity. i.e., extreme water repellency which allows e.g. the lotus leaf to optimize photosynthesis by keeping itself clean [3]. Considering the abundance of water on earth, various applications would require total repellence or the ability to manipulate water interaction with the surface.

In nature, these surfaces are observed on lotus leaves, rose petals, water striders, and cacti, to name a few, as shown in Figure 2.1(a,b,c) [4–6].The extreme water repellency of the surface cannot be explained by surface chemistry alone; instead, it presents itself as a physico-chemical property comprising the dual aspects of surface chemistry along with surface texture [7]. With the advent of advanced surface micro-nano modification techniques as shown in Figure 2.1(d,e), superhydrophobicity has received renewed interest, not just to repel

water $(71.9\,mN\,m^{-1}, 25°C)$, but also to lower surface tension liquids such as *n*-hexadecane $(27.5\,mN\,m^{-1}, 25°C)$ and even alcohols such as ethanol $(21.9\,mN\,m^{-1}, 25°C)$. The former is termed superoleophobic and the latter as superomniphobic surfaces [8].

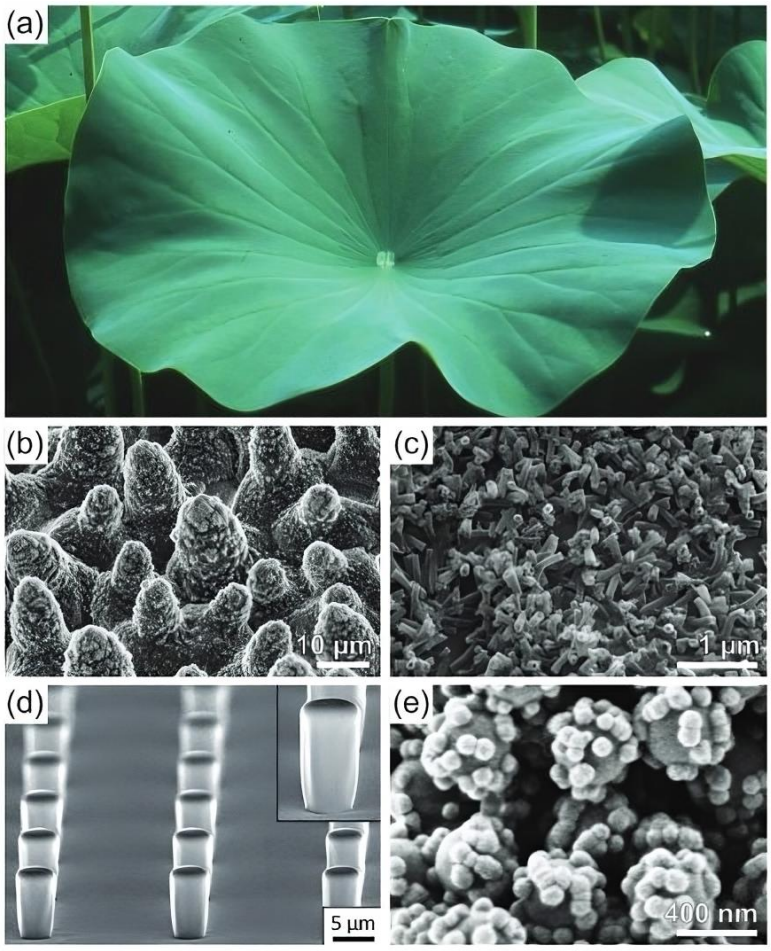

Figure 2.1. Natural and artificial superhydrophobic surfaces, (a) photograph of a lotus leaf; (b) microstructure of the lotus leaf; (c) nanostructure of lotus leaf; (d) superhydrophobic surface consisting of the SU-8 micropillar array; (e) artificial raspberry like nanostructure with lotus leaf like superhydrophobicity **[9]**.

2.1.1 Primary Aspects of surface wettability

Thomas Young (1805) was the first to propose the relationship between interfacial energy and the interfacial area [10]. Therefore, surface free energy could provide a means to quantitatively assess the surface properties based on

liquid interaction with the surface in contact. Thomas Young presented an expression for the contact angle over a flat surface as follows:

$$\cos\theta = \frac{\gamma_{SV} - \gamma_{SL}}{\gamma_{LV}} \quad (1)$$

where θ represents the contact angle, γ_{SV}, γ_{SL}, and γ_{LV} are the interfacial surface tensions between the corresponding interfaces of solid-vapor, solid-liquid, and liquid-vapor, respectively. This defines the contact angle that categorizes the wetting behavior into the following: (i) superhydrophilic $(0° < \theta < 10°)$; (ii) hydrophilic $(10° < \theta < 90°)$; hydrophobic $(90° < \theta < 150°)$, and superhydrophobic $(150° < \theta < 180°)$. By definition, superhydrophobic surfaces have a water contact angle higher than $CA > 150°$ and a sliding (roll-off) angle lower than $10°$ [11].

2.1.2 Dynamic Contact Angle and Contact Angle Hysterisis

Another essential aspect defining the liquid-surface interaction is the dynamic contact angle measurements, termed contact angle hysteresis (CAH). It is defined as the difference between the advancing (θ_A) and receding (θ_R) contact angles [12]. The advancing contact angle measures the solid-liquid cohesion as it is the maximum contact angle value before the droplet advances. In contrast, the latter provides a measure of solid-liquid adhesion, as shown in Figure 2.2(a,b). Hence, in general, $\theta_A > \theta_R$ where lower hysteresis values implies a better tendency of the droplet to roll-off, even at a slight tilt or perturbation of the surface [13].

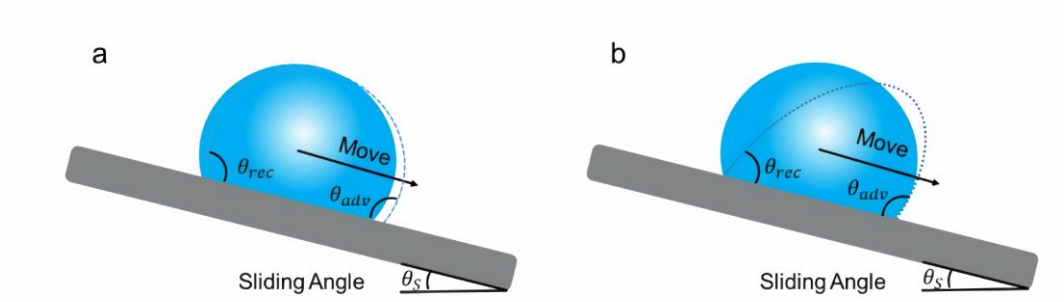

Figure 2.2. Depiction of dynamic contact angle for a droplet in motion at a sliding angle θS. The droplet slides from a to b in the figure.

2.1.3 Wenzel and Cassie-Baxter States of Superhydrophobicity

Amongst the different available models to predict the droplet contact angle over a rough surface, Wenzel and Cassie-Baxter models are the most popular and widely accepted. These models could well define the relationship of surface roughness with the droplet contact angle and the resulting superhydrophobicity. By definition, these models present the existence of two regimes: (i) the homogeneous regime with the existence of a two-phase solid-liquid interface; (ii) the heterogeneous regime with the existence of a three-phase solid-air-liquid interface.

In the case of the former (two-phase solid-liquid interface), Robert N. Wenzel proposed a model for a rough interface with chemical homogeneity, where the liquid completely penetrates the surface features, as shown in Figure 2.3(a). Because of complete penetration into the surface grooves, the liquid adhesion is more significant, and the surface displays high CAH. The following equation gives the contact angle in this case [14]:

$$\cos\theta_W = r\ \cos\theta \tag{2}$$

where θ_W and θ represents Wenzel and Young's contact angles, respectively. On the other hand, Cassie-Baxter (CB) model proposes an alternative case in which the droplet moves atop the rough surface texture without being pinned to the surface, as shown in Figure 2.3(b). He explained this occurrence through the heterogeneous surface composition, where the composite surface comprises a

fractional area and the corresponding members' contact angle. In such a case, the apparent contact angle would be represented by an effective medium flat surface with a contact angle θ_{CB} as follows [15]:

$$\cos\theta_{CB} = f_1 \cos\theta_1 + f_2 \cos\theta_2 \tag{3}$$

where (f_1, f_2) for which $f_1 + f_2 = 1$ and (θ_1, θ_2) represent the fractional area and the contact angles, respectively. According to the CB model, the water droplet stays in contact with the tip of the surface texture features as the intermediate air pockets prevent the droplet adhesion deeper into the surface features [16]. In the case of air as the intermediate composite interface, as in most cases, the CB equation is modified to the following form, with f as the solid-liquid contact area fraction:

$$\cos\theta_{CB} = f \cos\theta + 1 \ -1 \tag{4}$$

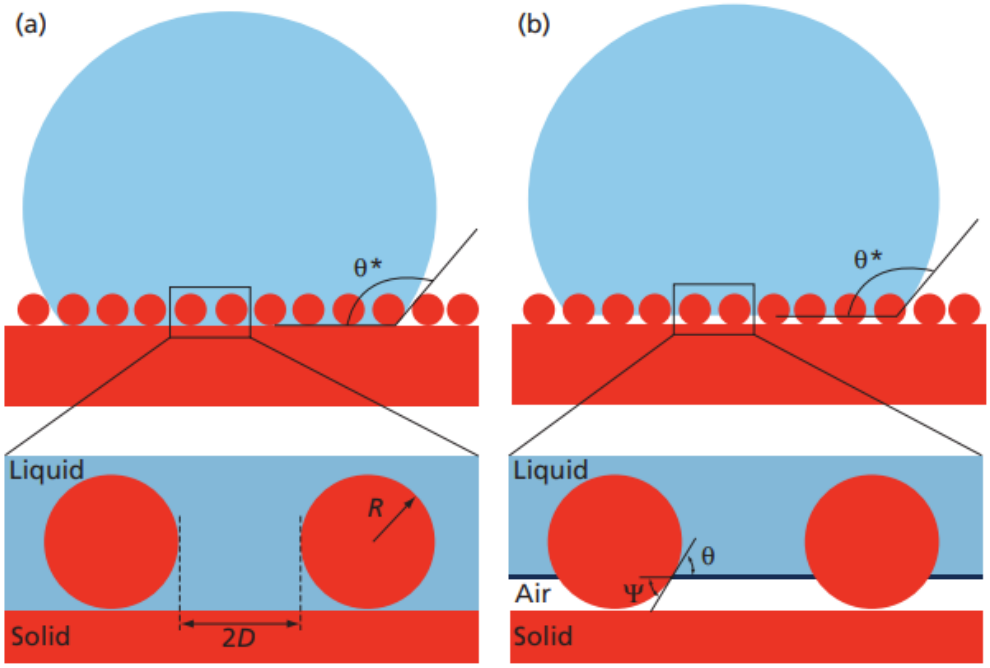

Figure 2.3. Droplet on a textured surface in (a) Wenzel and (b) Cassie-Baxter state. The enlarged image depicts the complete wetting and air pocket presence in the Wenzel and Cassie-Baxter states, respectively **[17]**.

The droplet transition between the Cassie to Wenzel states has received significant attention recently. This transition is well established and could be triggered by external perturbations such as pressure, mechanical vibration, or condensation [18]. On the other hand, the Wenzel to Cassie transition remains unclear and is a current topic of research interest. This transition is relatively difficult to achieve due to the significant energy barrier associated with the transition. Such a transition is suggested to be due to the manipulation of adhesion forces at specific geometries that favor spontaneous transition from Wenzel to Cassie-Baxter state.

2.2 Beyond Superhydrophobicity

In recent times, the research on liquid-repellent surfaces is not just limited to superhydrophobicity but also to repel liquids with lower surface energy. To make that possible, controlling the surface features and using an appropriate low surface energy coating is crucial. The following section briefly describes the necessary surface features for superoleophobicity and superomniphobicity.

2.2.1 Hierarchical Structures for Highly Liquid Repellent Surface

Liquid-repellent surfaces in nature generally present a hierarchical surface, essentially consisting of a finer nano-texture on an underlying coarser micro-texture, as shown in Figure 2.4. Such surface features have composite air-pockets present at both the micro-nano level, thus enhancing the liquid repulsion [19]. This higher fraction of trapped air results in higher contact angles, as evident from equation (3). These surfaces are, therefore, a minimal requirement to develop oil-repellent surfaces.

For superoleophobicity, the CB state can be defined in terms of two critical parameters, namely the apparent contact angle and the breakthrough pressure (P_{break}) [14]. The breakthrough pressure defines a threshold value of the pressure difference across the composite interface that initiates the CB to Wenzel transition. A study conducted by Tuteja et al. has defined a parameter spacing ratio D^* which is a dimensionless parameter as a measure of the surface porosity [20]. For cylindrical texture and the spherical texture, the parameter translated to

the following forms: $D^*_{cylinder} = \frac{R+D}{R}$; $D^*_{sphere} = \left(\frac{R+D}{R}\right)^2$, where R represents the cylinder (sphere) radius, and $2D$ is the spacing between the cylinder (sphere). Based on the above description, the CB equation is modified to the following:

$$\cos\theta^*_{cyl} = -1 + \frac{1}{D^*_{cylinder}}[\sin\theta + \ \pi - \theta \ \cos\theta] \tag{5}$$

$$\cos\theta^*_{sphere} = -1 + \frac{1}{D^*_{sphere}}\left[\frac{\pi}{2\sqrt{3}} \ 1 + \cos\theta \ \right]^2 \tag{6}$$

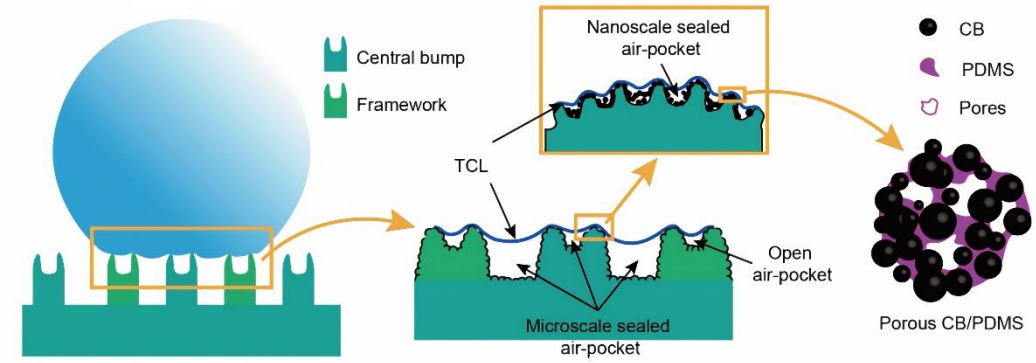

Figure 2.4. Illustration depicting hierarchical three-scale structure on stainless steel generated by laser texturing followed by spin coating carbon black (CB) dispersed in PDMS solution **[21]**.

The contact angle is directly proportional to the dimensionless quantity D^*, however, for relatively large values of $D^* \gg 1$, the surface cannot repel the droplet anymore, allowing the breakthrough to destroy the composite interface. The breakthrough pressure was parametrized by introducing a reference pressure P_{ref}, which was then used to define a robustness factor A^*, given by the following:

$$A^* = \frac{P_{break}}{P_{ref}}, \quad P_{ref} = \frac{2\ \gamma_{LV}}{l_{cap}} \tag{7}$$

2.2.2 Re-entrant Structures

Re-entrant surface features are essential for a stable CB state with low surface tension liquids such as oils and organic solvents for which the Youngs contact angle $\theta_Y \ll 90°$ [22]. Figure 2.5(a,b) shows two surface features with identical surface energy of the solid. In the first case, the geometry is concave with $(\psi \geq 90°)$ whereas the latter (Figure 2.5 (b)) is convex geometry with $(\psi < 90°)$. A stable CB state occurs only when $(\theta \geq \psi)$. The above property can be explained by the fact that if $\theta < \psi$, the liquid-vapor interface is pushed down due to the capillary force and can easily undergo the Wenzel transition. Low surface tension liquids such as organic solvents with $\theta_Y < 90°$ cannot experience a stable CB on such surfaces. On the contrary, convex surfaces with $\theta > \psi$ are called re-entrant surface features, necessary for obtaining a stable CB state with low surface tension liquids. J. Han et al. fabricated 3D re-entrant CuO nanograss on Cu microcones fabricated in a dual step using femtosecond laser micromachining and chemical treatment, as shown in Figure 2.5(c,d,e) [23]. The influence of the nanostructure types and the microcone distribution on the superamphiphobicity was studied, and the excellent mechanical durability of the fabricated surfaces was demonstrated.

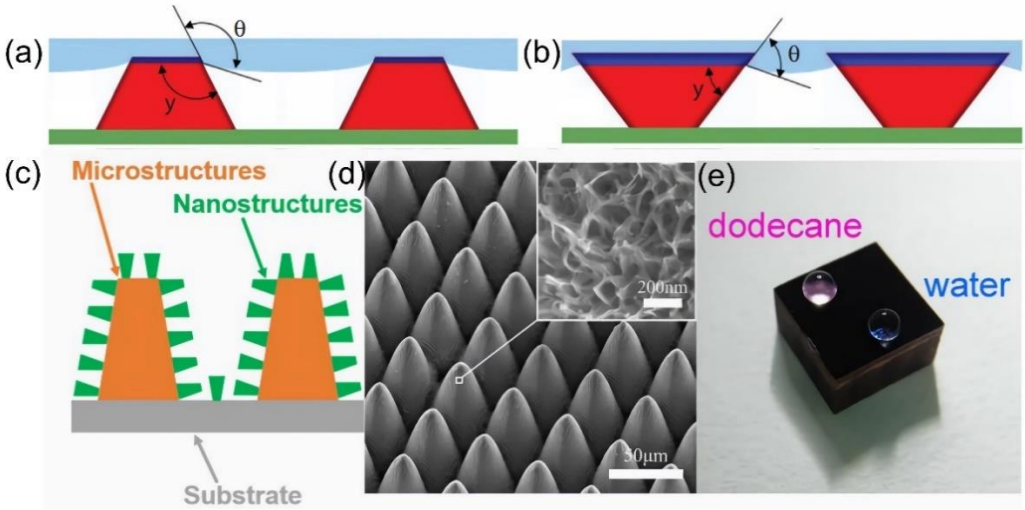

Figure 2.5. Schematics of a concave surface with ψ>90° that shows a liquid with θ>90°; (b) convex (re-entrant) texture with ψ<90° that shows a low surface tension liquid with θ<90°; (c) Illustration of hierarchical micro-nano-structures; (e) SEM image of 3D-reentrant Cuo nanograss on CuO micro-cones; (e) Photograph of 5 μL droplets of water and dodecane on the superamphiphobic surface **[23]**.

2.3 Coatings for Superhydrophobicity

The most popular coatings used for superhydrophobic surfaces are based on low surface energy silane agents, generally consisting of fluoro/chloro groups. The fluorosilane especially forms a covalently bonded self-assembled monolayer (SAM) over the target surface, along with the stable C-F bond of the fluorosilane is one of the strongest chemical bonds and is very stable [24]. Additionally, the carbon chain of the Fluorosilane shows a zig-zag structure producing a space shielding effect, protected further by other fluorine atoms [25]. The silane coating proceeds through four steps beginning with hydrolysis, followed by condensation and hydrogen bonding to the hydroxyl groups of the substrate. Finally, covalent bond formation occurs during the curing stage, accompanied by dehydration, as shown in Figure 2.6.

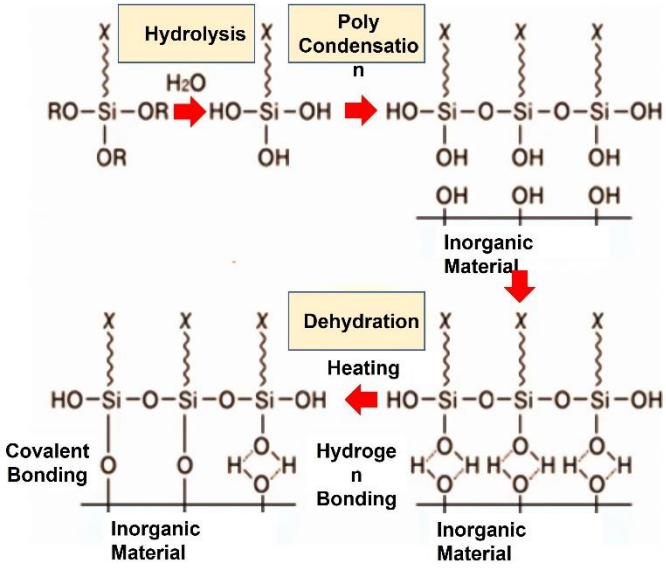

Figure 2.6. Illustration of steps involved in self-assembled monolayer formation of silane precursor on an inorganic substrate **[26]**.

Alternatively, hydrocarbon adsorption-based coatings have been used to attain superhydrophobicity on metals. The laser or plasma treated activated metal oxide surfaces automatically converts from superhydrophilic to superhydrophobicity through adsorption of volatile organic compounds [27]. However, this process takes weeks to complete. Many researchers have proposed alternative means to accelerate the adsorption process using thermal and vacuum

based treatments [28–30]. The hydrocarbon adsorption process is illustrated in Figure 2.7.

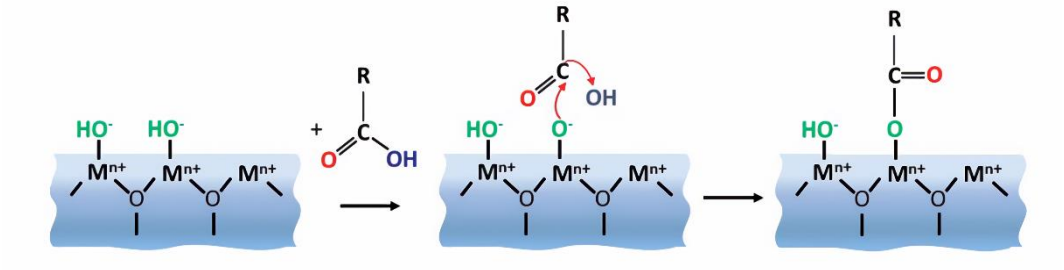

Figure 2.7. Schematics of a hydroxylic acid chemisorption on a hydroxylated metal-oxide surface. M corresponds to metal **[31]**.

Few researchers have used non-toxic silicone oil coatings to fabricate superhydrophobic surfaces on different metal substrates following laser treatment. A thermal treatment was devised to reduce superhydrophobic transition time to about 10 minutes. The silicone oil treatment was combined with laser texturing parameter of peak fluence to tune the water adhesion behavior [32].

2.4 Stability of Superhydrophobic Surfaces

A large number of studies have demonstrated superhydrophobic surfaces on various substrates such as metals, polymers, glasses, and ceramics [33,34]. However, for a fabrication approach to be adopted for large-scale production and use, superhydrophobicity must be stable under extreme conditions such as high Laplace and hydrostatic pressure, mechanical abrasion, and chemical corrosion [35,36]. The current section, therefore, briefly introduces various functional stability assessment techniques for superhydrophobicity, along with examples from previously reported studies that have used them to assess the performance of their functional surfaces.

2.4.1 Laplace Pressure Analysis

Amongst the large number of studies involving superhydrophobic surface fabrication, relatively few have characterized the stability of the CB state [37,38].

For a liquid droplet on a superhydrophobic surface, the Laplace pressure is given by

$$P_{Laplace} = \frac{2\gamma}{R} \tag{8}$$

where γ is the liquid surface tension, and R is the droplet radius of curvature. As the droplet evaporates gradually, its radius of curvature decreases, thereby increasing the Laplace pressure. For superhydrophobic surfaces, a critical Laplace pressure exists, beyond which the CB state transforms to the Wenzel state, pinning the droplet to that specific location [39]. In theory, the non-wetting of the surface is a force-balance phenomenon, where the capillary pressure overcomes the Laplace pressure of the liquid, as shown in Figure 2.8. However, beyond the critical Laplace pressure, the $P_{Laplace}$ overcomes the capillary pressure and forces itself into the surface microfeatures [40]. Therefore, Laplace pressure analysis has been used as a simple characterization technique to analyze the stability of the CB state. At this point, it is worth pointing out a common misunderstanding regarding the CB transition during droplet evaporation. The CB transition cannot be defined by the contact angle alone, as it would need information regarding the three-phase contact line (TPCL), and the Wenzel transition occurs when the TPCL measurement displays a constant value [41]. As an example, during droplet evaporation, the contact angle can be 151°, and be pinned with a constant TPCL signaling the Wenzel transition.

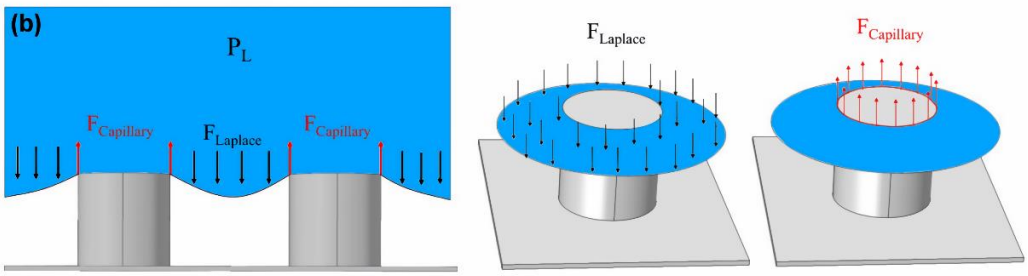

Figure 2.8. Schematics of downward-acting Laplace pressure and upward-acting capillary pressure on a liquid droplet on micropillars; (a) side-view; (b) top-view **[40]**.

As previously mentioned, multi-scale hierarchical textures improve CB stability. Long et al. fabricated dual-scale structures comprising uniform micro-pillar distribution decorated by nanoparticles through ultrafast laser fabrication [42]. The dual-scale structure displayed better CB stability compared to the single-scale structure at a Laplace pressure of about $400\,Pa$. However, for outdoor applications, the superhydrophobic surface needs robust CB stability to withstand high-pressure impact, such as in the case of heavy rain droplet impact at a pressure of about $10^5\,Pa$. Therefore, there is a need for higher critical Laplace pressure stability of the fabricated water-repellent surfaces. In this regard, Pan et al. [35] followed a hybrid fabrication strategy combining ultrafast laser interaction with a chemical treatment to generate triple scale texture comprising of laser-generated micro-cones covered by nanosheets and finally dispersedly decorated micro balls, all on a copper substrate, as shown in Figure 2.9. The authors demonstrated extremely high critical Laplace pressure of about $1450\,Pa$, the highest in comparison to state of the art.

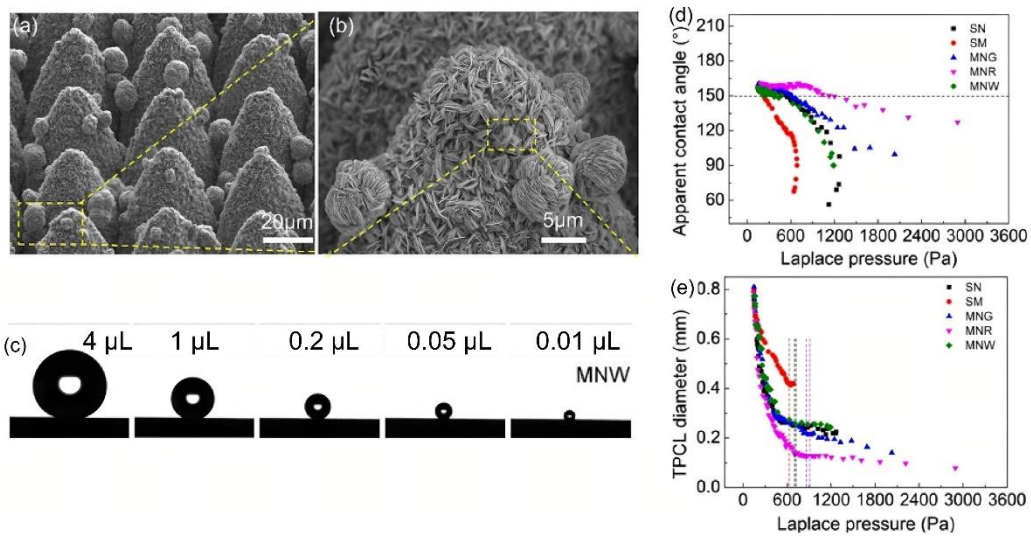

Figure 2.9. (a,b)SEM images of three-scale texture with a periodicity of 40 µm and height of 50 µm generated by ultrafast laser ablation and chemical treatment on a copper substrate; (c) camera images of the evaporation process of a water droplet on the three-scale structure; plots of (d) contact angle and (e) three-phase contact line vs Laplace pressure for the same surface **[35]**.

2.4.2 Corrosion Resistance

Another direct application of superhydrophobic metallic surfaces is for anti-corrosion applications, especially in marine environments [7]. In the case of the bare metal surfaces in a chlorine environment, the metal ions are rapidly hydrolyzed, which initiates the chloride ions to cause pitting corrosion due to the hydration of the aluminum followed by its dissolution on attack by the aggressive chloride ions which finally forms the $AlCl_3$ [43]. On the contrary, for superhydrophobic surfaces, the above situation is avoided by the water-repellent property, thereby blocking the infiltration from the ionic environment and providing corrosion resistance [44].

Guo et al. performed hydrothermal treatment on aluminum alloy followed by fluorosilane treatment to achieve superhydrophobicity [45]. The polarization curve obtained through potentiodynamic scanning in $NaCl\,(3.5\%)$ clearly showed the positive shift of the corrosion potential and the corrosion current density reduction by two orders of magnitude for the superhydrophobic surface. These measurements confirmed the superior corrosion resistance of the superhydrophobic surface compared to the bare metal surface. The corrosion inhibition efficiency of the superhydrophobic surface is given by the following:

$$\eta\,\% = \left(1 - \frac{I_{SPHB}}{I_{BARE}}\right) \times 100\% \tag{9}$$

where, in the above equation I_x represents the corrosion current density of the substrate x. The corrosion inhibition was calculated to be 99.67 %, indicating the reduction in the corrosion rate of the superhydrophobic surface compared to the bare substrate.

In another study, Feng et al. fabricated an eco-friendly superhydrophobic aluminum alloy surface through hydrothermal treatment followed by stearic acid-coating [46]. The superhydrophobic surface displayed excellent corrosion resistance in the electrochemical corrosion tests and even maintained a static contact angle above $150°$ for about ten days under immersion in $NaCl$ solution, as shown in Figure 2.10.

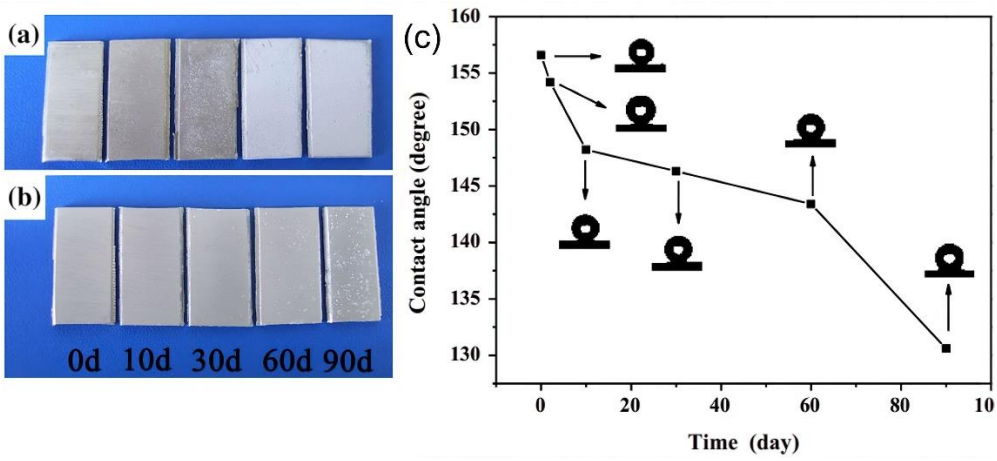

Figure 2.10. Camera images of (a) untreated; (b) superhydrophobic samples with different saltwater immersion time. Corresponding static contact angle measurements on superhydrophobic surface with immersion time **[47]**.

2.4.3 Mechanical Stability

Preserving surface features is vital to the long-term performance of the superhydrophobic surfaces [48]. During their use, these surfaces are prone to mechanical damage, such as scratches and abrasion. Once again, hierarchical micro-nano structures provide an advantage in terms of mechanical durability [49]. The microstructures can withstand significant pressure and act as a cushion towards the more fragile nanofeatures. Wang et al. fabricated hierarchical superhydrophobic surfaces on stainless steel using ultrafast laser processing [50]. Figure 2.11 shows the laser-textured surfaces that could withstand mechanical abrasion of 800 grit SiC paper for a distance of 2.3 m at an applied pressure of 5.5 kPa, maintaining the superhydrophobic property.

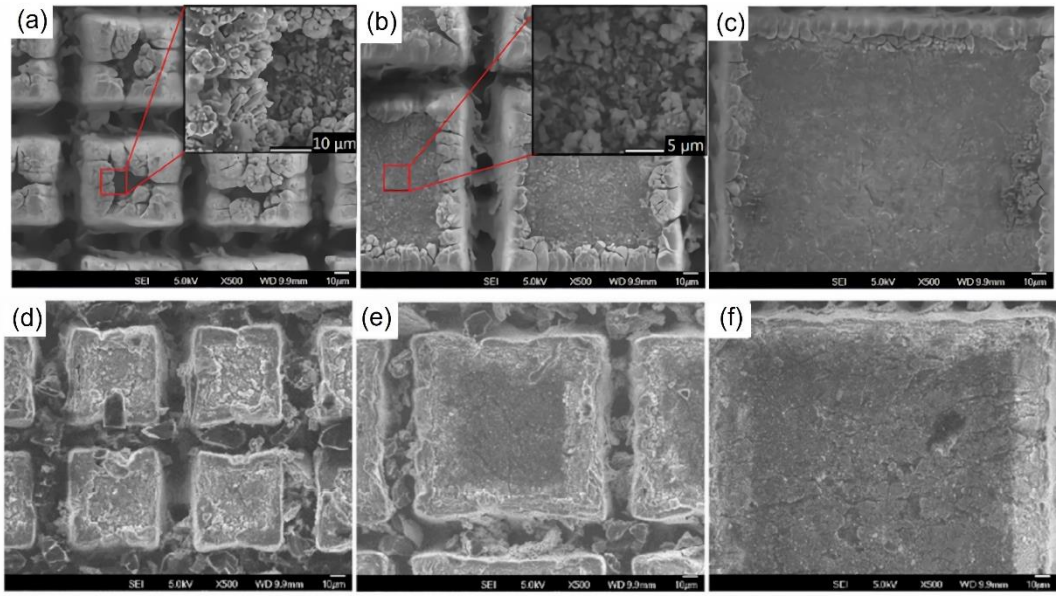

Figure 2.11. SEM images of the laser-generated superhydrophobic stainless steel substrate, at different scan pitches of (from left to right) 80 µm, 140 µm, and 240 µm; (a,b,c) before; (d,e,f) after abrasion with 800 grit SiC paper for a length of 4.7 m **[50]**.

2.5 Nanosecond Laser Micromachining for Superhydrophobicity

This study aims to fabricate superhydrophobicity on metal substrates using laser micromachining and appropriate chemical treatment. The study can be divided into two major sections, as mentioned below:

(i) **Part I**: Preliminary experimental trials study the laser-generated micro-nano hierarchical surface and its effect on superhydrophobic properties. Fluorosilane (FAS) coating is used as the surface energy reductant following laser texturing. A solely laser-generated hierarchical surface is compared to an alternate surface hierarchy comprising laser-based microstructure followed by hydrothermally generated nanostructure. Eventually, the ability of the nanosecond laser-generated surface to exhibit superoleophobicity is evaluated.

(ii) **Part II**: Appropriate laser parameters and pattern design in selected to fabricate superoleophobic surfaces. The importance of laser pulsewidth as a defining parameter to fabricate superoleophobicity is

demonstrated experimentally. In addition, an alternate eco-friendly vegetable oil-based superhydrophobic coating is introduced, competing with the state-of-the-art eco-friendly superhydrophobic coating techniques. The eco-friendly coating technique is compared to the FAS coating through various stability analysis techniques.

2.6 Laser Fabrication of Superhydrophobicity Based on Hierarchical Aluminum Surface

As previously mentioned, relatively long pulsed nanosecond laser machining induces rapid melt-solidification dynamics in the metallic material, accompanied by the ejection of micro-nano particles due to vaporization and re-deposition [51,52]. The phenomenon mentioned above results in a highly hierarchical surface texture with large microstructures decorated with smaller micro-nano particles. Even though the smaller surface feature generation cannot be controlled directly, the larger micro-features can be designed based on the laser parameters.

The ability to tune laser parameters to vary the micro-texture has advantages for specific applications such as superhydrophobicity [53]. Firstly, variations in the laser parameters, such as pulsewidth, pulse repetition rate (PRR), and pulse energy, can modify the thermal effect on the surface [54]. The rough texture generated because of the thermal effect is beneficial for repelling the liquid by enhancing the presence of air pockets and surface area. Secondly, by modifying laser parameters such as scan speed and scan line spacing, the geometry of the micro-features can be manipulated, directly affecting the robustness and liquid repellency of the resulting superhydrophobic surface [55].

This study selected the pulse repetition rate as the first variable parameter to study the laser-generated texture on aluminum (Al 6013) for fabricating a superhydrophobic surface. The lowest available pulsewidth of 4 ns was selected to minimize the thermal effect on the surface modification. The average power of the laser output was fixed at $18\ W$, and the scan speed at $10\ mm/s$. A specific triple scan geometry was selected as the design for surface modification. It includes moving the beam with a spot size of $60\ \mu m$ over three separate layered scan lines over the fixed area at angles of $0°, 45°$ and $135°$, as illustrated in Figure 2.12.

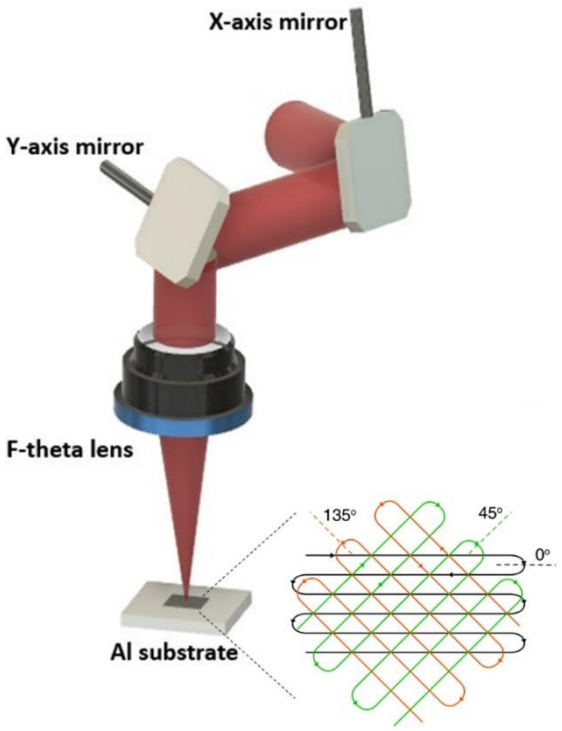

Figure 2.12. Illustration of the nanosecond laser beam scanned on the aluminum substrate with the galvanometric scan system. The magnified image depicts the triple layer scan pattern at angles of 0°, 45°, and 135°.

2.6.1 Surface Analysis of Laser Modification

As the only variable laser parameter, PRR was varied from $25\,kHz$ to $150\,kHz$, in steps of $25\,kHz$. Figure 2.13represents the field emission SEM (FESEM) images of the modified surfaces. As shown in the figure, the morphology of the surface resembles conical shapes. Interestingly, for the lower PRR of $25\,kHz$ (Figure 2.13(a)), the conical features appear well-separated, and the adjacent tip-to-tip spacing is greater at $\sim 46\,\mu m$. However, as the PRR increases, the tip surface appears relatively blunt (Figure 2.13(b)), and the adjacent tip spacing decreases slightly. Eventually, at the highest PRR of $150\,kHz$, the surface features are not anymore completely separated cones; instead, they form an almost continuous line of microfeatures with minimal spacing between the adjacent features, as shown in Figure 2.13(c). The generated surface features are uniform throughout the laser-modified region, as shown in Figure 2.13(d).

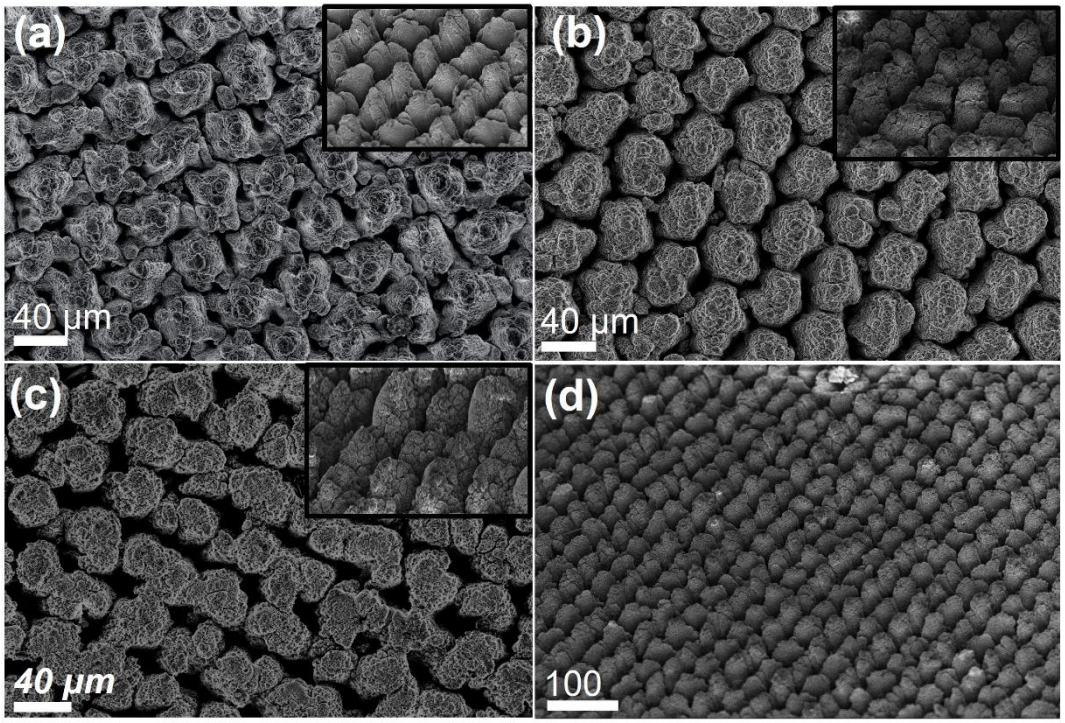

Figure 2.13. FESEM images of the laser textured aluminum surface at different pulse repetition rates of (a) 25 kHz; (b) 100 kHz; (c) 150 kHz; uniformity of surface micro-features generated in (b) shown at lower magnification.

The surface morphology analysis from FESEM images is further confirmed by the 3D surface profilometer images, which provide the topographical information of the laser-generated surface features, shown in Figure 2.14(a,b).

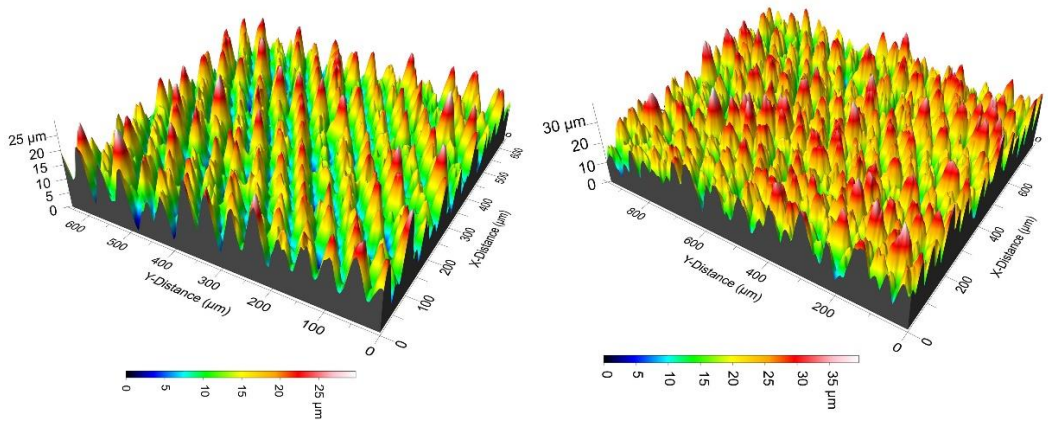

Figure 2.14. 3D Profilometer scan images of the laser-modified aluminum at a pulse repetition rate of (a) 25 kHz; (b) 150 kHz.

Immediately after the laser treatment, the surface was highly water-attracting, i.e., superhydrophilic, due to the formation of aluminum oxide Al_2O_3 by oxidation induced by high-temperature generation in an open atmosphere [56]. Figure 2.15shows the spectra of energy dispersive X-ray analysis performed on the laser-modified surface and the corresponding elemental composition information. As shown in the figure, the oxygen content on the surface increases after the laser treatment. The alumina formed after the laser treatment is a polar compound. It is well accepted that the resulting superhydrophilicity is a combined effect of the polar nature of alumina and the laser-generated surface texture [57,58].

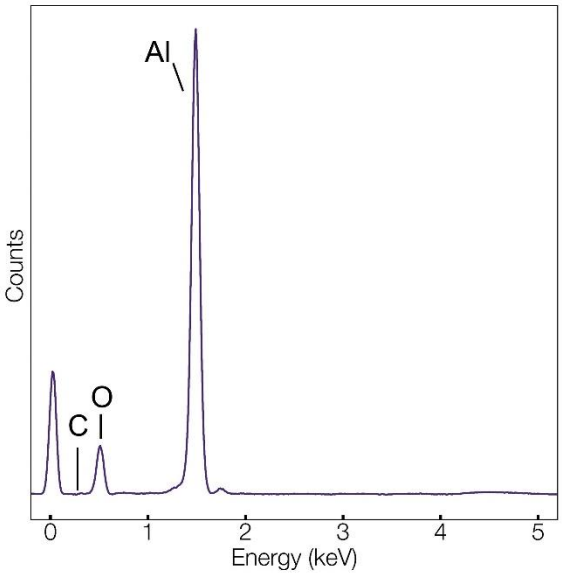

Elements	Atomic %
Al	34.6
O	57.6
C	4.5

Figure 2.15. EDS spectra and corresponding composition information of Laser treated Al 6013 sample.

After the laser surface modification of the aluminum alloy, a fluoroalkyl silane (FAS) based treatment was performed to render the surface superhydrophobic. As part of the FAS coating procedure, the laser-processed sample was first sonicated separately in ethanol and acetone solutions to remove contaminants and dust from the surface. The dried sample was then immersed in an ethanol solution of perfluorooctyl-triethoxy silane (POTES, 1.5 $wt\%$) for two hours, after which the samples were washed with ethanol and finally placed in an oven to undergo thermal treatment at $120\,^{\circ}C$ for fifteen minutes to stabilize the SAM to obtain the superhydrophobic surface [59].

2.6.2 Superhydrophobic Surface Based on FAS

Figure 2.16shows the obtained superhydrophobic surface following the laser modification and silanization treatment. All the laser modifications at different PRR exhibit high static water contact angles $(160°)$ as shown in Figure 2.16(a), compared to a contact angle of $115°$ for FAS silanized but plane metallic surface as shown in inset of Figure 2.16(a). For all the contact angle and roll-off angle measurements, a droplet volume of 5 µL was set. Moreover, the water roll-off angles are below $10°$, confirming the excellent superhydrophobicity, thanks to the laser-generated hierarchical surface features [49]. Furthermore, the

superhydrophobic surface is repellent to even relatively low surface tension ethylene glycol $(47.3\ mN\ m^{-}, 25\ ^{\circ}C)$, shown in Figure 2.16(b).

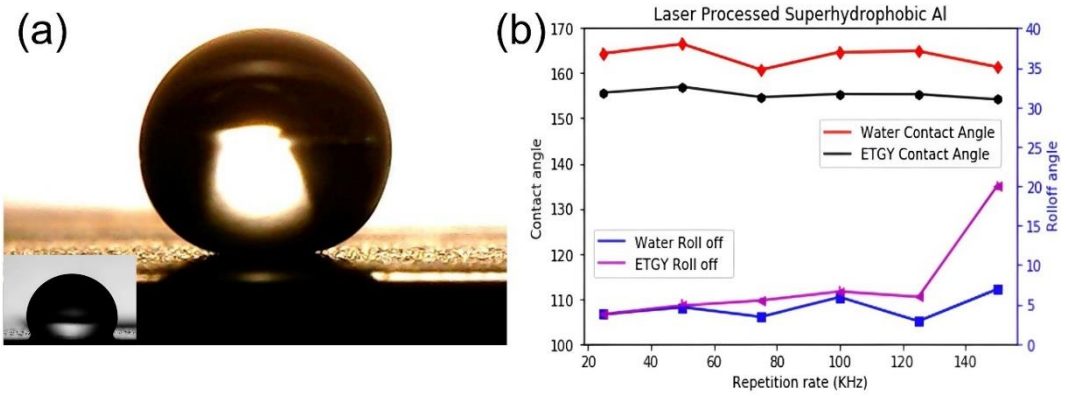

Figure 2.16. (a) Camera image of a droplet with high contact angle (167°) on laser-processed superhydrophobic Al; (b) water and ethylene glycol contact angle and roll-off measurements at varying pulse repetition rates for the laser-processed samples.

However, it can be observed from the figure that the roll-off angle of ethylene glycol on the surface modification at PRR of 150 kHz is 20° which is beyond the maximum limit of 10° for super-repellent surfaces. A closer analysis of the microfeature, as shown in Figure 2.17, could explain this phenomenon. As previously mentioned, the microfeatures are no more separated conical structures for the highest PRR of 150 kHz. Consequently, it results in two possible factors. Firstly, as seen in Figure 2.17(b), compared to the lower PRR modification of 25 kHz (Figure 2.17(a)), the tips of the microfeatures at PRR of 150 kHz have larger areas, thereby providing more contact area for the liquid droplet. Secondly, the micro features are relatively densely packed, and the spacing between the features is much smaller, as previously discussed. The above effect reduces the air pockets between the structures, increasing the solid contact area for the liquid. The factors mentioned above could increase droplet adhesion, resulting in relatively low contact angles and high roll-off angles for modifications performed at a higher PRR of 150 kHz.

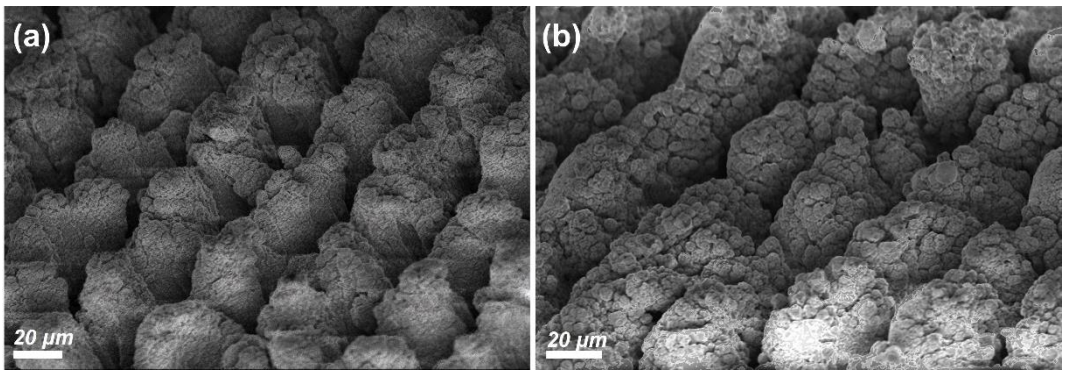

Figure 2.17. FESEM images of the conical surface features of the laser fabricated superhydrophobic Al at pulse repetition rates of (a) 25 kHz; (b) 150 kHz.

2.6.3 Alternative Nanostructure by Hydrothermal Treatment

In this study, the pseudo-boehmite (AlO(OH)) was generated on the laser-processed aluminum samples by immersing them in boiling water ($100\,°C$) for different treatment times. Figure 2.18 presents the high magnification FESEM images of the pseudo-boehmite structure generated on the laser-textured alumina microfeatures. It is well known that the hydrothermal treatment of alumina forms the hydrated alumina/pseudo-boehmite almost immediately [60–62]. Due to the low solubility, the hydrated alumina precipitates as nano-flakes with a few tens of nanometers diameter and a shape resembling desert rose crystals, as visible from the FESEM images. These flakes are usually rolled up on the edges, making them appear needle-like [63].

The pseudo-boehmite nanostructure was generated to fabricate a hierarchical superhydrophobic surface and to compare the same with laser-generated natural micro-nano hierarchy. Based on the hydrothermal treatment time, the pseudo-boehmite flake density varies, modifying the nanostructure, as shown in Figure 2.18(b,c,d). Hence, as part of the study, the boiling treatment was performed on the laser-processed samples for a different time duration of $1\ min$ and $20\ min$, to fabricate superhydrophobic surfaces.

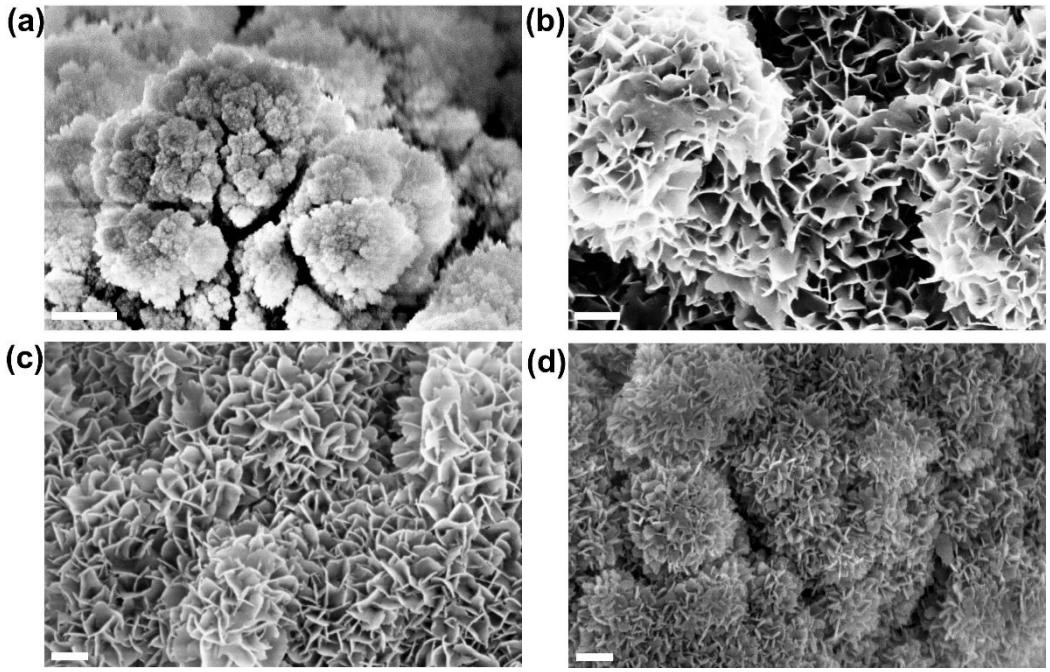

Figure 2.18. FESEM images of (a) laser textured sample; boiling water treated after laser texturing for a duration of (b) 1 min; (c) 4 min; (c) 20 min. Scale bar: (a) 1 μm; (b,c,d) 200 nm.

Figure 2.18 shows the X-ray diffractogram for the laser-modified aluminum surface and the laser-treated surface followed by boiling water treatment. The XRD results confirm the presence of alumina on the laser-treated surface, as shown in Figure 2.19(a) corresponding to angles (2θ) of 33.2°, 39.8°, 59.5°, and 82.5°, respectively [64]. The above results further confirm the EDS results of the laser-textured surface, as discussed in Figure 2.15. Also, the XRD analysis of the laser textured sample followed by hydrothermal treatment for $20\ min$ is shown in Figure 2.19(b). The diffractogram of the same clearly shows the formation of a pseudo-boehmite structure corresponding to the nanostructure generated after boiling water treatment. Newly formed diffraction peaks observed at angles of 13.5°, 27.8°, 48.9°, 66.7°, and 72° correspond to the pseudo-boehmite structure [65].

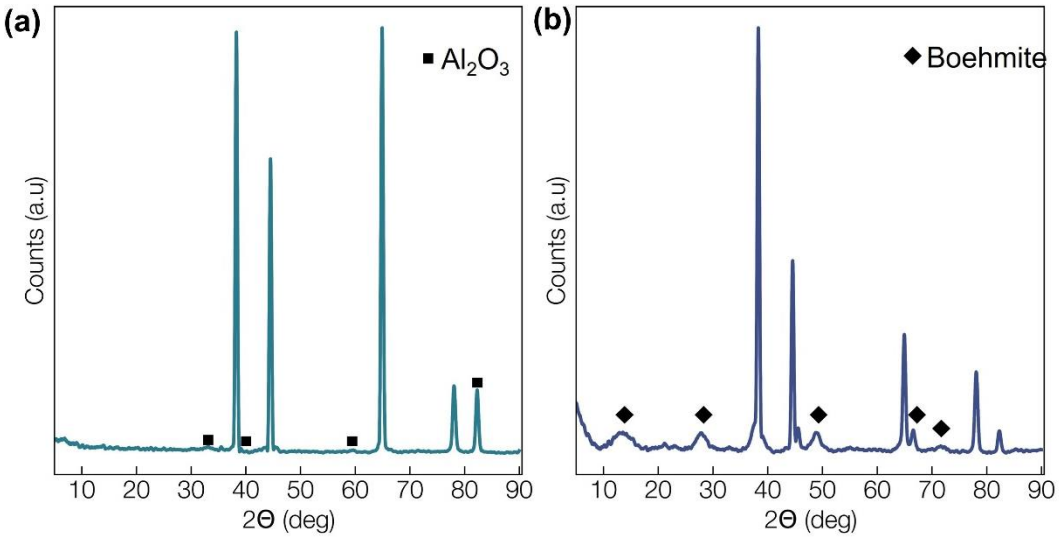

Figure 2.19. X-Ray diffraction results of (a) laser textured aluminum; (b) 20 min boiling water treatment after laser texturing.

The hydrothermally obtained pseudo-boehmite structure is a finely crystalline boehmite form with higher water content, either chemically bonded or adsorbed. Figure 2.20 depicts the chemical structural form of the pseudo-boehmite, which has shorter chains with terminal H_2O groups, and therefore results in higher specific water content compared to boehmite [66]. The presence of hydroxyl groups in abundance makes them highly hydrophilic. Notably, unlike the laser-treated alumina surface, which is well-known to gradually change from a superhydrophilic to superhydrophobic nature due to the adsorption of volatile organic compounds from the surroundings, the superhydrophilic boehmite structure is stable for a much longer duration (in terms of months) [67]. The chemical reaction involved in the formation of pseudo-boehmite is depicted in the equation below:

$$Al + 2H_2O \rightarrow AlOOH + \frac{3}{2}H_2 \tag{10}$$

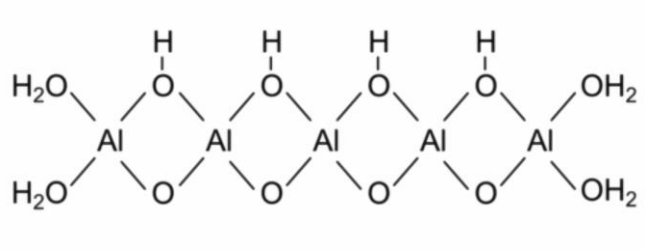

Figure 2.20. Chemical structure of the pseudo-boehmite

The previously mentioned fluorosilane (POTES) treatment was performed on the aluminum samples that underwent both laser processing and boiling water treatment $(1min, 20min)$. Figure 2.21shows the resulting contact angle and roll-off angle measurements on the boiling water treated samples, along with the camera image of droplets on the corresponding surfaces (Figure 2.21(b,c)). Interestingly, even though the boiling water treated samples had a porous and hierarchical micro (laser textured)-nano (pseudo-boehmite) structure, the water repellency property was relatively poor compared to the only laser-processed micro-nano texture.

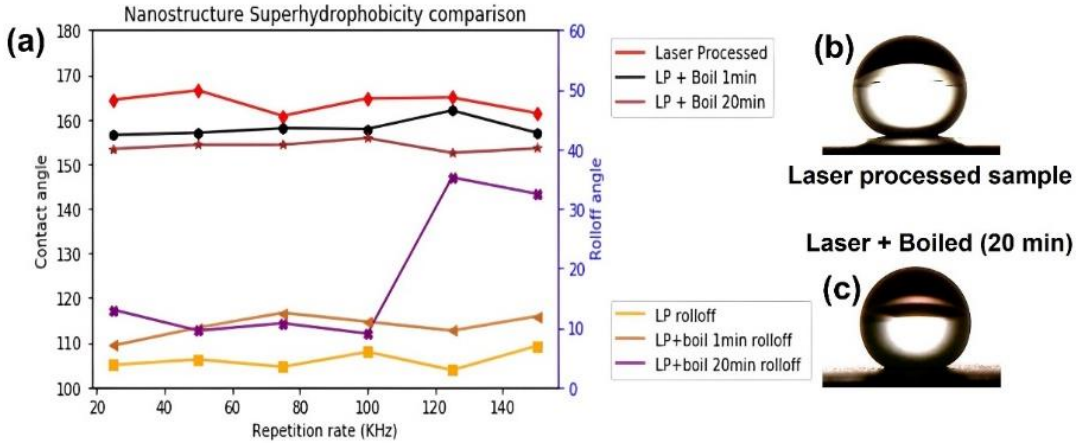

Figure 2.21. (a) Water contact angle and roll-off angle at varying PRR on laser processed and hydrothermally treated sample following laser processing; 5 µL water droplet on (b) laser processed; (c) laser processing followed by 20 min hydrothermal treatment.

In fact, from the plot in Figure 2.21(a), it is observed that the superhydrophobic performance deteriorates with the hydrothermal treatment time.

The static contact angle for the sample with $20\,min$ immersion in boiling water shows a drastic reduction in the order of $\sim 10°$ or more, in comparison to the laser-processed sample. Additionally, the roll-off angles reflect an identical behavior, wherein the hydrothermally treated samples exhibit greater roll-off angles.

Interestingly, the $20\,min$ hydrothermally treated sample displays a drastic increase in roll-off angles for the modifications performed at high repetition rates of $125\,kHz$ and $150\,kHz$. The micro and nanoscale factors could explain this behavior. Firstly, at the nanoscale, as shown in Figure 2.18, with the increasing hydrothermal treatment time, the porosity of the nano-flakes decreases while the flake density increases. This would correspond to a decrease in air-pocket presence, implying greater droplet adhesion to the substrate. Secondly, on the micro-scale, as previously discussed, the laser modifications performed at higher pulse repetition rates (PRR) have densely packed microfeatures with more surface contact area for the liquid droplet. The above reasons could result in an abrupt increase of droplet roll-off angles for modifications performed at both greater PRR and boiling time.

Considering that laser texturing and boiling water treatment provide a micro-nano surface hierarchy, it becomes important to investigate the surface functional groups after hydrothermal treatment and drying. The surface functional group investigation is crucial to assess the efficiency of the silanization treatment, which is highly sensitive to the presence of water. The silane polymerizes in the presence of water to form unstable multilayers that result in an inhomogeneous surface coverage [68]. Therefore, it is crucial that the hydrothermally treated sample has minimal water content after drying.

To study the relatively low superhydrophobicity of the hydrothermally treated samples, FTIR spectroscopy was performed to investigate the surface functional groups. Figure 2.22 shows the FTIR spectra obtained from the laser-processed aluminum sample and the boehmite sample, which underwent $20\,min$ boiling water treatment.

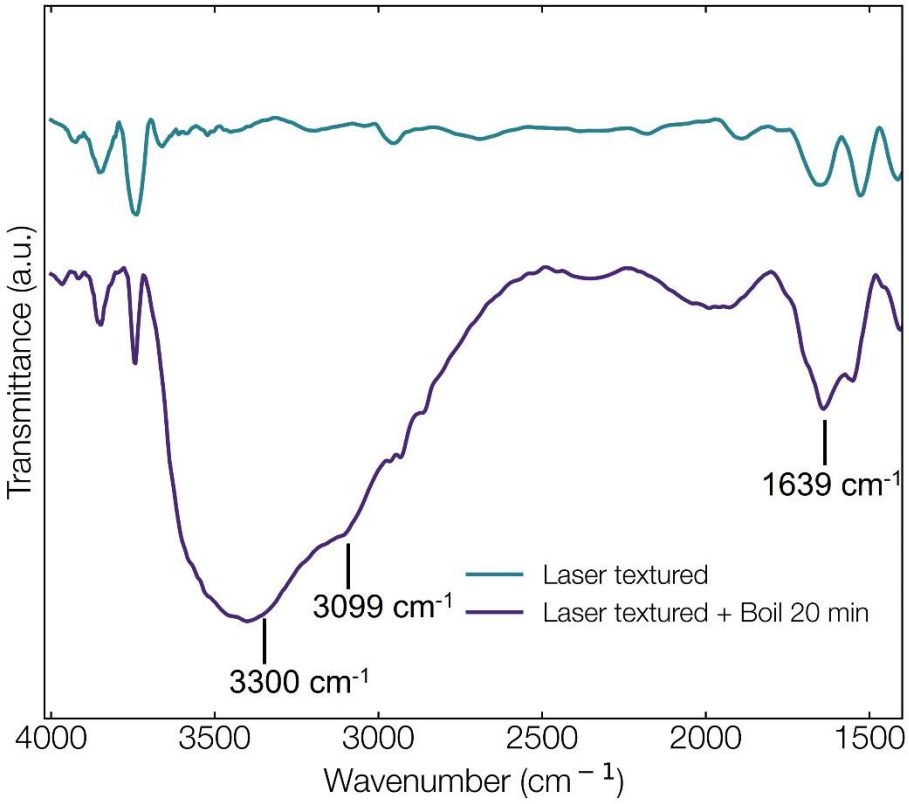

Figure 2.22. FTIR spectra of laser textured and laser texturing along with boiling water treatment for 20 min.

Interestingly, the FTIR spectra of the pseudo-boehmite sample show a strong and broad absorption band centered at $\sim 3300\ cm^{-}$ which well corresponds to the $O-H$ stretching vibrations of hydroxide structure and water molecules. The absorption is broad due to the hydrogen bridging between the water molecules. Also, there is an enhanced absorption at $3099 cm^{-}$ in the $O-H$ vibrations of $AlO(OH)$. The peak at $1639 cm^{-1}$ is ascribed to the bending mode of water molecules. On the contrary, the fresh laser-treated aluminum surface does not show the presence of strong $O-H$ adsorption to the surface [65,69,70].

The FTIR spectra reveal the relatively high-water content on the pseudo-boehmite structure, thereby possibly hindering the successful SAM formation by the fluorosilane. Thus, it can be concluded as the primary cause for the relatively inferior superhydrophobic property of the hydrothermally treated substrate, even though the surface had a uniform hierarchical micro-nano structure.

2.6.4 Corrosion Resistance

Anti-corrosion is an important functional aspect of superhydrophobic surfaces. A direct test through immersion in corrosive saline solution would help to understand the stability of the superhydrophobic coating before the Cl^- ions would begin the corrosive reaction. Therefore, a saltwater immersion test was performed to experimentally investigate the anti-corrosion performance of fabricated laser-textured and hydrothermal-treated superhydrophobic surfaces. Figure 2.23 shows the plot of static contact angle measurements performed at various intervals over one month on the fabricated superhydrophobic surfaces immersed in the saline solution.

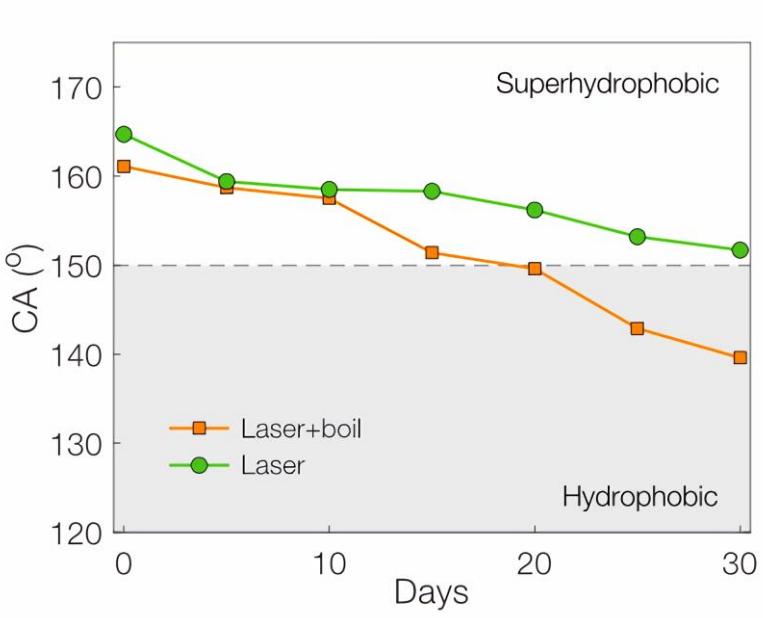

Figure 2.23. Static contact angle measurements performed under continuous salt water (3.5 wt%) immersion on laser processed and laser processing with hydrothermal treatment over one month.

As shown in the Figure 2.23, the laser-textured sample maintains the static contact angles above 150° even after continuous immersion in the saline solution for one month. On the other hand, the superhydrophobic pseudo-boehmite sample falls below the 150° mark at about 18 days into immersion. This result directly demonstrates the importance of durable superhydrophobicity for practical

applications despite the gradual decrease in contact angle values, which is expected due to the corrosive nature of the solution.

The corrosion pathway for aluminum/alumina in NaCl solution has been well studied due to its importance in marine applications [71]. The corrosion begins at first by exposure of the oxidized aluminum to the solution. The alumina is firstly hydrolyzed by water, following which the aggressive Cl^- ions dissolve the hydrolyzed alumina through the formation of $AlCl_3$ which is dissolved into the solution. The above cycle continues in the same manner through the exposure of fresh aluminum/alumina. The reactions mentioned above are shown in the following chemical reaction equations:

$$Al_2O_3 + 3\ H_2O \rightarrow 2\ Al\ OH\ _3 \tag{11}$$

The resulting hydrolyzed aluminum is then attacked by Cl^- ions sequentially,

$$Al\ OH\ _3 + Cl^- = Al\ OH\ _2Cl + OH^- \tag{12}$$

$$Al\ OH\ _2Cl + Cl^- = Al\ OH\ Cl_2 + OH^- \tag{13}$$

$$Al\ OH\ Cl_2 + Cl^- = AlCl_3 + OH^- \tag{14}$$

On the contrary, in the case of a superhydrophobic surface, the corrosive ions cannot penetrate the surface due to water repellency. However, in the case of the boiling water-treated samples, the presence of water on the sample results in a non-optimal silane coating. This allows the chloride ion penetration much faster, resulting in deterioration in superhydrophobicity.

2.6.5 Metastable Cassie State

To repel low surface tension liquids such as oil and organic solvents like ethanol, the suspension or capillary force experienced by the liquid on the surface must overcome the penetration force. It is well-known that with certain surfaces, such as re-entrant ones, the appropriate geometry could repel even ethanol, resulting in omniphobic surfaces. Therefore, even if not for re-entrant surfaces

that need specific fabrication techniques, a suitable surface geometry can be fabricated to repel liquids with intrinsic contact angles below 90° (i.e., oil).

Therefore, to study the ability of the laser-textured surface fabricated in this work to repel low surface tension liquids, an ethanol-water mixture of varying composition ratios was prepared, and the contact angle was measured. The reason behind the selection of such a mixture was due to the variability of the surface tension of the mixture, which ranges from $73\,mN\,m^{-}$ (100 % water - 0 % ethanol) to $22.3\,mN\,m^{-}$ (0 % water - 100 % ethanol), thereby providing a wide range of tunable surface tension values. Contact angle measurements were then taken for the different mixture ratios starting from 100 % water on all three silanized samples of well-polished aluminum alloy ($R_a = 0.56\,\mu m$) as intrinsic contact angle reference, laser-treated surface, and laser-treated surface followed by 20 minutes of hydrothermal treatment. Figure 2.24 shows the corresponding measurement plot between the intrinsic contact angle (polished surface) and the superhydrophobic surfaces.

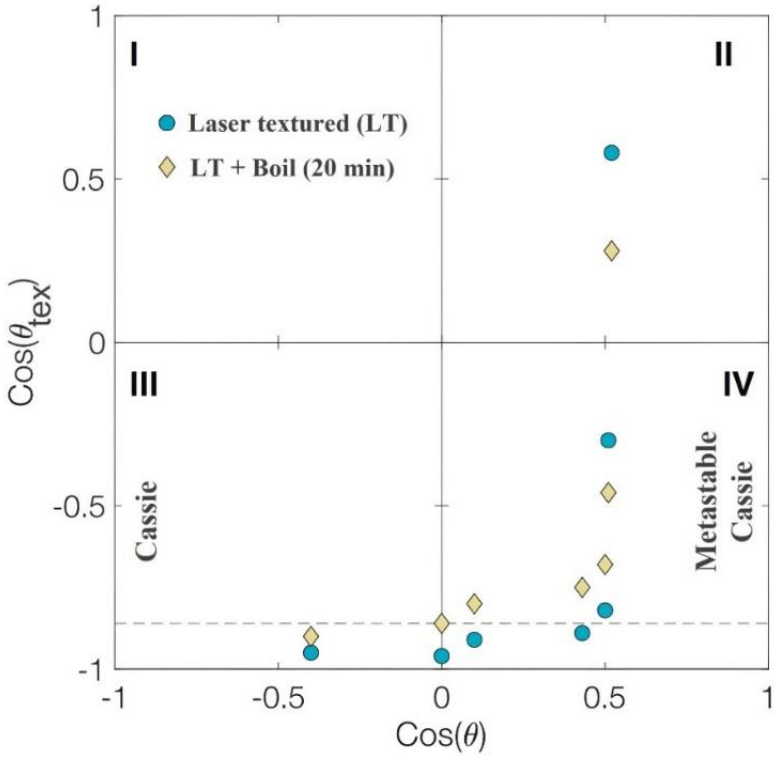

Figure 2.24. Cosθ of contact angle measurements performed on textured superhydrophobic surface vs polished planar surface for different water-ethanol mixture. The measurements are performed for both laser textured and laser textured surface along with hydrothermal treatment (20 min).

Interestingly, as seen from the Figure 2.24, it is observed that even for intrinsic contact angle values below $90°$ (i.e., $Cos\theta > 0$), the corresponding contact angle on laser textured surface stays $> 150°$ (i.e., quadrant IV). The above situation is only possible for the case of metastable Cassie state, where the intrinsic contact angle $< 90°$ but the textured surface behaves super-repellent towards low surface tension liquids [72]. Even though the boiling water treated sample exhibit slightly lower contact angle values, it follows a similar behavior where the hydrophobicity is lost at an intrinsic contact angle value of about $60°(Cos\theta = 0.5)$ which is still lower than the intrinsic contact angle of vegetable oils such as olive oil $(74°)$. This behavior confirms the ability of the laser-treated surface to repel even low-surface tension liquids. The above result can be interpreted as the following:

(i) The nanosecond laser texturing technique can fabricate superoleophobic surfaces with the design of appropriate surface texture, letting the liquid stay in a metastable Cassie state.

(ii) An appropriate low surface energy coating must be used apart from the surface texture. This is because the intrinsic contact angle corresponds to the highest possible contact angle on a flat surface and requires an appropriate low surface energy coating.

2.7 A Necessary Choice Between Superamphiphobicity and Eco-friendly Superhydrophobicity

The previous section concluded with the importance of surface texture and an appropriate coating for metals to repel low surface tension liquids. During the intended application lifetime of the superhydrophobic surfaces, there is a high possibility for the surface to encounter liquids with relatively lower surface tension than pure water, commonly used for characterizing Superhydrophobicity. Hence it becomes essential for the surface to exhibit superamphiphobicity, which refers to the ability to repel liquids with either high polar (e.g., water) or dispersive (e.g., diodomethane) components of surface energy [73]. Their need arises from various practical and industrial requirements, where such a surface property becomes essential to prevent oil spread on the surface which could even destroy superhydrophobicity. Especially for critical applications intended for long-term use, such as aerospace, marine, oil-gas, and chemical processing

industries, superhydrophobicity alone would not be enough; hence the need for oil-repellent surfaces arise [74].

On the other hand, there has been mounting interest in eco-friendly superhydrophobic surfaces. This is primarily because extreme water-repellent metallic surfaces are traditionally coated with low surface energy fluoro/chloro silanes. However, environmental protection agencies of several countries are introducing a ban on toxic chemicals such as fluoroalkyl substances (FAS) [75]. The use of FAS has been a topic of concern due to their toxicity and persistence in the environment, giving them the nickname 'forever chemicals.' These chemicals are known to cause bioaccumulation in living organism tissues and blood, harming the liver function, immune system, and reproductive system [76].

Hence eco-friendly superhydrophobic surfaces, primarily dependent on hydrocarbon-based coatings, have been considered a possible alternative to FAS-based coatings, as shown in Figure 2.25. Even though the Superhydrophobicity of these coatings are inferior to fluorosilanes, their eco-friendly nature makes them ideal for critical biomedical and food science and technology applications.

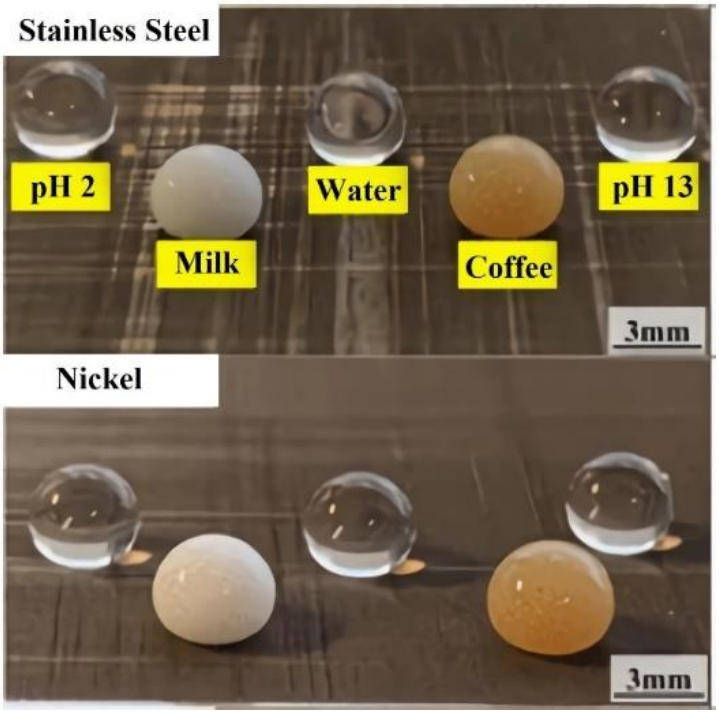

Figure 2.25. Droplets of consumable liquids, strong acid, and strong alkaline solutions on superhydrophobic metal substrates fabricated using laser texturing and silicone oil thermal treatment **[77]**.

2.7.1 Need for an Alternative and Truly Eco-friendly Approach for Rapid Fabrication of Superhydrophobic Surfaces

The current state-of-the-art eco-friendly fabrication of superhydrophobic metallic surfaces relies on hydrocarbon adsorption on the surface metal oxides. Previously, after the surface treatment step, the sample would be exposed to open air, resulting in volatile organic compound (VOC) adsorption, which initiates the transition of surface property from superhydrophilic to hydrophobic and finally superhydrophobic, in a duration of a few weeks.

As the above process is time-consuming and not industrially viable, several approaches to accelerate the adsorption process have been proposed by researchers, including thermal treatment, vacuum-based adsorption (Figure 2.26(a)) and silicone oil coating [27,32]. Even though such techniques have reduced the superhydrophobic transition time to about tens of minutes for the best case, the techniques mentioned above still face some drawbacks for large-scale applicability.

Firstly, despite the reduction in treatment time for the thermal treatment method, the whole duration of the procedure is still of the order of tens of hours. On the contrary, the high-vacuum treatment renders the superhydrophobicity in about an hour, as shown in Figure 2.26(b). Nonetheless, the requirement of a high vacuum makes the technique expensive. Also, the treatment naturally becomes complicated for large-size samples.

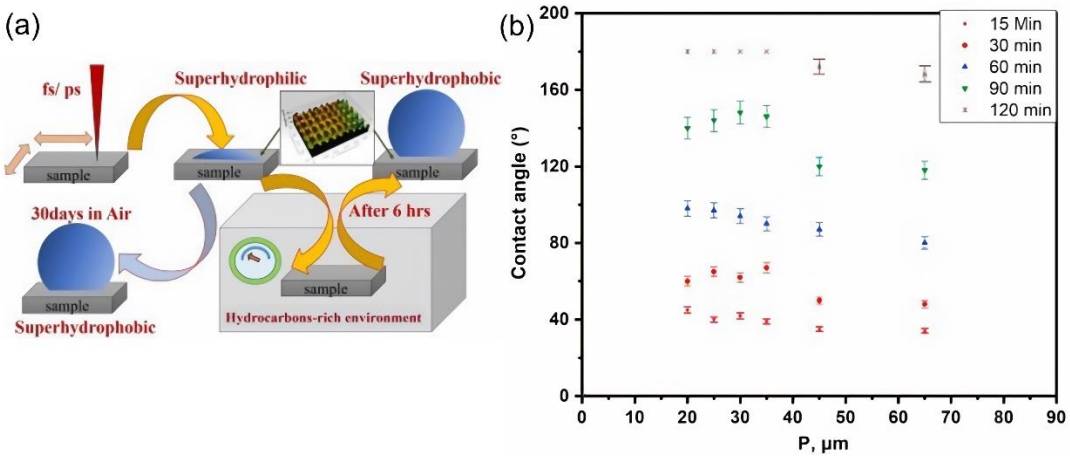

Figure 2.26. (a) Illustration explaining the vacuum treatment process after the laser surface texturing []; (b) plot representing contact angle vs laser scan pitch measurements on Ti-6Al-4V alloy for different vacuum treatment time **[78]**.

The silicone oil treatment offers speed and a non-toxic approach to fabricating superhydrophobicity. However, the recent large-scale production of silicone as a replacement for plastic for various applications has posed a significant challenge due to its large carbon footprint during production. Also, research studies have suggested the transmission of toxic and persistent siloxanes from silicone products into food [79,80].

Therefore, the need for an alternative, rapid, eco-friendly, and stable superhydrophobicity fabrication technique is compelling.

2.7.2 Eco-friendly Oil-Vapor Treatment for Rapid Superhydrophobicity

In this study, we propose an alternative method to fabricate superhydrophobic metal surfaces. After the laser surface treatment, the processed aluminum samples are sonicated in acetone, ethanol, and de-ionized water solutions for 5 min each to remove the loose debris. The procedure involves thermal treatment of the laser-textured metallic sample along with vegetable oil enclosed in a sealed container, as depicted in Figure 2.27. The closed container comprised the cleaned metal sample along with the vegetable oil (flaxseed oil, 2 ml) placed in a small separate beaker. Before inserting the sample, the container along with the oil beaker is thermally treated in the oven at 150 $^{\circ}$C for fifteen minutes, to saturate the

atmosphere. Upon thermal treatment at 120 °C for five hours, the vegetable oil-based hydrocarbon source is expected to cause vapor saturation within the container. The saturated hydrocarbon atmosphere is expected to accelerate the superhydrophobic transition of the metal substrate.

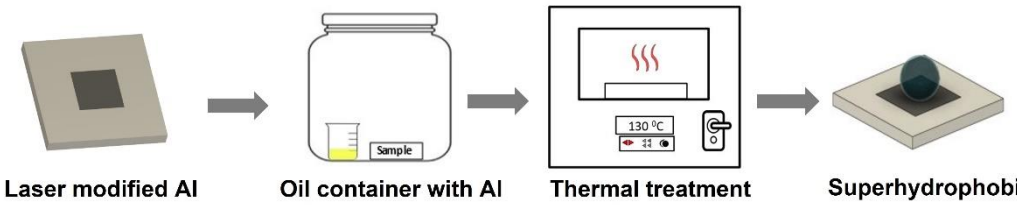

Figure 2.27. Illustration depicting the procedure used in this study for oil-vapor treatment on laser-textured aluminum surface to obtain superhydrophobicity.

The superhydrophobic surface obtained with the oil-vapor treatment is compared to the superhydrophobic surface fabricated using the fluorosilane treatment discussed in the previous sections. The comparison would therefore provide means to simultaneously characterize the functional stability with respect to a frequently employed technique.

2.8 Tunable Pulsewidth Nanosecond Laser Texturing

Several studies have been previously conducted on superhydrophobicity based on laser micromachining. In these studies, different laser parameters, such as scan speed, fluence, and scan line spacing, were varied to tune the superhydrophobicity. Y. Lu et al. used UV nanosecond laser texturing followed by fluorosilane treatment on stainless steel to obtain superhydrophobicity [81]. A laser fluence of 8.14 J/cm^2 at a scanning interval of 30 μm was determined to exhibit water repellency.

However, very few studies have been reported on the effect of nanosecond laser pulsewidth on the superhydrophobicity of the surface. The advancement of MOPA fiber laser technology has enabled nanosecond laser systems to have adjustable pulse duration and high pulse repetition rates. The following study investigates the effect of nanosecond laser pulsewidth on the superhydrophobicity of the aluminum alloy samples discussed in this work. Following the laser processing of aluminum alloy at varying pulsewidths, one set of samples is treated with Fluorosilane and another set with the oil vapor treatment as discussed previously.

Figure 2.28 shows the single laser line scan performed at an average power of 18 W, pulse repetition rate of 100 kHz, and different pulsewidths of 4, 8, 12, and 30 ns on the aluminum alloy (Al 6013).

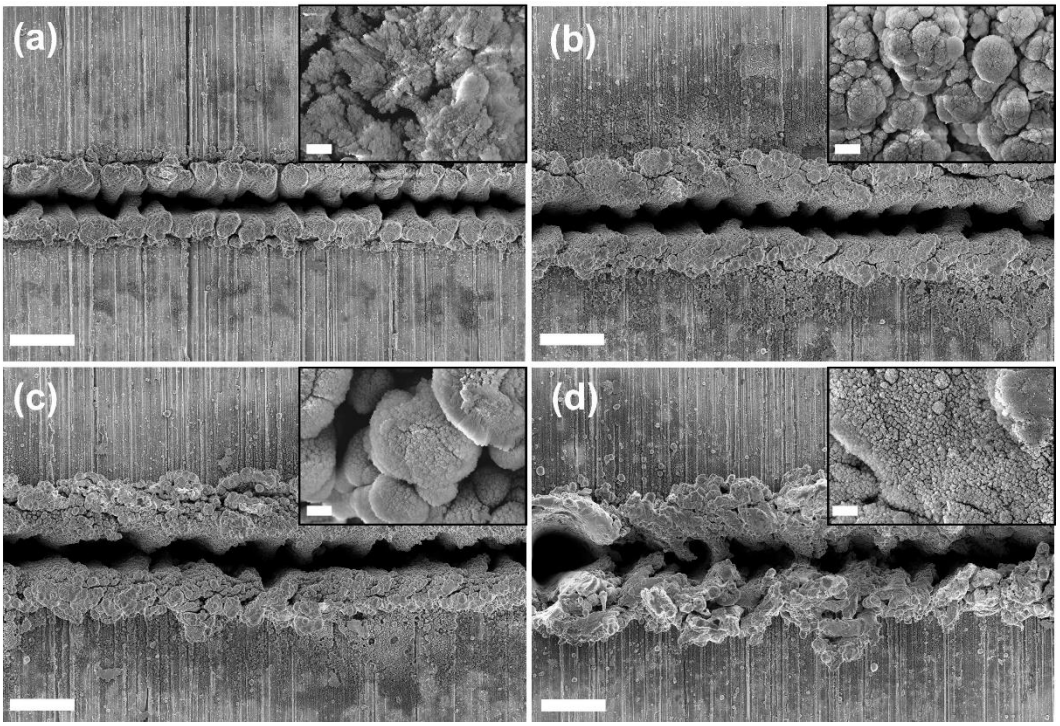

Figure 2.28. FESEM images of single laser line scans on aluminum surface at different pulsewidths of (a) 4 ns; (b) 8 ns; (c) 12 ns; (d) 30 ns. Scale bar: main image (40 μm); inset (300 nm).

FESEM images of laser-induced surface modifications reveal a drastic variation amongst the generated microstructure with respect to the interacting laser pulsewidth. The long pulsewidth (30 ns) induced thermal effects are visible along the laser scan path in Figure 2.28(d). An interesting observation regards the re-solidified melt recast around the laser modification edge for all the cases. Even though melt recast is present in all the modifications, however, for small pulsewidth modifications (4 ns), the recast formation is more uniform and predictable in shape, whereas with increasing pulsewidth, the recast formation becomes more non-uniform and random. The inset in the figure refers to the nanostructure for the corresponding modifications. The resulting nanostructure remains diverse; nonetheless, a strong surface hierarchy is visible for all the cases.

The pulsewidth, therefore, substantially affects the resulting laser modifications. For a constant pulse energy delivered by the laser system at a fixed focal spot size, the peak intensity is dependent only on the laser pulsewidth. For a Gaussian pulse, the peak intensity is given by the following formula [82]:

$$I_P = \frac{2F_o}{\Delta t}\sqrt{\frac{ln2}{\pi}} \simeq \frac{0.94F_o}{\Delta t} \tag{15}$$

Where I_P is the laser peak intensity, F_o is the pulse fluence, and Δt is the laser pulsewidth. Figure 2.29 shows the plot of pulse peak intensity vs the pulse fluence for different interacting laser pulsewidth, calculated using equation (15). The fluence range in the plot is selected based on the available range provided by the fiber nanosecond laser system used in this study.

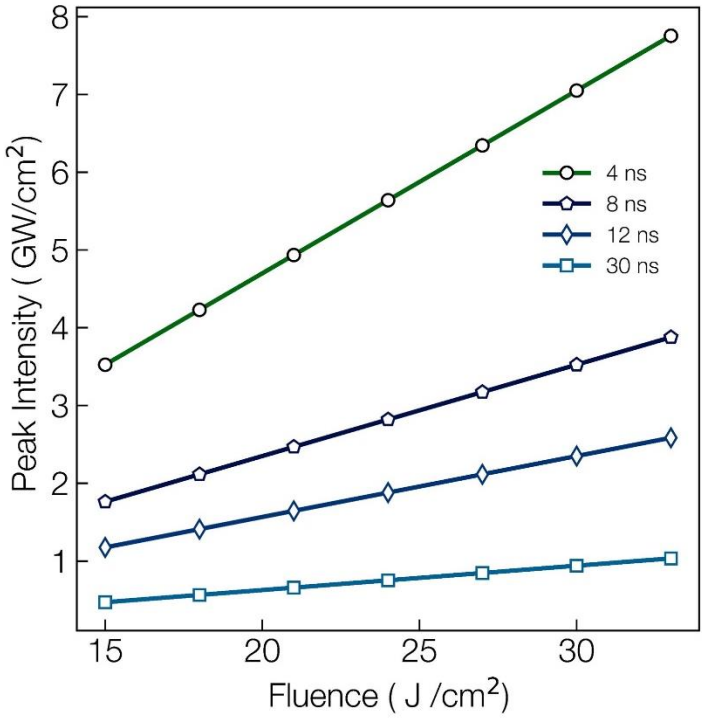

Figure 2.29. Calculated laser peak intensity vs. pulse fluence for different laser pulsewidth values.

Interestingly, the peak intensity has a linear relationship with the pulse fluence, even still the peak intensity shows a drastic variation at different laser

pulsewidths. For example, at a fluence of 30 J/cm^2, a 4 ns laser pulse delivers a peak intensity of about 7 GW/cm^2, whereas the 30 ns pulse provides only about 0.9 GW/cm^2. The precision of laser micromachining depends on the ability of the interacting pulse to vaporize material compared to melt and solidification. In the case of long pulsed interaction, heat diffusion depth (l_d) given by $l_d = \sqrt{D\Delta t}$, where Δt is the laser pulsewidth and D is the heat diffusion coefficient of the material. The above equation shows that for the same interacting material, l_d (30 ns) = 5 l_d (4 ns), explaining the relatively clean modification observed at Δt = 4 ns in Figure 2.28(a). Since the heat diffusion length is lower for the shorter pulsewidth, the delivered optical energy is concentrated near the focal spot and therefore predominantly vaporizes the material rather to generating melt and recast features.

To further investigate the role of laser pulsewidth on superhydrophobicity, the previously used triple scale texture depicted in Figure 2.12 is once again selected. As previously mentioned, Fluorosilane (POTES) and oil-vapor treatments are separately performed on the laser textured surface to convert the surface from superhydrophilic to superhydrophobic.

2.8.1 Surface Morphological and Topographical Analysis

The laser textured surfaces were first analyzed using field emission SEM and contact profilometer. Figure 2.30- shows the FESEM images of the surface modifications taken at different magnifications. As expected, the laser pulsewidth had a strong influence on the resulting surface morphology, as shown in the figure. The surface morphology evolves from separated conical features to a more random morphology with the increasing pulsewidth. The FESEM and 3D profilometer images in the figure show the initial conical features with an adjacent tip-to-tip spacing of 50 µm, generated at a pulsewidth of 4 ns (Figure 2.30 (a,d,g,j)) modify to separated line like features at pulsewidth of 12 ns (Figure 2.30(b,e,h,k)) and eventually result in the random rough surface texture at pulsewidth of 50 ns (Figure 2.30(c,f,i,l))

Another interesting observation can be made from Figure 2.30(a,b,c), where with increasing pulsewidth, there exists a greater presence of small micro-sized particles atop the larger base microfeature. For all the laser modifications, a strong micro/nano hierarchy is observed, ranging from about tens of microns to few hundred nanometers and even lower with a strong resemblance to cauliflower at

the nanoscale. Such a complex hierarchy is well known to be beneficial for superhydrophobicity [83].

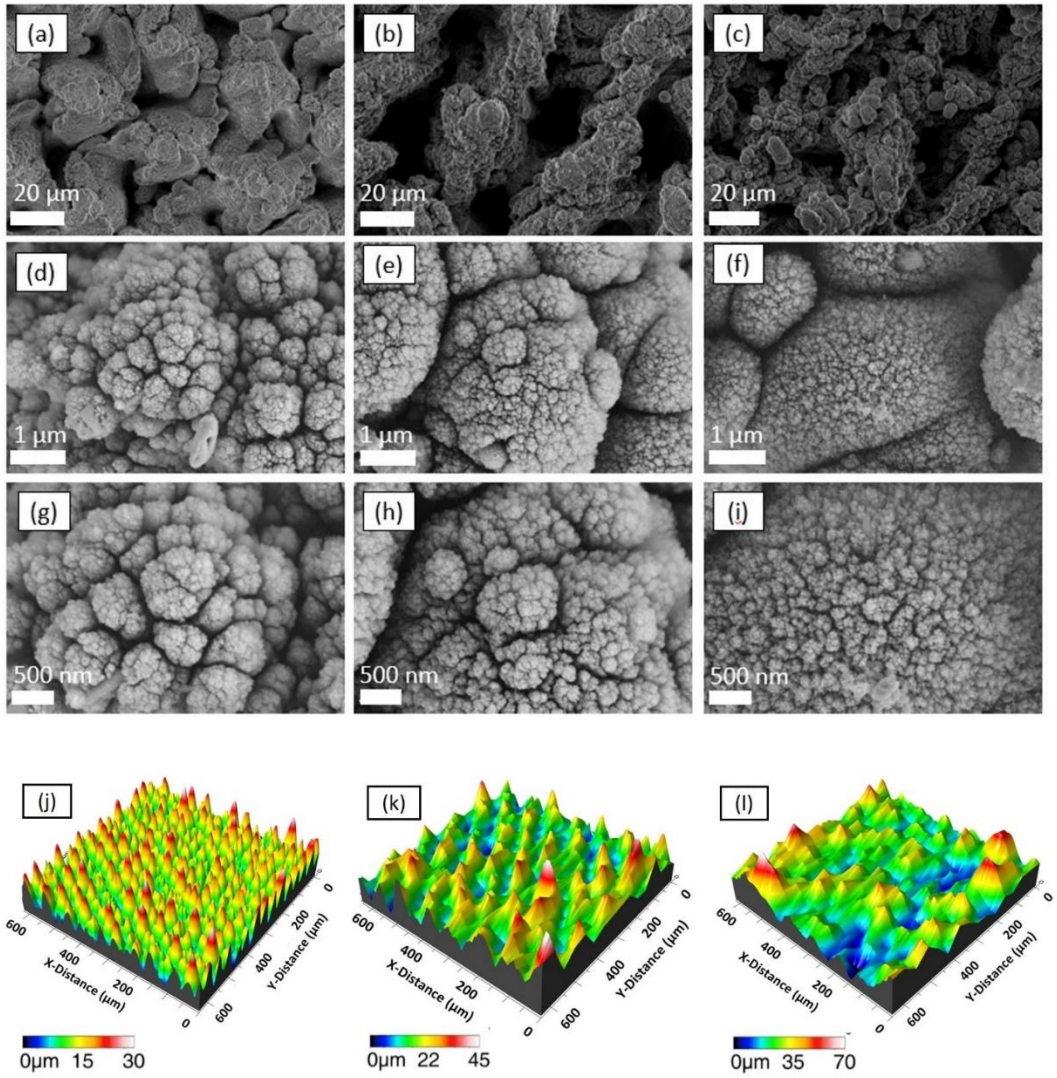

Figure 2.30. FESEM images of the laser modified surfaces at different pulsewidths of (a,d,g) 4 ns; (b,e,h) 12 ns; (c,f,i) 50 ns. The corresponding 3D profilometer images are shown respectively in (j,kl).

Furthermore, from the 3D profilometer image in Figure 2.30(j,k,l) it is evident that the protruding conical like surface features have a higher density at the lower pulsewidth of 4 ns as compared to higher values of pulsewidth. For superhydrophobic surfaces, the surface roughness has proven to be a significant

factor of influence. Important roughness parameters of average roughness (Sa), and peak to valley height (Sz) were measured as shown in Table 2.1, for all the laser textured surfaces.

Laser Pulsewidth (ns)	Sa (μm)	Sz (μm)
4	3.6	29.7
8	3.9	40.5
12	4.5	46.0
30	6.8	61.6
50	7.45	77.1

Table 2.1 Surface average and peak to valley roughness values of laser modified surfaces at different pulsewidth values.

The thermal effect of the nanosecond laser is clearly observed from the surface roughness measurements shown in the table above. Post the electron-lattice relaxation process at the picosecond timescales, the continuing nanosecond pulse interaction would result in thermal energy diffusion in the material, such as the formation of heat affected zones (HAZ). Therefore, with the increasing pulse duration, the enhanced thermal events produce a rough surface texture along with increased thermal diffusion. As a result, both the average roughness and the modification peak to valley height increases, as shown in Table 2.1.

2.8.2 Characterization of Superhydrophobicity

Following the laser processing, surface chemical modification was performed to reduce the surface energy and render the surface superhydrophobic. As mentioned previously, two sets of samples were prepared to treat them separately with perfluorooctyltriethoxy silane (POTES) and the oil vapor treatment. As expected, based on previous studies on superhydrophobicity, the POTES treated surface exhibited superior water repellency compared to the oil vapor treatment.

Nevertheless, the oil treated surface displays excellent superhydrophobicity for all the different surface textures, with static contact angles close to 160° and droplet roll-off angles below 5° for 5 µL water droplet. Figure 2.31 shows the plot of static contact angle and roll-off angle for a 5 µL droplet against varying pulsewidth for both POTES and oil vapor treated superhydrophobic surfaces.

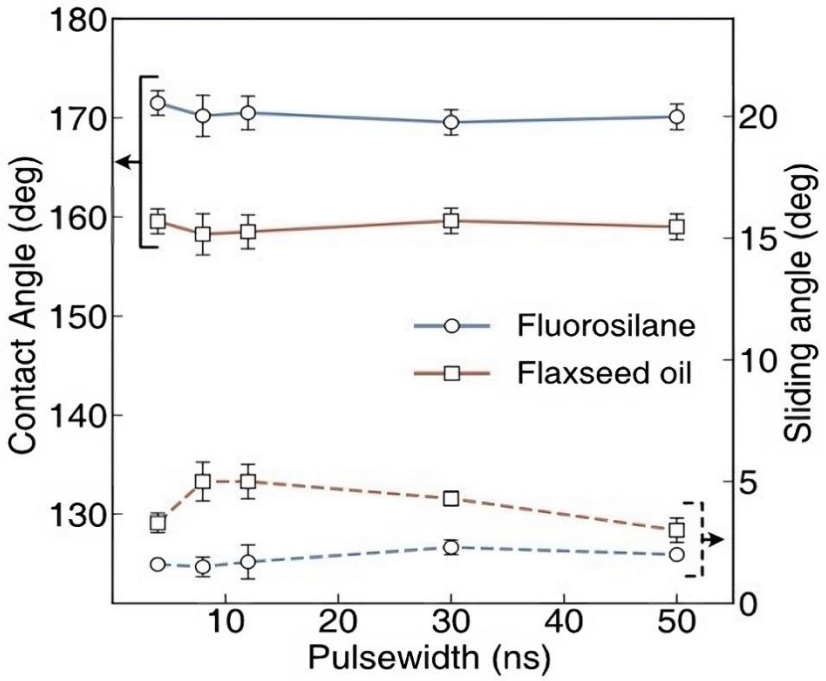

Figure 2.31. Water contact angle and roll-off angle measurements on both fluorosilane (POTES) and flaxseed oil vapor treated surface.

As depicted in the plot above (Figure 2.31), the contact angle values of the POTES surface ~170°, which is about 10° greater than the oil vapor treated surface. Moreover, the roll-off angle values follow the same trend of water repellence, where the POTES treated surface has lower droplet roll-off angles. The lower surface energy of the POTES coating compared to the carbon adsorption from the vegetable oil therefore results in the superior water repellence of the former.

Since the superhydrophobic surfaces exhibit excellent water repellency, the next step was to characterize the liquid repellency of even low surface tension liquids. The contact angle measurements were then conducted with the chosen low surface tension liquids, ethylene glycol (47.3 mN m^{-1}, 25°C), and olive oil

(33.3 mN m^{-1}, 25°C). Figure 2.32(a) shows the plot of static contact angle values of the above-mentioned liquids on the POTES coated surface. The contact angle measurements with the low surface tension liquids revealed some interesting characteristics of the laser fabricated superhydrophobic surfaces.

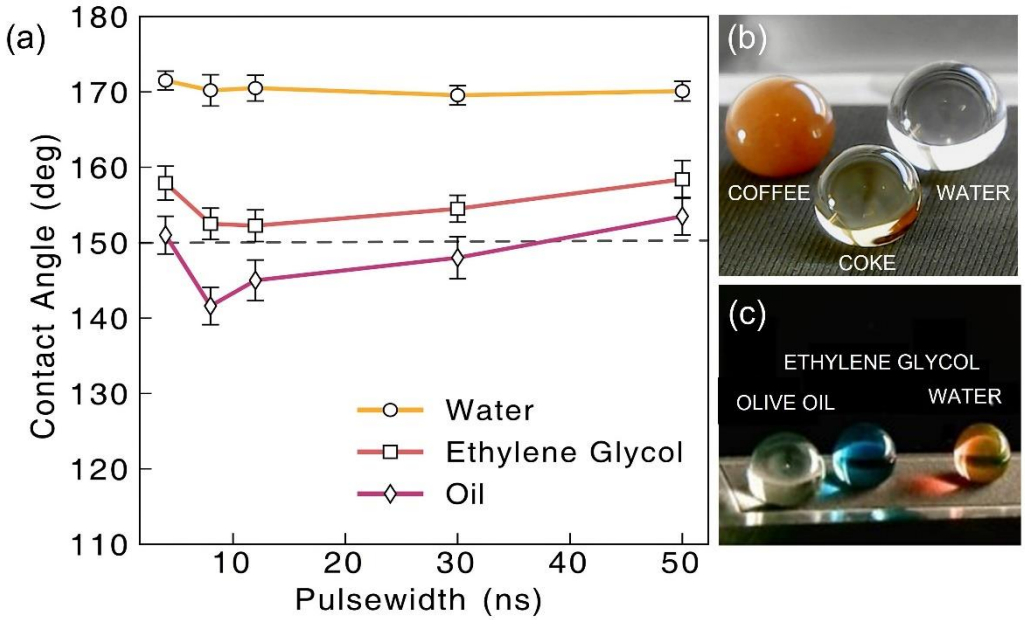

Figure 2.32. (a) Water, ethylene glycol, and olive oil contact angle vs laser pulsewidth for POTES treated surface; camera images of (b) consumable liquid droplets on oil vapor treated superhydrophobic surface; (c) corresponding liquid droplets in (a) on POTES treated surface.

Firstly, the low surface tension liquids amplify the ability of the surface texture to repel different liquids. Even though for water, the surface textures generated at different pulsewidths showed excellent repellency, the same behavior was not translated with ethylene glycol and olive oil. Especially for the latter, as shown in Figure 2.32(a), only the laser modifications at a pulsewidth of 4 ns and 50 ns maintained their super-repellency. Apart from the modifications at pulsewidth of 4 ns, the contact angle value of the low surface tension liquids (ethylene glycol, oil) increases with the pulsewidth, resulting in the best liquid repellence at pulsewidth of 50 ns. Figure 2.32(b,c) shows the camera images of common consumable liquids and low surface tension liquids on the oil vapor treated and POTES coated surfaces respectively. Contrary to the performance of POTES coated liquid repellent surface, the oil vapor treated superhydrophobic surface was unable to repel low surface tension liquids. Nevertheless, the oil vapor treated surface was still phobic to ethylene glycol with the highest contact angle of 140°

shown by the laser modification at 50 ns, as expected from the previous measurements. Figure 2.33 shows the camera images of the ethylene glycol droplet on the POTES and oil vapor treated surfaces.

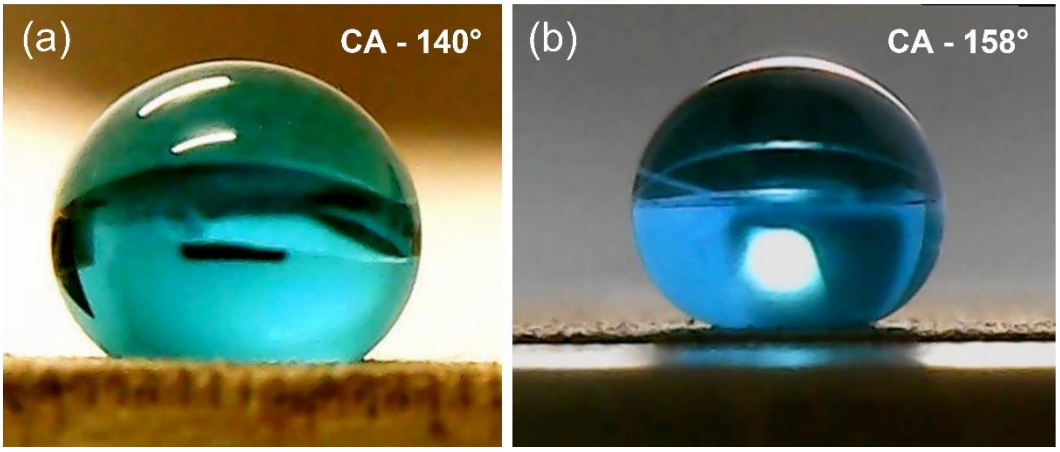

Figure 2.33. Camera images and corresponding contact angle values of ethylene glycol droplets on (a) oil vapor treated; (b) POTES treated surfaces.

To the best of our knowledge, very few studies are conducted on the low surface tension liquid repellency of hydrocarbon adsorption based superhydrophobic surfaces. It is important to mention that for the oil vapor superhydrophobic surface, ethylene glycol had a low contact angle of 108° on the laser generated surface at 8 ns, whereas at 50 ns the contact angle increased to 140°. The above variation in the contact angle for the hydrocarbon adsorbed surface treatment demonstrates the importance of the appropriate surface texture controlled by the laser pulsewidth.

2.8.3 Laser Pulsewidth: A Deciding Parameter for Superamphiphobicity

To better demonstrate the impact of laser pulsewidth, further studies were conducted with the POTES treated superhydrophobic surface. In the study, three different pulsewidth modifications at 4, 8 and 12 ns were selected as the pulsewidth parameters. Then for each of the selected pulsewidths, the laser scan line was varied from 20 µm to 140 µm in steps of 20 µm. The above study was designed to better depict the importance of laser pulsewidth as a parameter against another variable parameter such as scan line spacing, which has been commonly

reported in research studies involving nanosecond laser modification [84,85]. Figure 2.34 shows the FESEM images of the resulting modifications.

As shown in the FESEM images at different scan line spacings, at the largest scan spacing value of 140 µm, the surface features have either relatively greater unmodified triangular zones or random air gaps/holes. On the other hand, at lower scan spacing the surface texture maintains the conical shape at 4 ns and the rough hierarchical features at 50 ns. An important aspect of the surface regards the modifications performed at pulsewidth of 12 ns, where for both low and high scan spacings of 60 µm and 140 µm, there exists large random air gaps/holes and unmodified triangular zones respectively.

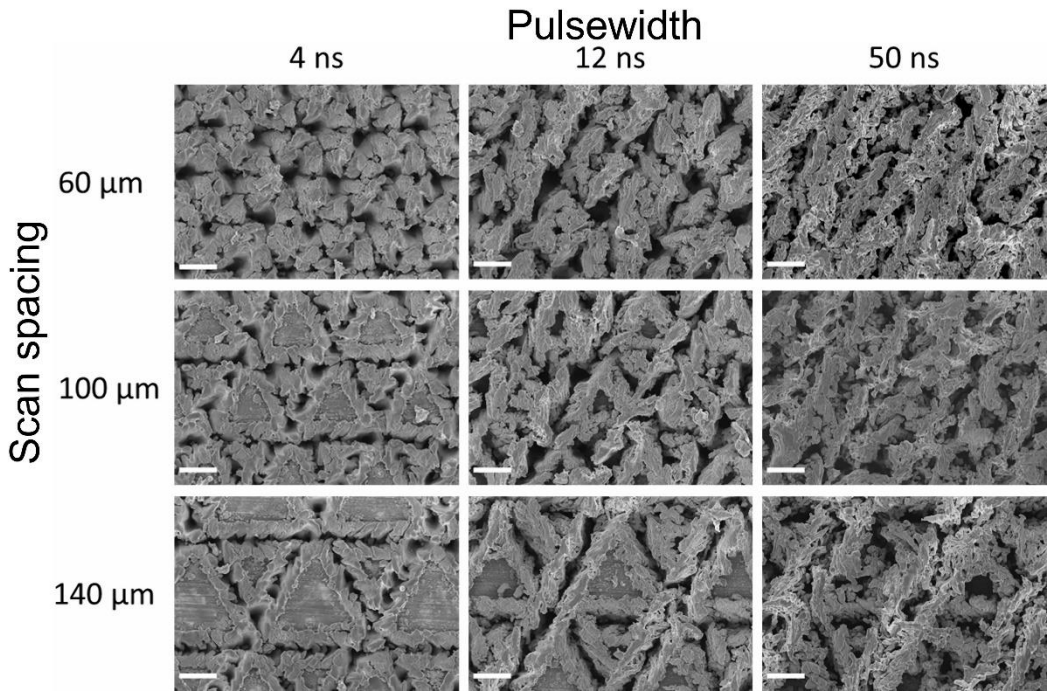

Figure 2.34. FESEM images showing the surface measurements for all three different pulsewidths (4, 12, and 30 ns), at varying scan line spacing (60, 100, and 140 µm).

Figure 2.35 shows the plot of contact angle measurements of olive oil on laser modifications performed at different pulsewidths and laser scan spacings.

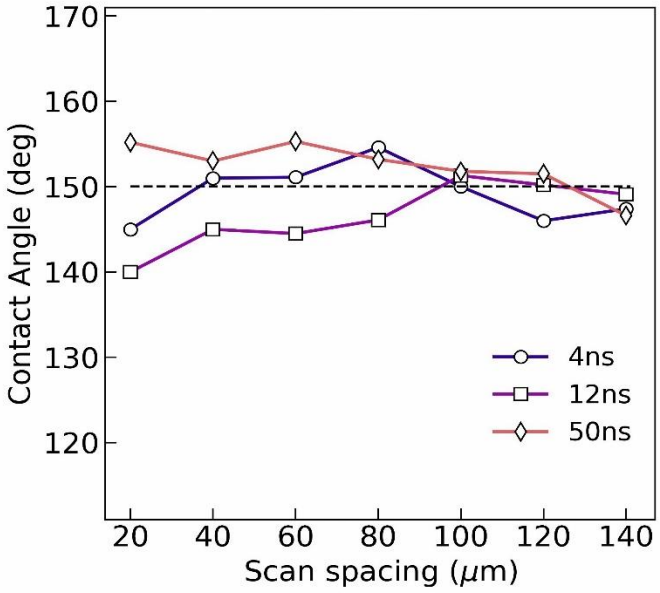

Figure 2.35. Plot showing contact angle vs laser scan spacing on the POTES coated surface for different pulsewidths.

The most important observation regards the effect of pulsewidth on superoleophobicity. It is observed from the plot that only for certain pulsewidth, the surface maintains the superoleophobicity with varying scan spacing. To better elaborate, in the case of different scan spacings performed at a pulsewidth of 50 ns, the surface remains superoleophobic for almost all cases except at 140 µm. On the contrary, for different scan spacings at a pulsewidth of 12 ns, the surface is almost never superoleophobic, except at a scan spacing of 100 µm.

Therefore, irrespective of the scan spacing, if not for an appropriate pulsewidth, then the surface cannot attain superoleophobicity. In fact, it must be pointed out that the surface is not just superoleophobic, but superamphiphobic due to its ability to repel both polar and dispersive liquids such as water and vegetable oil. The results therefore confirm the importance of laser pulsewidth in the nanosecond regime for the fabrication of superamphiphobic surfaces. Figure 2.36(a) shows the camera image of different liquid droplets on the

superamphiphobic surface fabricated at pulsewidth of 50 ns and spacing of 60 µm. Indeed, the superamphiphobic property of the surface enables it to repel even the standard reference liquid used for oleophobic measurements which is n-hexadecane with relatively low surface energy (27.6 mN m^{-1}, 25°C) as shown in the figure below, exhibiting a contact angle of 151°C. Furthermore, due to the extreme repellency, the olive oil drops are totally repelled by the surface and stick on to the dispensing needle, as shown in Figure 2.36(b). This demonstrates the excellent superamphiphobicity of the laser fabricated POTES coated surface.

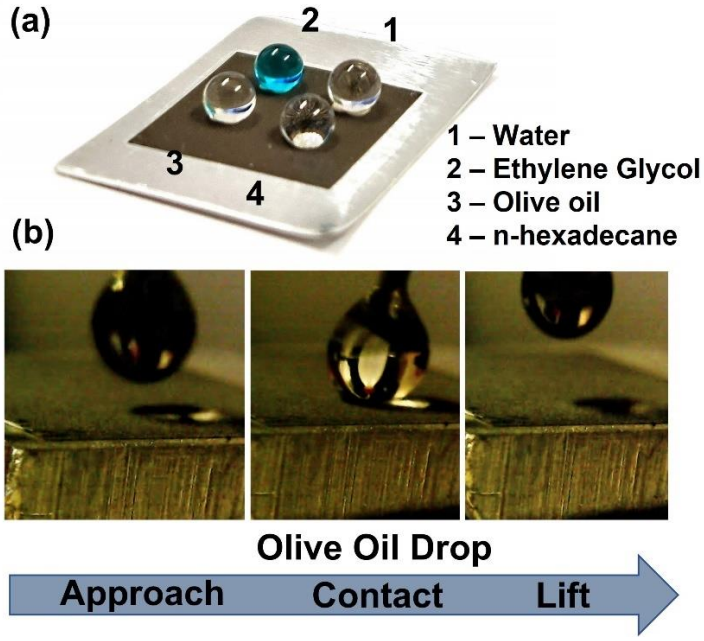

Figure 2.36. (a) Camera image of different liquid droplets on the POTES treated superamphiphobic surface; (b) image sequence depicting 5 µL olive oil droplet approaching, contacting, and removed with the droplet intact and without wetting the POTES treated superhydrophobic surface.

2.9 Chemical Surface Analysis

At first, as part of the chemical analysis, surface elemental composition of the prepared superhydrophobic coatings were analyzed using energy dispersive X-ray spectroscopy. Figure 2.37(a,b) shows the corresponding spectra of the oil vapor treated and POTES coated surfaces respectively. For the POTES treated surface as shown in Figure 2.37(c) an increased carbon and fluorine content was observed.

This corresponds to the self-assembled monolayer of covalently bonded long chain silane molecules.

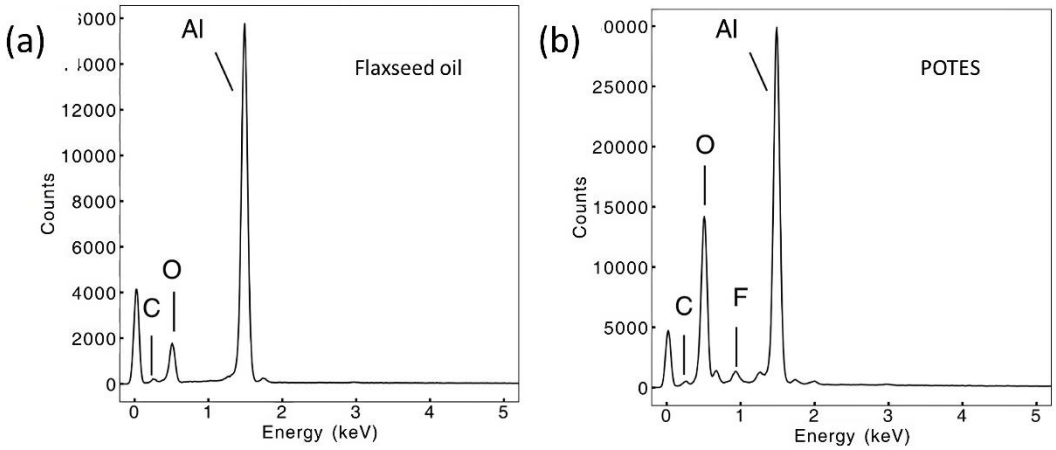

(c)

Elements	Laser Textured (At %)	Oil Vapor treated (At %)	POTES treated (At %)
Al	34.6	48.1	28.3
O	57.6	32.2	50.9
C	4.5	18.6	9.8
F	-	-	8.1

Figure 2.37. Energy dispersive X-ray spectra corresponding to (a) Flaxseed oil vapor treated surface; (b) POTES coated surface; (c) corresponding quantitative measurements of fresh laser textured, oil vaopr treated, and POTES coated surface.

Also, the quantitative EDS measurement in Figure 2.37(c) for the oil vapor treated surface, when compared to the fresh laser textured surface shows a high carbon content. This increase corresponds to the hydrocarbon adsorption during the oil vapor procedure. To further analyze the adsorbed hydrocarbon functional groups, FTIR spectroscopy was performed on the oil vapor-treated surface and was compared to that of pristine laser texture surface. Figure 2.38 shows the acquired FTIR spectra of the same.

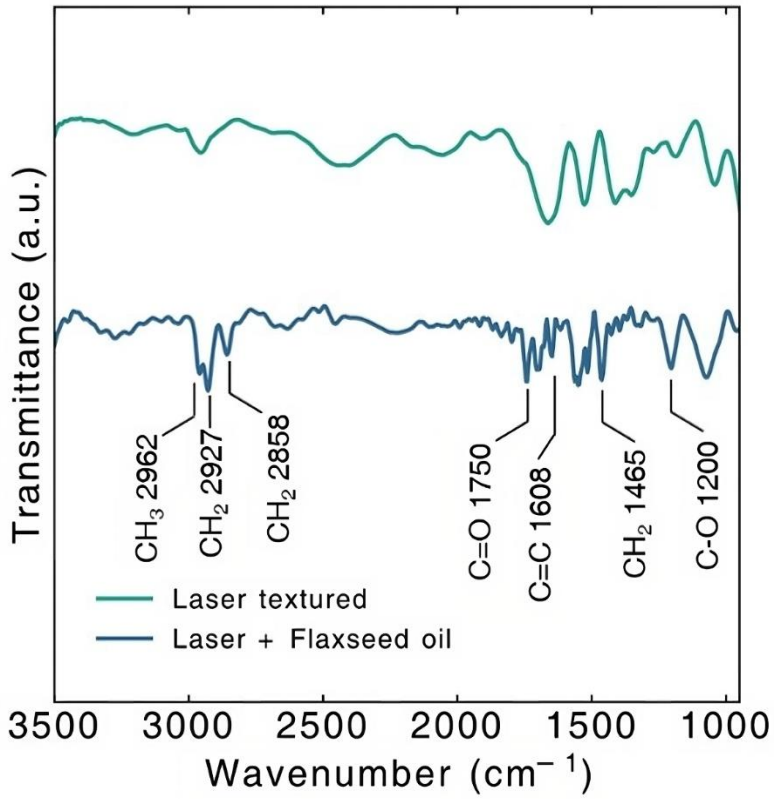

Figure 2.38. FTIR spectrum comparing laser textured surface with oil vapor treated superhydrophobic surface.

The oil vapor-treated surface showed new absorption peaks with respect to the pristine laser-textured surface. The absorbance peaks at 2958 cm^{-1}, 2927 cm^{-1}, and 2858 cm^{-1} are signature peaks corresponding to the asymmetric stretching of CH_3 groups and symmetric and asymmetric stretching of CH_2 groups. These peaks demonstrate the presence of hydrocarbon groups on the laser-treated alumina surface. Also, the peaks at 1465 cm^{-1} correspond to CH_2 bending. The absorption at 1608 cm^{-1} and 1750 cm^{-1} could be associated with the C=C and C=O bond stretching, respectively. Finally, the absorption at 1200 cm^{-1} could be attributed to the C-O-C vibrations [86–88]. Hence, the above-mentioned absorption peaks confirm the postulation of hydrocarbon functional group adsorption on the laser-modified aluminum because of the oil vapor treatment.

2.10 Droplet Bounce and Evaporation Dynamics on Superhydrophobic Surface

Apart from the static contact angle and roll-off angle measurements, it is essential to characterize the surface through other means to perform a complete surface analysis. In this respect, the following tests assess superhydrophobicity through static and dynamic means.

2.10.1 Dynamic Droplet Bounce Behavior

As a direct consequence of the Cassie state with stable air pockets, the superhydrophobic surface possesses the unique ability to repel and cause rebound of the free-fall droplet upon surface contact. Once the droplet impacts the superhydrophobic surface, it deforms to a maximum diameter. Following achieving the maximum spread diameter, the droplet begins to recede and eventually bounce back from the surface [89]. An important parameter called the Weber number (Wen) characterizes the droplet rebound dynamics following the impact, given by the following equation:

$$Wen = \frac{\rho v_{nl}^2 D}{\sigma} \tag{16}$$

Where ρ is liquid density, υ_{nl} represents the impact velocity, D is the drop diameter, and σ represents the liquid surface tension. Based on the Weber number of the impacting droplet, the further dynamics of the droplet are influenced. At lower Weber numbers (Wen < 5), the liquid is only slightly flattened before rebounding. At relatively larger Wen values, the liquid is flattened like a thin sheet, namely the lamella. Figure 2.39 shows the droplet spreading on a superhydrophobic surface at different Weber numbers of 8 and 38, respectively. The difference in the droplet spreading can be observed from the image based on the corresponding impact velocity. During the droplet spread and rebound back, the liquid surface tension competes with the inertial forces. If the liquid surface tension sufficiently exceeds that of the solid surface energy, then the droplet rebounds. However, there is a possibility of an alternative scenario, wherein with sufficient impact force, the droplet could completely penetrate the rough surface features and expel air from the composite interface [90]. The above situation

would transform the surface to the Wenzel state and complete adherence of the droplet to the surface, either entirely or partially.

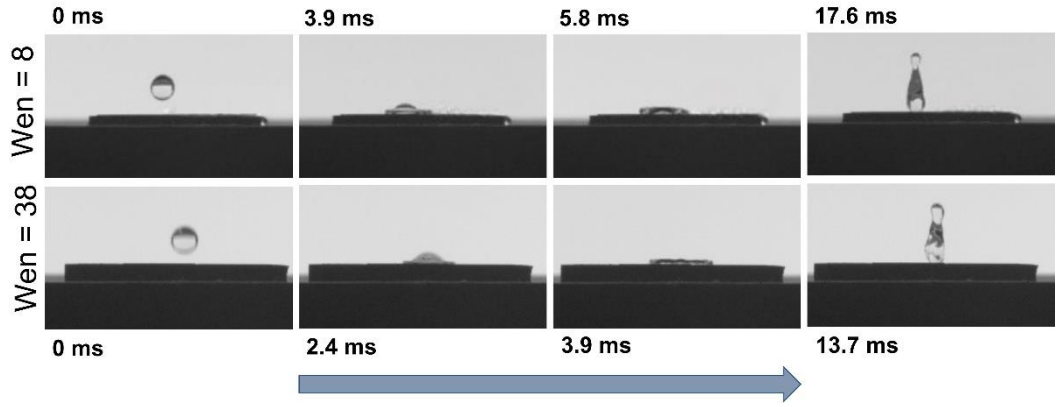

Figure 2.39. High-speed camera images of droplet bounce on oil vapor treated superhydrophobic surface at different Weber number values.

As previously mentioned, the droplet penetrates the surface partially or completely depending on the Weber number. The extent to which the droplet penetration occurs can be studied by defining the parameter coefficient of restitution (COR), which is given by the following [91]:

$$COR\ \varepsilon\ = \sqrt{\frac{h_r}{h_i}} \tag{17}$$

where h_r is the maximum droplet rebound height and h_i is the initial free-fall height. Therefore, analyzing the relationship between the Weber number and the COR would provide information about the extent of the droplet penetration. A lower COR value would result from decreased rebound height due to energy lost during liquid penetration. Figure 2.40 shows the relation between the Weber number and the COR for oil vapor and POTES treated surfaces. As discussed before, a negative correlation exists between the Weber number and the COR for both surfaces. Indeed, as observed from the figure, only a partial penetration occurs for the impacting droplet in the Weber number range due to non-zero COR values. Ideally, it would be difficult to have a COR=1 due to viscous and

vibrational energy losses. Therefore, the surfaces do not undergo Wenzel transition even at a relatively high impact velocity of 1.5 m/s (Wen=65), which confirms a stable superhydrophobicity.

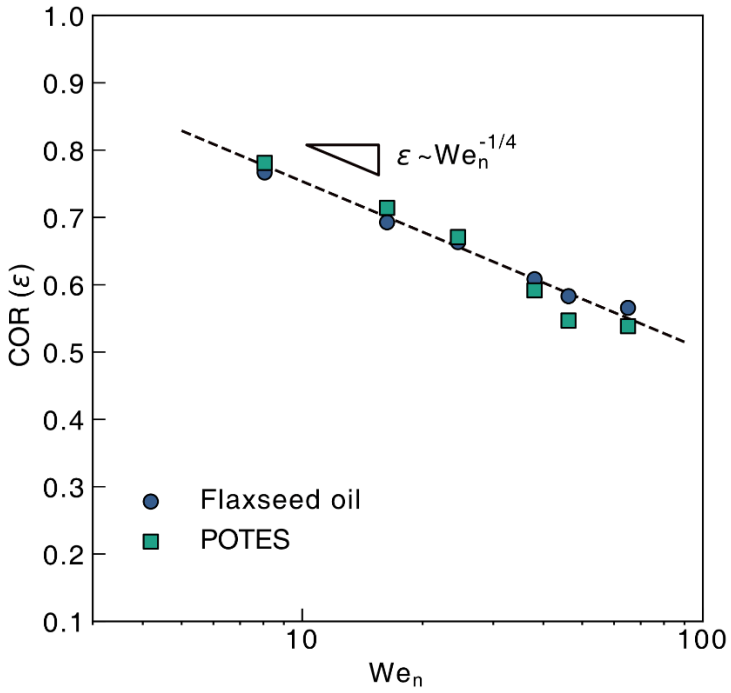

Figure 2.40. Power law fitting to COR vs. Weber number measurements for droplet bounce on oil vapor treated and POTES coated surfaces.

The droplet bounce dynamics on the superhydrophobic surface in this study follow the general scaling law given by the relation of the form [92]:

$$COR\ \varepsilon\ = \alpha We_n^{-1/4} \tag{18}$$

where α=1 in this study, the coefficient value depends on the specific superhydrophobic surface. Also, no significant difference is observed in the COR values for both surfaces, corresponding to identical droplet bounce dynamics.

2.10.2 Evaporation Triggered Transition of Superhydrophobicity

For a droplet on the superhydrophobic surface, a Laplace pressure always acts downward on the droplet, increasing with the decreasing droplet diameter, as

shown in Figure 2.41(a). As discussed in the introduction section of the chapter, it is essential to assess the critical Laplace pressure to characterize the superhydrophobicity's stability. In this study, the evolution of the droplet contact angle and the three-phase contact line diameter (TPCL) was monitored during the droplet evaporation process on both POTES and oil vapor-treated surfaces.

Specifically, the Wenzel state transition can be determined by the transition of the TPCL to a constant value and the reduction of contact angle values below 150°. Figure 2.41(b) shows that POTES treated surface could withstand higher Laplace pressure values, well beyond 600 Pa, where the droplet still maintains CA > 150°, with reducing TPCL diameter values.

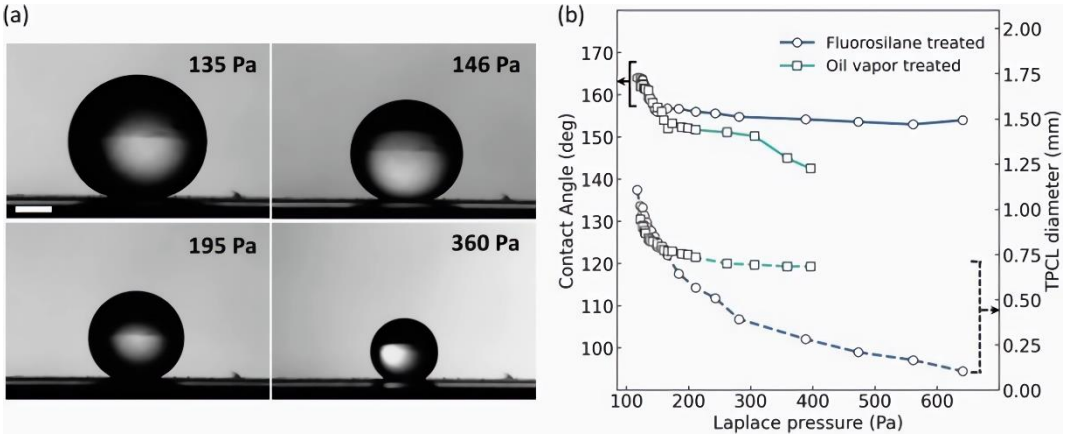

Figure 2.41. Camera images of droplet evaporation on oil vapor-treated superhydrophobic surface; (b) plot depicting static contact angle and TPCL diameter variation against Laplace pressure. The scale bar represents 500 µm.

On the other hand, the oil vapor-treated surface could withstand only about 300Pa, where the TPCL values reached a steady state, confirming the Wenzel transition. Nevertheless, the Laplace pressure values are comparable to the superhydrophobic surfaces fabricated with Fluorosilane treatment and femtosecond laser micromachining [93].

2.11 Thermal and Temporal Stability

For reliability of the fabricated superhydrophobicity, it must be stable with time and at extreme weather conditions. To assess the stability, contact angle

measurements were taken at varying temperatures and different durations after the sample preparation.

2.11.1Thermal Stability

The Fluorosilane coatings have been assessed previously for their thermal stability. Previous studies have reported their stability even at high temperatures of about 400°C. This could be attributed to silane covalent bonding to the surface. On the other hand, unlike the POTES coatings, the oil vapor-treated surface has only adsorbed hydrocarbon functional groups that are more susceptible to thermal damage. Therefore, this study's oil vapor-treated superhydrophobic surface was thermally tested to assess its stability at higher temperatures.

The prepared superhydrophobic surfaces were treated from 50°C to 300°C in an oven for one hour each. The static contact angles were measured immediately after removal from the oven and are shown in Figure 2.42. The superhydrophobic property is maintained up to about 180°C, after which the contact angle values deteriorate and transition to hydrophobic nature. In fact, at about 300°C, the surface turns superhydrophilic, signaling a strong reduction in hydrocarbon content from the surface and the resulting exposure of alumina.

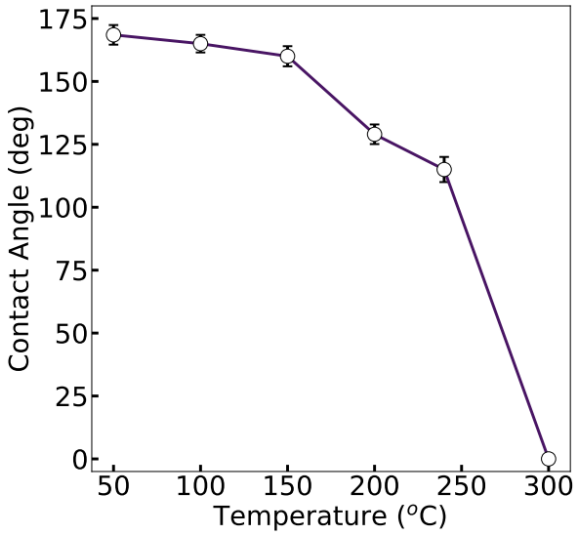

Figure 2.42. Evolution of contact angle variation with the temperature at a treatment time of 1 hour each.

To better understand the variations in elemental composition due to the thermal treatment, energy dispersive X-ray analysis (EDS) was performed for the thermally treated surface (100°C, 1 hour) and compared to the thermally treated superhydrophilic surface (300°C, 1 hour). Figure 2.43(a,b) shows the EDS spectra of the thermally treated samples at 100°C and 300°C, grespectively.

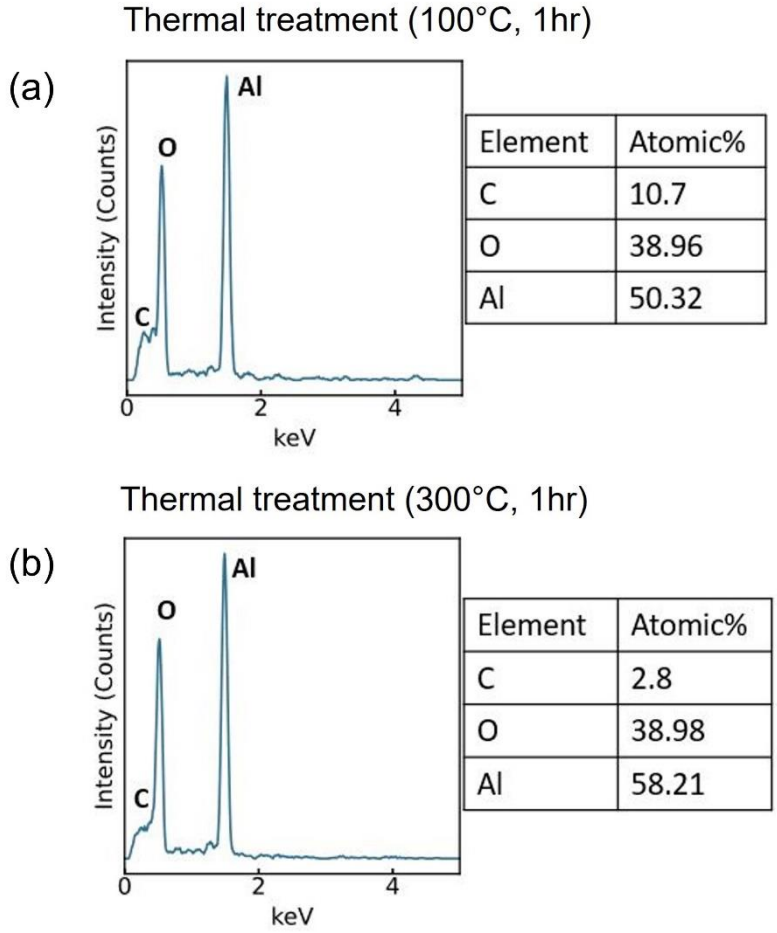

Figure 2.43. EDS spectra and corresponding compositional information on oil vapor treated surface after thermal treatment of 1 hr at (a) 100°C; (b) 300°C, respectively.

The EDS spectra shows the reduction in carbon content with increasing temperature, confirming the postulation of desorption of hydrocarbons from the surface, thereby rendering the surface superhydrophilic at 300°C. Another critical point is the ability to switch between the superhydrophobic and superhydrophilic states with oil vapor treatment and high-temperature thermal treatment, as illustrated in Figure 2.44.

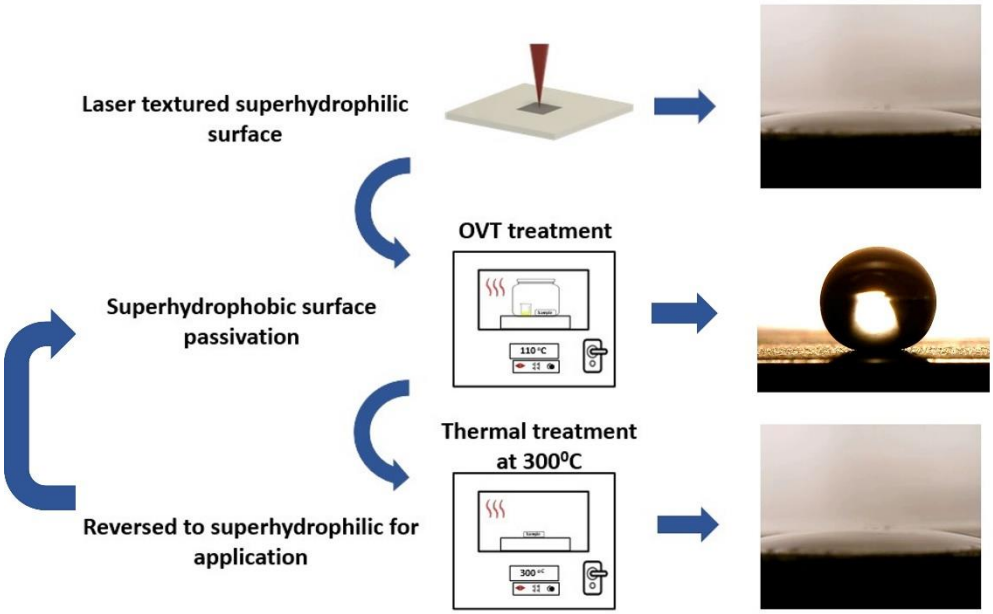

Figure 2.44. Illustration depicting the transition of laser textured superhydrophilic to oil vapor treated superhydrophobic surface and transition back to superhydrophilic on high-temperature treatment. Also, the superhydrophilic transition at high temperatures is repairable on oil vapor treatment.

2.11.2 Temporal and Mechanical Stability

The temporal and mechanical stability of the superhydrophobic surfaces are fundamentally critical for them to be even considered for real life applications [36]. Therefore, a stable superhydrophobicity with exposure to both open atmosphere and mechanical abrasion/scratches would be a desirable feature for long term use.

To assess the stability of both the POTES and oil vapor treated surface with time, the samples were left exposed to open atmosphere, while their contact and roll-off angles were measured at various intervals over a duration of one month. As shown in Figure 2.45, the superhydrophobicity is well maintained for both the surfaces. However, there is a minute reduction in the contact and roll-off angles over the one-month duration. This could be the result of surface contamination by dust particles from the surrounding air.

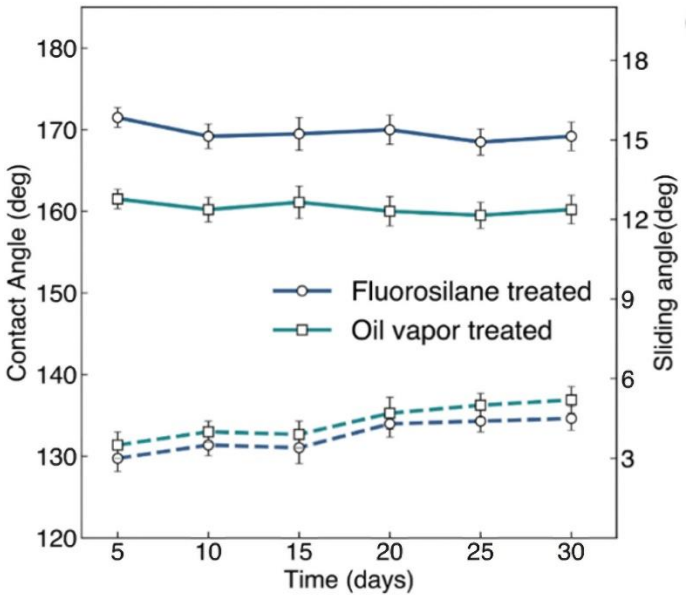

Figure 2.45. Stability of the fabricated superhydrophobic surfaces with storage in open air.

To assess the coating stability of both surfaces, a tape peeling test was conducted, wherein a scotch tape (Scotch 3M 810) was continuously stuck and gently pressed evenly to ensure uniform adhesion between tape-surface and then peeled out in a cyclic manner. After every 10 peeling cycles, the static contact angle was measured, as shown in Figure 2.46.

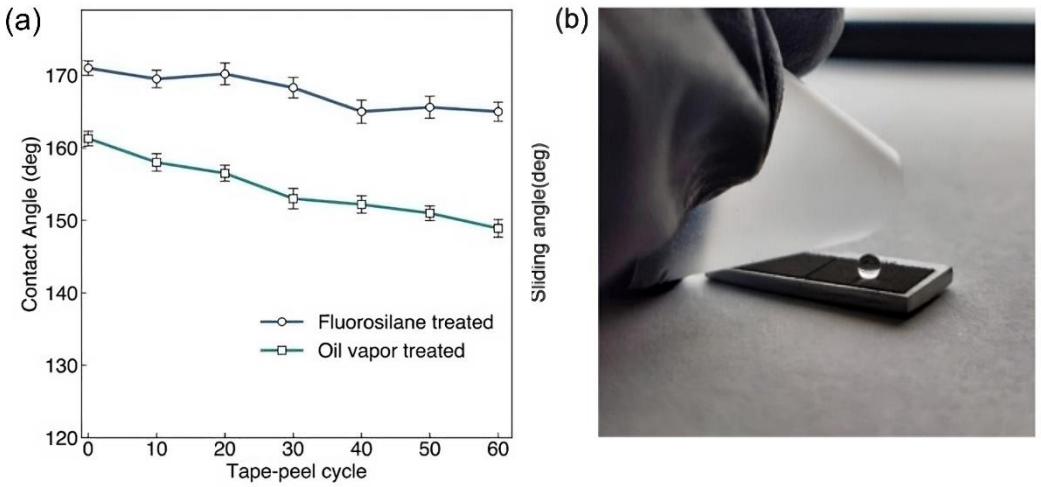

Figure 2.46. (a) Evolution of contact angles with tape peeling cycles on superhydrophobic surfaces, (b) water droplet on oil vapor treated surface after 60 tape-peel cycles.

The droplet contact angle on the oil vapor treated surface went below the 150℃ after 60 cycles, while the POTES treated surface was still superhydrophobic.

Following the peeling test, knife-scratch test was performed on the surfaces, where crosshatches of varying intensities were marked on the superhydrophobic surfaces. Interestingly, even at high densities of the crosshatch pattern, the 5 μL water droplet failed to wet both the surfaces, as shown in Figure 2.47.

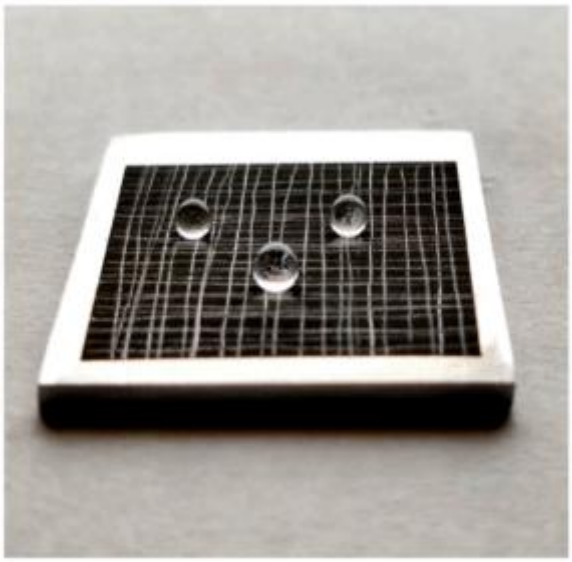

Figure 2.47. Knife scratch test with high density cross hatch pattern still maintaining superhydrophobicity on the oil vapor treated sample.

The above tests confirm the mechanical robustness of the fabricated superhydrophobic surfaces.

Another interesting property of the superhydrophobic surface is its ability to self-clean the surface from contaminants [94]. The liquid that is rolling off collects the dirt particles from the surface, thereby rendering it clean. The superhydrophobic surfaces fabricated in this study demonstrated the self-cleaning property. While the oil vapor treated surface was self-cleanable with water, the POTES treated amphiphobic surface was able to even self-clean with lower surface tension liquid ethylene glycol, As shown in Figure 2.48.

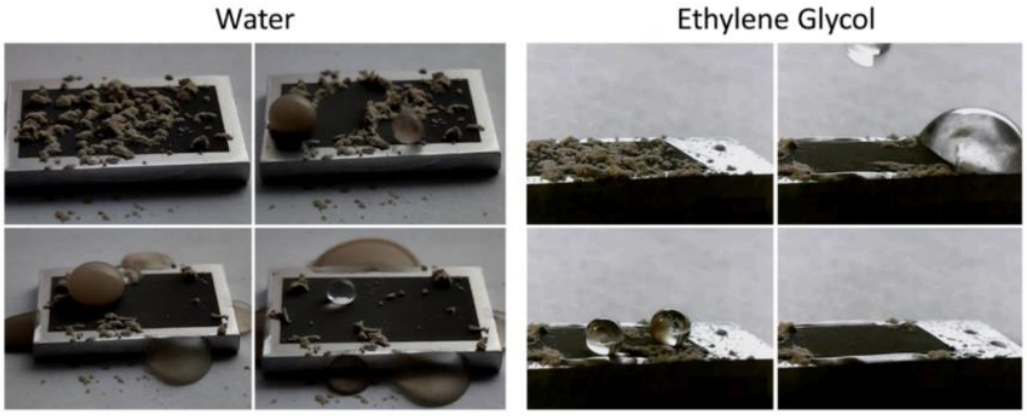

Figure 2.48. Self-cleaning of flaxseed oil with water (left) and of POTES coated laser treated superamphiphobic surface with Ethylene Glycol (right).

The experimental findings discussed in this chapter has demonstrated the crucial role of surface micro- and nanostructures in achieving superhydrophobicity. By appropriately tuning the surface geometry, we have successfully created surfaces with high liquid repellence, effectively repelling even oil droplets and preventing wetting. Moreover, the experimental investigations have uncovered the intricate interplay between surface roughness, surface energy, and the different wetting regimes. This understanding has paved the way for design and fabrication of novel superhydrophobic materials with enhanced performance and durability using a relatively inexpensive nanosecond laser.

References

1. Wang, Y.; Liu, P.; Vogelbacher, F.; Li, M. Bioinspired Multiscale Optical Structures towards Efficient Light Management in Optoelectronic Devices. *Materials Today Nano* **2022**, *19*, 100225, doi:10.1016/j.mtnano.2022.100225.
2. Zhu, H.; Huang, Y.; Lou, X.; Xia, F. Beetle-Inspired Wettable Materials: From Fabrications to Applications. *Materials Today Nano* **2019**, *6*, 100034, doi:10.1016/j.mtnano.2019.100034.
3. Wang, L. A Critical Review on Robust Self-Cleaning Properties of Lotus Leaf. *Soft Matter* **2023**, *19*, 1058–1075, doi:10.1039/D2SM01521H.
4. Katiyar, N.K.; Goel, G.; Hawi, S.; Goel, S. Nature-Inspired Materials: Emerging Trends and Prospects. *NPG Asia Mater* **2021**, *13*, 56, doi:10.1038/s41427-021-00322-y.
5. Chen, W.; Huang, X.; Zhou, M.; Liu, H.; Xu, M.; Zhu, J. Rose-Petal-Inspired Fabrication of Conductive Superhydrophobic/Superoleophilic Carbon with High Adhesion to Water from Orange Peels for Efficient Oil Adsorption from Oil-Water Emulsion. *Colloids and Surfaces A: Physicochemical and Engineering Aspects* **2023**, *661*, 130920, doi:10.1016/j.colsurfa.2023.130920.
6. Lee, S.J.; Ha, N.; Kim, H. Superhydrophilic–Superhydrophobic Water Harvester Inspired by Wetting Property of Cactus Stem. *ACS Sustainable Chem. Eng.* **2019**, *7*, 10561–10569, doi:10.1021/acssuschemeng.9b01113.
7. Wang, H.; Zhuang, J.; Qi, H.; Yu, J.; Guo, Z.; Ma, Y. Laser-Chemical Treated Superhydrophobic Surface as a Barrier to Marine Atmospheric Corrosion. *Surface and Coatings Technology* **2020**, *401*, 126255, doi:10.1016/j.surfcoat.2020.126255.
8. Yu, C.; Sasic, S.; Liu, K.; Salameh, S.; Ras, R.H.A.; Van Ommen, J.R. Nature–Inspired Self–Cleaning Surfaces: Mechanisms, Modelling, and Manufacturing. *Chemical Engineering Research and Design* **2020**, *155*, 48–65, doi:10.1016/j.cherd.2019.11.038.
9. Jayaramulu, K.; Geyer, F.; Schneemann, A.; Kment, Š.; Otyepka, M.; Zboril, R.; Vollmer, D.; Fischer, R.A. Hydrophobic Metal–Organic Frameworks. *Advanced Materials* **2019**, *31*, 1900820, doi:10.1002/adma.201900820.

10. An Essay on the Cohesion of Fluids.

11. Xiang, S.; Liu, W. Self-Healing Superhydrophobic Surfaces: Healing Principles and Applications. *Adv Materials Inter* **2021**, *8*, 2100247, doi:10.1002/admi.202100247.

12. Ismail, M.F.; Islam, M.A.; Khorshidi, B.; Tehrani-Bagha, A.; Sadrzadeh, M. Surface Characterization of Thin-Film Composite Membranes Using Contact Angle Technique: Review of Quantification Strategies and Applications. *Advances in Colloid and Interface Science* **2022**, *299*, 102524, doi:10.1016/j.cis.2021.102524.

13. Wang, J.; Wu, Y.; Cao, Y.; Li, G.; Liao, Y. Influence of Surface Roughness on Contact Angle Hysteresis and Spreading Work. *Colloid Polym Sci* **2020**, *298*, 1107–1112, doi:10.1007/s00396-020-04680-x.

14. Feyyisa, J.L.; Daniels, J.L.; Pando, M.A.; Ogunro, V.O. Relationship between Breakthrough Pressure and Contact Angle for Organo-Silane Treated Coal Fly Ash. *Environmental Technology & Innovation* **2019**, *14*, 100332, doi:10.1016/j.eti.2019.100332.

15. Jiang, G.; Hu, J.; Chen, L. Preparation of a Flexible Superhydrophobic Surface and Its Wetting Mechanism Based on Fractal Theory. *Langmuir* **2020**, *36*, 8435–8443, doi:10.1021/acs.langmuir.0c00823.

16. Li, J.; Jiao, W.; Wang, Y.; Yin, Y.; He, X. Spraying Pressure-Tuning for the Fabrication of the Tunable Adhesion Superhydrophobic Coatings between Lotus Effect and Petal Effect and Their Anti-Icing Performance. *Chemical Engineering Journal* **2022**, *434*, 134710, doi:10.1016/j.cej.2022.134710.

17. Kota, A.K.; Mabry, J.M.; Tuteja, A. Superoleophobic Surfaces: Design Criteria and Recent Studies. *Surface Innovations* **2013**, *1*, 71–83, doi:10.1680/si.12.00017.

18. Shamim, J.A.; Takahashi, Y.; Goswami, A.; Shaukat, N.; Hsu, W.-L.; Choi, J.; Daiguji, H. Suppression of Wetting Transition on Evaporative Fakir Droplets by Using Slippery Superhydrophobic Surfaces with Low Depinning Force. *Sci Rep* **2023**, *13*, 2368, doi:10.1038/s41598-023-29163-1.

19. Zhang, Y.; Wang, T.; Wu, M.; Wei, W. Durable Superhydrophobic Surface with Hierarchical Microstructures for Efficient Water Collection. *Surface and Coatings Technology* **2021**, *419*, 127279, doi:10.1016/j.surfcoat.2021.127279.

20. Kota, A.K.; Kwon, G.; Tuteja, A. The Design and Applications of Superomniphobic Surfaces. *NPG Asia Mater* **2014**, *6*, e109–e109, doi:10.1038/am.2014.34.

21. Li, K.; Lei, J.; Xie, Y.; Lu, L.; Zhang, S.; Zhou, P.; Liang, R.; Wan, Z.; Tang, Y. An Easy-to-Implement Method for Fabricating Superhydrophobic

Surfaces Inspired by Taro Leaf. *Sci. China Technol. Sci.* **2021**, *64*, 2676–2687, doi:10.1007/s11431-021-1855-2.

22. Yamaguchi, M.; Kato, S. Direct-Micro-Fabrication of Hydrophobic Surface with Re-Entrant Texture on Metal Produced by Femtosecond-Pulsed Laser. *Lasers Manuf. Mater. Process.* **2023**, *10*, 64–76, doi:10.1007/s40516-022-00198-y.
23. Han, J.; Cai, M.; Lin, Y.; Liu, W.; Luo, X.; Zhang, H.; Zhong, M. 3D Re-Entrant Nanograss on Microcones for Durable Superamphiphobic Surfaces via Laser-Chemical Hybrid Method. *Applied Surface Science* **2018**, *456*, 726–736, doi:10.1016/j.apsusc.2018.06.126.
24. Cui, B.; Jia, S.; Tokunaga, E.; Shibata, N. Defluorosilylation of Fluoroarenes and Fluoroalkanes. *Nat Commun* **2018**, *9*, 4393, doi:10.1038/s41467-018-06830-w.
25. Shao, J.; Zhao, Y.; Li, D.; Xu, S.; Dou, Z.; Sun, Z.; Cao, M.; Fu, K.; Liu, Y.; Zhou, Y. Synthesis and Characterization of Superhydrophobic Fluorinated Mesoporous Silica for Oil/Water Separation. *Microporous and Mesoporous Materials* **2022**, *344*, 112240, doi:10.1016/j.micromeso.2022.112240.
26. Xu, J.; Sun, J.; Wang, Y.; Sheng, J.; Wang, F.; Sun, M. Application of Iron Magnetic Nanoparticles in Protein Immobilization. *Molecules* **2014**, *19*, 11465–11486, doi:10.3390/molecules190811465.
27. Radhakrishnan, J.; Diaz, M.; Cordovilla, F.; Ocaña, J.L. Tunable Superhydrophobic Titanium Nitride Surface by Ultrafast Laser Processing. *Ceramics International* **2022**, *48*, 37264–37274, doi:10.1016/j.ceramint.2022.08.304.
28. Khan, S.A.; Boltaev, G.S.; Iqbal, M.; Kim, V.; Ganeev, R.A.; Alnaser, A.S. Ultrafast Fiber Laser-Induced Fabrication of Superhydrophobic and Self-Cleaning Metal Surfaces. *Applied Surface Science* **2021**, *542*, 148560, doi:10.1016/j.apsusc.2020.148560.
29. Fürbacher, R.; Liedl, G.; Otto, A. Fast Transition from Hydrophilic to Superhydrophobic, Icephobic Properties of Stainless Steel Samples after Femtosecond Laser Processing and Exposure to Hydrocarbons. *Procedia CIRP* **2022**, *111*, 643–647, doi:10.1016/j.procir.2022.08.016.
30. Karapanagiotis, I.; Manoudis, P.N.; Zurba, A.; Lampakis, D. From Hydrophobic to Superhydrophobic and Superhydrophilic Siloxanes by Thermal Treatment. *Langmuir* **2014**, *30*, 13235–13243, doi:10.1021/la503583c.
31. Jagdheesh, R.; Diaz, M.; Marimuthu, S.; Ocana, J.L. Robust Fabrication of μ-Patterns with Tunable and Durable Wetting Properties: Hydrophilic to

Ultrahydrophobic via a Vacuum Process. *J. Mater. Chem. A* **2017**, *5*, 7125–7136, doi:10.1039/C7TA01385J.

32. Tran, N.G.; Chun, D.-M. Simple and Fast Surface Modification of Nanosecond-Pulse Laser-Textured Stainless Steel for Robust Superhydrophobic Surfaces. *CIRP Annals* **2020**, *69*, 525–528, doi:10.1016/j.cirp.2020.04.012.
33. Xu, M.; Feng, Y.; Li, Z.; Wang, X.; Li, C.; Jiang, H.; Chen, Y. A Novel, Efficient and Cost-Effective Synthesis Technique for the Development of Superhydrophobic Glass Surface. *Journal of Alloys and Compounds* **2019**, *781*, 1175–1181, doi:10.1016/j.jallcom.2018.12.084.
34. Zheng, J.; Qu, G.; Yang, B.; Wang, H.; Zhou, L.; Zhou, Z. Facile Preparation of Robust Superhydrophobic Ceramic Surfaces with Mechanical Stability, Durability, and Self-Cleaning Function. *Applied Surface Science* **2022**, *576*, 151875, doi:10.1016/j.apsusc.2021.151875.
35. Pan, R.; Zhang, H.; Zhong, M. Triple-Scale Superhydrophobic Surface with Excellent Anti-Icing and Icephobic Performance via Ultrafast Laser Hybrid Fabrication. *ACS Appl. Mater. Interfaces* **2021**, *13*, 1743–1753, doi:10.1021/acsami.0c16259.
36. Wang, P.; Li, C.; Zhang, D. Recent Advances in Chemical Durability and Mechanical Stability of Superhydrophobic Materials: Multi-Strategy Design and Strengthening. *Journal of Materials Science & Technology* **2022**, *129*, 40–69, doi:10.1016/j.jmst.2022.01.045.
37. Pan, R.; Cai, M.; Liu, W.; Luo, X.; Chen, C.; Zhang, H.; Zhong, M. Ultrafast Laser Hybrid Fabrication of Hierarchical 3D Structures of Nanorods on Microcones for Superhydrophobic Surfaces with Excellent Cassie State Stability and Mechanical Durability. *Journal of Laser Applications* **2020**, *32*, 022047, doi:10.2351/7.0000110.
38. Tian, Z.; Fan, P.; Zhu, D.; Wang, L.; Zhao, H.; Chen, C.; Peng, R.; Li, D.; Zhang, H.; Zhong, M. Anti-Ice-Pinning Superhydrophobic Surfaces for Extremely Low Ice Adhesion. *Chemical Engineering Journal* **2023**, *473*, 145382, doi:10.1016/j.cej.2023.145382.
39. Cai, T.; Jia, Z.; Yang, H.; Wang, G. Investigation of Cassie-Wenzel Wetting Transitions on Microstructured Surfaces. *Colloid Polym Sci* **2016**, *294*, 833–840, doi:10.1007/s00396-016-3836-4.
40. Annavarapu, R.K.; Kim, S.; Wang, M.; Hart, A.J.; Sojoudi, H. Explaining Evaporation-Triggered Wetting Transition Using Local Force Balance Model and Contact Line-Fraction. *Sci Rep* **2019**, *9*, 405, doi:10.1038/s41598-018-37093-6.

41. Hou, B.; Wu, C.; Li, X.; Huang, J.; Chen, M. Contact Line-Based Model for the Cassie-Wenzel Transition of a Sessile Droplet on the Hydrophobic Micropillar-Structured Surfaces. *Applied Surface Science* **2021**, *542*, 148611, doi:10.1016/j.apsusc.2020.148611.

42. Long, J.; Fan, P.; Zhong, M.; Zhang, H.; Xie, Y.; Lin, C. Superhydrophobic and Colorful Copper Surfaces Fabricated by Picosecond Laser Induced Periodic Nanostructures. *Applied Surface Science* **2014**, *311*, 461–467, doi:10.1016/j.apsusc.2014.05.090.

43. Natishan, P.M.; O'Grady, W.E. Chloride Ion Interactions with Oxide-Covered Aluminum Leading to Pitting Corrosion: A Review. *J. Electrochem. Soc.* **2014**, *161*, C421–C432, doi:10.1149/2.1011409jes.

44. Li, X.; Jiang, Y.; Jiang, Z.; Li, Y.; Wen, C.; Zhang, D.; Lian, J.; Zhang, Z. Improvement of Corrosion Resistance of H59 Brass through Fabricating Superhydrophobic Surface Using Laser Ablation and Heating Treatment. *Corrosion Science* **2021**, *180*, 109186, doi:10.1016/j.corsci.2020.109186.

45. Guo, Z.; Chen, X.; Li, J.; Liu, J.-H.; Huang, X.-J. ZnO/CuO Hetero-Hierarchical Nanotrees Array: Hydrothermal Preparation and Self-Cleaning Properties. *Langmuir* **2011**, *27*, 6193–6200, doi:10.1021/la104979x.

46. Feng, L.; Che, Y.; Liu, Y.; Qiang, X.; Wang, Y. Fabrication of Superhydrophobic Aluminium Alloy Surface with Excellent Corrosion Resistance by a Facile and Environment-Friendly Method. *Applied Surface Science* **2013**, *283*, 367–374, doi:10.1016/j.apsusc.2013.06.117.

47. Feng, L.; Yan, Z.; Qiang, X.; Liu, Y.; Wang, Y. Facile Formation of Superhydrophobic Aluminum Alloy Surface and Corrosion-Resistant Behavior. *Appl. Phys. A* **2016**, *122*, 165, doi:10.1007/s00339-016-9700-z.

48. Chen, C.; Tian, Z.; Luo, X.; Jiang, G.; Hu, X.; Wang, L.; Peng, R.; Zhang, H.; Zhong, M. Micro–Nano-Nanowire Triple Structure-Held PDMS Superhydrophobic Surfaces for Robust Ultra-Long-Term Icephobic Performance. *ACS Appl. Mater. Interfaces* **2022**, *14*, 23973–23982, doi:10.1021/acsami.2c02992.

49. Wu, S.; Zhang, D.; Gong, H.; Wang, Z.; Huang, Y.; Guo, L.; Hu, C.; Yan, H.; Kang, J.; Han, J.; et al. Controlling Superhydrophobicity of Aluminum with Hierarchical Micro-Nanostructure Film for Superb Self-Cleaning and Anti-Corrosion. *ChemistrySelect* **2022**, *7*, e202200525, doi:10.1002/slct.202200525.

50. Wang, H.; He, M.; Liu, H.; Guan, Y. One-Step Fabrication of Robust Superhydrophobic Steel Surfaces with Mechanical Durability, Thermal Stability, and Anti-Icing Function. *ACS Appl. Mater. Interfaces* **2019**, *11*, 25586–25594, doi:10.1021/acsami.9b06865.

51. Long, J.; He, Z.; Zhou, P.; Xie, X.; Zhou, C.; Hong, W.; Hu, W. Low-Cost Fabrication of Large-Area Broccoli-Like Multiscale Micro- and Nanostructures for Metallic Super-Hydrophobic Surfaces with Ultralow Water Adhesion and Superior Anti-Frost Ability. *Adv Materials Inter* **2018**, *5*, 1800353, doi:10.1002/admi.201800353.

52. Cao, Y.; Shin, Y.C. Multi-Scale Modeling of Phase Explosion in High Fluence Nanosecond Laser Ablation and Clarification of Ablation Depth Prediction Criterion. *Applied Surface Science* **2015**, *357*, 74–85, doi:10.1016/j.apsusc.2015.08.251.

53. Emelyanenko, K.A.; Sanzharovsky, N.A.; Chulkova, E.V.; Ganne, A.A.; Emelyanenko, A.M.; Boinovich, L.B. Superhydrophobic Corrosion Resistant Coatings for Copper via IR Nanosecond Laser Processing. *Mater. Res. Express* **2018**, *5*, 115001, doi:10.1088/2053-1591/aadc16.

54. Jeon, J.-W.; Yoon, S.; Choi, H.; Kim, J.; Farson, D.; Cho, S.-H. The Effect of Laser Pulse Widths on Laser—Ag Nanoparticle Interaction: Femto- to Nanosecond Lasers. *Applied Sciences* **2018**, *8*, 112, doi:10.3390/app8010112.

55. Maghsoudi, K.; Momen, G.; Jafari, R. The Thermodynamic Stability of the Cassie–Baxter Regime Determined by the Geometric Parameters of Hierarchical Superhydrophobic Surfaces. *Applied Materials Today* **2023**, *34*, 101893, doi:10.1016/j.apmt.2023.101893.

56. Rauh, S.; Wöbbeking, K.; Li, M.; Schade, W.; Hübner, E.G. From Femtosecond to Nanosecond Laser Microstructuring of Conical Aluminum Surfaces by Reactive Gas Assisted Laser Ablation. *ChemPhysChem* **2020**, *21*, 1644–1652, doi:10.1002/cphc.202000418.

57. Zhao, J.; Nie, X.; Guo, J.; Zhang, Y.; Wang, Y.; Cui, Y.; Shrotriya, P. Rapid Laser Fabrication of Long-Term Stable Superhydrophilic Aluminum Surface. *SN Appl. Sci.* **2020**, *2*, 697, doi:10.1007/s42452-020-2522-9.

58. Cao, Q.; Wang, Z.; He, W.; Guan, Y. Fabrication of Super Hydrophilic Surface on Alumina Ceramic by Ultrafast Laser Microprocessing. *Applied Surface Science* **2021**, *557*, 149842, doi:10.1016/j.apsusc.2021.149842.

59. Samanta, A.; Wang, Q.; Shaw, S.K.; Ding, H. Roles of Chemistry Modification for Laser Textured Metal Alloys to Achieve Extreme Surface Wetting Behaviors. *Materials & Design* **2020**, *192*, 108744, doi:10.1016/j.matdes.2020.108744.

60. Fedotov, A.V.; Belyakov, A.V. Features of Nanosize Boehmite Hydrothermal Synthesis. *Refract Ind Ceram* **2022**, *62*, 658–662, doi:10.1007/s11148-022-00657-1.

61. Fedel, M.; Deflorian, F. Influence of a Boiling Water Treatment on the Electrochemical Properties of a Sol–Gel Film on AA1050. *Transactions of the IMF* **2015**, *93*, 313–320, doi:10.1080/00202967.2015.1117261.

62. López, C.; Galmés, B.; Soberats, B.; Frontera, A.; Rotger, C.; Costa, A. Surface Modification of Pseudoboehmite-Coated Aluminum Plates with Squaramic Acid Amphiphiles. *ACS Omega* **2019**, *4*, 14868–14874, doi:10.1021/acsomega.9b01459.

63. Ono, S. Nanostructure Analysis of Anodic Films Formed on Aluminum-Focusing on the Effects of Electric Field Strength and Electrolyte Anions. *Molecules* **2021**, *26*, 7270, doi:10.3390/molecules26237270.

64. Yilbas, B.S.; Khaled, M.; Abu-Dheir, N.; Aqeeli, N.; Furquan, S.Z. Laser Texturing of Alumina Surface for Improved Hydrophobicity. *Applied Surface Science* **2013**, *286*, 161–170, doi:10.1016/j.apsusc.2013.09.040.

65. Sun, T.; Zhuo, Q.; Chen, Y.; Wu, Z. Synthesis of Boehmite and Its Effect on Flame Retardancy of Epoxy Resin. *High Performance Polymers* **2015**, *27*, 100–104, doi:10.1177/0954008314540312.

66. Maeda, K.; Mizukami, F.; Niwa, S.; Toba, M.; Watanabe, M.; Masuda, K. Thermal Behaviour of Alumina from Aluminium Alkoxide Reacted with Complexing Agent. *Faraday Trans.* **1992**, *88*, 97, doi:10.1039/ft9928800097.

67. Tran, N.G.; Chun, D.-M. Green Manufacturing of Extreme Wettability Contrast Surfaces with Superhydrophilic and Superhydrophobic Patterns on Aluminum. *Journal of Materials Processing Technology* **2021**, *297*, 117245, doi:10.1016/j.jmatprotec.2021.117245.

68. Gunda, N.S.K.; Singh, M.; Norman, L.; Kaur, K.; Mitra, S.K. Optimization and Characterization of Biomolecule Immobilization on Silicon Substrates Using (3-Aminopropyl)Triethoxysilane (APTES) and Glutaraldehyde Linker. *Applied Surface Science* **2014**, *305*, 522–530, doi:10.1016/j.apsusc.2014.03.130.

69. Zu, G.; Shen, J.; Wei, X.; Ni, X.; Zhang, Z.; Wang, J.; Liu, G. Preparation and Characterization of Monolithic Alumina Aerogels. *Journal of Non-Crystalline Solids* **2011**, *357*, 2903–2906, doi:10.1016/j.jnoncrysol.2011.03.031.

70. Mojet, B.L.; Ebbesen, S.D.; Lefferts, L. Light at the Interface: The Potential of Attenuated Total Reflection Infrared Spectroscopy for Understanding Heterogeneous Catalysis in Water. *Chem. Soc. Rev.* **2010**, *39*, 4643, doi:10.1039/c0cs00014k.

71. Sherif, E.-S.M.; Mohammed, J.A.; Abdo, H.S.; Almajid, A.A. Corrosion Behavior in Highly Concentrated Sodium Chloride Solutions of

Nanocrystalline Aluminum Processed by High Energy Ball Mill. *International Journal of Electrochemical Science* **2016**, *11*, 1355–1369, doi:10.1016/S1452-3981(23)15927-X.

72. Cao, L.; Hu, H.-H.; Gao, D. Design and Fabrication of Micro-Textures for Inducing a Superhydrophobic Behavior on Hydrophilic Materials. *Langmuir* **2007**, *23*, 4310–4314, doi:10.1021/la063572r.
73. Farsinezhad, S.; Waghmare, P.R.; Wiltshire, B.D.; Sharma, H.; Amiri, S.; Mitra, S.K.; Shankar, K. Amphiphobic Surfaces from Functionalized TiO_2 Nanotube Arrays. *RSC Adv.* **2014**, *4*, 33587–33598, doi:10.1039/C4RA06402J.
74. Cao, L.; Price, T.P.; Weiss, M.; Gao, D. Super Water- and Oil-Repellent Surfaces on Intrinsically Hydrophilic and Oleophilic Porous Silicon Films. *Langmuir* **2008**, *24*, 1640–1643, doi:10.1021/la703401f.
75. O'Connor, J.; Bolan, N.S.; Kumar, M.; Nitai, A.S.; Ahmed, M.B.; Bolan, S.S.; Vithanage, M.; Rinklebe, J.; Mukhopadhyay, R.; Srivastava, P.; et al. Distribution, Transformation and Remediation of Poly- and per-Fluoroalkyl Substances (PFAS) in Wastewater Sources. *Process Safety and Environmental Protection* **2022**, *164*, 91–108, doi:10.1016/j.psep.2022.06.002.
76. Ambaye, T.G.; Vaccari, M.; Prasad, S.; Rtimi, S. Recent Progress and Challenges on the Removal of Per- and Poly-Fluoroalkyl Substances (PFAS) from Contaminated Soil and Water. *Environ Sci Pollut Res* **2022**, *29*, 58405–58428, doi:10.1007/s11356-022-21513-2.
77. Tran, N.G.; Chun, D.-M. Ultrafast and Eco-Friendly Fabrication Process for Robust, Repairable Superhydrophobic Metallic Surfaces with Tunable Water Adhesion. *ACS Appl. Mater. Interfaces* **2022**, *14*, 28348–28358, doi:10.1021/acsami.2c04824.
78. Jagdheesh, R.; Diaz, M.; Marimuthu, S.; Ocaña, J.L. Hybrid Laser and Vacuum Process for Rapid Ultrahydrophobic Ti-6Al-4 V Surface Formation. *Applied Surface Science* **2019**, *471*, 759–766, doi:10.1016/j.apsusc.2018.12.047.
79. Bridges, J.; Solomon, K.R. Quantitative Weight-of-Evidence Analysis of the Persistence, Bioaccumulation, Toxicity, and Potential for Long-Range Transport of the Cyclic Volatile Methyl Siloxanes. *Journal of Toxicology and Environmental Health, Part B* **2016**, *19*, 345–379, doi:10.1080/10937404.2016.1200505.
80. He, Y.; Su, S.; Cheng, J.; Tang, Z.; Ren, S.; Lyu, Y. Bioaccumulation and Trophodynamics of Cyclic Methylsiloxanes in the Food Web of a Large Subtropical Lake in China. *Journal of Hazardous Materials* **2021**, *413*, 125354, doi:10.1016/j.jhazmat.2021.125354.

81. Lu, Y.; Guan, Y.; Li, Y.; Yang, L.; Wang, M.; Wang, Y. Nanosecond Laser Fabrication of Superhydrophobic Surface on 316L Stainless Steel and Corrosion Protection Application. *Colloids and Surfaces A: Physicochemical and Engineering Aspects* **2020**, *604*, 125259, doi:10.1016/j.colsurfa.2020.125259.

82. Itina, T.E.; Shcheblanov, N. Electronic Excitation in Femtosecond Laser Interactions with Wide-Band-Gap Materials. *Appl. Phys. A* **2010**, *98*, 769–775, doi:10.1007/s00339-009-5540-4.

83. Chen, C.; Tian, Z.; Luo, X.; Jiang, G.; Hu, X.; Wang, L.; Peng, R.; Zhang, H.; Zhong, M. Cauliflower-like Micro-Nano Structured Superhydrophobic Surfaces for Durable Anti-Icing and Photothermal de-Icing. *Chemical Engineering Journal* **2022**, *450*, 137936, doi:10.1016/j.cej.2022.137936.

84. Sierra, D.R.; Edwardson, S.P.; Dearden, G. Laser Surface Texturing of Titanium with Thermal Post-Processing for Improved Wettability Properties. *Procedia CIRP* **2018**, *74*, 362–366, doi:10.1016/j.procir.2018.08.143.

85. Yang, Z.; Tian, Y.L.; Yang, C.J.; Wang, F.J.; Liu, X.P. Modification of Wetting Property of Inconel 718 Surface by Nanosecond Laser Texturing. *Applied Surface Science* **2017**, *414*, 313–324, doi:10.1016/j.apsusc.2017.04.050.

86. Yeganeh, M.; Mohammadi, N. Superhydrophobic Surface of Mg Alloys: A Review. *Journal of Magnesium and Alloys* **2018**, *6*, 59–70, doi:10.1016/j.jma.2018.02.001.

87. Fockaert, L.I.; Pletincx, S.; Boelen, B.; Hauffman, T.; Terryn, H.; Mol, J.M.C. Effect of Zirconium-Based Conversion Treatments of Zinc, Aluminium and Magnesium on the Chemisorption of Ester-Functionalized Molecules. *Applied Surface Science* **2020**, *508*, 145199, doi:10.1016/j.apsusc.2019.145199.

88. Hosseini, M.S.; Sadeghi, M.T.; Khazaei, M. Wettability Alteration from Superhydrophobic to Superhydrophilic via Synthesized Stable Nano-Coating. *Surface and Coatings Technology* **2017**, *326*, 79–86, doi:10.1016/j.surfcoat.2017.07.032.

89. Lin, D.-J.; Zhang, L.-Z.; Yi, M.-C.; Gao, S.-R.; Yang, Y.-R.; Wang, X.-D. Contact Time on Inclined Superhydrophobic Surfaces Decorated with Parallel Macro-Ridges. *Colloids and Surfaces A: Physicochemical and Engineering Aspects* **2020**, *599*, 124924, doi:10.1016/j.colsurfa.2020.124924.

90. Kim, H.; Kim, S.H. Nonwettable Hierarchical Structure Effect on Droplet Impact and Spreading Dynamics. *Langmuir* **2018**, *34*, 5480–5486, doi:10.1021/acs.langmuir.8b00707.

91. Farhangi, M.M.; Graham, P.J.; Choudhury, N.R.; Dolatabadi, A. Induced Detachment of Coalescing Droplets on Superhydrophobic Surfaces. *Langmuir* **2012**, *28*, 1290–1303, doi:10.1021/la203926q.

92. Aboud, D.G.K.; Kietzig, A.-M. On the Oblique Impact Dynamics of Drops on Superhydrophobic Surfaces. Part II: Restitution Coefficient and Contact Time. *Langmuir* **2018**, *34*, 9889–9896, doi:10.1021/acs.langmuir.8b01233.

93. Long, J.; Pan, L.; Fan, P.; Gong, D.; Jiang, D.; Zhang, H.; Li, L.; Zhong, M. Cassie-State Stability of Metallic Superhydrophobic Surfaces with Various Micro/Nanostructures Produced by a Femtosecond Laser. *Langmuir* **2016**, *32*, 1065–1072, doi:10.1021/acs.langmuir.5b04329.

94. Aparna, A.; Sethulekshmi, A.S.; Saritha, A.; Joseph, K. Recent Advances in Superhydrophobic Epoxy Based Nanocomposite Coatings and Their Applications. *Progress in Organic Coatings* **2022**, *166*, 106819, doi:10.1016/j.porgcoat.2022.106819.

Chapter 3

Laser Surface Modification for Joining Enhancement

3.1 Adhesive Bonding for Similar/Dissimilar Materials

Dissimilar material joining is a challenging topic of huge industrial interest, especially in the automotive and aerospace sectors [1,2]. Adhesive bonding is a solution for joining dissimilar materials that offer a variety of advantages, such as uniform load distributions and improved joint stiffness [3]. Compared to the traditionally available joining techniques, adhesive joining offers reduced cost and joining weight while simultaneously protecting against galvanic corrosion through improved corrosion resistance properties [4,5].

In general, for adhesive-bonded joining, various factors control the effective performance of the joint such as adhesive, bond line thickness, and curing treatment parameters [6,7]. Nonetheless, an optimal surface condition of the adherent plays a crucial role in the bonding strength and fracture mode. Generally, interface, and cohesive fracture modes are commonly observed for joints, wherein the cohesive fracture mode is more desired as it signals the maximum joining strength of the used adhesive [8,9]. Cohesive failure represents the situation where a layer of the adhesive remains on the adherend surfaces. This indicates that the adherend failed before the adhesive, which is desired. Therefore, various surface modification techniques have been used to pursue the cohesive failure mode. The following section discusses some of the more common approaches:

Mechanical Abrasion

To obtain ideal surface conditions, mechanical treatments could be used before the bonding process to eliminate organic and inorganic contaminants [10]. Different types of mechanical treatments, such as shot blasting, sandblasting, and grit blasting, support the formation of geometrical features with increased contact area and intermolecular interactions between the adhesive and adherent [11]. Amongst the different techniques, grit-blasting is considered the most effective due to its good surface roughness control.

Chemical Etching

As an alternative method, chemical etching removes the weak native oxide. It generates a newly formed oxide layer with microfeatures, as shown in Figure 3.1. Golru et al. investigated different chemical cleaning procedures on the epoxy-aluminum (AA1050) substrates [12]. Even though the alkaline medium removed the native oxide layer, some additional corrosion oxide products were formed, which reduced overall bonding performance. However, acidic (50% HNO_3) etching following the alkaline etching generated a strong oxide layer removing any contaminants and intermetallic particles, thereby increasing the overall surface energy and the joining performance.

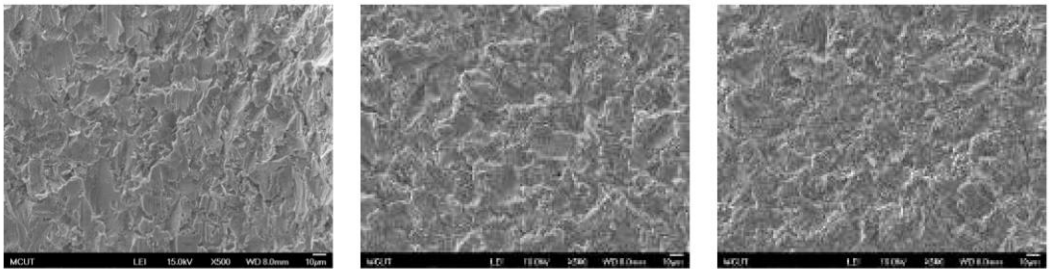

(a) (b) (c)

Figure 3.1. SEM images of acid etching on titanium surfaces (a) sandblasted sample; (b)H_2SO_4 for 10 min; (c) HCl for 10 min **[13]**.

Plasma Treatment

This is another popular technique for creating surface roughness on the treated samples, as shown in Figure 3.2. Saleema et al. used atmospheric pressure plasma to clean AA6061-T6 to improve the bonding durability [14]. The plasma treatment conditions could be tuned to render the treated surface with oxides and hydroxides, resulting in enhanced wettability and better bonding performance.

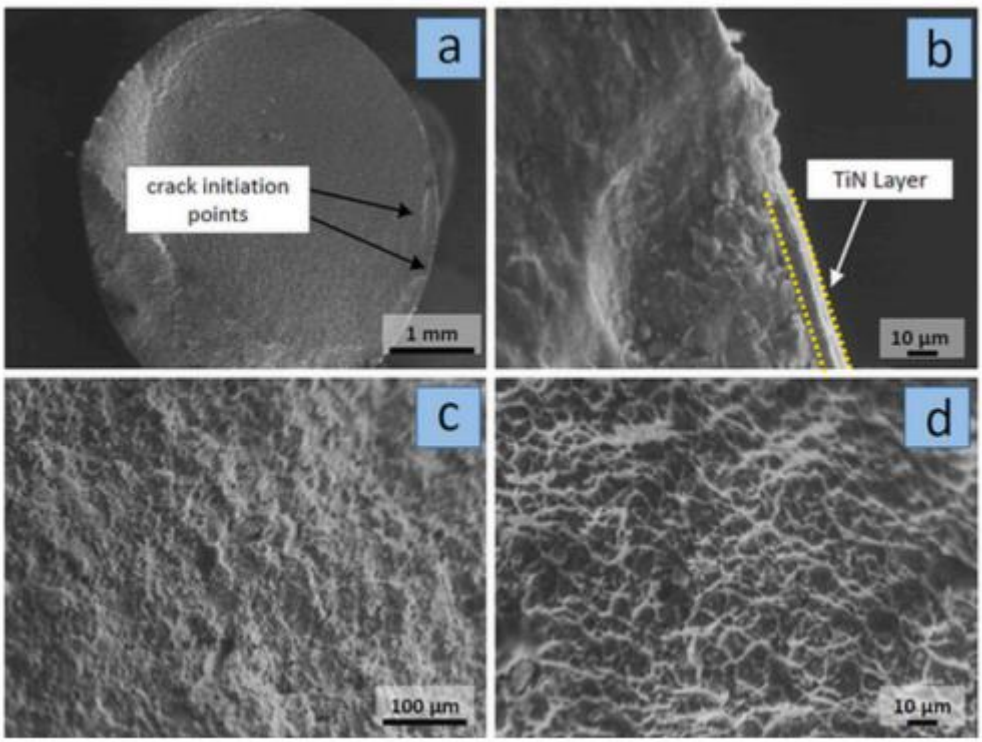

Figure 3.2 (a) SEM image of fatigue fracture on plasma nitrided Ti6Al4V; (b)crack initiation; (c) crack propagation; (d) final fractured surface **[15]**.

3.2 Laser Surface Modification

With the advancement of technology, lasers have increasingly been used for surface treatments of materials before bonding [16–18]. Compared to the techniques mentioned above, laser micromachining offers a variety of industrial advantages in terms of patternability, efficiency, automation, and eco-friendliness. Rechner et al. investigated the bonding strength of laser treated aluminum and reported increased strength and durability of the fabricated bonding [19]. Another significant advantage associated with laser treatment is the ability to protect against corrosive environments, which entails promising durability [20]. On the other hand, many treatments may provide good joining strength, but with time the joining fails due to corrosion. Furthermore, flexible laser processing parameters could be controlled depending on the desired applications. For example, low energy parameters could be used for cleaning the surface, whereas for strong bonding performance, a rough surface texture could be generated [21].

3.2.1 Morphological Evolution

On laser surface modification of the target substrate, the physical and chemical aspects of the surfaces are altered depending on the selected laser parameters [22]. The laser generated morphology includes features such as grooves, holes, melt-recast, etc., that increase the contact surface area and material interlocking at the adhesive/substrate interface, contributing to enhanced joining strength. Therefore, surface roughness is a quantitative reference parameter to assess the resulting modified surface [23]. Laser parameters such as fluence (power/area) are considered to have a strong fluence on surface modification. Spadaro et al. modified aluminum AA2024 using laser ablation with variable beam diameter and fluence ranging from 1-2 mm, and 0.5-10 J/cm^2, respectively [24]. Analyzing the resulting surface morphology, it was observed that there existed a strong difference between the modification patterns at the largest fluence value of 10 J/cm^2. However, for all the higher fluence modifications, the outer modification region displayed a highly corrugated surface.

3.2.2 Chemical Composition Modifications

Depending on the surrounding atmosphere in which the modifications are performed, the surface chemical composition is altered [25]. In particular, to perform the surface modification, a threshold fluence value exists depending on the laser pulse characteristics and the material type [26]. Below threshold fluence values are typically selected to clean the surface from contaminants, especially adsorbed organic compounds. Beyond the threshold fluence values, visible surface modification is observed, and for modifications performed in an open environment, the oxide thickness increases with the fluence values [27]. Material ejection could occur through vaporization, spallation, and phase-explosion processes on further increase of the laser fluence beyond the melting regime.

3.3 Laser Surface Processing for Solid Oxide Fuel Cell Applications

The first part of this chapter is devoted to discussing results obtained from the study on laser surface treatments on a steel employed in solid oxide fuel cell (SOFC) interconnect and the resulting enhancement in the glass sealant-interconnect joining strength. Solid oxide fuel cells are electrochemical devices

that are used to convert the oxidation of a fuel to electricity [28–30]. This type of fuel cell's advantages includes high power efficiency, long term stability, fuel flexibility, and relatively low cost [31,32]. The functional efficiency of the fuel cell relies critically on the joining between the interconnects and the adjacent ceramic components to form the SOFC stack, as shown in Figure 3. 3.

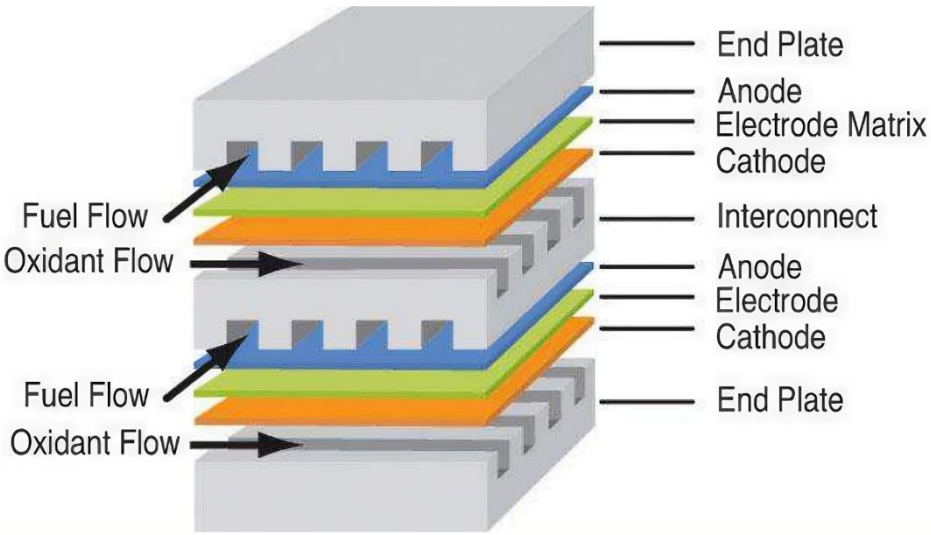

Figure 3. 3. Schematic illustration of SOFC stack components **[33]**.

In particular, the glass based sealings between the corresponding interfaces plays a crucial role in the long-term performance and durability of the cell stack [34,35]. In this context, the glass sealing and the metallic interconnect interface have received considerable attention with the evaluation of the bond strength through the bending and tensile tests [36,37]. However, the glass sealant is also exposed to significant shear stress, and therefore it is critically necessary to evaluate the shear strength of the glass sealant and interconnect joining. Therefore, this study mainly uses laser surface modification to generate variable surface morphology and modify the chemical composition of the as-received special stainless-steel sample (Crofer), which is specially designed for high temperature fuel-cell applications [38]. Apart from the morphological and compositional analysis, the ability to tune the laser parameters appropriately to obtain the desired surface features, such as average roughness, is demonstrated. Finally, two laser parameters are selected to modify an hourglass-shaped interconnect sample to be tested for torsional strength by our colleagues and collaborators, who are in charge of the study.

3.3.1 Laser Surface Patternability

The ability to perform selective and precision patterning on the target surface sets laser micromachining apart from other surface modification techniques [39–41]. Especially for the applications in SOFC, interconnect texturing is required along a specific pattern on the interconnect following that of the glass sealant, as shown in Figure 3.4(a). The galvanometric scan system enables the patterning of any complex design by the nanosecond fiber laser with precision in the micrometer regime. Figure 3.4(b) shows the university logo (Politecnico di Torino) printed on the stainless-steel substrate to demonstrate the ability to pattern. Apart from the flexibility for pattern generation, the processing time can be reduced by the appropriate choice of laser parameters resulting in strong modifications yet fast laser scan speeds and lower processing times.

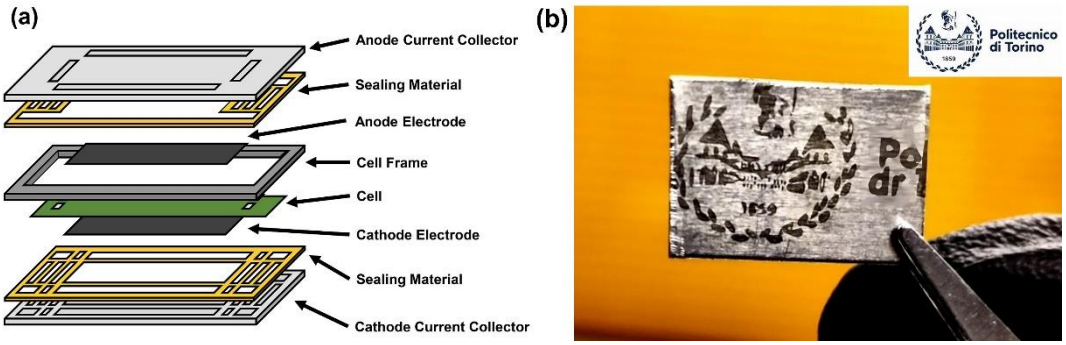

Figure 3.4. (a) Schematic illustration of a solid oxide fuel cell with the glass sealant **[42]**; (b) University logo (Politecnico di Torino) pattern printed on a stainless steel substrate using the nanosecond fiber laser used in this study.

3.3.2 Laser Surface Modification Control

The choice of appropriate laser parameters is critical to perform the desired surface modification [43]. The variable laser parameters include average power, scan speed, pulse repetition rate (PRR), scan spacing, and pulsewidth. As part of the preliminary study on the crofer sample, the average laser power and the pulse repetition rate were varied to observe the resulting surface modifications. Figure 3.5 shows the camera image of the single laser scan line modifications at different laser parameters performed on the crofer sample to evaluate the extent of laser modification visually.

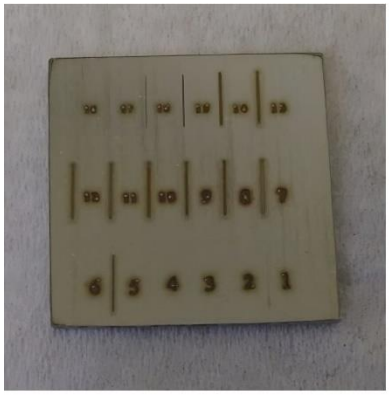

PRR (KHz)	15	30	50	100
	Index number-Fluence (J/cm²)			
Laser Power (W)				
3.0	1- 7.0	2- 3.5	3- 2.1	4- 1.0
4.2	5- 9.9	6- 4.9	7- 2.9	8- 1.4
5.4	9- 12.7	10- 6.3	11- 3.8	12- 1.9
6.0	13- 14.1	14- 7.0	15- 4.2	16- 2.1

No modification
Partial/Strong modification

Figure 3.5. Camera image of the single laser scan lines written on the crofer sample using different laser parameters and the corresponding laser parameter table.

From Figure 3.5, it can be observed that the laser parameters have a strong influence on the resulting surface modifications. The initial observation regards the importance of the fluence as a laser parameter to generate surface modification. As observed from the table inFigure 3.5, the low fluence values in modification index 2,3, and 4 (blue color cells) cause no visible laser modification on the crofer sample. However, this is not a general case because even at low fluence values, if the pulse repetition rate is sufficiently high, a visible surface modification is observed, such as in the case of modification number 8 (1.4 J/cm^2, 100 kHz). This is due to the high pulse repetition rate effect, since at high PRR values, a combination of low pulse temporal spacing and greater pulse deposition at a single spot. Indeed, in that case the thermal energy deposition at the focal spot increases and produce the modification [44,45].

An interesting observation regards the laser processing of stainless steel at lower fluence values, as shown in Figure 3.6. This phenomenon on stainless steel substrates using a long-pulsed laser has been previously reported. Unlike the nanostructure coloring based on incident light interference with surface feature size comparable to the visible wavelength, the surface coloring, in this case, is primarily due to the inherent color variation dependent on the content of the Fe^{2+}, Fe^{3+}, and Cr^{3+} states [46]. Reportedly, even a minor change in the composition could cause a drastic variation in the color. However, we do not further dwell into the responsible parameters and composition for the color formation as this study is out of scope.

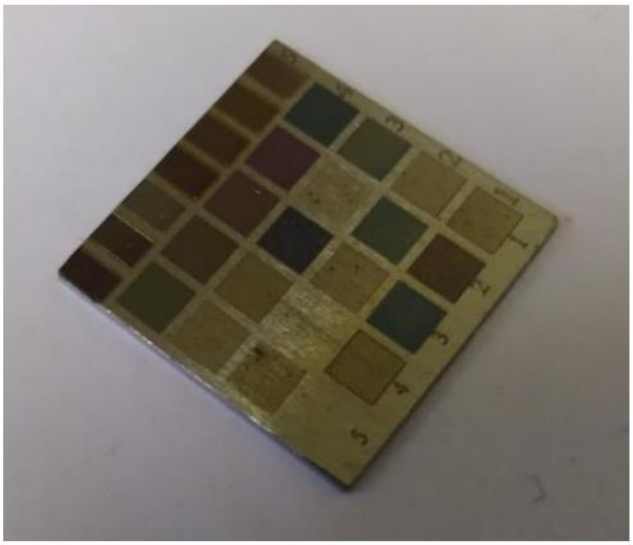

Figure 3.6. Nanosecond laser induced coloration of the crofer sample.

Besides the pulse repetition rate and the average power, the laser scan speed also wields importance for defining the surface features. Figure 3.7 shows the plot of average surface roughness (Ra) vs laser average power for two different scan speeds of 50 mm/s and 100 mm/s.

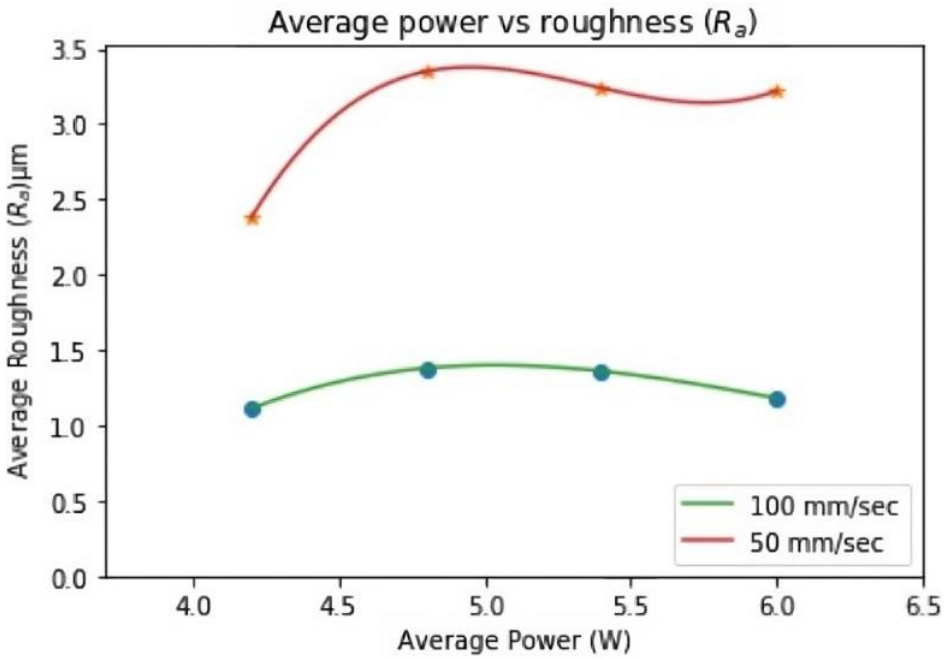

Figure 3.7. Variation of average line roughness value of laser modified crofer sample with varying average power at two different scan speeds of 50 mm/s and 100 mm/s.

As the plot above shows, the single line scan average roughness Ra value increase at a lower scan speed of 50 mm/s. The scan speed essentially controls the temporal presence of the beam focus at a given focal spot, thereby controlling the pulse deposition per spot [47]. Therefore, increased pulse deposition results in stronger surface modification and greater surface roughness.

Depending on the material substrates and the applicational requirements, the appropriate laser parameters could be selected to cover a whole range of surface roughness values for joining strength enhancement. Figure 3.8 shows the tunability of the obtained surface features based on the appropriate combination of laser parameters of laser scan speed and average power at a constant pulse repetition rate of 25 kHz. In the same study, while the effect of variable scan speed was studied, the average power was kept constant at 15 W, whereas while the average power was varied, the scan speed was kept constant at 1 mm/s.

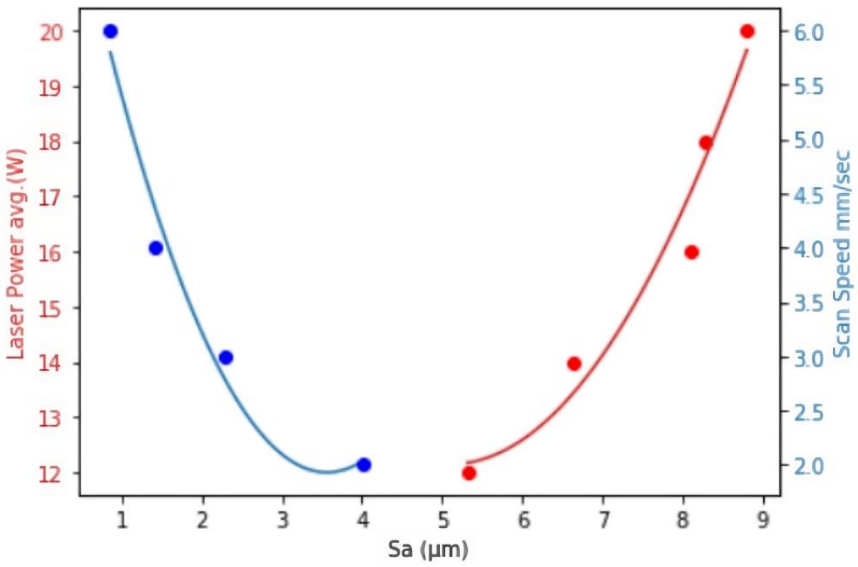

Figure 3.8. Plot of laser average power and scan speed vs average surface roughness. The scan speed was varied at constane average power of 15 W (blue), and the average power was varied at constant scan speed of 1 mm/s (red).

Figure 3.8 shows that the tunable laser parameters enable intermediate average surface roughness values in the range of 1-9 µm. This demonstrates the ability of laser patterning to generate variable surface roughness for joining applications.

3.4 Morphological and Compositional Analysis

Scanning electron microscopy was used to analyze the morphological features of the laser modification. The mechanism of nanosecond laser interaction has been discussed in detail in the previous chapters, therefore, only a brief description is provided in the current section. Figure 3.9 shows the SEM images of the laser modified crofer at an average power of 18 W, pulse repetition rate of 25 kHz, scan speed of 3 mm/s, pulsewidth of 4 ns, and scan spacing of 40 µm.

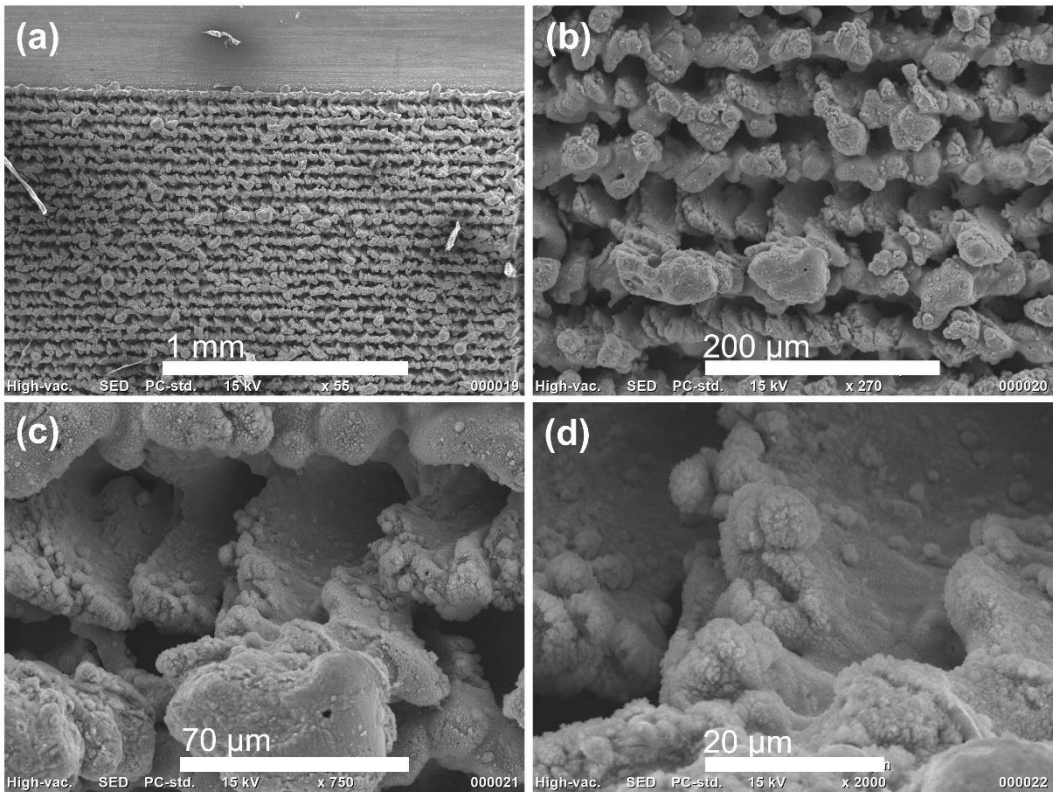

Figure 3.9. SEM images of laser modification on crofer sample at different magnifications and an average power of 18 W, PRR of 25 kHz, scan speed of 3 mm/s, scan spacing of 40 µm, and puilsewidth of 4 ns.

The SEM images show a complex surface morphology as a result of the rapid melt-solidification of the metal surface. The laser scan path is visible as a groove where the maximum material removal has occurred. As shown in Figure 3.9(b), along the groove, there are holes representing the concentrated energy deposition at the beam center, hence more vaporization at the center. Beside the groove are large microfeatures that could represent the recast material deposited because of the Marangoni convection of the generated melt [48,49]. The central groove region is formed because of rapid vaporization at the Gaussian center due to phase

explosion [50]. The phase explosion leads to rapid vaporization, melt ejection and micro/nano-particle material redeposition on the laser treated surface, as seen from Figure 3.9(b,c,d). The rough surface morphology would be ideal for providing an interlocking mechanism resulting in a successful bonding and improved joining strength in comparison to the plane surface. The effect of laser interaction on the chemical composition of the surface is investigated using energy dispersive X-ray spectroscopy. Figure 3.10 shows the obtained EDS spectra on the as-received crofer sample and the laser textured surface.

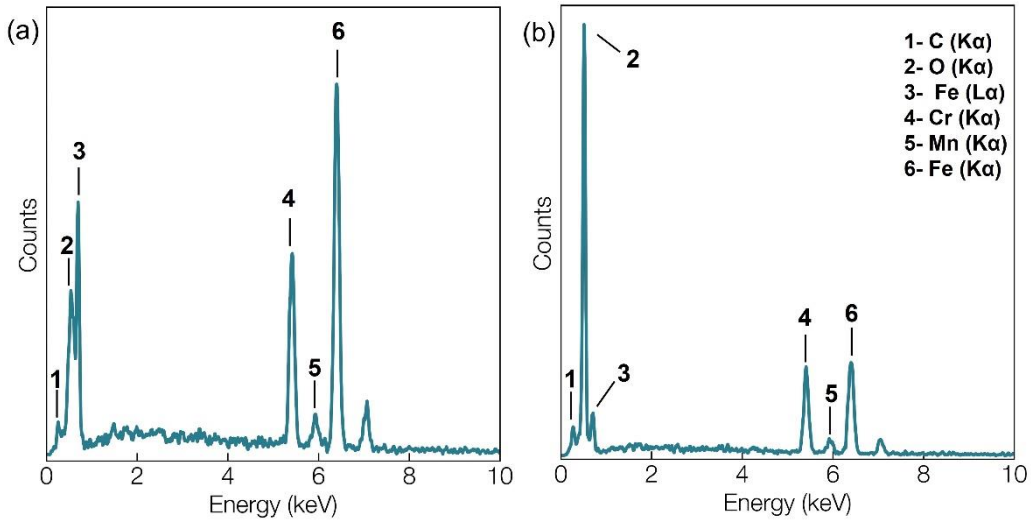

Figure 3.10. EDS spectra of the crofer sample (a) as received; (b) laser processed.

Table 3.1 Elemental composition information of EDS from Figure 3.10.

Elements	As received Crofer (At%)	Laser textured Crofer (At %)
C	8.1	11.1
O	4.6	58.2
Cr	19.8	10.3
Mn	1.0	0.3
Fe	64.6	19.5
Cu	0.7	-

The corresponding quantitative information of EDS analysis is shown in Table 3.1. As expected, the laser processing resulted in strong oxidation, evident from the dominating presence of oxygen on the laser processed sample. Apart from iron, there is visible reduction in the presence of other alloying elements such as chromium and manganese. Interestingly, the carbon content on the laser treated sample is particularly high. This could result from organic compound adsorption from the atmosphere by the activated metal oxide structure [51,52]. Since the EDS measurements were not immediately performed on the laser processed samples, the VOC adsorption could have resulted in increased carbon content. The above results provide a preliminary set of results for the laser processing of crofer.

3.5 Joining Strength Test for Laser Processed Crofer

3.5.1 Fluence Based Roughness Characterization on Torsion Test Samples

After performing a preliminary study on the laser processed crofer samples, the interconnect samples as an hourglass were designed for torsional analysis, as shown in Figure 3.11.

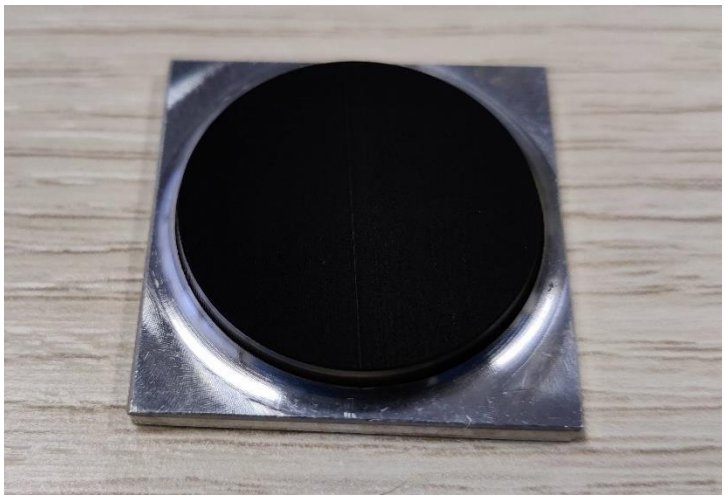

Figure 3.11. Laser modified crofer interconnect sample for torsional analysis in an hourglass shape.

A roughness characterization was performed on the crofer sample with only laser fluence as the variable parameter to select the roughness parameters for the torsional analysis. The laser scan speed was set at 5 mm/s, pulse repetition rate at 25 kHz, scan line spacing of 40 μm, and laser pulsewidth of 12 ns. To have

complete information about the surface roughness, both average roughness (Sa) and the maximum peak to valley height (Sz) were considered. Post laser processing, the crofer samples were sequentially sonicated in acetone and ethanol to remove any undesirable loose debris.

Figure 3.12 shows the variation of surface roughness parameters with the laser fluence.

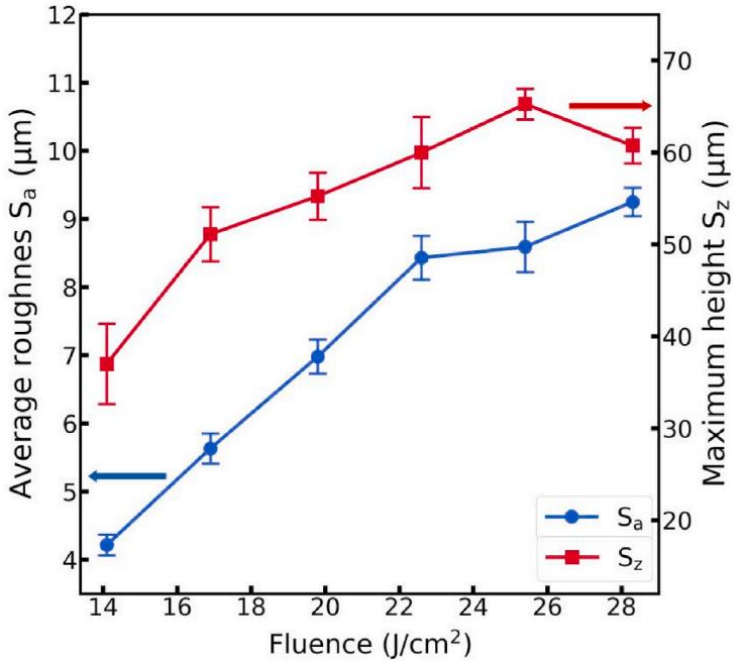

Figure 3.12. Plot of roughness parameters (Sa, Sz)of laser textured crofer with varying laser fluence, to select laser parameters for the torsional test analysis samples.

Both the surface roughness parameters increase with the laser fluence due to greater delivered pulse energy causing enhanced vaporization and melt formation. The enhanced vaporization result in deeper groove formation, which is reflected in the increasing Sz values [53]. A pair of low and high average roughness values shown in Table 3.2.

Table 3.2 were selected for the laser processing of the torsional test samples. Also, the 3D surface profile of the selected modifications is shown in Figure 3.13.

Table 3.2. Selected laser fluence values based on Figure 3.12, and the corresponding roughness values.

Fluence (J/cm^2)	Sa (µm)	Sz (µm)
14.1	4.6	39.7
28.3	8.8	61.6

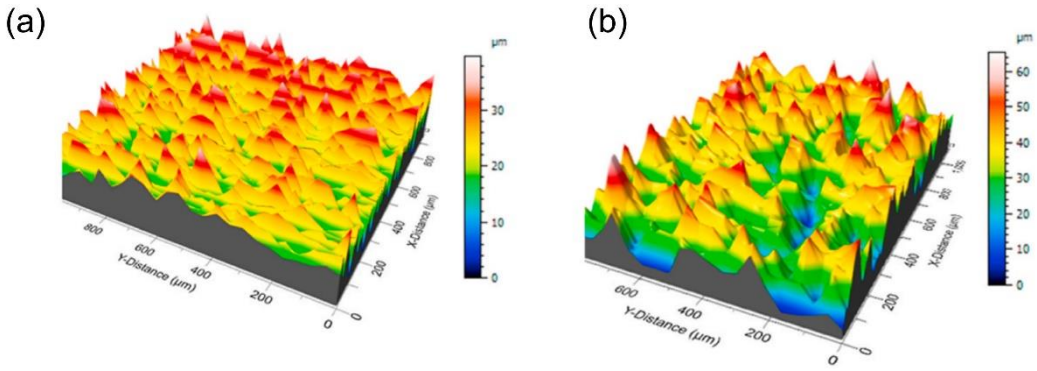

Figure 3.13. 3D surface profile of the crofer surface processed with the selected laser parameters (a) 14.1 J/cm^2; (b) 28.3 J/cm^2.

The profilometer maps clearly show the laser grooves generated on the modification at a lower fluence of 14.1 J/cm^2. In contrast, for the higher roughness, the excessive thermal effects and the resulting melt formation resulted in random peak distribution on the surface.

3.5.2 Mechanical Characterization of Joined Samples

The morphological tests on the provided laser processed and glass-joined samples suggests a better bonding of the glass with the interconnect without defect formation. Based on the SEM observations of the joined and thermally cured samples, our collaborators chose the lower average roughness sample generated at a fluence of 14.1 J/cm^2 for the final torsional test analysis. Indeed, the laser processed interconnect samples demonstrated a greater shear strength of 32±5 MPa compared to the as-received glass-joined crofer samples with 24±7

MPa. Interestingly, the laser processed joints on torsional analysis showed a different fracture mode, where the fracture propagation is mainly through the sealant in a desirable cohesive mode. The glass presence within the laser microfeatures provides an interlocking that supports the cohesive failure mode. Therefore, the glass sealant is present on both the fracture surface, as shown in Figure 3.14.

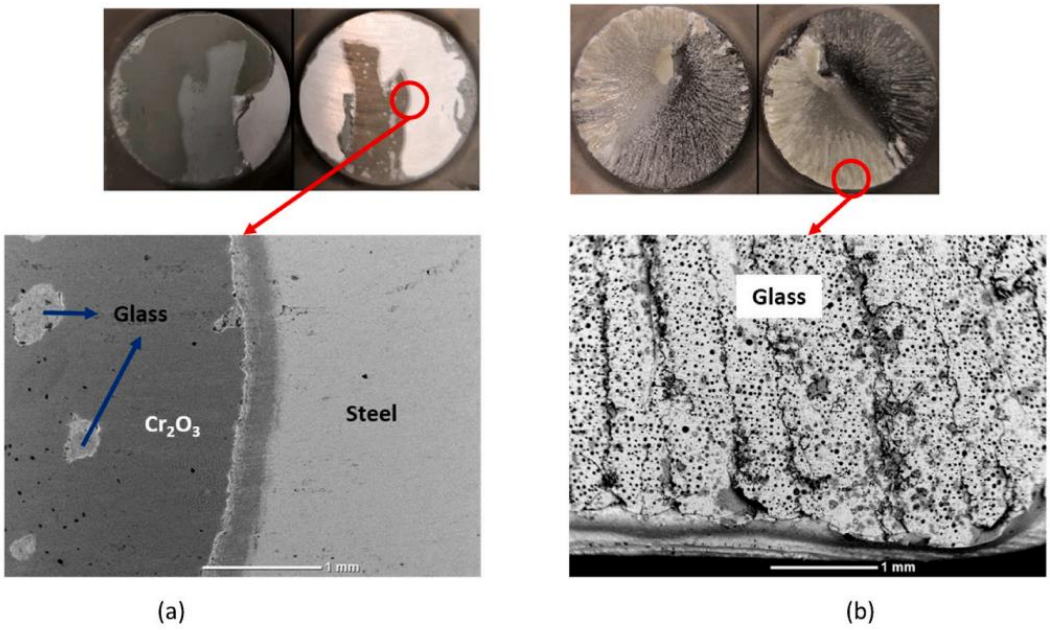

Figure 3.14. SEM images of the samples after the fracture test where the composition was investigated with the help of EDS analysis (a) as received samples (b) laser processed samples. The difference in the fracture surface for both samples are clearly visible, where glass is present on both surfaces for laser processed samples suggesting a cohesive failure mode **[54]**.

The laser processing of the metallic interconnect with the appropriate parameters has resulted in a cohesion failure mode, whereas the as received sample underwent an adhesive failure mode, suggesting an enhanced bonding performance in case of the former.

3.6 Silicon Nitride Ceramics

Silicon Nitride has drawn tremendous attention for its properties as a ceramic material [53,55,56]. Indeed, it has a low thermal expansion coefficient and displays high thermal shock resistance properties [57,58]. Additionally, it has

other properties such as chemical inertness, high temperature stability (up to 1800°C), and high strength. However, a major problem that Si_3N_4 faces relates to fracture behavior [59]. Crack generation in the material could rapidly propagate, leading to material failure. That is a problem of paramount importance when joining silicon nitride applications with similar/dissimilar materials. In this thesis, a preliminary study was started on the laser processing of Si_3N_4 ceramic sample and following morphological, topographical and elemental composition analysis.

3.6.1 Laser Processing of Si_3N_4 Ceramics

The average surface roughness of the as-received silicon nitride sample was 300 nm based on profilometer analysis. The first step of the study would be to laser process the ceramic sample with variable average surface roughness values. Therefore, laser scan speed was set as the variable parameter with values of 1, 5, 15, and 20 mm/s, while rest of the laser parameters were fixed as follows: laser average power at 20 W, scan line spacing at 40 µm, pulsewidth of 4 ns, and pulse repetition rate of 20 kHz. Figure 3.15 shows the SEM image of the laser processed silicon nitride sample at the slowest scan speed of 1 mm/s.

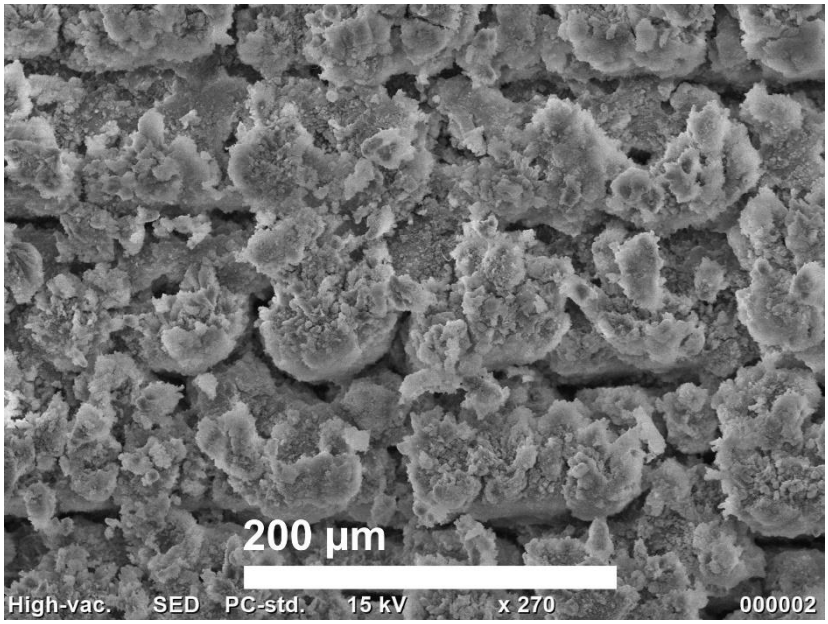

Figure 3.15. SEM image of laser processed silicon nitride sample at scan speed of 1 mm/s.

The slowest scan speed is expected to have the highest roughness due to the greater thermal effect at the laser focus. The figure shows a very rough surface morphology with the laser scan path barely visible due to the redeposition of

ablated particles and melt solidification. Previous reports on laser ablation of Si_3N_4 in air have reported silica formation on the surface due to surface oxidation supported by the high temperatures achieved at the laser focus [60]. The redeposited particles on the surface would be mainly silica, which will be investigated using elemental composition analysis.

The plot in Figure 3.16 clearly demonstrates the effect of the laser scan speed, where the Sa value varies from about 6.8 µm at 1 mm/s to about 2.6 µm at a scan speed of 20 mm/s. The scan speed is therefore sufficient as a parameter to vary the average roughness for preliminary joining trials.

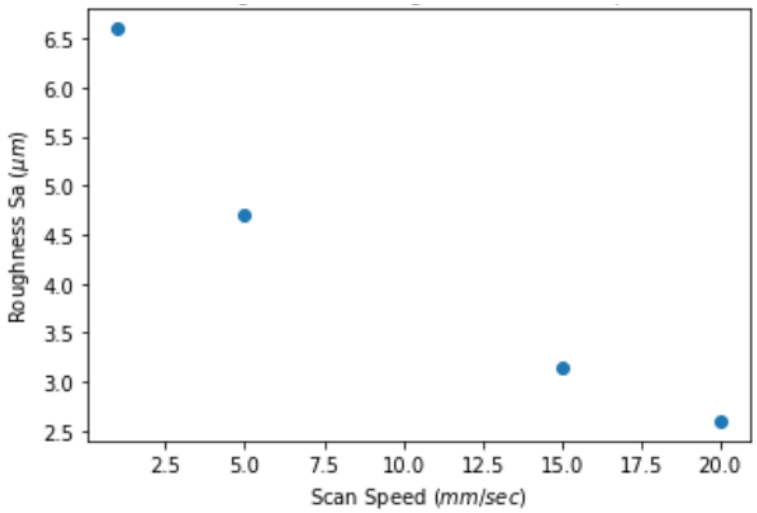

Figure 3.16. Average surface roughness of the laser processed sample against the laser scan speed.

In fact, the effect of laser parameters and appropriate scan pattern for specific microstructure shape would be later steps of this ongoing study, all based on preliminary results from the joining tests. Following the SEM analysis, EDS analysis was performed on the laser modified samples and compared to the pristine silicon nitride samples. Table 3.3 displays the obtained EDS results on the different samples.

The EDS data shows decreasing nitrogen content with reducing scan speed, while the opposite is true for elemental oxygen content as shown in the table below. The EDS results, therefore, confirm the silica formation on laser processing. The strong laser interaction at low scanning speed would enhance the

silica formation, hence the increased oxygen content. On the other hand, the nitrogen would be removed by forming N_2 gas, escaping the surface [61].

Table 3.3. EDS quantitative elemental compositional information of laser processed samples at different laser scan speeds.

Scan Speed (mm/sec)	Nitrogen (mass%)	Oxygen (mass%)	Silicon (mass%)
As received	39.6	11.4	48.9
1	-	53.2	46.7
5	1.6	52.3	45.9
15	22.8	41.1	36.0

3.6.2 Silica Removal Through Chemical Etching

Hydrofluoric acid etching of silica is a widely used and established process, especially in the glass industry. In the case of the laser processed silicon nitride surface, the effect of silica formation on the joining strength needs to be investigated. Therefore, it is important to remove the silica formation on the surface following which joining strength analysis must be conducted on laser processed ceramic samples with and without the silica formation. To this aim, dilute HF (3.5%) was selected as the etchant to treat the laser processed samples. An etching time of 8 min was selected for the treatment. Figure 3.17 shows the SEM and profilometer images of the fresh laser textured samples (1 mm/s) to that of the HF treated sample.

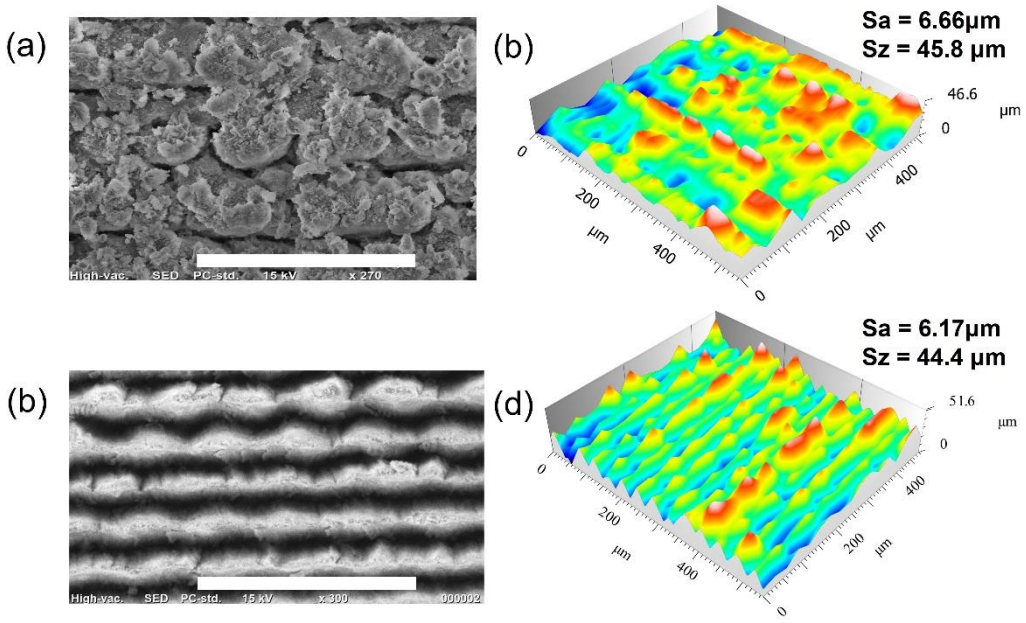

Figure 3.17. SEM images of the laser processed silicon nitride sample at scan speed of 1 mm/s (a) before HF etching; (c) after HF etching; correspondign 3D profilometer images (b) for surface in (a); (d) for surface in (c).

Indeed, the surface morphology exhibit a drastic modification after the acid treatment. After the removal of the laser deposited debris through the etching process, the laser modified grooves are visible, and the profilometer images also reflect the same, as shown in Figure 3.17(c,d). These images therefore suggest a strong removal of the laser generated silica which is to be verified through EDS analysis. Table 3.4 shows the average surface roughness values variation for the laser processed samples after the HF etching.

Table 3.4. Average surface roughness (Sa) values before and after etching for the different laser processed surfaces.

Laser Scan Speed (mm/sec)	Sa Before Etching [µm]	Sa After HF Etching [µm] 8 minutes
1	6.6	6.2
5	4.7	5.5
15	3.15	3.10

Figure 3.18 shows the complete EDS results of the measurements performed on the as-received, laser processed, and HF etched samples are compared to better visualize the variations in elemental composition.

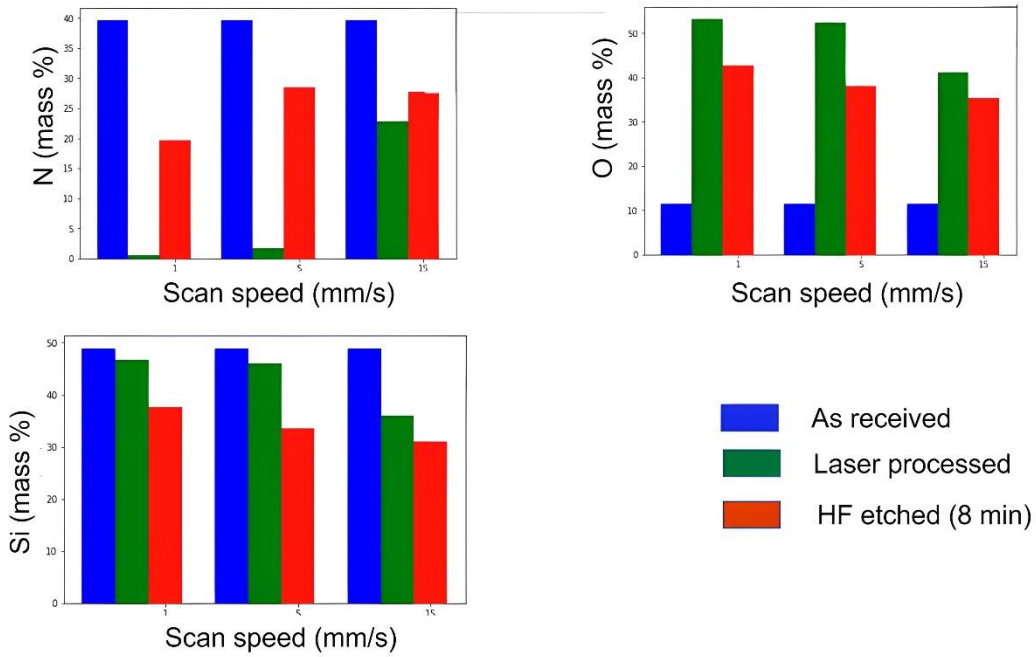

Figure 3.18. EDS data plots for the different compositional elements for all the different stages of the ceramic surface processing in this stuidy, which includes, as received sample, laser processed, and laser processing followed by HF etching.

The EDS results in Figure 3.18 clearly demonstrate the reduction in oxidation in the HF treated samples as compared to the laser textured ceramic surface. The drastic increase in the nitrogen content of the HF etched surface further confirms the exposure of the non-oxidized silicon nitride surface.

Therefore, the study has successfully used selected laser parameters to texture the silicon nitride surface with variable surface roughness, and the laser generated silica is removed through a HF acid based chemical etching following the laser processing step. Further joining strength tests are ongoing to assess the possible enhancement of the joining strength for the laser treated surfaces.

References

1. Singh, V.P.; Kumar, R.; Kumar, A.; Dewangan, A.K. Automotive Light Weight Multi-Materials Sheets Joining through Friction Stir Welding Technique: An Overview. *Materials Today: Proceedings* **2023**, S2214785323007101, doi:10.1016/j.matpr.2023.02.171.
2. Kumar, M.; Das, A.; Ballav, R. Influence of Tool Geometry on Morphology and Mechanical Properties of Friction Stir Welded Dissimilar Joints: A Review. *Materials Today: Proceedings* **2020**, *33*, 4951–4955, doi:10.1016/j.matpr.2020.02.689.
3. Pizzorni, M.; Lertora, E.; Parmiggiani, A. Adhesive Bonding of 3D-Printed Short- and Continuous-Carbon-Fiber Composites: An Experimental Analysis of Design Methods to Improve Joint Strength. *Composites Part B: Engineering* **2022**, *230*, 109539, doi:10.1016/j.compositesb.2021.109539.
4. Quan, D.; Deegan, B.; Byrne, L.; Scarselli, G.; Ivanković, A.; Murphy, N. Rapid Surface Activation of Carbon Fibre Reinforced PEEK and PPS Composites by High-Power UV-Irradiation for the Adhesive Joining of Dissimilar Materials. *Composites Part A: Applied Science and Manufacturing* **2020**, *137*, 105976, doi:10.1016/j.compositesa.2020.105976.
5. Schanz, J.; Nester, S.; Meinhard, D.; Pott, T.; Riegel, H.; De Silva, A.K.M.; Harrison, D.K.; Knoblauch, V. Adhesively Bonded CFRP/Al Joints: Influence of the Surface Pretreatment on Corrosion during Salt Spray Test. *Materials & Corrosion* **2022**, *73*, 158–170, doi:10.1002/maco.202112752.
6. Zhang, D.; Huang, Y. Influence of Surface Roughness and Bondline Thickness on the Bonding Performance of Epoxy Adhesive Joints on Mild Steel Substrates. *Progress in Organic Coatings* **2021**, *153*, 106135, doi:10.1016/j.porgcoat.2021.106135.
7. Pizzorni, M.; Lertora, E.; Mandolfino, C. Low Pressure Plasma Treatment of CFRP Substrates for Adhesive Bonding: An Investigation of Joint Durability under Severe Temperature-Moisture Conditioning. *International Journal of Adhesion and Adhesives* **2020**, *99*, 102592, doi:10.1016/j.ijadhadh.2020.102592.
8. Wang, Z.; Xian, G. Cohesive Zone Model Prediction of Debonding Failure in CFRP-to-Steel Bonded Interface with a Ductile Adhesive. *Composites Science and Technology* **2022**, *230*, 109315, doi:10.1016/j.compscitech.2022.109315.
9. Xu, L.Y.; Lu, J.R.; Li, K.M.; Hu, J. Experimental Study of CFRP Laser Surface Modification and Bonding Characteristics of CFRP/Al6061 Heterogeneous Joints. *Composite Structures* **2022**, *283*, 115030, doi:10.1016/j.compstruct.2021.115030.

10. Gursel, A.; Yildiz, S. Surface Preparation and Activation Only by Abrasion and Its Effect on Adhesion Strength. *Journal of Adhesion and Interface* **2022**, *23*, 101–107, doi:10.17702/JAI.2022.23.4.101.

11. Nguyen, V.-T.; Fang, T.-H. Molecular Dynamics Simulation of Abrasive Characteristics and Interfaces in Chemical Mechanical Polishing. *Applied Surface Science* **2020**, *509*, 144676, doi:10.1016/j.apsusc.2019.144676.

12. Golru, S.S.; Attar, M.M.; Ramezanzadeh, B. Effects of Different Surface Cleaning Procedures on the Superficial Morphology and the Adhesive Strength of Epoxy Coating on Aluminium Alloy 1050. *Progress in Organic Coatings* **2015**, *87*, 52–60, doi:10.1016/j.porgcoat.2015.05.005.

13. Hung, K.-Y.; Lin, Y.-C.; Feng, H.-P. The Effects of Acid Etching on the Nanomorphological Surface Characteristics and Activation Energy of Titanium Medical Materials. *Materials* **2017**, *10*, 1164, doi:10.3390/ma10101164.

14. Saleema, N.; Gallant, D. Atmospheric Pressure Plasma Oxidation of AA6061-T6 Aluminum Alloy Surface for Strong and Durable Adhesive Bonding Applications. *Applied Surface Science* **2013**, *282*, 98–104, doi:10.1016/j.apsusc.2013.05.064.

15. Yetim, A.F.; Kovacı, H.; Uzun, Y.; Tekdir, H.; Çelik, A. A Comprehensive Study on the Fatigue Properties of Duplex Surface Treated Ti6Al4V by Plasma Nitriding and DLC Coating. *Surface and Coatings Technology* **2023**, *458*, 129367, doi:10.1016/j.surfcoat.2023.129367.

16. Altan, B.; Cinar, S.; Tuncelli, B. Evaluation of Shear Bond Strength of Zirconia-Based Monolithic CAD-CAM Materials to Resin Cement after Different Surface Treatments. *Niger J Clin Pract* **2019**, *22*, 1475, doi:10.4103/njcp.njcp_157_19.

17. Erdur, E.A.; Basciftci, F.A. Effect of Ti:Sapphire Laser on Shear Bond Strength of Orthodontic Brackets to Ceramic Surfaces: EFFECT OF TI:SAPPHIRE LASER ON CERAMIC SURFACES. *Lasers Surg. Med.* **2015**, *47*, 512–519, doi:10.1002/lsm.22371.

18. Henriques, B.; Sampaio, M.; Buciumeanu, M.; Souza, J.C.M.; Gomes, J.R.; Silva, F.; Carvalho, O. Laser Surface Structuring of Ti6Al4V Substrates for Adhesion Enhancement in Ti6Al4V-PEEK Joints. *Materials Science and Engineering: C* **2017**, *79*, 177–184, doi:10.1016/j.msec.2017.04.157.

19. Rechner, R.; Jansen, I.; Beyer, E. Influence on the Strength and Aging Resistance of Aluminium Joints by Laser Pre-Treatment and Surface Modification. *International Journal of Adhesion and Adhesives* **2010**, *30*, 595–601, doi:10.1016/j.ijadhadh.2010.05.009.

20. Arenas, J.M.; Alía, C.; Narbón, J.J.; Ocaña, R.; González, C. Considerations for the Industrial Application of Structural Adhesive Joints in the Aluminium–Composite Material Bonding. *Composites Part B: Engineering* **2013**, *44*, 417–423, doi:10.1016/j.compositesb.2012.04.026.

21. Rotella, G.; Alfano, M.; Schiefer, T.; Jansen, I. Enhancement of Static Strength and Long Term Durability of Steel/Epoxy Joints through a Fiber Laser Surface Pre-Treatment. *International Journal of Adhesion and Adhesives* **2015**, *63*, 87–95, doi:10.1016/j.ijadhadh.2015.08.009.

22. Lei, Z.; Tian, Z.; Chen, X.; Chen, Y.; Bi, J.; Wu, S.; Sun, H. Large Spot Diameter Nanosecond Laser Treatment of Aluminum Alloy Sheets for High-Speed Superhydrophobic Hierarchical Micro- and Nanostructured Surface Preparation. *Surface and Coatings Technology* **2019**, *361*, 249–254, doi:10.1016/j.surfcoat.2019.01.020.

23. Rzeczkowski, P.; Krause, B.; Pötschke, P. Characterization of Highly Filled PP/Graphite Composites for Adhesive Joining in Fuel Cell Applications. *Polymers* **2019**, *11*, 462, doi:10.3390/polym11030462.

24. Spadaro, C.; Sunseri, C.; Dispenza, C. Laser Surface Treatments for Adhesion Improvement of Aluminium Alloys Structural Joints. *Radiation Physics and Chemistry* **2007**, *76*, 1441–1446, doi:10.1016/j.radphyschem.2007.02.047.

25. Scaramuzza, S.; Agnoli, S.; Amendola, V. Metastable Alloy Nanoparticles, Metal-Oxide Nanocrescents and Nanoshells Generated by Laser Ablation in Liquid Solution: Influence of the Chemical Environment on Structure and Composition. *Phys. Chem. Chem. Phys.* **2015**, *17*, 28076–28087, doi:10.1039/C5CP00279F.

26. Dittrich, S.; Spellauge, M.; Barcikowski, S.; Huber, H.P.; Gökce, B.; Technical Chemistry I and Center of Nanointegration Duisburg-Essen (CENIDE), University of Duisburg-Essen, Universitaetsstr. 7, 45141 Essen, Germany; Department of Applied Sciences and Mechatronics, Munich University of Applied Sciences, Lothstr. 34, 80335 Munich, Germany; Materials Science and Additive Manufacturing, School of Mechanical Engineering and Safety Engineering, University of Wuppertal, Gaußstraße 20, 42119 Wuppertal, Germany Time Resolved Studies Reveal the Origin of the Unparalleled High Efficiency of One Nanosecond Laser Ablation in Liquids. *OEA* **2022**, *5*, 210053–210053, doi:10.29026/oea.2022.210053.

27. Chen, M.; Wang, X.; Qi, D.; Deng, H.; Liu, Y.; Shen, X. Temperature Field Simulation of Chalcogenide Glass Ablation by Nanosecond Pulsed Laser-Based on Pump–Probe Technology. *Optics & Laser Technology* **2022**, *149*, 107771, doi:10.1016/j.optlastec.2021.107771.

28. Ndubuisi, A.; Abouali, S.; Singh, K.; Thangadurai, V. Recent Advances, Practical Challenges, and Perspectives of Intermediate Temperature Solid Oxide Fuel Cell Cathodes. *J. Mater. Chem. A* **2022**, *10*, 2196–2227, doi:10.1039/D1TA08475E.

29. Zhu, K.; Luo, B.; Liu, Z.; Wen, X. Recent Advances and Prospects of Symmetrical Solid Oxide Fuel Cells. *Ceramics International* **2022**, *48*, 8972–8986, doi:10.1016/j.ceramint.2022.01.258.

30. Zarabi Golkhatmi, S.; Asghar, M.I.; Lund, P.D. A Review on Solid Oxide Fuel Cell Durability: Latest Progress, Mechanisms, and Study Tools. *Renewable and Sustainable Energy Reviews* **2022**, *161*, 112339, doi:10.1016/j.rser.2022.112339.

31. Afroze, S.; Reza, M.S.; Amin, M.R.; Taweekun, J.; Azad, A.K. Progress in Nanomaterials Fabrication and Their Prospects in Artificial Intelligence towards Solid Oxide Fuel Cells: A Review. *International Journal of Hydrogen Energy* **2022**, S0360319922056944, doi:10.1016/j.ijhydene.2022.11.335.

32. Kumar, P.; Singh, O. A Review of Solid Oxide Fuel Cell Based Hybrid Cycles. *Intl J of Energy Research* **2022**, *46*, 8560–8589, doi:10.1002/er.7766.

33. Eziashi, J.J.; Key, C.; Smith, R.; Amendola, R.; Gannon, P.E.; Froitzheim, J. Measuring Cr Volatility from Ferritic Stainless Steels: Novel and Conventional Methods Compared. *ECS Trans.* **2013**, *50*, 43–49, doi:10.1149/05044.0043ecst.

34. Peksen, M.; Al-Masri, A.; Blum, L.; Stolten, D. 3D Transient Thermomechanical Behaviour of a Full Scale SOFC Short Stack. *International Journal of Hydrogen Energy* **2013**, *38*, 4099–4107, doi:10.1016/j.ijhydene.2013.01.072.

35. Jiang, W.; Zhang, Y.-C.; Zhang, W.Y.; Luo, Y.; Woo, W.; Tu, S.T. Growth and Residual Stresses in the Bonded Compliant Seal of Planar Solid Oxide Fuel Cell: Thickness Design of Window Frame. *Materials & Design* **2016**, *93*, 53–62, doi:10.1016/j.matdes.2015.12.145.

36. Lin, C.-K.; Lin, T.-W.; Wu, S.-H.; Shiu, W.-H.; Liu, C.-K.; Lee, R.-Y. Creep Rupture of the Joint between a Glass-Ceramic Sealant and Lanthanum Strontium Manganite-Coated Ferritic Stainless Steel Interconnect for Solid Oxide Fuel Cells. *Journal of the European Ceramic Society* **2018**, *38*, 2417–2429, doi:10.1016/j.jeurceramsoc.2018.01.016.

37. Rodríguez-López, S.; Wei, J.; Laurenti, K.C.; Mathias, I.; Justo, V.M.; Serbena, F.C.; Baudín, C.; Malzbender, J.; Pascual, M.J. Mechanical Properties of Solid Oxide Fuel Cell Glass-Ceramic Sealants in the System

BaO/SrO-MgO-B2O3-SiO2. *Journal of the European Ceramic Society* **2017**, *37*, 3579–3594, doi:10.1016/j.jeurceramsoc.2017.03.054.

38. Reddy, M.J.; Kamecki, B.; Talic, B.; Zanchi, E.; Smeacetto, F.; Hardy, J.S.; Choi, J.P.; Mazur, Ł.; Vaßen, R.; Basu, S.N.; et al. Experimental Review of the Performances of Protective Coatings for Interconnects in Solid Oxide Fuel Cells. *Journal of Power Sources* **2023**, *568*, 232831, doi:10.1016/j.jpowsour.2023.232831.
39. Sahu, A.K.; Malhotra, J.; Jha, S. Laser-Based Hybrid Micromachining Processes: A Review. *Optics & Laser Technology* **2022**, *146*, 107554, doi:10.1016/j.optlastec.2021.107554.
40. Lu, Z.; Wang, M.; Zhang, P.; Li, C. Femtosecond Laser Machining of Flexible Printed Circuit Boards. *J. Phys.: Conf. Ser.* **2022**, *2185*, 012082, doi:10.1088/1742-6596/2185/1/012082.
41. Clabel H., J.L.; P., K.T.; Marega, E.; M., C.R. Patterning of BaTiO3:Er/Yb Perovskite Films Using Fs-Laser Micromachining to Photonics Devices. In Proceedings of the Latin America Optics and Photonics (LAOP) Conference 2022; Optica Publishing Group: Recife, 2022; p. Tu1C.1.
42. Lee, H.; Kim, U.S.; Kim, S.D.; Woo, S.K.; Chung, W.J. SiO2–B2O3-BaO-WO3 Glasses with Varying Al2O3 Content as a Sealing Material for Reversible Solid Oxide Fuel Cells. *Ceramics International* **2020**, *46*, 18256–18261, doi:10.1016/j.ceramint.2020.04.148.
43. Kumar, D.; Sarkar, N.S.; Acherjee, B.; Kuar, A.S. Beam Wobbling Effects on Laser Transmission Welding of Dissimilar Polymers: Experiments, Modeling, and Process Optimization. *Optics & Laser Technology* **2022**, *146*, 107603, doi:10.1016/j.optlastec.2021.107603.
44. Ren, N.; Gao, F.; Wang, H.; Xia, K.; Song, S.; Yang, H. Water-Induced Effect on Femtosecond Laser Layered Ring Trepanning in Silicon Carbide Ceramic Sheets Using Low-to-High Pulse Repetition Rate. *Optics Communications* **2021**, *496*, 127040, doi:10.1016/j.optcom.2021.127040.
45. Zhou, Y.; Li, X.; Wu, W.; Jiang, Y.; Fan, R.; Chen, D.; Yan, R. 500 Hz, 47.1 mJ, Sub-Nanosecond MOPA Laser System. *Optics & Laser Technology* **2021**, *134*, 106592, doi:10.1016/j.optlastec.2020.106592.
46. Lu, Y.; Shi, X.; Huang, Z.; Li, T.; Zhang, M.; Czajkowski, J.; Fabritius, T.; Huttula, M.; Cao, W. Nanosecond Laser Coloration on Stainless Steel Surface. *Sci Rep* **2017**, *7*, 7092, doi:10.1038/s41598-017-07373-8.
47. Xing, Y.; Liu, L.; Wu, Z.; Wang, X.; Huang, P.; Tang, L. Fabrication and Characterization of Micro-Channels on Al2O3/TiC Ceramic Produced by Nanosecond Laser. *Ceramics International* **2018**, *44*, 23035–23044, doi:10.1016/j.ceramint.2018.09.106.

48. Yuan, P.; Gu, D. Molten Pool Behaviour and Its Physical Mechanism during Selective Laser Melting of TiC/AlSi10Mg Nanocomposites: Simulation and Experiments. *J. Phys. D: Appl. Phys.* **2015**, *48*, 035303, doi:10.1088/0022-3727/48/3/035303.

49. Antony, K.; Arivazhagan, N. STUDIES ON ENERGY PENETRATION AND MARANGONI EFFECT DURING LASER MELTING PROCESS. **2015**, *10*.

50. Elsied, A.M.; Dieffenbach, P.C.; Diwakar, P.K.; Hassanein, A. Nanosecond Laser-Metal Ablation at Different Ambient Conditions. *Spectrochimica Acta Part B: Atomic Spectroscopy* **2018**, *143*, 26–31, doi:10.1016/j.sab.2018.02.012.

51. Cao, Z.; Ouyang, Z.; Liu, Z.; Li, Y.; Ouyang, Y.; Lin, J.; Xie, X.; Long, J. Effects of Surface Oxides and Nanostructures on the Spontaneous Wettability Transition of Laser-Textured Copper Surfaces. *Applied Surface Science* **2021**, *560*, 150021, doi:10.1016/j.apsusc.2021.150021.

52. Radhakrishnan, J.; Diaz, M.; Cordovilla, F.; Ocaña, J.L. Tunable Superhydrophobic Titanium Nitride Surface by Ultrafast Laser Processing. *Ceramics International* **2022**, *48*, 37264–37274, doi:10.1016/j.ceramint.2022.08.304.

53. Abrego Serrano, P.A.; Kim, M.; Kim, D.-R.; Kim, D.-H.; Kim, G.-H.; Ahn, S.-H. Spherical Mirror and Surface Patterning on Silicon Carbide (SiC) by Material Removal Rate Enhancement Using CO2 Laser Assisted Polishing. *Int. J. Precis. Eng. Manuf.* **2020**, *21*, 775–785, doi:10.1007/s12541-019-00304-9.

54. Smeacetto, F.; Zanchi, E.; Meena Narayana Menon, D.; Janner, D.; Lamnini, S.; Salvo, M.; De La Pierre, S.; Javed, H.; Ferraris, M. Torsional Behaviour of Glass-Joined, Laser-Processed Crofer 22 APU Interconnect: Unravelling the Effect of Surface Roughness on the Shear Strength. *Ceramics International* **2022**, *48*, 32837–32843, doi:10.1016/j.ceramint.2022.07.210.

55. Mir, A.H.; Ahmad, S. A Study on Fabrication of Silicon Nitride-Based Advanced Ceramic Composite Materials via Spark Plasma Sintering. *Proceedings of the Institution of Mechanical Engineers, Part L: Journal of Materials: Design and Applications* **2021**, *235*, 1739–1756, doi:10.1177/14644207211013560.

56. Li, S.; Chen, H.; Wang, W.; Yao, D.; Xia, Y.; Zeng, Y. Effects of Y_2O_3/MgO Ratio on Mechanical Properties and Thermal Conductivity of Silicon Nitride Ceramics. *Int J Applied Ceramic Tech* **2022**, ijac.14067, doi:10.1111/ijac.14067.

57. Dresch, A.B.; Venturini, J.; Bergmann, C.P. Improving the Flexural-Strength-to-Density Ratio in Alumina Ceramics with the Addition of Silicon

Nitride. *Ceramics International* **2021**, *47*, 3964–3971, doi:10.1016/j.ceramint.2020.09.260.

58. Qian, H.; Chen, S.; Wang, T.; Cheng, G.; Chen, X.; Xu, Z.; Zeng, Q.; Liu, Y.; Yan, D. Silicon Nitride Modified Enamel Coatings Enable High Thermal Shock and Corrosion Resistances for Steel Protection. *Surface and Coatings Technology* **2021**, *421*, 127474, doi:10.1016/j.surfcoat.2021.127474.
59. Chen, M.; Wang, H.; Jin, H.; Pan, X.; Jin, Z. Effect of Pores on Crack Propagation Behavior for Porous Si3N4 Ceramics. *Ceramics International* **2016**, *42*, 5642–5649, doi:10.1016/j.ceramint.2015.12.086.
60. Yu, X.; Jiang, L.; Luan, Q.; Cai, Y.; Song, Q.; Wang, B.; Liu, Z. Investigation of Mechanism and Surface Morphology on the Femtosecond Laser Ablation of Silicon Nitride under Different Auxiliary Processing Environments. *Ceramics International* **2023**, *49*, 13425–13434, doi:10.1016/j.ceramint.2022.12.217.
61. Azarhoushang, B.; Soltani, B.; Zahedi, A. Laser-Assisted Grinding of Silicon Nitride by Picosecond Laser. *Int J Adv Manuf Technol* **2017**, *93*, 2517–2529, doi:10.1007/s00170-017-0440-9.

Chapter 4

Laser Micromachining of Bioresorbable Glass

4.1 Glass Processing: A Brief Introduction

Glass production has long been practiced by humans, with the earliest known reference dating back to 5000B.C. in Syria by Phoenician merchants [1]. Archeological surveys suggest the presence of man-made glass as early as 1500 BC In Egypt and Mesopotamia [2]. Since then, glass materials have been present for various applications, ranging from household, building, and industrial applications. Their optical transparency, chemical inertness, and hardness make them attractive for various applications [3].

The most common glass types comprise soda-lime, quartz, and borosilicate. Due to its large presence in our daily life, glass processing is a well-established sector with many available techniques to bulk process glass materials through cutting and machining. Common industrial scale techniques for glass processing include abrasive jet machining, milling, laser cutting, diamond cutting and dicing, as shown in Figure 4.1 [4–6].

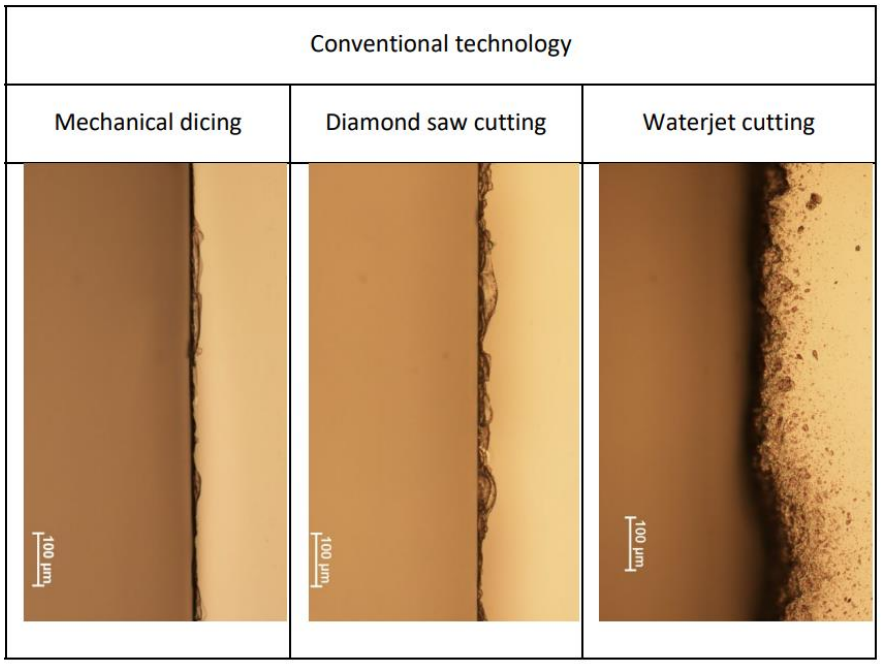

Figure 4.1. Micrographs of glass cutting performed with different conventional techniques **[7]**.

Apart from the traditional use, the past few decades have seen glass materials receive a renewed interest for their applications in the fields of fiber optical communications, micro-electromechanical systems (MEMS), opto-electronics, microfluidics, and biomedical applications [8–11]. These applications are relatively new and drove the need for better, more precise, and scalable micro-/nano-fabrication techniques. In this aspect, the conventional glass processing techniques manifests significant drawbacks such as brittle fractures and micro-cracks along the machined path [12]. The formation of these features is highly detrimental to the intended performance quality of the product. Therefore, serious attention has been devoted to developing new competent techniques for the microfabrication of glass materials.

In this context, some of the non-conventional techniques used for the microprocessing of glass materials are briefly discussed in the following:

Photolithography: It is an established technique for micro processing of glass substrates [13,14]. The technique involves using short-wavelength UV light to transfer a specific pattern using a photomask onto a light-sensitive photoresist with which the glass surface is coated. A treatment is then used to either chemically engrave the exposed pattern or deposit a thin film in a desired pattern. However, the fabrication process involves a relatively complex, multi-step

procedure to obtain the desired features, hence time-consuming and expensive. Furthermore, the technique also requires a dedicated clean room environment for fabrication [15,16].

Micro-milling: As a widely used fabrication technique, it is a direct scale-down of the macro-scale milling process. It is a precise technique offering flexibility in the type of processing materials ranging from metals, composites to polymers [17]. However, the technique faces a few disadvantages, such as tool wear or breakage, large processing time, burr formation, and inadequate finishing surface quality [18].

Ultrasonic machining: The technique is widely used for micro-processing hard and brittle materials [19]. This technique uses an abrasive material suspended in a solution forming a slurry that locally performs glass etching, in the presence of an ultrasonic source/head. The major drawback associated with this technique is the processing time and tool wear, as the abrasive particle is in contact with both the workpiece and the tool [20].

Electrochemical discharge machining (ECDM): In this technique, an electrochemical reaction is facilitated between the electrode and the workpiece, which generates a spark on the latter. The workpiece is immersed in an appropriate electrolyte, and the applied potential difference cause the formation of an oxide layer on the workpiece surface that cause micro-explosions resulting in material removal from the surface [21], as shown in Figure 4.2. This technique, however, faces the disadvantages of inaccurate and inconsistent machining as the depth increases and high-power consumption.

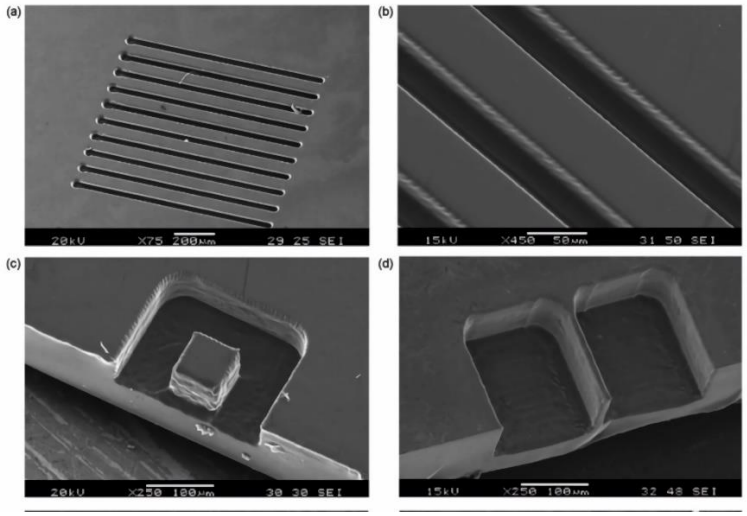

Figure 4.2. Micro-grooves; (c) micro-pillar; (d) micro-walls machined on a glass substrate using the ECDM method (KOH 30%) **[22]**.

Compared to the techniques mentioned above, laser micromachining offers a flexible and relatively inexpensive method for the microfabrication of glass materials [23,24]. The industrial setting has long used laser machining for drilling, cutting, and welding applications. Most common among the different available laser types are the CO_2 and NIR fiber laser systems that have high average power and can generate sufficient thermal energy to perform the machining of materials [25]. However, in the case of machining transparent glass materials, traditional laser processing using long wavelength beams cannot achieve high precision machining. The following briefly points out the challenges involved in machining glass using conventional laser machining:

(1) Glass materials have a broad transparency window, especially in the visible and NIR region. Thus, the linear optical processing of glass would therefore resort to the ultraviolet wavelength for precision laser glass processing.

(2) The hard and brittle nature of glass makes it difficult process it with continuous lasers due to the generation of local mechanical stress caused by thermal gradients formed even over short time scales.

(3) Glass based functional devices are of recent interest for lab on a chip application. The fabrication of microfluidic and optical components on glasses

requires clean surface/bulk processing, therefore the use of common industrially used CO_2 and IR lasers is a challenge by itself due to the nature of glass materials.

Ultrafast lasers offer an excellent solution to the challenges mentioned above through their precise and bulk processing ability, as shown in Figure 4.3 [26,27]. However, the cost and processing speed factor hinders their large-scale fabrication use. Therefore, many applications have resorted to nanosecond ultraviolet lasers for glass processing [28]. Alternatively, researchers have used relatively transparent NIR wavelength with an intermediate absorbent medium, such as a metal thin film or ions dispersed in a liquid medium, which acts as a sacrificial layer for energy absorption and thermal transfer to the nearby glass material [29,30]. The following section describes the direct and indirect techniques for processing glasses using UV-VIS-NIR wavelength-based nanosecond laser.

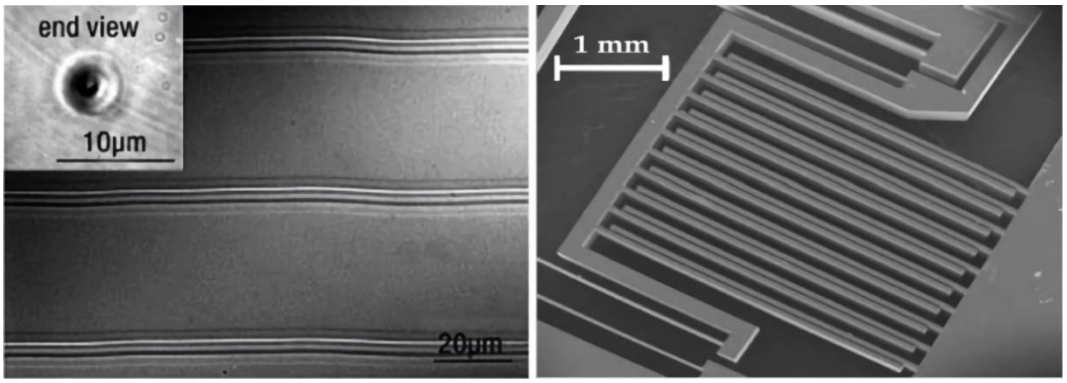

Figure 4.3. Optical micrograph of an oscillator-only femtosecond laser machined waveguide inside borosilicate glass. Inset shows the waveguide end-face [6]. SEM image of a micro-actuator fabricated on a fused silica by femtosecond laser and chemical etching **[30]**.

4.1.1 UV Nanosecond laser modification of glass

Typically, oxide glass materials have absorption bands in the UV region. This corresponds to a linear absorption process that UV lasers can exploit for processing. Amongst the different glass compositions known, silica-based glasses are the most used. Pure silica shows good UV transmittance properties, with first absorption occurring at about 10.2eV (122nm). Thus, laser modification of fused silica glasses is generally performed through a non-linear absorption process using ultrafast laser systems [31]. However, in the case of addition of modifier oxides such as Na_2O, BaO, CaO, Li_2O, the modifiers break up the glass network, simultaneously increasing the concentration of non-bridging oxygen atoms and the relatively mobile metal ion. The introduction of various metal oxides, alkali

ions, and transition metal atoms causes the shifting of absorption peaks towards the longer wavelengths, hence the possibility of machining at UV wavelengths. For example, the band gap of soda lime glass is ~3.5eV(355nm). The greater absorption at the UV wavelengths would cause the material modification to proceed through melting, vaporization, and plasma formation, as shown in Figure 4.4.

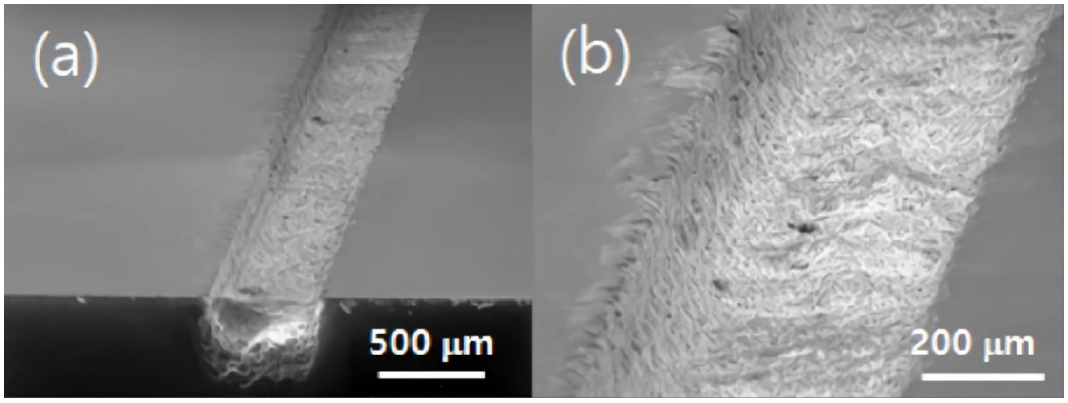

Figure 4.4. SEM image of groove generated on soda-lime glass through multiple scans using a UV nanosecond laser (355 nm) **[32]**.

4.1.2 Laser-induced plasma-assisted ablation

Laser-induced plasma-assisted ablation (LIPAA) was introduced to perform quality micromachining on glass substrates even with visible and infrared wavelengths. For linear absorption-based modification, the transparency window would need high laser power and intensity to perform modifications which would invariably cause micro-cracks and unpredictable surface damages. The principle of LIPAA leverages the laser beam passing through a transparent material and focusing on an absorbing substrate, e.g., a thin metal sheet, close to its surface. The plasma generation resulting from metal ablation in the vicinity of the transparent material would interact and, in turn, modify the transparent material, as shown in Figure 4.5 [33,34]. As a direct consequence of the processing settings, along with the laser parameters, the distance of the transparent substrate from the metal target would influence the dimension of the generated micro features. T.U. Rahman et al. studied the effect of laser fluence on the variation in the size of micro-craters during LIPAA. The plasma characteristics were investigated using optical emission spectroscopy, and the laser fluence effect on micro-feature was demonstrated to be dependent on electron temperature and

electron density in the plasma [35]. C. Pan et al. combined LIPAA along with chemical etching to fabricate microfluidic channels on soda lime glass [36].

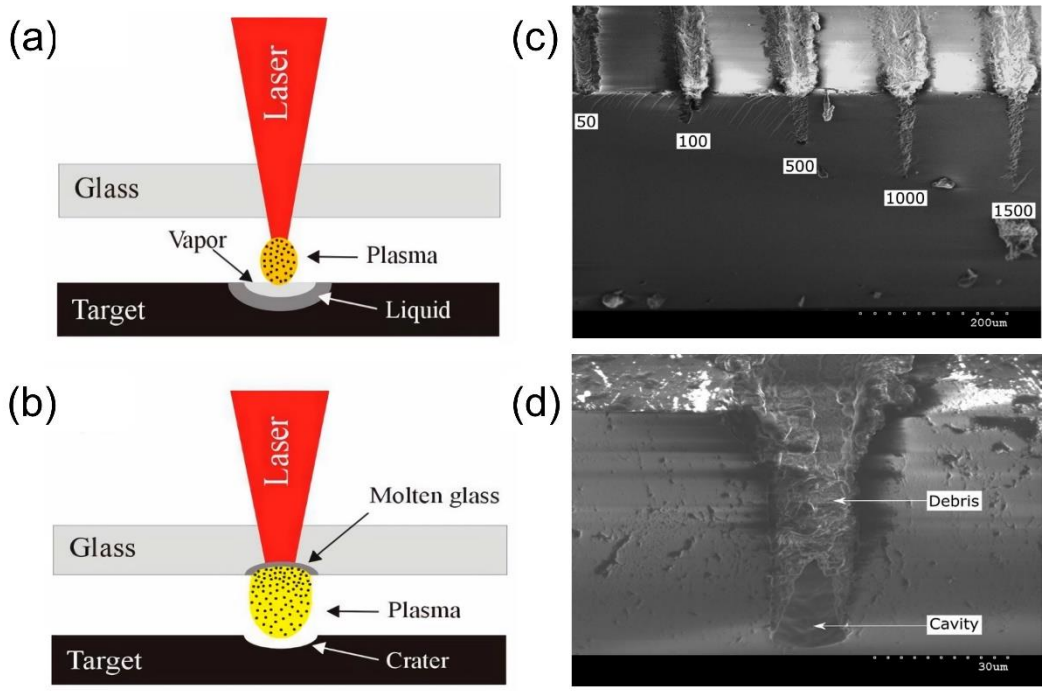

Figure 4.5. (a,b) Schematic illustration depicting LIPAA (a) laser ablation of the target material; (b) isothermal plume expansion and subsequent interaction with the glass substrate ; (c) cross-section SEM images of laser engravings on sapphire substrate at different pulse number; (d) magnified image depicting debris and accumulation **[36]**.

4.1.3 Laser-induced backside etching

Laser-induced backside (LIBE) etching works on a principle similar to LIPAA. However, in this case, the absorbing material is in contact with the backside of the transparent substrate. Based on the absorbing medium, the LIBE technique can be of two types: LIBDE or LIBWE, where DE and WE stand for dry etching and wet etching, respectively. In the LIBDE technique, the absorbing material is in the form of a metal film. In contrast, in the latter case, the transparent substrate is placed in contact with an absorbing liquid for the corresponding laser wavelength. Kwon et al. proposed a novel laser scanning method along with the LIBWE process avoiding the detrimental effect of bubble formation and geometrical error caused such as overlapping of scan lines and uneven laser irradiation distribution. The finally generated micro-structures

exhibited minimal shape errors and desired surface roughness [37]. Another study proposed an enhancement in the quality of the NIR laser based LIBWE of microstructures by adding phosphoric acid to the absorbent to prevent crack generation in the laser modification. As a result of phosphoric acid addition, the maximum machining depth could be increased fivefold, generating high aspect ratio micro-features, as shown in Figure 4.6.

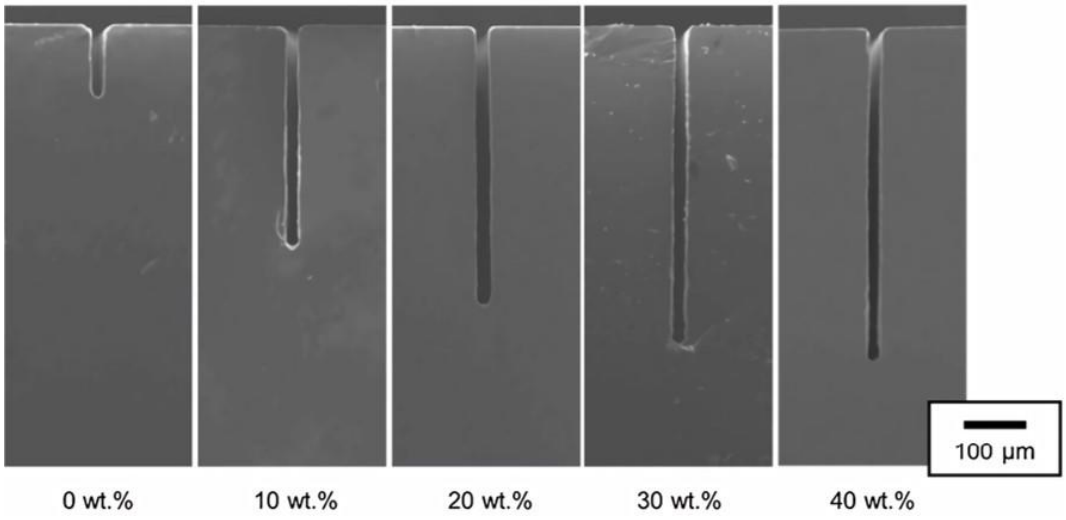

Figure 4.6. SEM images of LIBWE machined channels in soda lime glass substrate using copper sulfate absorbent solution with varying concentrations of phosphoric acid content **[37]**.

4.1.4 Infrared nanosecond laser processing of calcium phosphate glass

The techniques presented so far enable surface modifications on transparent materials in a relatively inexpensive manner, being also more suitable for large-scale fabrication. In this context, the study of the current thesis is focused on the use of an infrared nanosecond laser to perform surface modification. This type of laser processing is the cheaper and more viable option in an industrial scenario. Moreover, the laser employed in this work is a commercial model normally used for marking in production lines.

The material used for processing is a Cu-doped bioresorbable calcium phosphate glass (CaPh). The CaPh glass has been developed by our research group over the last decade [38–40]. Its potential use in biomedical applications and its antimicrobial properties drove the research towards the study of microfabrication of this type of soft glass. The thesis work on this topic can be

divided into two phases: a fundamental and an application phase. In the first stage, a primary study was conducted to explore the laser induced modifications on the CaPh glass and to identify the suitable laser parameters for controlled fabrication of surface microfeatures in any desired pattern. In the second stage, appropriate laser parameters were used to fabricate high quality micro-optics on the anti-bacterial and bioresorbable CaPh glass surface. The ability to generate precise micro-features such as scaffolds and micro-optics on the glass surface, coupled with the interesting application prospects offered by the fiber drawable phosphate glass system, can represent a step towards to add to the devices based on this glass functionalities towards in-vivo theranostics.

4.2 Phosphate Glasses

Before diving into the experimental aspects of phosphate glass modifications with laser, we'll present an introduction to this material with an accent on its properties that will be useful to explain its behavior in the interaction with a laser. Glass systems based on silica matrix are the oldest and most common glass materials. Even though pure silica glass (fused silica) is available, silicate glasses generally have compounds such as soda, alumina, and potassium carbonate as part of the glass composition to increase their processability. These glasses represent the majority of manufactured glasses and have well-established applications in optics, fiber communication, construction, storage, and many more daily life applications. Even though silicate glasses are widely used, certain applications where characteristics like biocompatibility, resorbability and optical amplification demand better performance are pushing for specialty glasses [41–43]. Hence, research on alternative glass compositions is an active topic of interest to the glass community.

4.2.1 Composition

In the phosphate glass system, phosphorous pentoxide (P_2O_5) is the primary glass former. Similar to the case of silicate glasses, depending on the intended application, various oxide compounds can be added during the preparation stage. However, an interesting difference between the phosphate and silicate-based glass systems is in the melting point. In fact, while additional components are typically added for silicate glasses to reduce the processing temperatures, in phosphate glasses other components are mixed to increase the durability of the glass system

[44,45]. Indeed, phosphate glasses exhibit the distinctive property of complete dissolution in aqueous media, offering use in biomedical applications [46]. However, their dissolution rates can be tailored through the addition of oxides [47,48].

P-tetrahedron PO_4 is the fundamental unit of the phosphate glass. The different properties of the resulting glass is primarily controlled by the number of bridging-oxygen atoms, which gives rise to the popular Q^n terminology, as depicted in Figure 4.7(a), where n represents the number of bridging oxygen atoms per tetrahedron. The structure of phosphate glasses could be depicted through various arrangements of the tetrahedron shown in the Figure 4.7(b). The vitreous form of phosphate glass is formed by the Q^3 groups where the $P = O$ bonds make the structure hydrophilic in the form of $P - OH$. In the presence of modifier oxides, $P - O - P$ bonds cleave to form $P - NBO$, where the modifier cation link to the terminal oxygen. Depending on the quantity of the modifier oxide, the metaphosphate form with O/P ratio as 3 is reached (MPO_3 , where M is a modifier). In this phase, only the Q^2 form exists. As the modifier content increase, Q^2 changes to Q^1 to eventually cause depolymerization of the structure until the orthophosphate (PO_4^{3-}) remains [49,50].

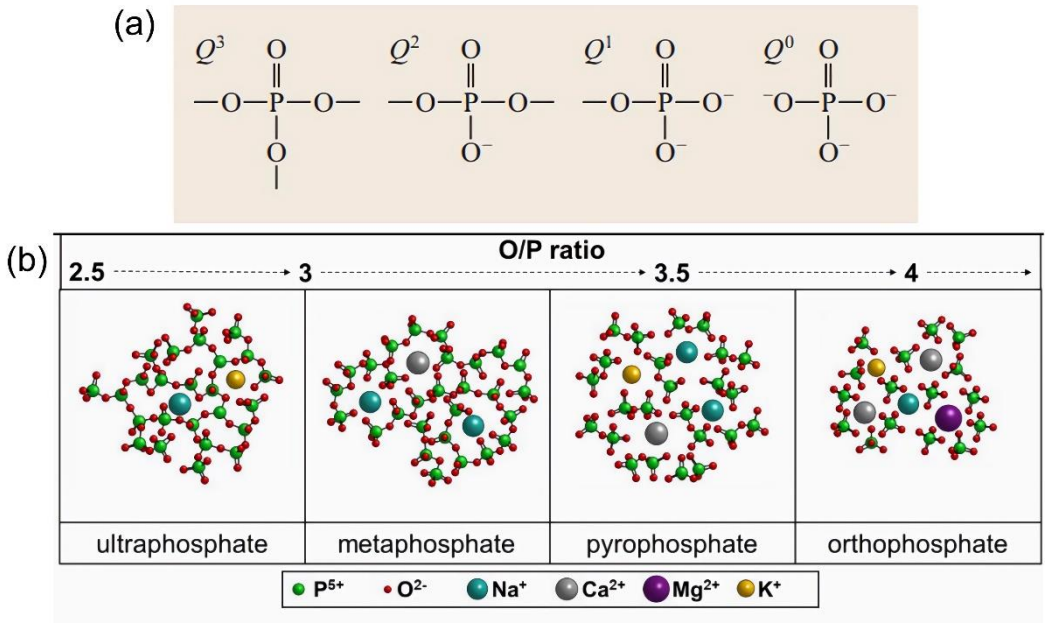

Figure 4.7. Representation of the building Qn units of the phosphate tetrahedron (a) and the corresponding matrix network based on differing O/P ratio **[1]**.

4.2.2 Applications of Phosphate Glass

Silicate-based bioactive glasses have traditionally been used for orthopedic and dental applications [51]. However, they face major limiting factors such as high crystallization tendency, limiting their use in porous scaffold fabrication. Also, these glasses were found to have low biodegradability, an undesirable factor for use in medical applications [52,53]. On the other hand, phosphate glass can be prepared to have a chemical composition mimicking parts of the mineral bone, and as shown in Figure 4.8 [54], they exhibit strong prospects for biomedical use, thanks to their biocompatibility and bioresorbable nature. A significant interest for phosphate glass involves their use in targeted tissue healing applications. The key benefit of phosphate systems is their regulated degradation rates, ion release, and cytocompatibility [55]. Apart from the variation of dissolution rates based on their composition, surface modifications were found to influence their dissolution rates to some extent [56].

Wettability and surface texture significantly influence protein adsorption or bacterial adhesion to a bioactive glass surface. In this approach, patternable surface texture could facilitate scaffolding by enabling the selective growth of a certain cell strain, such as organoids, while inhibiting the growth of potentially hazardous bacteria. Sol-gel-based bioactive glasses can be prepared with functional surface properties, besides the commonly available surface texturing techniques such as chemical etching, lithography, sandblasting, and electrochemical treatments [57–59]. In fact, they have micro-nano pores that increase surface area to better interact with the surrounding biological environment. However, compared to melt-quench synthesized glasses, sol-gel derived glasses exhibit significantly lower mechanical strength, which hinders their usability.

Phosphate glass systems present as an interesting host for laser gain medium. Their relatively open structure allows large amounts of rare earth ions to be incorporated without any clustering effects [60,61]. Also, they are well suited as solid-state matrices for laser emission due to their large emission cross-section and low nonlinear refractive indices [62]. Due to their interesting properties, neodymium-doped phosphate glasses have been successfully used for crucial projects such as National Ignition Facility (NIF, USA) and the Shenguang project

(China). Furthermore, the possibility of fiber-drawing phosphate glass makes them interesting for fiber laser fabrication. Fiber laser technology has witnessed tremendous improvements in their efficient gain medium, innovative feedback loop based on Bragg gratings, and robust optical cavity. The high ionic solubility in the glass matrix supports reducing the device dimension for the same emission characteristics.

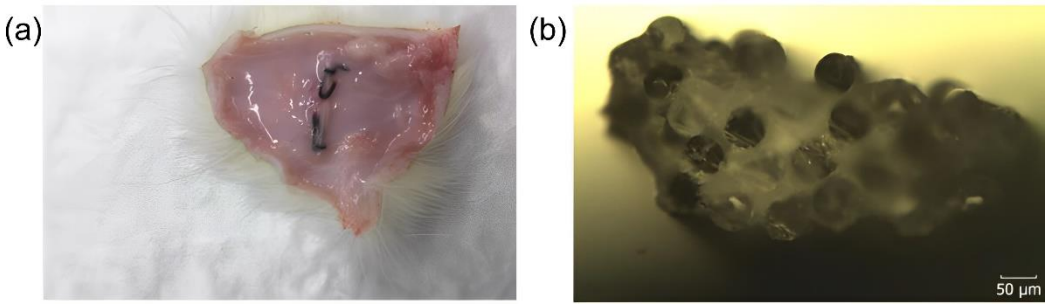

Figure 4.8. (a) Phosphate fibers in the subcutaneous tissue of a male rat; (b) micrograph of the implanted fiber bundle extracted after 4 weeks **[63]**.

4.2.3 Cu-doped antibacterial bioresorbable glass preparation

Biofilm formation on the surface of phosphate glass could hinder their dissolution rate in an aqueous solution posing chemical and technological limitations and eventually compromising the biological device. Thus, bioresorbable devices that can release anti-bacterial ions would be necessary to avoid such functional compromise.

The Environmental Protection Agency acknowledged copper as a metallic anti-microbial agent in 2008 [64]. Cu-doped materials provide interesting prospects and have seen a strong research interest for their use in bio-ceramics, biocomposites, biometallic materials, and bioactive glasses. Cu-doped phosphate glasses are an excellent platform for their use in biomedical applications, especially for implantable devices and bioscaffolds that can inhibit bacterial development and can support specialized cell cultures [65].

Another important factor is the quantity of antimicrobial ions since large numbers could significantly impact the dissolution rates and other thermo-mechanical and optical properties. Also, beyond a certain amount, the ions could be toxic to the surrounding tissues.

During this thesis work, the antibacterial glass was prepared using the conventional melt-quench technique, as shown in Figure 4.9. The weighing and mixing of the high-purity oxide and carbonate powder reagents were performed in the dry box under N_2 atmosphere to minimize the OH^- and impurity content during the glass preparation procedure. The weighed powder was then mixed overnight using an automatic mixing system to maintain the compositional homogeneity of reagents. The batched powder mixture was then placed in a quartz crucible. The quartz crucible was then heated to a temperature of $1200\,^{\circ}C$ for one hour under constant N_2 flux, to ensure complete fusion and homogenization of the formed glass mixture. The melt was then cast onto a cold metal plate (melt-quench) or a 8 mm diameter steel pre-heated mold. In case of the latter, it is important for the mold to be pre-heated to the precise temperature to prevent thermal stress formation in the final casted glass. Once cast into the final mold, the glass is annealed, which involves re-heating to the glass transition temperature $T_g = 443^{\circ}C$, and then stabilized at that temperature to release the generated internal thermal stress during the melt-quench procedure. The annealing was then performed at about the glass transition temperature for about $5\,h$ and was eventually cooled down to room temperature.

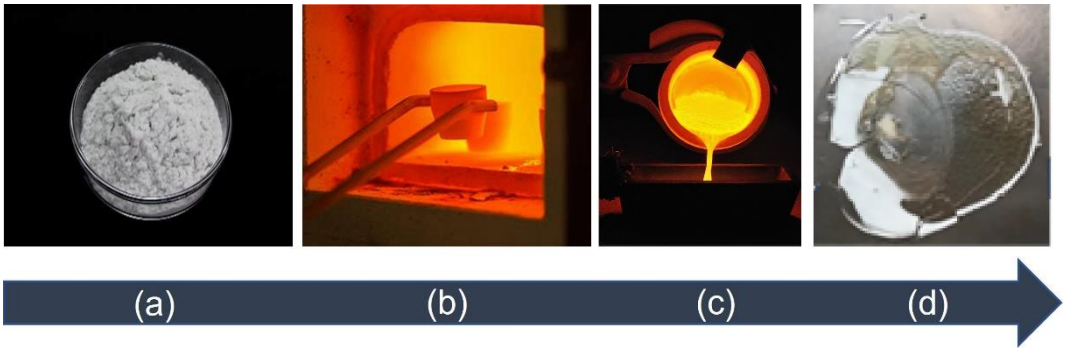

Figure 4.9. Schematics of the melt-quench technique from powder making to casting.

The molar composition of the Cu-doped CaPh glass used in this work is as follows (composition in $mol\%$): $[(50\,P_2O_5 - 25CaO - 8MgO - 11.5Na_2O - 2.5B_2O_3 - 3SiO_2)x - (CuO)y$, with $x = 1$, when $y = 0$ and $x = 0.99$ when $y = 1$. Figure 4.10 shows the prepared Cu-doped and undoped CaPh glass discs, obtained from the glass rods.

Figure 4.10. Circular disk-shaped samples of undoped (white) and Cu-doped (blue) calcium phosphate glasses, obtained from their corresponding glass rods.

After providing a brief introduction on various available techniques for glass processing, composition and application of phosphate glasses, the following sections focus on the obtained results and discussions based on nanosecond laser micromachining of the bioresorbable calcium phosphate glass fabricated by our research group.

4.3 Glass Characterization

After the glass fabrication, a primary optical and thermal characterization of the glass was performed. As previously mentioned, silicate glasses require either UV or nonlinear optical interaction, resulting in absorption and substrate modification. An understanding of the UV-to-NIR absorption by the glass system would help to determine the feasibility of laser processing at 1064nm. This is an important factor towards laser modification of glass in a precise and controlled manner using the optimal laser processing parameters. UV-VIS-NIR absorption spectroscopy was performed on both the Cu-doped and undoped glass substrates.

Figure 4.11 represents the UV-VIS-NIR absorption spectra of both glass samples. The undoped calcium phosphate glass does not absorb appreciably in the NIR wavelength. However, introducing the copper metal ions into the phosphate glass matrix would essentially reduce the bandgap. The enhanced absorption at

the infrared wavelength could be attributed to the Cu^{2+} ions in the octahedral coordination and facilitating intra-configuration $d-d$ transitions [66,67]. The NIR absorption for the doped glass in Figure 4.11 is coherent with the above explanation. The absorption characteristics of the doped glass confirms the possibility of processing the Cu-doped CaPh glass with the IR $(1064nm)$ nanosecond (ns) laser mentioned in this work. As for any glass system, the UV absorption edge is visible in the absorption spectra for both phosphate glasses. However, this thesis's work has focused on the possibility of using an industrial laser system to fabricate microstructures on the glass surface, compared to more expensive UV ns or ultrafast laser systems.

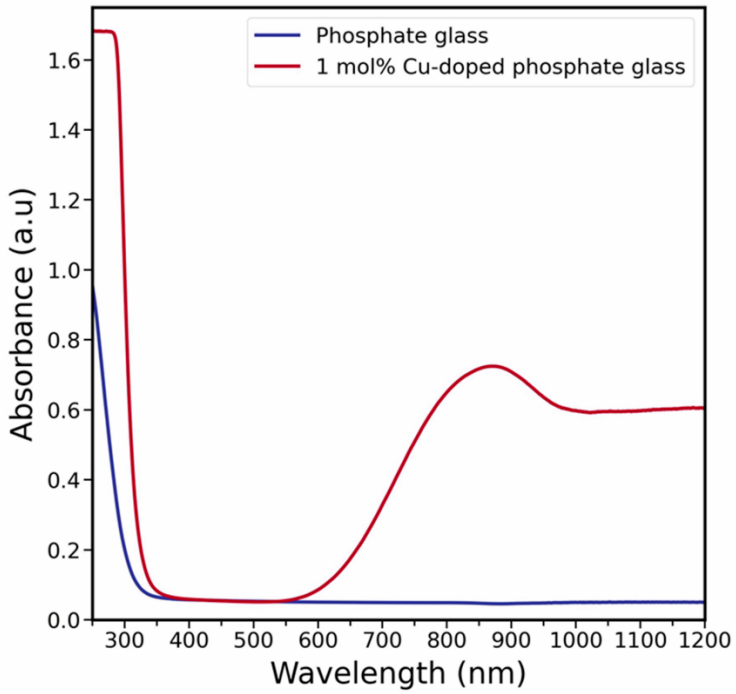

Figure 4.11. UV-VIS-NIR absorption spectra of the undoped and Cu-doped calcium phosphate glasses.

Choosing the right composition of the glass system is pivotal for its intended performance. Our research group has been working towards optimizing the phosphate glass composition for various optical and biomedical applications. As a result, the thermal analysis of the fabricated glass has been previously performed. Figure 4.12 shows the DTA analysis curve of the different antibacterial ion doped CaPh glasses. In the case of Cu-doped glass, the glass transition temperature (T_g) is $443\,^{\circ}C$, whereas the undoped CaPh has a T_g of $437\,^{\circ}C$ with an error of $\pm 1\,^{\circ}C$.

The metal ion doping does not cause a major change in the glass transition temperature. Therefore, a combination of improved NIR absorbance along with glass transition temperature below $500\,°C$ would make it possible for laser ablation of the glass through a linear absorption mechanism at a wavelength of $1064\ nm$, corresponding to the laser emission.

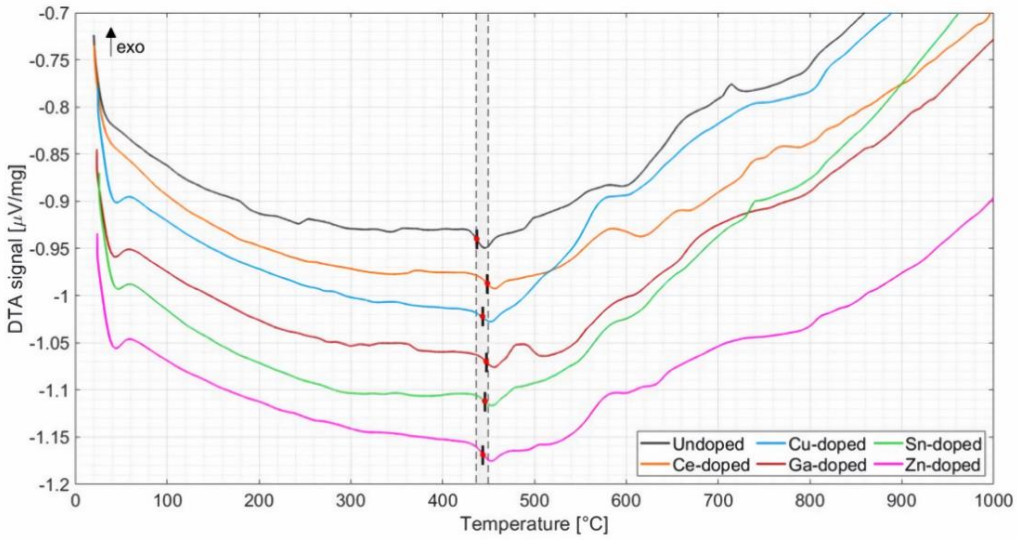

Figure 4.12. DTA curves of the bioresorbable phosphate glass with 1 mol% doping of different antibacterial metal ions. The shaded area represents Tg of the glasses.

4.4 Surface modification of Cu-doped CaPh glass

As a first step, the minimum required average laser power to cause visible modification on the glass substrate was determined. A pulsewidth of $4\ ns$ was fixed throughout the study to minimize the thermal effects and the HAZ [68], taking a cue from the optical and thermal characteristics of the glass previously discussed. Also, the pulse repetition rate (PRR) and the laser scan speed were fixed at $20\ kHz$ and $3\ mm/s$, respectively. As reference geometry, single scan lines were drawn on the glass surface to study the effect of the laser parameters on the surface modification.

An interesting feature was observed on inspection of the laser generated modification under optical microscope, as shown in Figure 4.13. At the power of laser operation, unlike the more common laser-induced effects [69], material removal did not occur in the laser interaction with the Cu-doped CaPh glass. On

the contrary, micro-protrusions were observed above the reference glass surface, all along the laser scan path. The formation of such micro-protrusions are previously reported in a few materials that experience a positive temperature coefficient of surface tension $d\gamma/dt$, also known as the Inverse Marangoni effect [70,71].

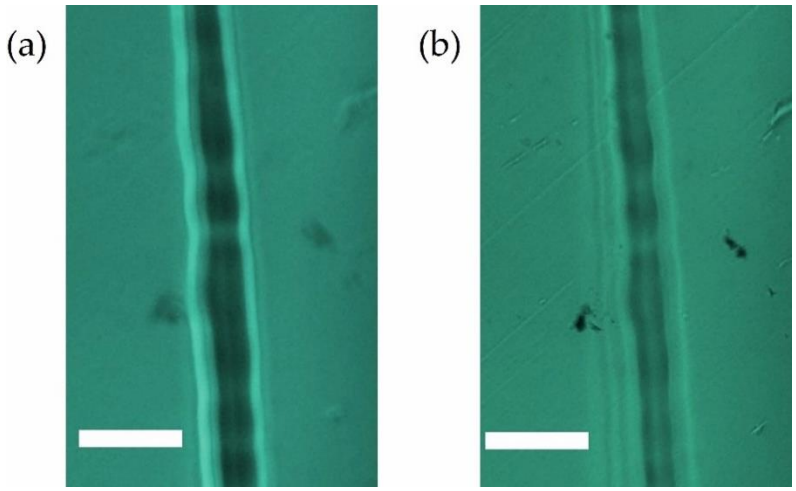

Figure 4.13. Micrographs of the laser modification on the CaPh glass at the same region but different focal planes. (a) focus on the laser modification above the glass surface; (b) focus on the unmodified glass surface. The scale bar represents 50 µm.

The laser pulse has a Gaussian profile at the focal spot, as shown in Figure 4.14(a,b). Therefore, beyond the minimal energy to cause glass melting, the gaussian distribution would invariably generate the highest temperature at the center of the focal spot/molten pool. Simultaneously, the positive $d\gamma/dt$ would result in the highest surface tension at the center of the molten pool. Hence, the temperature gradient would cause a radially inward flow of the glass melt towards the spot center, as depicted in Figure 4.14(c). Due to the volume constraint, the melt collected at the center rises upward, resulting in a micro-protrusion. Also, an inward recoil pressure effect exists due to the rapid vaporization of the melt as a result of the highest temperature at the center of the Gaussian [72]. To observe the micro-protrusion, the radial inward flow must overcome the recoil pressure effect that forces the rising liquid meltdown.

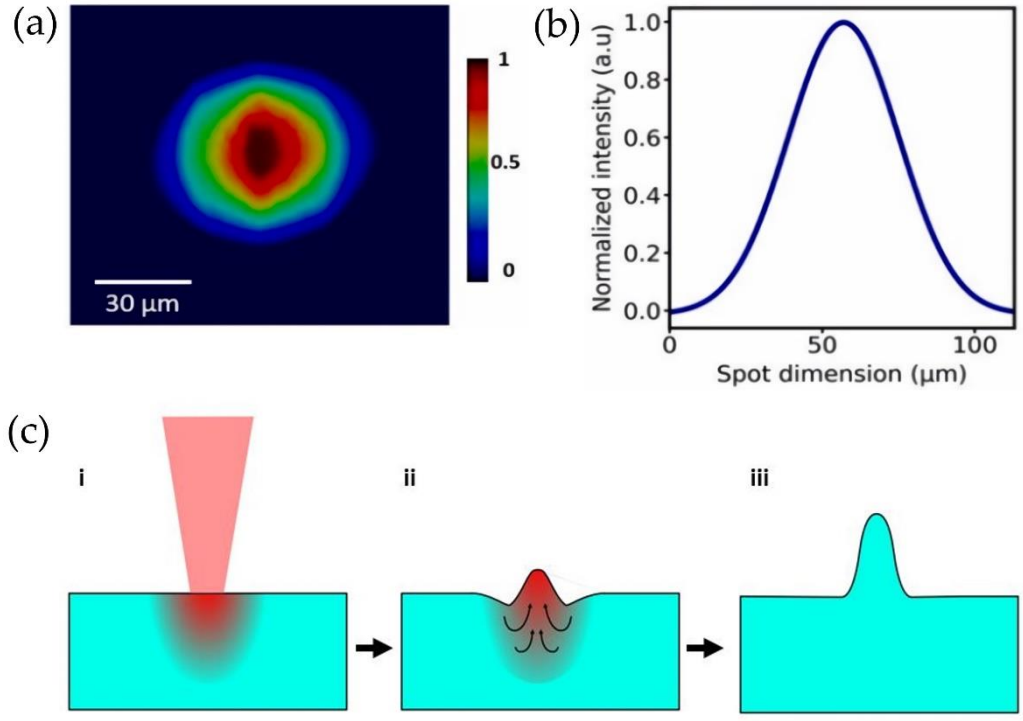

Figure 4.14. (a) Representation of the laser intensity distribution at the focal plane (colorbar represents normalized intensity); (b) plot of normalized intensity along the focal spot cross-section; (c) mechanism of the micro-protrusion formation: (i) laser energy transfer and melt formation; (ii) inward melt flow leading to uoward expansion; (iii) resulting micro-protrusion on rapid cooling.

For a limited range of parameters, controlled surface modifications can be accomplished for laser interaction with materials. Since the pulsewidth is longer than the electron-phonon interaction timescale, the thermal effects play a significant role dominating the process dynamics [73]. Therefore, it has become crucial to determine the ideal laser parameters to limit undesirable effects such as HAZ and thermally generated fissures in glass materials.

4.2.4 Characterization of glass with laser parameters

Average power and laser scan speed were set as the dynamic parameters to study their influence on the resulting modified surface features. Figure 4.15 shows the phase contrast micrographs of laser modified scan lines at increasing average power at a constant scan speed of 3 mm/s. The micro-protrusions begin to appear from an average power of 16 W. From the figure, it is observed that the modification width increases with average laser power. The low power

modification presented irregular edges, whereas at the highest power of $20\ W$, a crack formation was observed. On the other hand, a relatively clean modification was observed at an average power of $18\ W$ as seen in Figure 4.15(c).

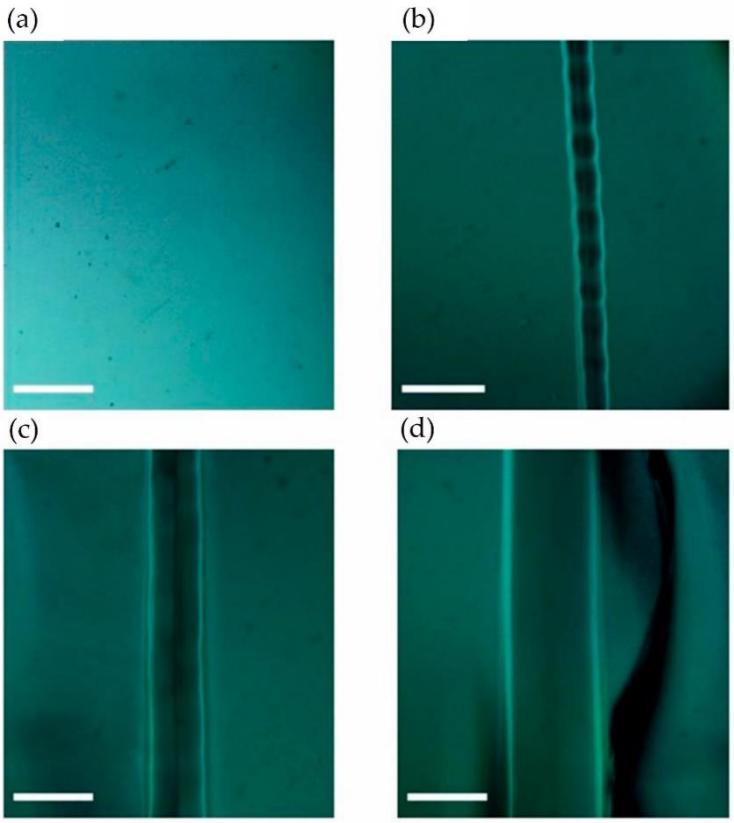

Figure 4.15. Micrographs of the laser modifications at varying average power at a fixed scan speed of 3 mm/s (a) 14 W; (b) 16 W; (c) 18 W; (d) 20 W. Scale bar represents 50 μm.

Figure 4.16 shows the height and width of the protrusions generated at different laser average power, measured by the contact profilometer. Increasing average power at constant PRR implies greater pulse energy, resulting in greater melt formation and enhanced fluid flow towards the Gaussian center, thus increasing the height and width of the modifications. The unevenly distributed and random crack formation can be attributed to the thermal stress generated due to excessive heating and cooling in a rapid manner [74]. At this point, it is worth mentioning that the Inverse Marangoni based effect would inherently minimize the HAZ generally observed with nanosecond laser glass modification. Therefore, the sides of the laser modified regions are free of thermal effects such as HAZ and thermal melt effects.

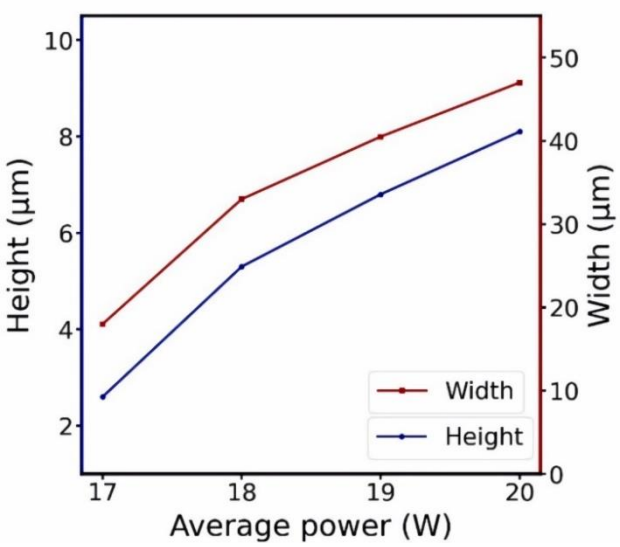

Figure 4.16. Plot representing surface modification characteristics at varying laser average power and a fixed scan speed of 3 mm/s.

Figure 4.17 shows the 3D and cross-section profilometer image of the laser scan line written at an average power of $19\,W$. The 1D cross-sectional view clearly depicts the Gaussian nature of the pulse.

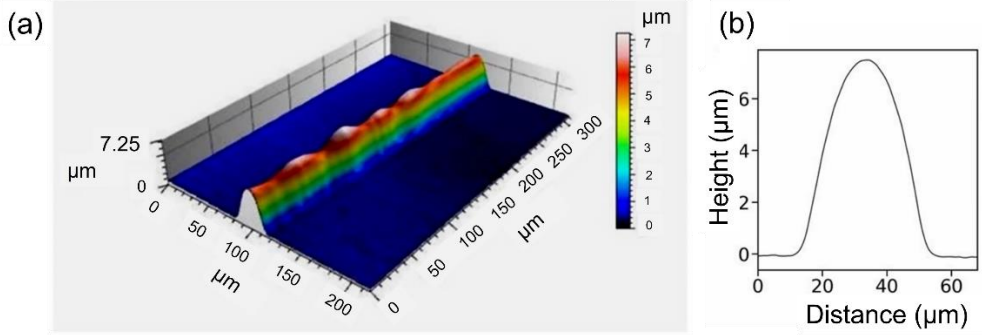

Figure 4.17. 3D surface view of the laser modification generated at 19 W and 3 mm/s obtained from the profilometer (a) and cross-section view of the same (b).

Following the study on the influence of average laser power on surface modifications, laser scan speed was varied to study its effect on the topography. More pulse deposition occurs per spot for lower scan speeds at a constant PRR. In this study, the scan speed was varied between 1,3,5 and 7 mm/s. Figure 4.18(a) shows the plot of microstructure width and height against laser scan speed at a

constant average power of 19 W. The width and height of the features steadily decrease with scan speed as fewer pulses per spot are deposited. The micrographs of the laser modification are reported in Figure 4.18(b,c,d). As expected, crack formation was evident at slow speed of 1 mm/s because of greater energy deposition. The laser scan speed of 3 mm/s at 19 W was determined to be optimal for fabrication of microfeatures.

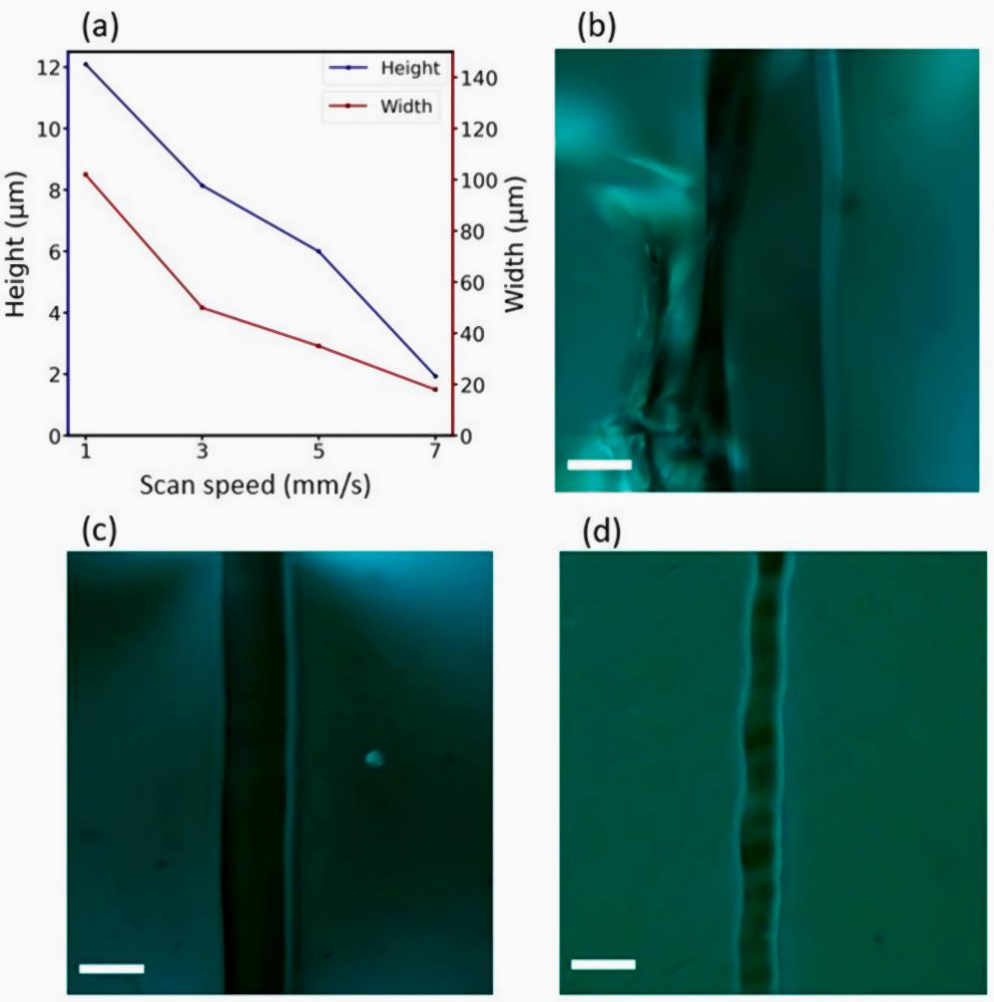

Figure 4.18. (a) Plot representing height and width of the laser modifications at different scan speeds and a constant average power of 19 W. Micrographs of the same laser modifications at a scan speed of (a) 1 mm/s; (b) 3 mm/s and at (c) 5 mm/s.

Following the characterization of surface modification with laser parameters of average power and scan speed, an optimal processing regime is defined, considering both parameters. This provides a complete characterization for

controlled surface modification devoid of cracks and undesired thermal effects. Here, we also describe in terms of the more commonly used parameter of laser fluence (F), given by the following,

$$F = \frac{E_p}{FA} \tag{1}$$

$$E_p = \frac{P_{avg}}{PRR} \tag{2}$$

where E_p is the pulse energy, FA represents the focal area, P_{avg} is the average power, and PRR is the pulse repetition rate. Figure 4.19 represents the plot with a defined region of optimal processing parameters.

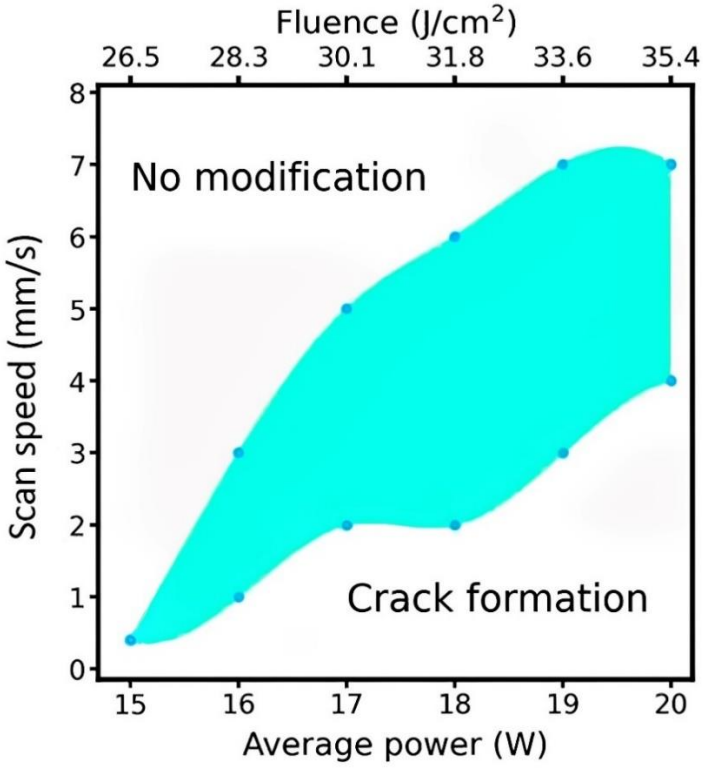

Figure 4.19. Optimal IR ns-laser processing region (green) of the Cu-doped calcium phosphate glass at a PRR of 20 kHz.

The laser modifications performed at non-ideal processing parameter range had chances of either cracking or no modifications. Figure 4.20(a,b) shows the laser modifications performed at the parameters of $(17\,W, 1\,mm/s)$, and $(19\,W, 2\,mm/s)$ respectively. The modifications show micro-crack formations around the laser processed region. Therefore, optimal processing parameters provide the means for advanced patterning complex surface textures for functional surfaces.

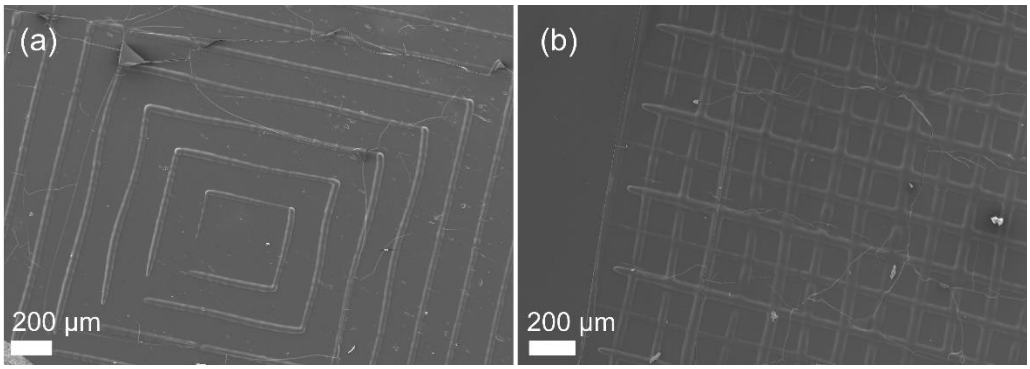

Figure 4.20. SEM images of laser modified phosphate glass surface with non-ideal processing parameters.

To demonstrate the ability to use an optimal parameter for a clean surface processing, we demonstrate the texturing of the glass surface in a grid pattern at an average power of $17\,W$, at a scan speed of $2\,mm/s$, well within the optimal processing regime of Figure 4.19. Figure 4.21 shows the SEM and profilometer images of the grid pattern. Surface features with an average height of $\sim 7\,\mu m$ could be obtained. The laser texturing technique therefore provides a powerful yet inexpensive approach for the Cu-doped bioresorbable glass modification with a strong prospect for in-vivo medical applications. These microstructures could be used as cell scaffolds or to enhance antibacterial properties of the glass surface by increasing the effective area.

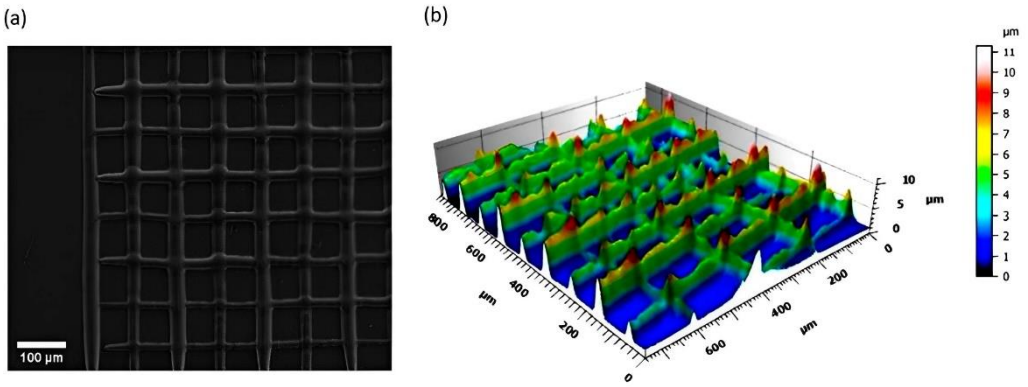

Figure 4.21. (a) SEM image of the cross-pattern written at a fixed laser average power of 17 W and 2 mm\/s; (b) 3D surface view of the same obtained from the profilometer analysis.

4.5 Fabrication of micro-optics on Cu-doped CaPh glass

In the following sections, the application of laser patterning on the glass is demonstrated through the fabrication and characterization of microlenses and diffraction gratings on the glass surface. The feasibility of leaving behind the biomaterial after the intended function strengthens the possibility towards the fabrication of microfluidic and micro-optical devices for theranotics [75,76]. In recent years, there has been a tremendous research interest in biopolymers and natural silk as an alternative to bioresorbable glass materials [77,78]. Biopolymers have been previously used to fabricate optical components. Still, hydrogels have become a viable biopolymeric material thanks to their properties such as reversible volume change and analyte-specific structural modifications [79,80]. However, some of the common hydrogels, including polylactic and polyglycolic acids, have the potential to degrade into dangerous crystalline particles, hindering their bioresorbability [81]. On the other hand, natural silk fiber offers good biocompatibility and superior mechanical property. Amongst various silk materials for deep tissue light delivery is best demonstrated by spider based spidroin protein [82]. Nonetheless, obtaining spider silk in large quantities for industrial-scale production is difficult.

Fabrication of micro-nano features on biomaterials offers a variety of applications, such as in-vivo imaging, sensing, and optical manipulation [83,84]. The common approach to fabricating these structures uses complex techniques such as lithography, ultrafast laser micromachining, hot embossing, and nanoimprinting, to name a few [85,86]. However, this study work offered an

inexpensive alternative to such complex surface processing techniques through a single-step direct fabrication of micro-optics on the Cu-doped bioresorbable glass substrate. The generated micro-optics can be finely tuned with respect to their shape and size and are free from the impact of HAZ and other thermal effects. Firstly, their optical characterization demonstrates the feasibility of fabricating micro-optics.

4.5.1 Morphological and topographical analysis

Micro lenses were fabricated by fixing the laser focal spot at a single location. The pulse deposition time was set at $1\ s$ throughout this study and therefore, PRR decides the number of pulses per spot. In the case of the diffraction grating, the focal spot was scanned at $3\ mm/s$. The PRR, average power and the spacing between scan line were set at $23\ kHz, 13\ W$ and $40\ \mu m,$ respectively.

Figure 4.22 shows the SEM images of the microlens and diffraction gratings on the Cu-doped phosphate glass. The fabricated features do not show any evident defects that could harm the optical performance. As discussed, the rapid melt formation and cooling mechanism and the Inverse Marangoni flow results in the final microstructures. At this point, it is worth highlighting that the single step direct fabrication is advantageous, particularly compared to the usually adopted approach where a primary modification is performed by the appropriate surface modification technique, such as ultrafast laser modification, followed by a secondary process such as thermal reflow or wet etching [87].

The feature size can be varied with the PRR due to greater melt pool formation due to enhanced thermal effect as shown in Figure 4.22(c), where PRR is varied between 20 and $23\ kHz$ at an average power of $11\ W$. However, Figure 4.22(d) shows the SEM images of the microfeatures fabricated at an average power of $16\ W$ at a PRR of $20\ kHz$. Even though the PRR is relatively low, the increased pulse energy cause a slight depression at the tip of the microstructure, resembling red blood cells. This observation is attributed to the effect of the rapid vaporization induced recoil pressure at increased pulse energy which forces the liquid to melt at the gaussian center inward, and hence the depression.

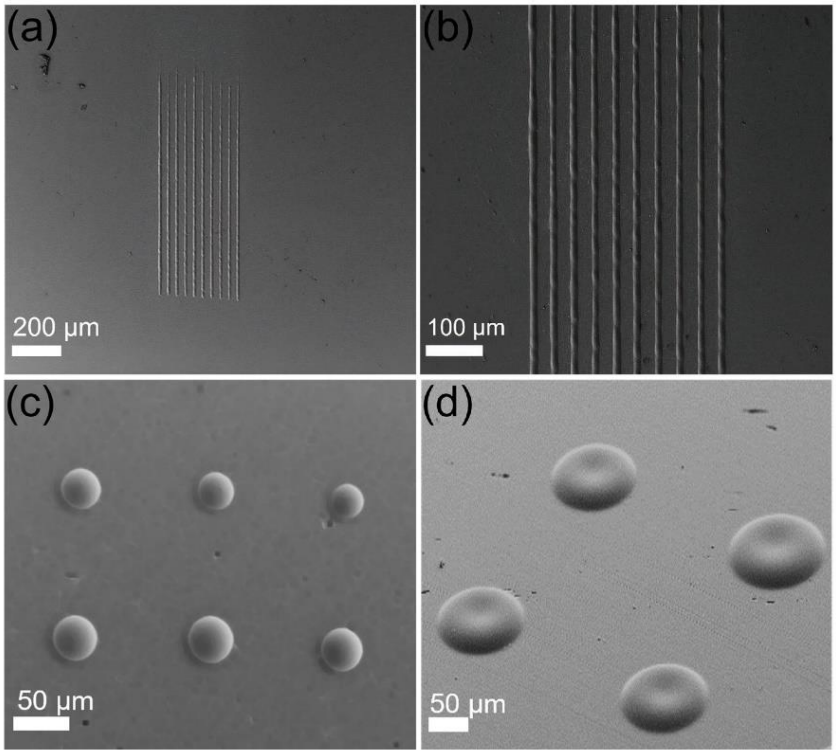

Figure 4.22. SEM images of the micro-optical structures on the Cu-doped CaPh glass: (a,b) 1D diffraction gratings at different magnifications; (c) microlenses fabricated at average power of 11 W and varying PRR of 20 kHz (above row) and 23 kHz (below row); (d) tilted view of the micro-features with a dip on the tip written at 16 W and 20 kHz.

In agreement with the SEM images, the 3D profilometer image shows the smooth and regular optical features depicted in Figure 4.23(a,c). Interestingly, for the microfeatures, the average power could control the shape and size of the microlens. Figure 4.23(b) shows the profilometer trace of the microlens generated at fixed PRR of $20\ kHz$ at varying average power. As for the further studies on the PRR is fixed at $20\ kHz$. The height and diameter of the microlens increased up to $12\ W$, beyond which the height and width showed a negative correlation, as observed for $14\ W$. This trend is due to the recoil pressure effect. The tunability of microlens features in a single step process on the same substrate would be advantageous for compact optical system with tunable imaging properties [88,89].

Figure 4.23(c) shows the profilometer image of the diffraction grating on the glass surface written at an average power of $13\ W$. In this case, the moving laser beam causes the glass beam formation along the laser scan path. As shown in Figure 4.23(d), the gratings had a pitch of $40\ \mu m$ and height of about $4.30\ \pm$

$0.17\ \mu m$. The obtained features confirm the ability to achieve tunable and precise micro-optical devices on a bioresorbable calcium phosphate glass using the nanosecond IR laser.

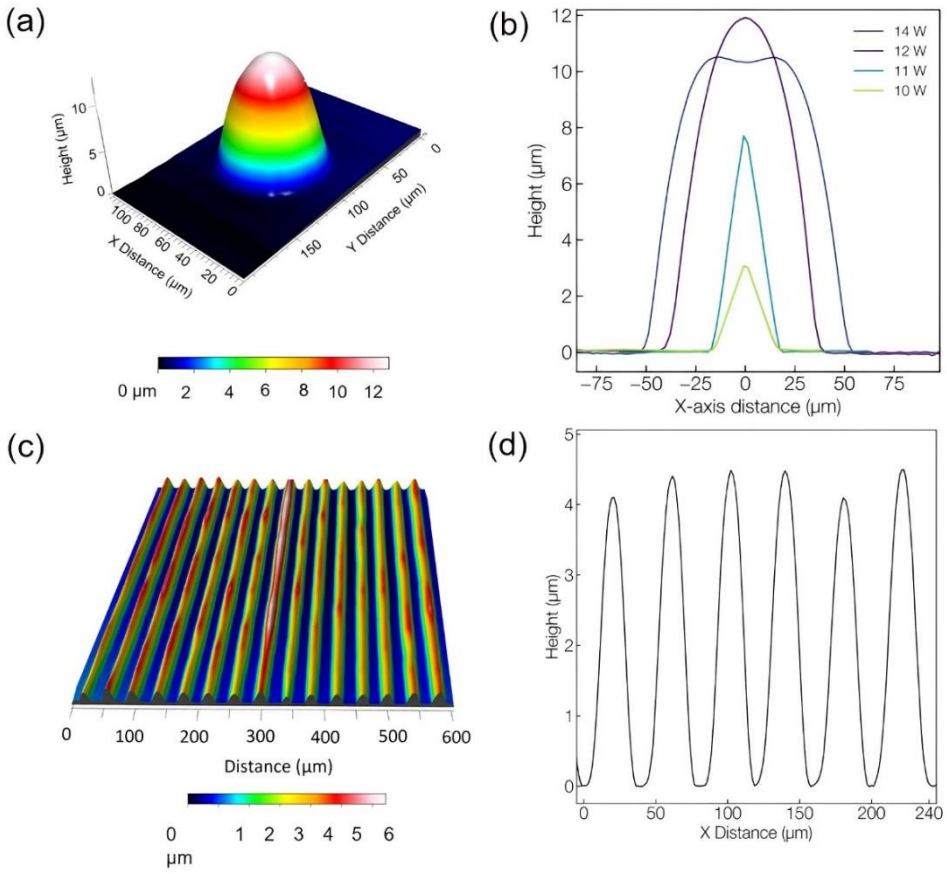

Figure 4.23. 3D and cross-sectional view of the micro-features generated by the profilometer: (a) microlens fabricated at 12 W; (b) 1D trace of microlens fabrication at different laser average power; (c) 3D image of the diffraction gratings; (d) corresponding 1D cross-section of the same.

4.5.2 Optical characterization

The final step to assess the functionality of the micro-optic devices was the optical characterization. Figure 4.24 depicts the optical set-up used to determine the focusing performance of the microlens array (MLA). As depicted in the figure, an optical mask comprising the letter 'A' was fabricated on a transparent soda lime glass substrate. The mask was inserted in between MLA and the illumination source below. The former was placed on a translation stage which was then

moved along the illumination axis to determine the focal length of the fabricated MLA. The focused image of the mask was then captured by an objective coupled to a CCD.

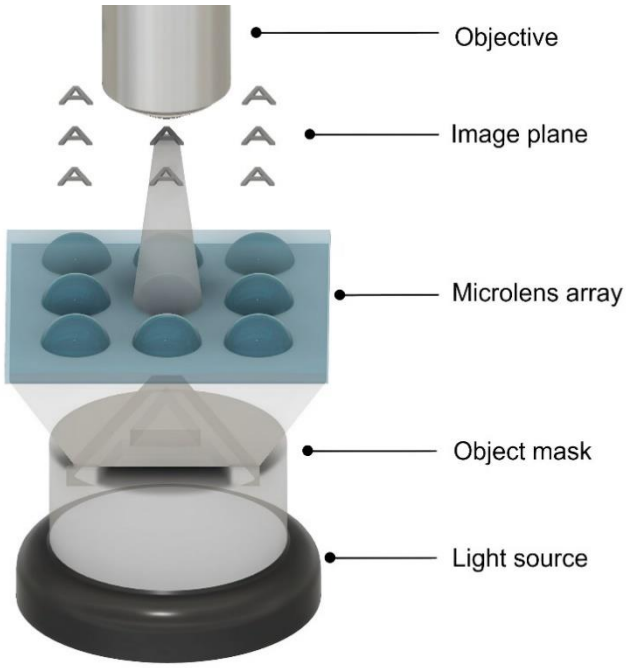

Figure 4.24. Illustration of the set-up used for the optical characterization of the MLA.

Figure 4.25(a,b) represents the corresponding images of the MLA and the images mask 'A', as captured by the CCD. The laser fabricated microlens exhibited excellent uniformity along with good focusing performance. As previously mentioned, the direct laser fabrication technique allows tuning the microlens features and hence the focal length on a single substrate. Figure 4.25(c,d) demonstrates the ability to both pattern and tune the microlens by fabricating their shape as 'S', 'A', and 'T', wherein each pattern was written at a different average power of 12,13 and 14 W respectively. In Figure 4.25(c), the mask is focused by the microlens belonging to the letter 'S', whereas in Figure 4.25(d), the micrograph taken on a different plane shows the focused mask by the microlens belonging to a pattern of letter 'T'. This clearly demonstrates the multi-focal imaging performance on a single platform, an interesting aspect for 3D imaging optics.

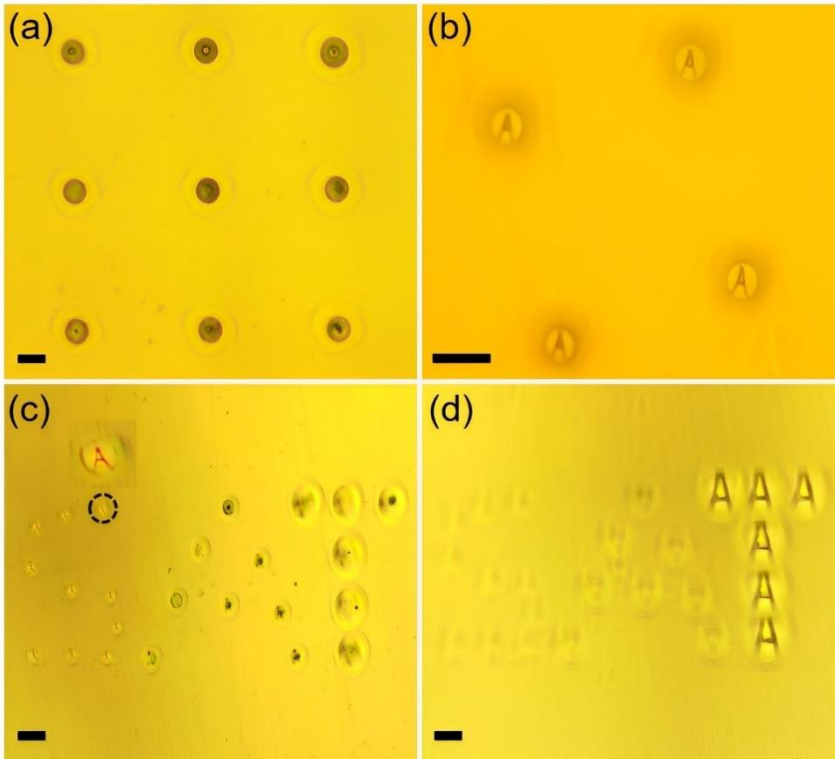

Figure 4.25. Optical micrographs of (a) MLA; (b) mask 'A' imaged by the MLA; (c,d) mask imaging performance of the patterned MLA, where each microlens letter pattern has a different focal length Scale bar represents 100 μm.

The focal length of the fabricated microlens were then measured experimentally. To measure the focal length, the distance between the microlens based on the glass surface and the focal plane was considered.

4.5.3 Shape tunable microlens

An interesting aspect of the microlens fabricated in this work involves shape tunability with variation in the average laser power. The geometric feature dependence on average laser power was previously discussed using image Figure 4.23(b). Specifically, the microlens shape could be tuned between the more commonly fabricated spherical microlens at higher average power. And the hyperbolic shape was obtained at a lower average power of 10 and 11 W. Hyperbolic microlens receives special interest in optics due to their ability to overcome spherical aberration and achieve improved imaging performance

[90,91]. However, the hyperboloid microlens are challenging to achieve through the common fabrication techniques involving thermal reflow or chemical etching, which inherently render a spherical profile.

Figure 4.26 represents the profilometer trace of the microlens with a fitting of an ideal hyperbolic line following the below equation,

$$\frac{y^2}{a^2} - \frac{x^2}{b^2} = 1 \tag{3}$$

where a and b are the hyperbolic profile parameters with the appropriate values given by: (a)$a = 1, b = 3.97$; (b)$a = 1, b = 1.95$. The figure shows that the hyperbolic profile fits well with the measured profilometer trace. The resulting focal length can be calculated using the below relation:

$$F = \frac{r^2 + \ n^2 - 1 \ \ h^2}{2 \ \ n - 1 \ \ h} \tag{4}$$

where F represents the focal length, r, and h are the lens radius and height, respectively and n is the refractive index of the calcium phosphate glass, experimentally determined as $n = 1.526 \ \ 633nm$.

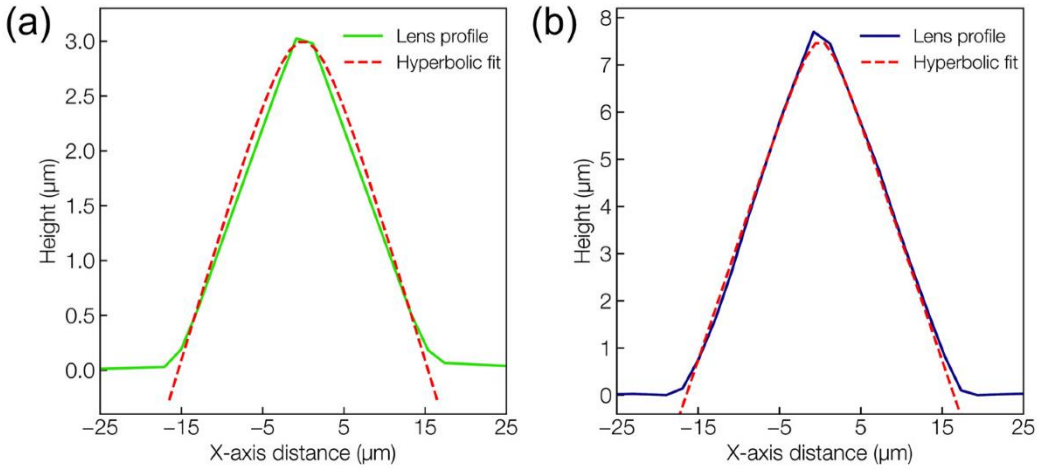

Figure 4.26. Hyperbolic line fitting to the profilometer measured lens profile fabricated at (a) 10 W and (b) 11 W.

Similarly, in the case of the spherical microlens generated at higher average power, the plano-convex lens formulation of the following form was used:

$$F = \frac{r^2 + h^2}{2\ h\ \ n-1} \tag{5}$$

The calculated and experimentally measured focal length of all the fabricated microlens at varying laser average power is depicted inFigure 4.27. The focal length of the fabricated microlens could be tuned from 50 to $250\ \mu m$, which makes it interesting for in-vivo optical diagnosis applications. An interesting observation regards the relatively larger deviation between the estimated and experimental focal length values of the microlens fabricated at $14\,W$. Additionally, the focusing performance of the microlens is relatively poor, in terms of image sharpness as previously demonstrated in Figure 4.25(d). This effect could be attributed to the deviation from the ideal spherical nature of the microlens due to the recoil pressure effect that generates a depression at the tip of the microstructure. Therefore, the 14 W modification acts as the upper limit to obtain microlenses of reasonable good performance.

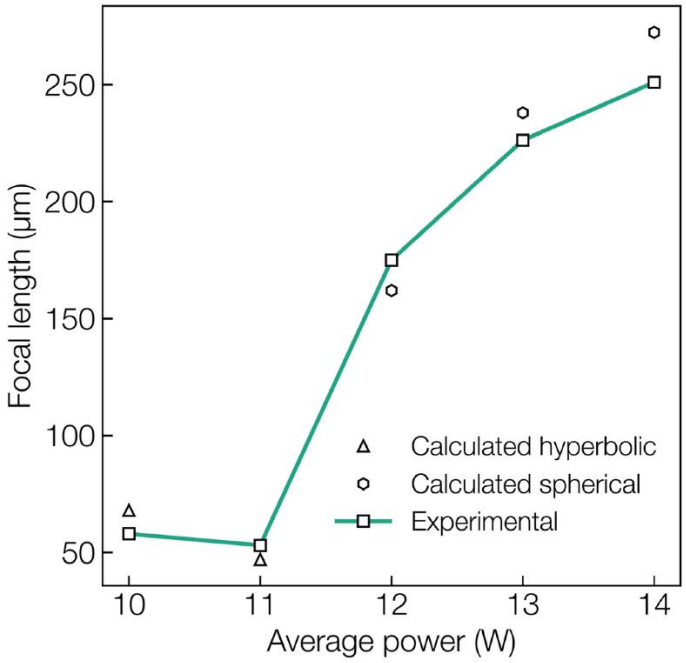

Figure 4.27. Calculated and experimental focal length values of the microlens fabricated at different laser average powers.

In Figure 4.28(a), a collimated diode laser beam is diffracted by the gratings on the CaPh glass, while the optical power of the appropriate diffraction order is measured by the power meter. The higher order diffraction patterns are easily recognizable and exhibit an excellent diffractive characteristic, as seen in the Figure 4.28(b). It should be noted that the groove spacing decides the spatial propagation of the diffracted wavefront. The spatial properties of the diffraction pattern can therefore be tuned based on the spacing between the laser scan lines during the fabrication. Additionally, the optical performance of the fabricated gratings was quantitatively assessed by determining the diffraction efficiency, which is provided by the following relation:

$$\eta = \frac{P_m}{P_o} \times 100 \tag{6}$$

where P_m is the optical power measured at the mth order, while P_o is the input optical power. The diffraction efficiencies measured for the first, second, and third order were 5.1,3.3, and 2.2%, respectively.

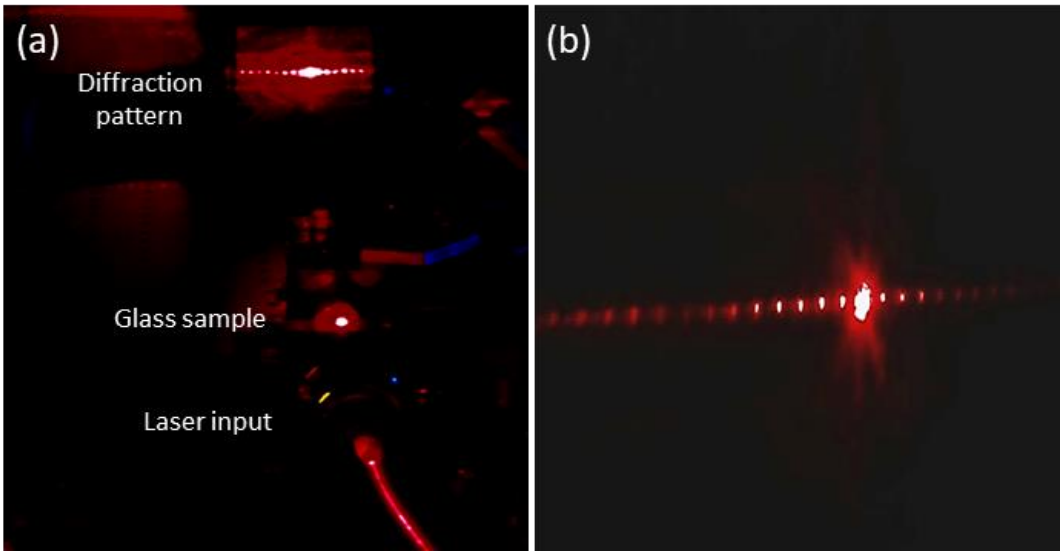

Figure 4.28. (a) Diffraction pattern generated from the Cu-doped CaPh glass with an input from a fiber fed collimated laser beam (660 nm) used for experimental measurement; (b) Close range image of the resulting diffraction pattern.

4.6 Dissolution characteristics

The dissolution characteristics of the fabricated laser microstructure were studied by immersion in PBS solution (pH=7.4). For the dissolution experiments, microlens features fabricated at an average power of $10.5\,W$ and a PRR of $20\,kHz$ was considered, and the topography was analyzed with dissolution time, as shown inFigure 4.29. In agreement with previously reported results, the microlens' height decreased by about $2.5\ \mu m$ [92]. However, since the cross-sectional diameter of the microlens is not uniform with the height, a specific rate cannot be defined. Another interesting aspect is that a preferential dissolution occurs along the laser modified region compared to the pristine glass surface. Hence, the rate of dissolution along the laser-modified region proceeds faster.

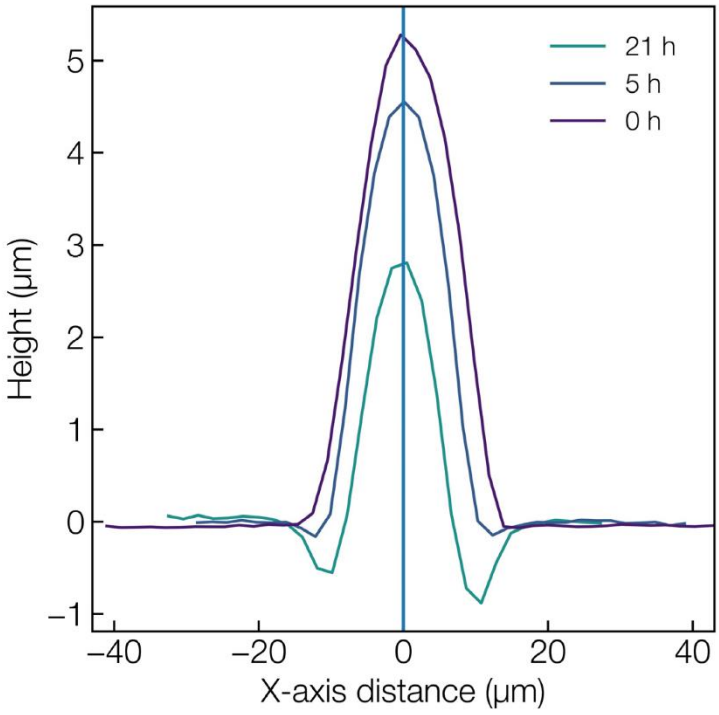

Figure 4.29. 1D profilometer trace of the microlens generated at an average laser power of 10.5 W taken at different dissolution time intervals in PBS solution.

The hydrolysis of the glass modifier cation, which fills the gap between $[PO_4]$ units, is a crucial element in the phosphate glass dissolution. According to our research groups previous investigation on the dissolution dynamics of the CaPh glass which begins with the hydrolysis of the modifier cation, the dissolution in aqueous solution is further sustained by the bonding of the hydroxyl group to the phosphate network [93]. The $P-O-P$ bridge can be broken down to the form $P-O-P+H_2O \rightarrow 2\ P-OH$, or through cation chain breakage as in $P-O-M+H_2O \rightarrow P-OH+M-OH$, where M is the modifier cation. The de-polymerization of the glass network caused by the cleaving of the $P-O$ might be the reason for increased dissolution rate of laser modified region. Figure 4.30(a,b) shows the 3D profilometer images of the preferential etching at the laser modified region after $72\,hrs$ immersion in the PBS solution. Interestingly, the laser modifed region could be etched to remove a depth of about $3\,\mu m$ in a timescale of about $72\,hrs$. This demonstrates the ability of laser processing to generate both positive and negative dimensional structures in the doped CaPh glass.

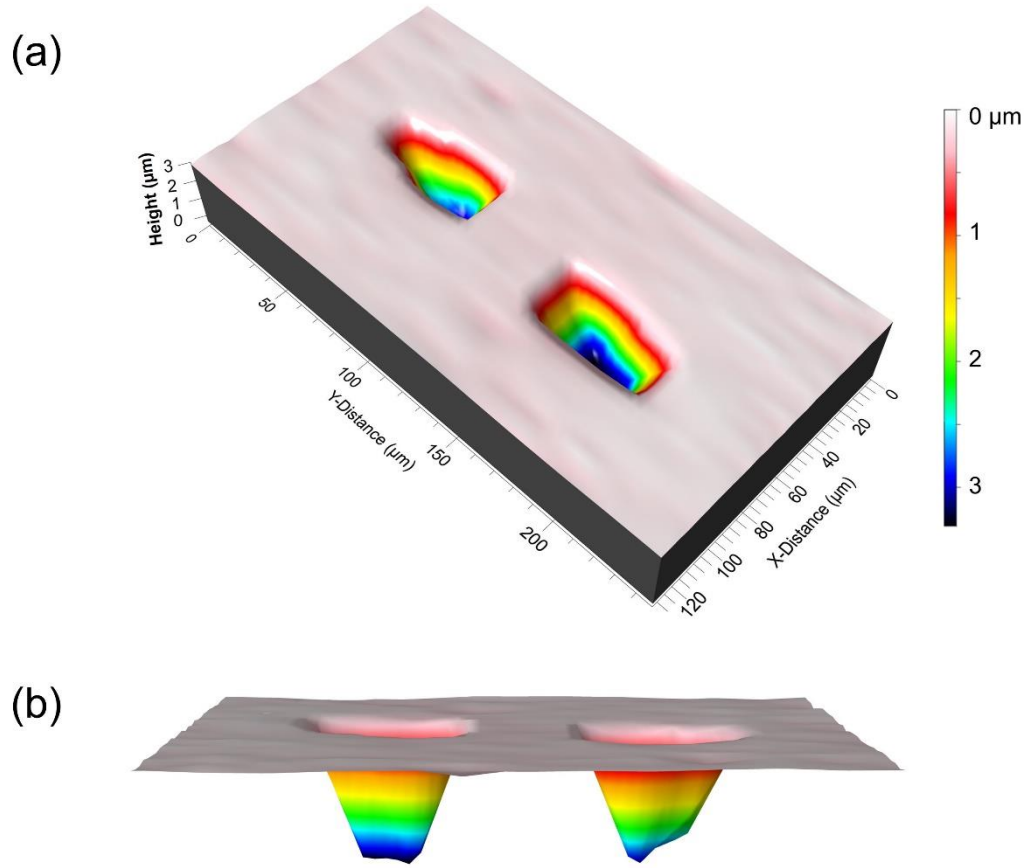

Figure 4.30. 3D profilometer images of the preferential etching on the laser modified region after immersion in PBS (pH=7.4) for a total time of 72 hrs.

Finally, in addition to the bioresobability of the glass system, the anti-bacterial property is also present due to the Cu^{+} ions. A multifunctional capability in both diagnostics and the distribution of therapeutic drugs or ions upon dissolution after the intended optical functionality would all be simultaneously fabricated on a Cu-doped CaPh glass. This study also combines the control of positive or negative volume modifications on the Cu-doped glass surface to fabricating shape and dimension tunability of the micro-optics, all in a single-step fabrication procedure. Furthermore, the fabrication process is affordable, relying on an industrial grade nanosecond laser system. A potent combination of precision surface texturing on the glass surface with fabrication of micro-optics could combine the biomedical applications of scaffold fabrication for tissue engineering along with in-vivo optical imaging and focusing performance for minimally invasive diagnostics and treatment.

References

1. *Springer Handbook of Glass*; Musgraves, J.D., Hu, J., Calvez, L., Eds.; Springer Handbooks; Springer International Publishing: Cham, 2019; ISBN 978-3-319-93726-7.
2. Varberg, J.; Gratuze, B.; Kaul, F.; Hansen, A.H.; Rotea, M.; Wittenberger, M. Mesopotamian Glass from Late Bronze Age Egypt, Romania, Germany, and Denmark. *Journal of Archaeological Science* **2016**, *74*, 184–194, doi:10.1016/j.jas.2016.04.010.
3. Kotz, F.; Plewa, K.; Bauer, W.; Schneider, N.; Keller, N.; Nargang, T.; Helmer, D.; Sachsenheimer, K.; Schäfer, M.; Worgull, M.; et al. Liquid Glass: A Facile Soft Replication Method for Structuring Glass. *Adv. Mater.* **2016**, *28*, 4646–4650, doi:10.1002/adma.201506089.
4. Saravanan, S.; Vijayan, V.; Suthahar, S.T.J.; Balan, A.V.; Sankar, S.; Ravichandran, M. A Review on Recent Progresses in Machining Methods Based on Abrasive Water Jet Machining. *Materials Today: Proceedings* **2020**, *21*, 116–122, doi:10.1016/j.matpr.2019.05.373.
5. Bukieda, P.; Lohr, K.; Meiberg, J.; Weller, B. Study on the Optical Quality and Strength of Glass Edges after the Grinding and Polishing Process. *Glass Struct Eng* **2020**, *5*, 411–428, doi:10.1007/s40940-020-00121-x.
6. Verma, A.K.; Mishra, D.K.; Pawar, K.; Dixit, P. Investigations into Surface Topography of Glass Microfeatures Formed by Pulsed Electrochemical Discharge Milling for Microsystem Applications. *Microsyst Technol* **2020**, *26*, 2105–2116, doi:10.1007/s00542-020-04770-4.
7. Dudutis, J.; Pipiras, J.; Gečys, P. Glass Processing with Different Techniques. **2019**.
8. Kant Bajpai, V.; Kumar Mishra, D.; Dixit, P. Fabrication of Through-Glass Vias (TGV) Based 3D Microstructures in Glass Substrate by a Lithography-Free Process for MEMS Applications. *Applied Surface Science* **2022**, *584*, 152494, doi:10.1016/j.apsusc.2022.152494.
9. Kang, S.; Dong, G.; Qiu, J.; Yang, Z. (INVITED) Hybrid Glass Optical Fibers-Novel Fiber Materials for Optoelectronic Application. *Optical Materials: X* **2020**, *6*, 100051, doi:10.1016/j.omx.2020.100051.
10. Li, K.; Liang, L.; Du, P.; Cai, Z.; Xiang, T.; Kanetaka, H.; Wu, H.; Xie, G. Mechanical Properties and Corrosion Resistance of Powder Metallurgical Mg-Zn-Ca/Fe Bulk Metal Glass Composites for Biomedical Application.

Journal of Materials Science & Technology **2022**, *103*, 73–83, doi:10.1016/j.jmst.2021.07.006.

11. Frey, N.; Sönmez, U.M.; Minden, J.; LeDuc, P. Microfluidics for Understanding Model Organisms. *Nat Commun* **2022**, *13*, 3195, doi:10.1038/s41467-022-30814-6.
12. Konari, P.R.; Clayton, Y.-D.; Vaughan, M.B.; Khandaker, M.; Hossan, M.R. Experimental Analysis of Laser Micromachining of Microchannels in Common Microfluidic Substrates. *Micromachines* **2021**, *12*, 138, doi:10.3390/mi12020138.
13. Adelegan, O.J.; Coutant, Z.A.; Wu, X.; Yamaner, F.Y.; Oralkan, O. Design and Fabrication of Wideband Air-Coupled Capacitive Micromachined Ultrasonic Transducers With Varying Width Annular-Ring and Spiral Cell Structures. *IEEE Trans. Ultrason., Ferroelect., Freq. Contr.* **2021**, *68*, 2749–2759, doi:10.1109/TUFFC.2021.3076143.
14. Fang, Z.; Gao, L.; Chen, H.; Deng, B.; Jili, X.; Li, W.; Liang, T.; Qu, S.; Chen, Y.; Liang, K.; et al. 3D Interdigital Electrodes Dielectric Capacitor Array for Energy Storage Based on Through Glass Vias. *Adv Materials Technologies* **2022**, *7*, 2101530, doi:10.1002/admt.202101530.
15. Cardoso, S.; Silverio, V. Introduction to Microfabrication Techniques for Microfluidics Devices. In *Drug Delivery Devices and Therapeutic Systems*; Elsevier, 2021; pp. 19–30 ISBN 978-0-12-819838-4.
16. Gautam, G.P.; Burger, T.; Wilcox, A.; Cumbo, M.J.; Graves, S.W.; Piyasena, M.E. Simple and Inexpensive Micromachined Aluminum Microfluidic Devices for Acoustic Focusing of Particles and Cells. *Anal Bioanal Chem* **2018**, *410*, 3385–3394, doi:10.1007/s00216-018-1034-6.
17. Chen, N.; Li, H.N.; Wu, J.; Li, Z.; Li, L.; Liu, G.; He, N. Advances in Micro Milling: From Tool Fabrication to Process Outcomes. *International Journal of Machine Tools and Manufacture* **2021**, *160*, 103670, doi:10.1016/j.ijmachtools.2020.103670.
18. Wang, T.; Wu, X.; Zhang, G.; Xu, B.; Chen, Y.; Ruan, S. Experimental Study on Machinability of Zr-Based Bulk Metallic Glass during Micro Milling. *Micromachines* **2020**, *11*, 86, doi:10.3390/mi11010086.
19. Zhou, H.; Zhang, J.; Yu, D.; Feng, P.; Wu, Z.; Cai, W. Advances in Rotary Ultrasonic Machining System for Hard and Brittle Materials. *Advances in Mechanical Engineering* **2019**, *11*, 168781401989592, doi:10.1177/1687814019895929.
20. Arab, J.; Mishra, D.K.; Dixit, P. Measurement and Analysis of the Geometric Characteristics of Microholes and Tool Wear for Varying Tool-

Workpiece Gaps in Electrochemical Discharge Drilling. *Measurement* **2021**, *168*, 108463, doi:10.1016/j.measurement.2020.108463.

21. Goud, M.; Sharma, A.K. On Performance Studies during Micromachining of Quartz Glass Using Electrochemical Discharge Machining. *J Mech Sci Technol* **2017**, *31*, 1365–1372, doi:10.1007/s12206-017-0236-8.
22. Xu, Y.; Chen, J.; Jiang, B.; Liu, Y.; Ni, J. Experimental Investigation of Magnetohydrodynamic Effect in Electrochemical Discharge Machining. *International Journal of Mechanical Sciences* **2018**, *142–143*, 86–96, doi:10.1016/j.ijmecsci.2018.04.020.
23. Hamed, H.; Eldiasty, M.; Seyedi-Sahebari, S.-M.; Abou-Ziki, J.D. Applications, Materials, and Fabrication of Micro Glass Parts and Devices: An Overview. *Materials Today* **2023**, *66*, 194–220, doi:10.1016/j.mattod.2023.03.005.
24. Soldera, M.; Alamri, S.; Sürmann, P.A.; Kunze, T.; Lasagni, A.F. Microfabrication and Surface Functionalization of Soda Lime Glass through Direct Laser Interference Patterning. *Nanomaterials* **2021**, *11*, 129, doi:10.3390/nano11010129.
25. Crimella, D.; Jwad, T.; Demir, A.G. Microcutting of Glass with High Ablation Efficiency by Means of a High Power Ps-Pulsed NIR Laser. *Optics & Laser Technology* **2023**, *166*, 109645, doi:10.1016/j.optlastec.2023.109645.
26. Ali, B.; Litvinyuk, I.V.; Rybachuk, M. Femtosecond Laser Micromachining of Diamond: Current Research Status, Applications and Challenges. *Carbon* **2021**, *179*, 209–226, doi:10.1016/j.carbon.2021.04.025.
27. Stoian, R.; Bhuyan, M.K.; Rudenko, A.; Colombier, J.-P.; Cheng, G. High-Resolution Material Structuring Using Ultrafast Laser Non-Diffractive Beams. *Advances in Physics: X* **2019**, *4*, 1659180, doi:10.1080/23746149.2019.1659180.
28. Kočica, J.J.; Mur, J.; Didierjean, J.; Guillossou, A.; Saby, J.; Petelin, J.; Mincuzzi, G.; Petkovšek, R. Pulse-on-Demand Operation for Precise High-Speed UV Laser Microstructuring. *Micromachines* **2023**, *14*, 843, doi:10.3390/mi14040843.
29. Wen, Q.; Chen, J.; Lu, J.; Mu, D.; Jiang, F. Effect of Target on Micromachining of Sapphire Using Laser-Induced Plasma-Assisted Ablation. *Ceramics International* **2023**, *49*, 14470–14477, doi:10.1016/j.ceramint.2023.01.035.
30. Cheng, J.-Y. Crack-Free Micromachining of Glass Ceramic Using Visible LIBWE. *JLMN* **2013**, *8*, 253–258, doi:10.2961/jlmn.2013.03.0011.

31. Liao, K.; Wang, W.; Mei, X.; Liu, B. Fabrication of Millimeter-Scale Deep Microchannels in Fused Silica by Femtosecond Laser Filamentation Effect. *Optics & Laser Technology* **2021**, *142*, 107201, doi:10.1016/j.optlastec.2021.107201.

32. Liu, H.; Lin, W.; Hong, M. Hybrid Laser Precision Engineering of Transparent Hard Materials: Challenges, Solutions and Applications. *Light Sci Appl* **2021**, *10*, 162, doi:10.1038/s41377-021-00596-5.

33. *Advances in Unconventional Machining and Composites: Proceedings of AIMTDR 2018*; Shunmugam, M.S., Kanthababu, M., Eds.; Lecture Notes on Multidisciplinary Industrial Engineering; Springer Singapore: Singapore, 2020; ISBN 978-981-329-470-7.

34. Ahlawat, S.; Singh, A.; Mukhopadhyay, P.K.; Singh, R.; Bindra, K.S. Nanosecond Laser Induced Glass Particle Deposition over Steel Mesh for Long-Term Superhydrophilicity and Gravity Driven Oil Water Separation. *Materials Chemistry and Physics* **2021**, *263*, 124343, doi:10.1016/j.matchemphys.2021.124343.

35. Rahman, T.U.; Rehman, Z.U.; Ullah, S.; Qayyum, H.; Shafique, B.; Ali, R.; Liaqat, U.; Dogar, A.H.; Qayyum, A. Laser-Induced Plasma-Assisted Ablation (LIPAA) of Glass: Effects of the Laser Fluence on Plasma Parameters and Crater Morphology. *Optics & Laser Technology* **2019**, *120*, 105768, doi:10.1016/j.optlastec.2019.105768.

36. Pan, C.; Chen, K.; Liu, B.; Ren, L.; Wang, J.; Hu, Q.; Liang, L.; Zhou, J.; Jiang, L. Fabrication of Micro-Texture Channel on Glass by Laser-Induced Plasma-Assisted Ablation and Chemical Corrosion for Microfluidic Devices. *Journal of Materials Processing Technology* **2017**, *240*, 314–323, doi:10.1016/j.jmatprotec.2016.10.011.

37. Kwon, K.-K.; Song, K.Y.; Seo, J.M.; Chu, C.N.; Ahn, S.-H. Precise Glass Microstructuring with Laser Induced Backside Wet Etching Using Error-Compensating Scan Path. *Journal of Materials Processing Technology* **2021**, *291*, 117046, doi:10.1016/j.jmatprotec.2021.117046.

38. Sglavo, V.M.; Pugliese, D.; Sartori, F.; Boetti, N.G.; Ceci-Ginistrelli, E.; Franco, G.; Milanese, D. Mechanical Properties of Resorbable Calcium-Phosphate Glass Optical Fiber and Capillaries. *Journal of Alloys and Compounds* **2019**, *778*, 410–417, doi:10.1016/j.jallcom.2018.11.033.

39. Ceci-Ginistrelli, E.; Pontremoli, C.; Pugliese, D.; Barbero, N.; Boetti, N.G.; Barolo, C.; Visentin, S.; Milanese, D. Drug Release Kinetics from Biodegradable UV-Transparent Hollow Calcium-Phosphate Glass Fibers. *Materials Letters* **2017**, *191*, 116–118, doi:10.1016/j.matlet.2016.12.103.

40. Massera, J.; Shpotyuk, Y.; Sabatier, F.; Jouan, T.; Boussard-Plédel, C.; Roiland, C.; Bureau, B.; Petit, L.; Boetti, N.G.; Milanese, D.; et al.

Processing and Characterization of Novel Borophosphate Glasses and Fibers for Medical Applications. *Journal of Non-Crystalline Solids* **2015**, *425*, 52–60, doi:10.1016/j.jnoncrysol.2015.05.028.

41. Ahmed, I.; Collins, C.A.; Lewis, M.P.; Olsen, I.; Knowles, J.C. Processing, Characterisation and Biocompatibility of Iron-Phosphate Glass Fibres for Tissue Engineering. *Biomaterials* **2004**, *25*, 3223–3232, doi:10.1016/j.biomaterials.2003.10.013.
42. Babu, S.; Seshadri, M.; Reddy Prasad, V.; Ratnakaram, Y.C. Spectroscopic and Laser Properties of Er3+ Doped Fluoro-Phosphate Glasses as Promising Candidates for Broadband Optical Fiber Lasers and Amplifiers. *Materials Research Bulletin* **2015**, *70*, 935–944, doi:10.1016/j.materresbull.2015.06.033.
43. Li, G.S.; Zhang, C.M.; Zhu, P.F.; Jiang, C.; Song, P.; Zhu, K. Broadband Near-Infrared Emission in Pr3+–Er3+ Codoped Phosphate Glasses for Optical Amplifiers. *Ceramics International* **2016**, *42*, 5558–5561, doi:10.1016/j.ceramint.2015.12.026.
44. Elalaily, N.A.; Zahran, A.H.; Saad, E.A.; Sallam, O.I.; Ezz-Eldin, F.M. Corrosion and Infrared Study of Some γ-Irradiated Lead-Phosphate Glasses Doped with MoO3. *Silicon* **2018**, *10*, 1613–1623, doi:10.1007/s12633-017-9645-7.
45. Es-soufi, H.; Bih, L. *Structural Investigation, Chemical Durability, And Kinetic Characterization of Sodium-Tungsten-Titanium Phosphate Glasses*; In Review, 2022;
46. Oosterbeek, R.N.; Margaronis, K.I.; Zhang, X.C.; Best, S.M.; Cameron, R.E. Non-Linear Dissolution Mechanisms of Sodium Calcium Phosphate Glasses as a Function of pH in Various Aqueous Media. *Journal of the European Ceramic Society* **2021**, *41*, 901–911, doi:10.1016/j.jeurceramsoc.2020.08.076.
47. Çelikbilek Ersundu, M.; Kuzu, B.; Ersundu, A.E. Structural Properties and Dissolution Behavior of New Generation Controlled Release Phosphate Glass Fertilizers. *Journal of Non-Crystalline Solids* **2022**, *576*, 121239, doi:10.1016/j.jnoncrysol.2021.121239.
48. Dutta, D.P.; Roy, M.; Mishra, R.K.; Meena, S.S.; Yadav, A.; Kaushik, C.P.; Tyagi, A.K. Structural Investigations on Mo, Cs and Ba Ions-Loaded Iron Phosphate Glass for Nuclear Waste Storage Application. *Journal of Alloys and Compounds* **2021**, *850*, 156715, doi:10.1016/j.jallcom.2020.156715.
49. Bødker, M.S.; Mauro, J.C.; Goyal, S.; Youngman, R.E.; Smedskjaer, M.M. Predicting Q-Speciation in Binary Phosphate Glasses Using Statistical Mechanics. *J. Phys. Chem. B* **2018**, *122*, 7609–7615, doi:10.1021/acs.jpcb.8b04604.

50. Wang, Y.; Wang, F.; Zhou, J.; Zhu, H.; Liao, Q.; Li, L.; Zhu, Y.; Yuan, Y.; Zhang, J. Effect of Molybdenum on Structural Features and Thermal Properties of Iron Phosphate Glasses and Boron-Doped Iron Phosphate Glasses. *Journal of Alloys and Compounds* **2020**, *826*, 154225, doi:10.1016/j.jallcom.2020.154225.

51. Kermani, F.; Nazarnezhad, S.; Mollaei, Z.; Mollazadeh, S.; Ebrahimzadeh-Bideskan, A.; Askari, V.R.; Oskuee, R.K.; Moradi, A.; Hosseini, S.A.; Azari, Z.; et al. Zinc- and Copper-Doped Mesoporous Borate Bioactive Glasses: Promising Additives for Potential Use in Skin Wound Healing Applications. *IJMS* **2023**, *24*, 1304, doi:10.3390/ijms24021304.

52. Islam, M.T.; Felfel, R.M.; Abou Neel, E.A.; Grant, D.M.; Ahmed, I.; Hossain, K.M.Z. Bioactive Calcium Phosphate–Based Glasses and Ceramics and Their Biomedical Applications: A Review. *J Tissue Eng* **2017**, *8*, 204173141771917, doi:10.1177/2041731417719170.

53. Cannio, M.; Bellucci, D.; Roether, J.A.; Boccaccini, Dino.N.; Cannillo, V. Bioactive Glass Applications: A Literature Review of Human Clinical Trials. *Materials* **2021**, *14*, 5440, doi:10.3390/ma14185440.

54. Pupilli, F.; Ruffini, A.; Dapporto, M.; Tavoni, M.; Tampieri, A.; Sprio, S. Design Strategies and Biomimetic Approaches for Calcium Phosphate Scaffolds in Bone Tissue Regeneration. *Biomimetics* **2022**, *7*, 112, doi:10.3390/biomimetics7030112.

55. Hossain, K.M.Z.; Patel, U.; Kennedy, A.R.; Macri-Pellizzeri, L.; Sottile, V.; Grant, D.M.; Scammell, B.E.; Ahmed, I. Porous Calcium Phosphate Glass Microspheres for Orthobiologic Applications. *Acta Biomaterialia* **2018**, *72*, 396–406, doi:10.1016/j.actbio.2018.03.040.

56. Sabbaghian, M.; Mahmudi, R.; Shin, K.S. Effect of Texture and Twinning on Mechanical Properties and Corrosion Behavior of an Extruded Biodegradable Mg–4Zn Alloy. *Journal of Magnesium and Alloys* **2019**, *7*, 707–716, doi:10.1016/j.jma.2019.11.001.

57. Deshmukh, K.; Kovářík, T.; Křenek, T.; Docheva, D.; Stich, T.; Pola, J. Recent Advances and Future Perspectives of Sol–Gel Derived Porous Bioactive Glasses: A Review. *RSC Adv.* **2020**, *10*, 33782–33835, doi:10.1039/D0RA04287K.

58. Owens, G.J.; Singh, R.K.; Foroutan, F.; Alqaysi, M.; Han, C.-M.; Mahapatra, C.; Kim, H.-W.; Knowles, J.C. Sol–Gel Based Materials for Biomedical Applications. *Progress in Materials Science* **2016**, *77*, 1–79, doi:10.1016/j.pmatsci.2015.12.001.

59. Huang, C.-L.; Fang, W.; Chen, I.-H.; Hung, T.-Y. Manufacture and Biomimetic Mineral Deposition of Nanoscale Bioactive Glasses with

Mesoporous Structures Using Sol-Gel Methods. *Ceramics International* **2018**, *44*, 17224–17229, doi:10.1016/j.ceramint.2018.06.180.

60. Nguyen, H.; Tuomisto, M.; Oksa, J.; Salminen, T.; Lastusaari, M.; Petit, L. Upconversion in Low Rare-Earth Concentrated Phosphate Glasses Using Direct NaYF 4 :Er 3+ , Yb 3+ Nanoparticles Doping. *Scripta Materialia* **2017**, *139*, 130–133, doi:10.1016/j.scriptamat.2017.06.050.
61. Galleani, G.; Santagneli, S.H.; Messaddeq, Y.; De Oliveira, M.; Eckert, H. Rare-Earth Doped Fluoride Phosphate Glasses: Structural Foundations of Their Luminescence Properties. *Phys. Chem. Chem. Phys.* **2017**, *19*, 21612–21624, doi:10.1039/C7CP03927A.
62. He, D.; Kang, S.; Zhang, L.; Chen, L.; Ding, Y.; Yin, Q.; Hu, L. Research and Development of New Neodymium Laser Glasses. *High Pow Laser Sci Eng* **2017**, *5*, e1, doi:10.1017/hpl.2016.46.
63. Podrazký, O.; Peterka, P.; Kašík, I.; Vytykáčová, S.; Proboštová, J.; Mrázek, J.; Kuneš, M.; Závalová, V.; Radochová, V.; Lyutakov, O.; et al. In-vivo Testing of a Bioresorbable Phosphate-based Optical Fiber. 8.
64. Vincent, M.; Duval, R.E.; Hartemann, P.; Engels-Deutsch, M. Contact Killing and Antimicrobial Properties of Copper. *J Appl Microbiol* **2018**, *124*, 1032–1046, doi:10.1111/jam.13681.
65. Peng, X.; Ai, F.; Yan, L.; Ha, E.; Hu, X.; He, S.; Hu, J. Synthesis Strategies and Biomedical Applications for Doped Inorganic Semiconductor Nanocrystals. *Cell Reports Physical Science* **2021**, *2*, 100436, doi:10.1016/j.xcrp.2021.100436.
66. Jiménez, J.A.; Hansen, D. Insights into the Composition-Structure-Property Relationship in P2O5CaO Na2O CuO Bio-Relevant Glasses. *Chemical Physics Impact* **2021**, *3*, 100029, doi:10.1016/j.chphi.2021.100029.
67. Paulose, P.I.; Jose, G.; Thomas, V.; Jose, G.; Unnikrishnan, N.V.; Warrier, M.K.R. Spectroscopic Studies of Cu2+ Ions in Sol-Gel Derived Silica Matrix. *Bull Mater Sci* **2002**, *25*, 69–74, doi:10.1007/BF02704598.
68. Kumar, P.; Sinha, A.N. Effect of Pulse Width in Pulsed Nd:YAG Dissimilar Laser Welding of Austenitic Stainless Steel (304 L) and Carbon Steel (St37). *Lasers Manuf. Mater. Process.* **2018**, *5*, 317–334, doi:10.1007/s40516-018-0069-z.
69. Butkutė, A.; Jonušauskas, L. 3D Manufacturing of Glass Microstructures Using Femtosecond Laser. *Micromachines* **2021**, *12*, 499, doi:10.3390/mi12050499.
70. Tsang, S.; Sun, C. Utilizing the Inverse Marangoni Convection to Facilitate Extremely-Low-Flow-Rate Intermittent Spray Cooling for Large-Area

Systems. *Applied Thermal Engineering* **2020**, *166*, 114725, doi:10.1016/j.applthermaleng.2019.114725.

71. Qian, Y.; Jiang, M.; Zhang, Z.; Huang, H.; Yan, J. On the Transformation between Micro-Concave and Micro-Convex in Nanosecond Laser Ablation of a Zr-Based Metallic Glass. *Journal of Manufacturing Processes* **2021**, *68*, 1114–1122, doi:10.1016/j.jmapro.2021.06.034.
72. Du, D.; He, Y.F.; Sui, B.; Xiong, L.J.; Zhang, H. Laser Texturing of Rollers by Pulsed Nd:YAG Laser. *Journal of Materials Processing Technology* **2005**, *161*, 456–461, doi:10.1016/j.jmatprotec.2004.07.083.
73. Shih, C.-Y.; Shugaev, M.V.; Wu, C.; Zhigilei, L.V. The Effect of Pulse Duration on Nanoparticle Generation in Pulsed Laser Ablation in Liquids: Insights from Large-Scale Atomistic Simulations. *Phys. Chem. Chem. Phys.* **2020**, *22*, 7077–7099, doi:10.1039/D0CP00608D.
74. Chen, H.; Rong, Y.; Huang, Y.; Wu, C. Crack Suppression of Glass Welding by Ultrafast Laser without Optical Contact Based on Light Modulation. *Optics & Laser Technology* **2023**, *164*, 109466, doi:10.1016/j.optlastec.2023.109466.
75. Cha, G.D.; Lee, W.H.; Sunwoo, S.-H.; Kang, D.; Kang, T.; Cho, K.W.; Kim, M.; Park, O.K.; Jung, D.; Lee, J.; et al. Multifunctional Injectable Hydrogel for In Vivo Diagnostic and Therapeutic Applications. *ACS Nano* **2022**, *16*, 554–567, doi:10.1021/acsnano.1c07649.
76. Lee, Y.; Kang, T.; Cho, H.R.; Lee, G.J.; Park, O.K.; Kim, S.; Lee, B.; Kim, H.M.; Cha, G.D.; Shin, Y.; et al. Localized Delivery of Theranostic Nanoparticles and High-Energy Photons Using Microneedles-on-Bioelectronics. *Adv. Mater.* **2021**, *33*, 2100425, doi:10.1002/adma.202100425.
77. Jonušauskas, L.; Gailevičius, D.; Mikoliūnaitė, L.; Sakalauskas, D.; Šakirzanovas, S.; Juodkazis, S.; Malinauskas, M. Optically Clear and Resilient Free-Form μ-Optics 3D-Printed via Ultrafast Laser Lithography. *Materials* **2017**, *10*, 12, doi:10.3390/ma10010012.
78. Moughames, J.; Jradi, S.; Chan, T.M.; Akil, S.; Battie, Y.; Naciri, A.E.; Herro, Z.; Guenneau, S.; Enoch, S.; Joly, L.; et al. Wavelength-Scale Light Concentrator Made by Direct 3D Laser Writing of Polymer Metamaterials. *Sci Rep* **2016**, *6*, 33627, doi:10.1038/srep33627.
79. Shan, D.; Gerhard, E.; Zhang, C.; Tierney, J.W.; Xie, D.; Liu, Z.; Yang, J. Polymeric Biomaterials for Biophotonic Applications. *Bioactive Materials* **2018**, *3*, 434–445, doi:10.1016/j.bioactmat.2018.07.001.
80. Guimarães, C.F.; Ahmed, R.; Marques, A.P.; Reis, R.L.; Demirci, U. Engineering Hydrogel-Based Biomedical Photonics: Design, Fabrication,

and Applications. *Adv. Mater.* **2021**, *33*, 2006582, doi:10.1002/adma.202006582.

81. Foroutan, F.; McGuire, J.; Gupta, P.; Nikolaou, A.; Kyffin, B.A.; Kelly, N.L.; Hanna, J.V.; Gutierrez-Merino, J.; Knowles, J.C.; Baek, S.-Y.; et al. Antibacterial Copper-Doped Calcium Phosphate Glasses for Bone Tissue Regeneration. *ACS Biomater. Sci. Eng.* **2019**, *5*, 6054–6062, doi:10.1021/acsbiomaterials.9b01291.
82. Qiao, X.; Qian, Z.; Li, J.; Sun, H.; Han, Y.; Xia, X.; Zhou, J.; Wang, C.; Wang, Y.; Wang, C. Synthetic Engineering of Spider Silk Fiber as Implantable Optical Waveguides for Low-Loss Light Guiding. *ACS Appl. Mater. Interfaces* **2017**, *9*, 14665–14676, doi:10.1021/acsami.7b01752.
83. Wang, S.; Li, J.; Zhou, Z.; Zhou, S.; Hu, Z. Micro-/Nano-Scales Direct Cell Behavior on Biomaterial Surfaces. *Molecules* **2018**, *24*, 75, doi:10.3390/molecules24010075.
84. Kapat, K.; Shubhra, Q.T.H.; Zhou, M.; Leeuwenburgh, S. Piezoelectric Nano-Biomaterials for Biomedicine and Tissue Regeneration. *Adv. Funct. Mater.* **2020**, *30*, 1909045, doi:10.1002/adfm.201909045.
85. Limongi, T.; Dattola, E.; Botta, C.; Coluccio, M.L.; Candeloro, P.; Cucè, M.; Scopacasa, B.; Gallo Cantafio, M.E.; Critello, C.D.; Pullano, S.A.; et al. Influence of the Fabrication Accuracy of Hot-Embossed PCL Scaffolds on Cell Growths. *Front. Bioeng. Biotechnol.* **2020**, *8*, 84, doi:10.3389/fbioe.2020.00084.
86. De Zanet, A.; Pedroni, M.; Salvo, M.; Vassallo, E.; Casalegno, V. Plasma Etching as a Surface Engineering Technique for SiC/SiC Composites to Improve Joint Strength. *Ceramics International* **2023**, *49*, 10608–10614, doi:10.1016/j.ceramint.2022.11.248.
87. Zhang, F.; Wang, C.; Yin, K.; Dong, X.R.; Song, Y.X.; Tian, Y.X.; Duan, J.A. Quasi-Periodic Concave Microlens Array for Liquid Refractive Index Sensing Fabricated by Femtosecond Laser Assisted with Chemical Etching. *Sci Rep* **2018**, *8*, 2419, doi:10.1038/s41598-018-20807-1.
88. Yang, T.; Li, M.; Yang, Q.; Lu, Y.; Cheng, Y.; Zhang, C.; Du, B.; Hou, X.; Chen, F. Femtosecond Laser Fabrication of Submillimeter Microlens Arrays with Tunable Numerical Apertures. *Micromachines* **2022**, *13*, 1297, doi:10.3390/mi13081297.
89. Lu, D.-X.; Zhang, Y.-L.; Han, D.-D.; Wang, H.; Xia, H.; Chen, Q.-D.; Ding, H.; Sun, H.-B. Solvent-Tunable PDMS Microlens Fabricated by Femtosecond Laser Direct Writing. *J. Mater. Chem. C* **2015**, *3*, 1751–1756, doi:10.1039/C4TC02737J.

90. Im, B.; Prasetyo, F.D.; Yudistira, H.T.; Khalil, S.M.; Cho, D.-H.; Byun, D. Drop-on-Demand Electrohydrodynamic Jet Printing of Microlens Array on Flexible Substrates. *ACS Appl. Polym. Mater.* **2023**, *5*, 2264–2271, doi:10.1021/acsapm.3c00054.

91. Deng, C.; Kim, H.; Ki, H. Fabrication of a Compound Infrared Microlens Array with Ultrashort Focal Length Using Femtosecond Laser-Assisted Wet Etching and Dual-Beam Pulsed Laser Deposition. *Opt. Express* **2019**, *27*, 28679, doi:10.1364/OE.27.028679.

92. Ceci-Ginistrelli, E.; Pugliese, D.; Boetti, N.G.; Novajra, G.; Ambrosone, A.; Lousteau, J.; Vitale-Brovarone, C.; Abrate, S.; Milanese, D. Novel Biocompatible and Resorbable UV-Transparent Phosphate Glass Based Optical Fiber. *Opt. Mater. Express* **2016**, *6*, 2040, doi:10.1364/OME.6.002040.

93. Pugliese, D.; Konstantaki, M.; Konidakis, I.; Ceci-Ginistrelli, E.; Boetti, N.G.; Milanese, D.; Pissadakis, S. Bioresorbable Optical Fiber Bragg Gratings. *Opt. Lett.* **2018**, *43*, 671, doi:10.1364/OL.43.000671.

Chapter 5

Polymers: Laser Induced Graphene

5.1 Graphene: A Brief Introduction

Graphene has been receiving prime attention in the past couple of decades in scientific research. This allotrope of carbon has a 2D arrangement of carbon atoms. As a 2D material, graphene possesses multiple desirable functional properties, such as good electrical conductivity, thermal conductivity, mechanical stability, and biocompatibility, to name a few. Another interesting property of graphene is its zero bandgap, as shown in Figure 5.1. The planar carbon atoms share sp^2 electrons with their neighboring three members. Perpendicular to the sp^2 hybrid orbitals, there exists $2sp$ orbitals which have delocalized π bonded electrons that contribute to electrical conductivity [1]. Furthermore, the sp^2 hybridization forms a strong binding, hence the high mechanical strength. Specifically, the unique electronic properties in combination with good mechanical stability has resulted in enhanced interest for their application in the field of electronics for integrated circuits as electrodes and sensors [2]. Moreover, its high surface area and the possibility to functionalize with selective chemical groups provide an efficient platform to detect adsorbed molecules, especially for biosensing. Recently, apart from graphene, graphene oxide (GO) has also been receiving interest for a variety of reasons. The oxygen functional groups make GO polar and therefore excellent dispersibility in a variety of solvents. Additionally,

the oxygen functional groups can serve as reactive sites for functionalization of GO. Eventhough, GO does not conduct well, the reduced form of GO conducts well enough for it to mimic applications of graphene, such as in strain and gas sensing. Moreover, GO has the advantage of possibility for large scale production at relatively low cost when compared to graphene.

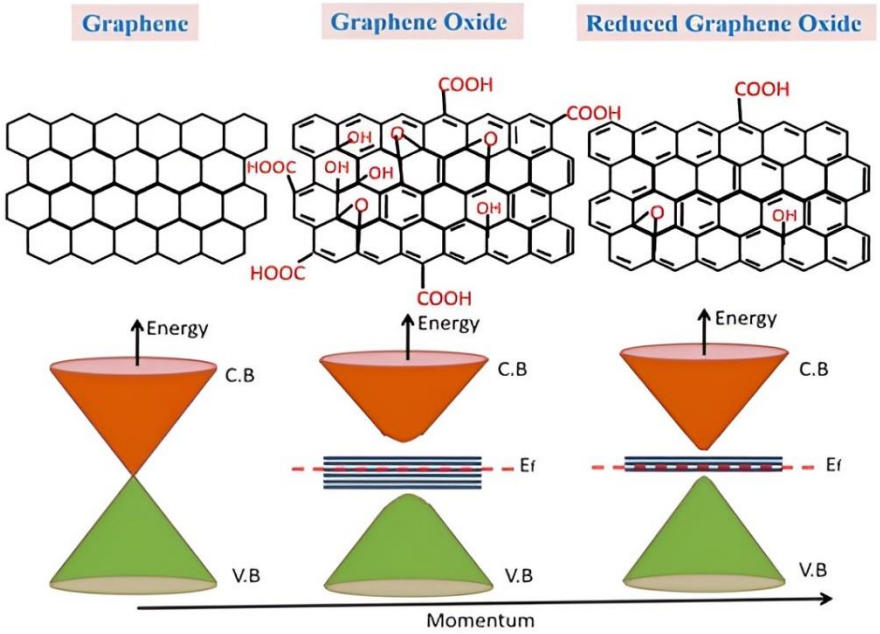

Figure 5.1. Lattice structure and associated band diagram of graphene, graphene oxide, and reduced graphene oxide **[3]**.

5.1.1 Applications Using Graphene/Graphene oxide

The interest surrounding graphene is primarily due to the possibility of employing this single material for various applications. Herein, some of the many applications of graphene are briefly mentioned.

Graphene Field-Effect Transistor

The band structure of graphene renders it a semiconductor with zero bandgap. Interestingly, the carrier density of graphene could be tuned based on the applied gate voltage. This property of graphene makes it an able competitor to the most popular semiconductor material, i.e., silicon. Besides the zero bandgap, in comparison to silicon, the charge carriers can travel much faster without

interaction with surrounding atoms or defects. Therefore, they are an ideal candidate for field-effect transistor fabrication, as shown in Figure 5.2, with switching speeds of more than twice the current silicon-based transistors [4]. Also, the switching speed remains significantly high even at high carrier densities. Along with electrical conductivity, the thermal conductivity of graphene would make it ideal for dissipation of excess heat generated in electronic components [5].

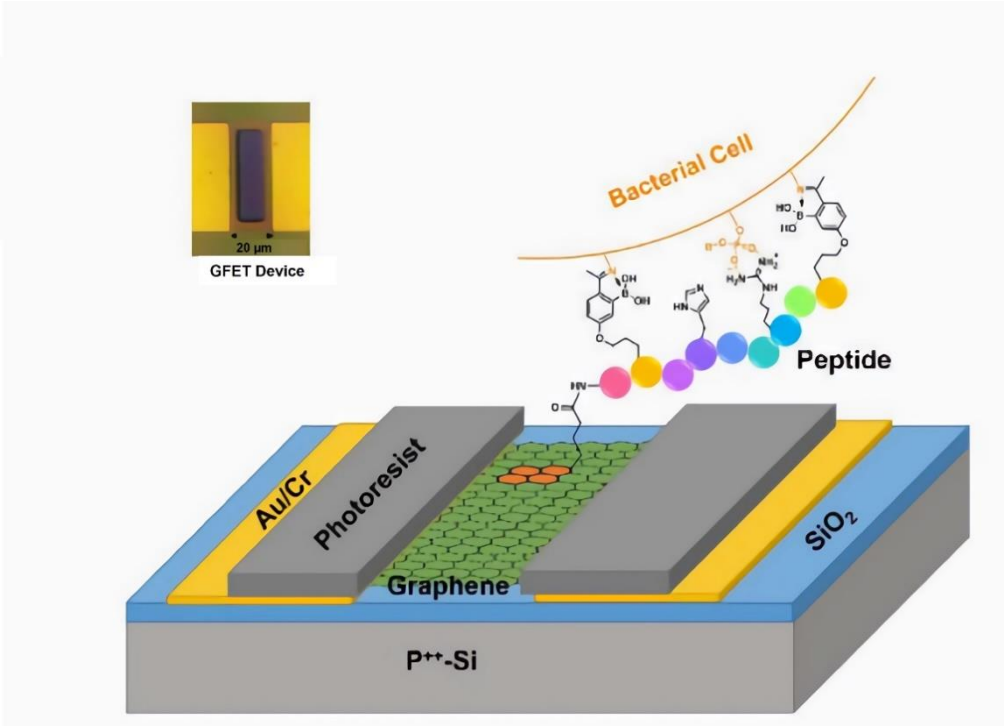

Figure 5.2. Illustration of a Graphene-FET functionalized by a pyrene-conjugated peptide probe binding to a bacterium surface **[6]**.

Gas Detection

Molecular adsorption on graphene layers modifies the conductance/resistance of the material in a significant manner. Once adsorbed, the gas molecules could create scattering centers leading to a fluctuation in charge transport properties. Apart from the sensing property by itself, the long mean free path of the charge carriers sets graphene apart from traditional solid-state devices where the inherent thermal noise acts as a barrier towards single molecule level detection. The carrier density of graphene-based gas sensors linearly increases with adsorption

providing a predictable trend up to saturation wherein the sensor property can be restored by thermal annealing, causing desorption of the gas molecules [7].

Biosensors

The biocompatibility, high surface area, and enhanced signal response of graphene-based materials make them an ideal candidate for detecting biomolecules such as DNA, antibodies, and proteins, as shown in Figure 5.3[8]. The conjugated graphene structure is ideal for electron transfer from the bio-receptor molecules resulting in high sensitivity. Also, the members of the graphene family are efficient quenchers for fluorescent molecules compared to metals. That is especially interesting for studying protein interactions and biomolecular level changes. However, the graphene property such as layer numbers, functionalization, and oxidation state would dictate the selectivity towards the bio-receptor molecules.

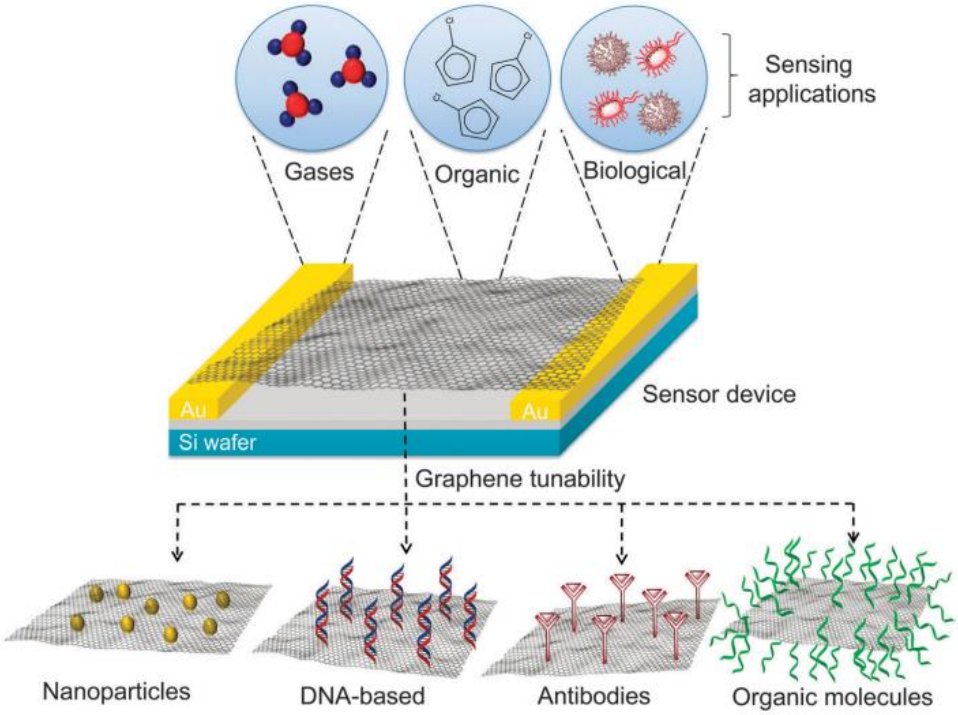

Figure 5.3. Schematics of a graphene based sensing platform demonstrating potential applications in detection of biomolecules, organic molecules, microbial cells and nanoparticles **[9]**.

5.1.2 Graphene Preparation

Graphene and its related forms can be produced through various techniques, as illustrated in Figure 5.4. These multiple approaches offer specific advantages in terms of quantity, quality, and cost. The single application requirements drive the choice of the most appropriate fabrication technique.

Exfoliation

This method for graphene preparation can be broadly classified into mechanical and chemical exfoliation methods. The former approach is suitable for generating high-quality graphene, especially for research purposes. In mechanical exfoliation, the Van der Waals attraction forces between adjacent layers of bulk graphene structure are overcome by the applied mechanical force. However, the yield is relatively low, so it is not suitable for large-scale production. Common mechanical techniques include micromechanical cleavage, sonication and ball milling [10,11].

In the case of chemical exfoliation, the yield is relatively higher and is feasible for large-scale production. Common techniques include liquid-phase, electrochemical, and supercritical fluid exfoliation. However, the disadvantage of this technique lies in the low quality of prepared graphene in terms of oxidation, defects, and inhomogeneous nature [12].

Chemical Vapor Deposition

Large graphene sheets can be produced through electrochemical deposition of graphene onto transition metal substrates such as copper and nickel. This occurs through the simple thermal decomposition of hydrocarbons on the metal surface [13]. To be used for electronic sensing or flexible substrates, the graphene must be transferred on substrates such as SiO_2 and SiC. After linking of generated graphene to polymers such as PMMA and PDMS, the transfer can be performed by wet etching of the substrate metal and the transfer of the graphene onto the target. Eventually, the polymer can be removed in acetone. Recent advancements in this technique yield graphene with remarkable electronic properties.

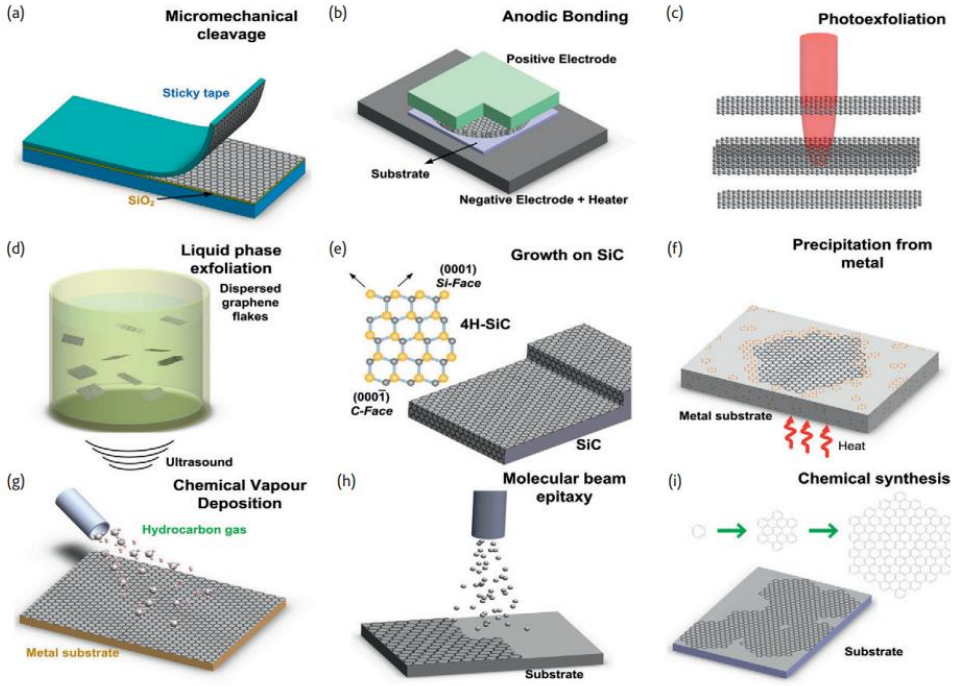

Figure 5.4. Schematic illustration of different graphene production techniques **[14]**.

Reduction of Graphene Oxide

Bulk production of graphene is a current hot research topic towards a more scalable fabrication process. Amongst different available methods, graphene oxide (GO) reduction is considered the most feasible method. GO intrinsically contains hydrophilic functional groups. The oxygen-containing functional groups, such as hydroxy, carbonyl, and carboxy groups, are removed to provide the intrinsic properties of graphene, especially in terms of electrical conductivity. Therefore, reduced graphene oxide (rGO) quality is generally assessed through electrical conductivity measurements. The different approaches to generating rGO are briefly described below:

- Chemical: The most widely used chemical reduction method involves the use of hydrazine monohydrate ($N_2H_4.H_2O$). rGO prepared using this approach most closely resembles pristine graphene. Other chemical

alternatives include using catalysts such as aluminium and zinc in acidic environments and organic solvents like DMF and alcohols [15].

- Photoreduction: Plasma and photocatalysis methods are two major mechanisms of photoreduction of GO. In the case of plasma-mediated reduction, multiple mechanisms were suggested, such as rupturing of oxygen functional groups through collision with ions. The released oxygen ions form oxygen molecules through covalently binding with other oxygen species. Another possibility involves the formation of nitric oxide (NO) Through reaction with atmospheric nitrogen and oxygen. The NO further reacts with oxygen functional groups to form NO_2 and rGO [16]. On the other hand, photocatalysis mainly involves the generation of radicals and electron-hole pair, which cause the reduction of GO, as illustrated in Figure 5.5[17].

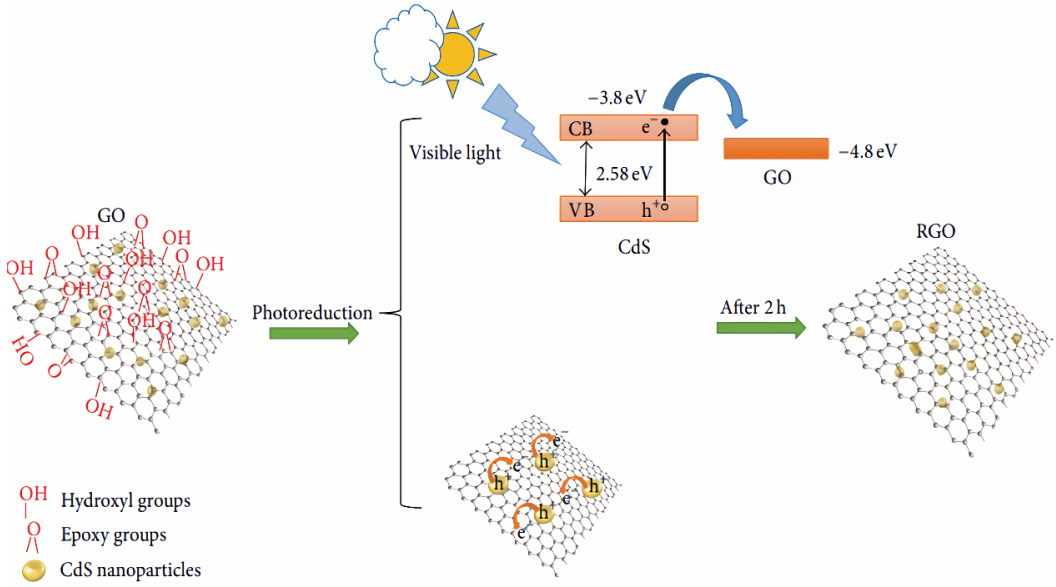

Figure 5.5. Schematic illustration of photoreduction process of graphene oxide where CdS nanoparticle provided electrons for reduction under visible-light radiation **[18]**.

- Thermal: This approach involves the removal of oxygen functional groups as CO/CO_2 gas at different annealing temperatures. The removal occurs in the order of intercalated water molecules followed by carboxyl groups and eventually epoxide groups at high temperatures of about $1000^\circ C$ [19]. Microwave has also been used to rapidly reduce rGo [20]. Nonetheless, the removal mechanism is similar to the thermal annealing case.

This chapter uses a photothermal approach based on pulsed laser interaction to generate rGO from a polymer material (polyimide). A more detailed description is provided in the following sections.

5.1.3 Laser Induced Graphene

Laser induced graphene is a relatively recent technique and was first demonstrated in 2014 using a CO_2 laser to photothermally transform commercial polyimide (PI) into rGO [21]. This technique has garnered tremendous attention from this initial demonstration due to its ability to to possess different functionalities such as piezoresistive, biosensing, gas sensing, and many more, resulting in a truly multifunctional nature with excellent mechanical, electrical, and thermal properties.

The flexibility in fabrication offered by laser processing in terms of the ability to pattern makes it possible to print the laser induced graphene (LIG) onto any substrate for the intended functionality, either for physical/chemical sensing or to improve the mechanical strength. In a single fabrication step, this technique combines large-scale patterning without the need for a clean-room environment, wet chemical treatment, or toxic solvents. Consequently, this technique has stimulated interest in fundamental and applied research areas. The application of LIG forms a substantial set, ranging from chemical sensing of analyte molecules such as glucose and dopamine, gas sensing to energy storage devices and speech recognition systems [22–25].

Depending on the interacting laser wavelength, the formation mechanism can be either photochemical or photothermal [26] in the case of infrared and visible laser wavelengths. In the infrared wavelength, CO_2 laser (10.6 μm) remains the most popular choice for LIG formation. In photothermal ablation, due to the low photon energy, insufficient to directly break atomic bonds, absorbed light is first converted to thermal energy which enables the carbonization of the polymer material. The transformation involves thermal induced breaking of the $C-N$

bonds in the polymer chain and conversion of sp^3 hybridized carbon atoms to sp^2 hybridization, along with the formation of side products such as CO, C_2, CN AND HCN, as shown in Figure 5.6[27].

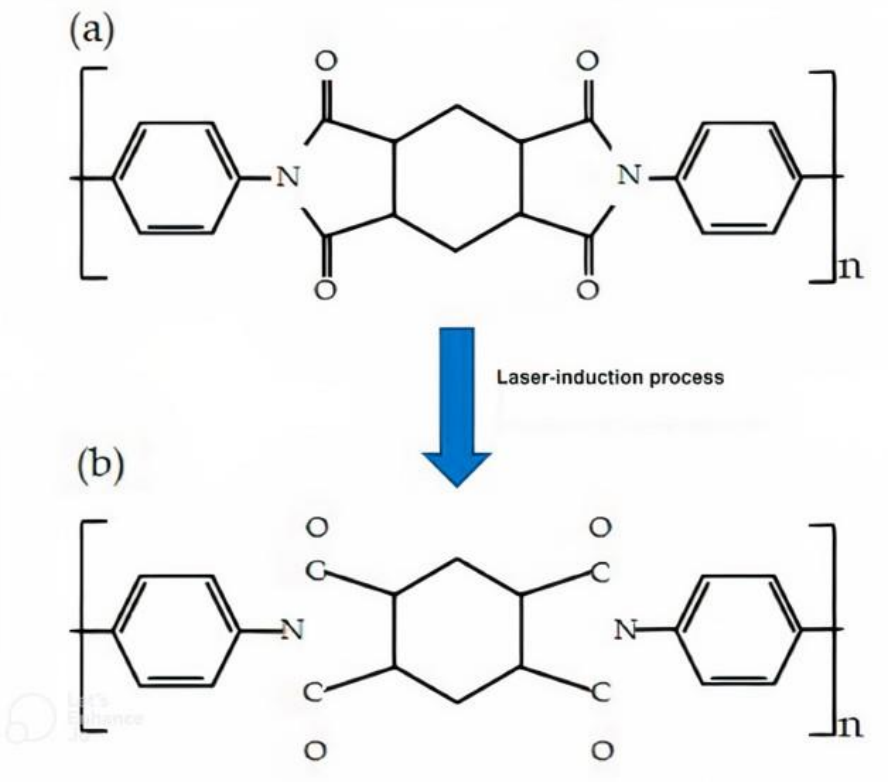

Figure 5.6. Mechanism of formation of LIG. Chemical structure of polyimide film (a) before and (b) after ablation process **[28]**.

In the case of UV laser (i.e. $\lambda < 400\,nm$), the mechanism proceeds via photochemical ablation, where the photon has sufficient energy to perform direct chemical bond cleavage resulting in a minimal thermal effect on the sample [29]. The photochemical ablation route is especially beneficial for applications that require minimal thermal damage to the substrate material. Also, the relatively low wavelength makes obtaining smaller focal spot size possible.

In this thesis's work, a NIR nanosecond laser (1064 nm) was used to generate LIG from polyimide starting from a commercial Kapton tape. The galvanometric scan system of the laser enables LIG formation in any pre-designed pattern as exemplified in Figure 5.7. The laser interaction with polymers presents a complex process. For polymers, the NIR laser wavelength has relatively low absorption

compared to UV and mid-infrared wavelengths. Therefore, the laser interaction process can be expected to proceed via a photothermal ablation mechanism, as described before.

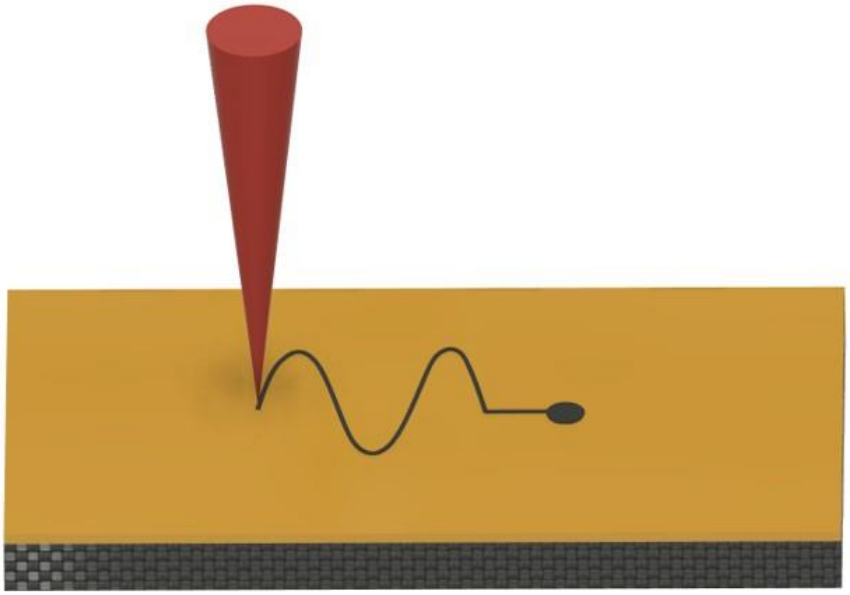

Figure 5.7. Laser patterning of LIG on polyimide tape adhered to a CFRP substrate.

5.2 Results and Discussion

5.2.1 Surface Morphology

The ablation characteristics evolve along with the material modification for ablation at a single spot. Due to chemical structure alteration induced by the primary pulse, the ablation characteristics from the following consecutive pulses can significantly differ. Especially for transparent polymer materials, the incubation effect plays an important role by increasing the material absorption coefficient during the multi-pulse interaction [30].

Such an absorption enhancement can be explained through the carbonization of the polymer material caused by thermal reactions. Moreover, nano-scale absorbing particles can strongly influence the absorption properties through local temperature spike induced carbonization [31]. Figure 5.8demonstrates the incubation effect during IR nanosecond laser modification of the Kapton tape

material at a scan speed of 1 mm/s and an average power of $(9W)$. Two laser line scans were performed using identical laser parameters with slight difference in the scan approach. Interestingly, LIG was generated for only one line scan. For the first case involving a direct line scan, the LIG transformation ceased to occur due to insufficient energy deposition. However, for the latter case prior to line scan, the laser spot was made stationary at a single spot for 1 sec to deposit larger number of pulses (20 kHz), causing greater localized thermal effect which induces carbonization of the polyimide. With this carbonized spot as the starting point, the LIG transformation proceeds along the laser scan path, thereby confirming the influence of incubation effect [32]. In the second case, carbonization at the starting point of the scan enhanced the absorption and thermal effect, inducing the LIG transformation for the neighboring regions.

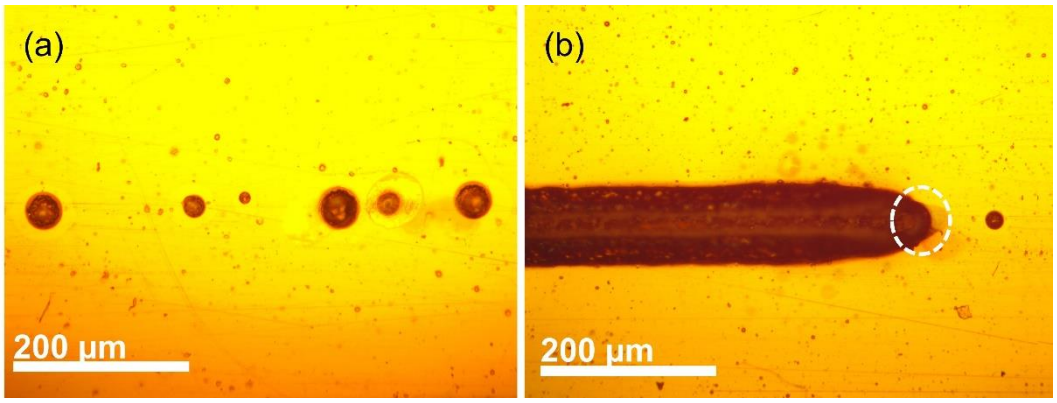

Figure 5.8. Modifications performed on Kapton substrate at an average power of 9 W and scan speed of 1 mm/s (a) direct laser written scan line (no incubation); (b) laser scan line written after initial stationary spot (white dot circle) inducing carbonization (incubation).

The carbonization of the transparent polymer has a dual role in this case. As mentioned before, during the initial phase of interaction and modification, carbonization enhances optical absorption. However, at the later stage of material modification, the carbonized layer becomes increasingly resistant to further ablation, making it difficult to etch deep modification features.

Laser ablation of the polyimide presents a hierarchical surface morphology. The interaction and optical absorption by the polymer cause complex thermal events such as swelling and bubble formation during rapid polymer melt-cooling and material removal due to ablation at higher intensities [32–35]. These events

form the micro-features along the laser-processed region. Figure 5.9shows SEM images of the laser-processed region on the polyimide surface. From Figure 5.9(a), a combination of different surface modifications can be observed along the laser scan path. Following the Gaussian intensity distribution of the pulse, the central region is completely removed through ablation. Apart from the material removal, micro-surface features such as swelling and bubble formation exist.

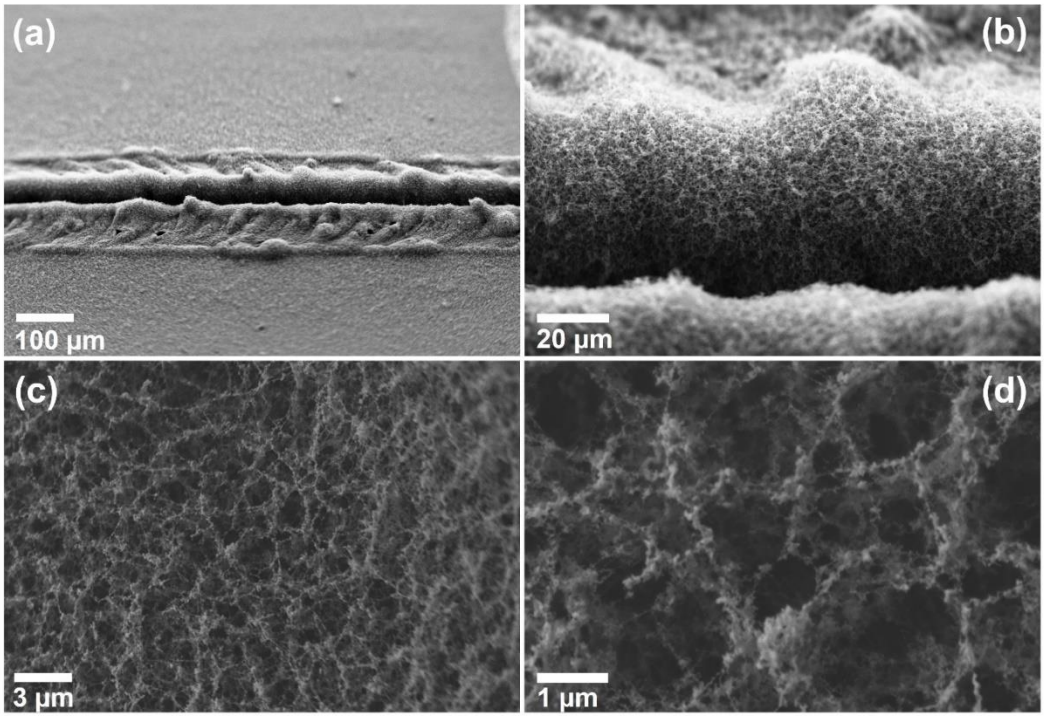

Figure 5.9. FESEM images of the fabricated LIG, (a,b) Side view of the laser ablated region at different magnifications; (c,d) porous and fiber like LIG nanostructure at different magnifictions.

As shown in Figure 5.9(a,b), besides the ablated region, the polymer material appears to be swollen, representing a convex structure. At regions close to the Gaussian wings, the laser fluence is below the ablation threshold of the polymer. The swelling indicated decreasing material density because of laser interaction and melt formation. The laser induced electronic excitation is transferred as intra-/inter-molecular vibrational and rotational energy. The photo-decomposition mechanism causes volume expansion through the formation of small fragments with high kinetic energy. Apart from the non-equilibrium melt-cooling due to photothermal interaction with the polymer, gaseous compounds are generated,

resulting in increased pressure and eventual expansion, leading to swell formation [36–38].

Apart from swelling, random bubble formations can be observed besides the ablated region. Such bubble formations could be attributed to first-order phase transitions, commonly observed with laser interaction of relatively transparent polymers. As a result of the rapid phase transformation, bulk boiling and rapid cooling resulting in a bubble like structural features [39]. The above-mentioned microfeatures confirm a photo-thermal ablation mechanism for the polyimide substrate modification. These microstructures are not commonly reported during LIG fabrication as either UV or CO_2 sources are mostly sought and have a better absorption cross-section for polyimide material. However, the former is rather expensive, and the latter has MIR wavelength emission, resulting in a relatively large focal spot size which might be a limiting factor for certain applications [40].

Besides the microstructure, a porous and fibrous network like nanostructure exists as shown in Figure 5.9(c,d). This nanostructure agrees well with LIG generation reported in previous studies, which have confirmed a heptagon-pentagon and hexagon hybrid lattice due to laser induced temperature and pressure at a short timescale [41,42].

5.2.2 Raman Spectroscopic Characterization

Raman spectroscopy is one of the most employed techniques for graphene characterization. Information about structural defects and number of layers can be obtained through the Raman analysis. The Raman spectra obtained from the LIG samples in this work, shown in Figure 5.10, suggests the presence of reduced graphene oxide. The two peaks of relatively higher intensity, typical to carbonaceous materials correspond to the characteristic G and D Raman bands. The graphitic lattice stretching of sp^2 carbon atoms result in the G band at $1580\ cm^{-1}$, whereas the breathing vibrations of the sp^2 hybridized carbon is responsible for the disorder (D band) at $1335\ cm^{-1}$ [43]. As the name suggests, the latter arises mainly because of hampered carbon vibrations due to the oxygen-containing functional groups acting as defects in the material structure. The analysis of disorder and defects in the graphene structure can be performed through the intensity ratio measurements of D and G bands. The value of I_D/I_G ratio at about 0.99 is typical of graphene and reduced graphene oxide. Specifically, unlike graphene oxide (GO), reduced graphene oxide (rGO) is conductive due to the removal of oxygen containing functional groups [44].

The removal of oxygen functional groups as gases proceed at first through the detachment of oxygen functional groups and the formation of radicals at high temperatures ($\sim 1000\,K$). These radicals, along with the atmospheric oxygen, interact with defects of graphene oxide, resulting in the release of CO or CO_2 gases. The thermal-based events that control the graphene oxide reduction occur in the picosecond timescale [45]. A broadened 2D region exists in the Raman spectra, apart from the D and G bands. The 2D band is another signature of graphene, which denotes a second-order process of double resonance Raman scattering causing two phonon emissions near the K point of the Brillouin zone and is strongly dependent on the graphene phonon structure. The monolayer graphene has a rather symmetrical Raman shift peak at about $2700\,cm^{-1}$, and therefore the broadening in the 2D region confirms the presence of a multilayer structure, as reported in previous studies [46,47]. In addition to the broadening effect, the presence of oxygen functional groups prevents efficient stacking of graphene layers, thereby causing a slight shift in the peak [48]. Interestingly, there exist Raman shift peaks at $2930cm^{-1}$ and $3165cm^{-1}$. The former has been previously reported to be caused by $C-H$ bond presence. The latter Raman shift is due to the presence of hydroxyl and carboxylic functional groups [49].

It is important to reiterate that the LIG mentioned in this study solely refers to the conductive rGO resulting from the laser ablation of polyimide-based substrate. However, the conductive and piezoresistive properties of the LIG makes it an able large-scale application-oriented alternative to monolayer graphene or other carbonaceous forms such as carbon nanotubes, which are yet to be realized for large-scale production in an affordable manner [50].

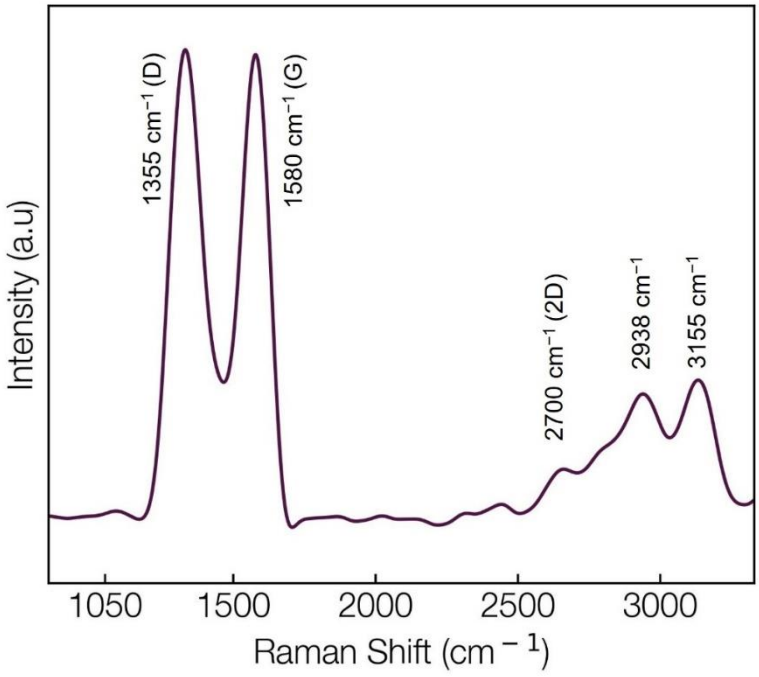

Figure 5.10. Raman spectra of the generated LIG.

5.2.3 LIG Strain Sensor Fabrication and Analysis

LIG can be generated on the polyimide material (Kapton) attached to any substrate, ranging from glass, polymers metals, and composite materials. Specifically, LIG fabrication on composite materials is interesting to fabricate inexpensive strain sensors taking advantage of their piezoresistive properties. Fiber-reinforced polymer substrates have been considered an ideal replacement for conventional metals and ceramics in aerospace, construction, and maritime industries [51,52]. However, these composite materials are prone to operational failures in their matrix phase and can also cause debonding [53,54]. Therefore, it becomes important to perform structural health monitoring to prevent failure accumulation of the composite materials, leading to catastrophic events [55].

Therefore, LIG generation is used in this study to fabricate a strain sensor on a CFRP composite material. Furthermore, the laser parameters are selected such that the fabricated strain sensor has superhydrophobic properties, which will be discussed in the following sections. The LIG pattern consists of a simple serpentine design of about 2 cm in length between the inner contact points, as

shown in Figure 5.11(a). The contact points were prepared on the LIG pattern using fast-drying silver paste and copper lead wires to measure the four-wire resistance using a Keithley multimeter, as shown in Figure 5.11(b).

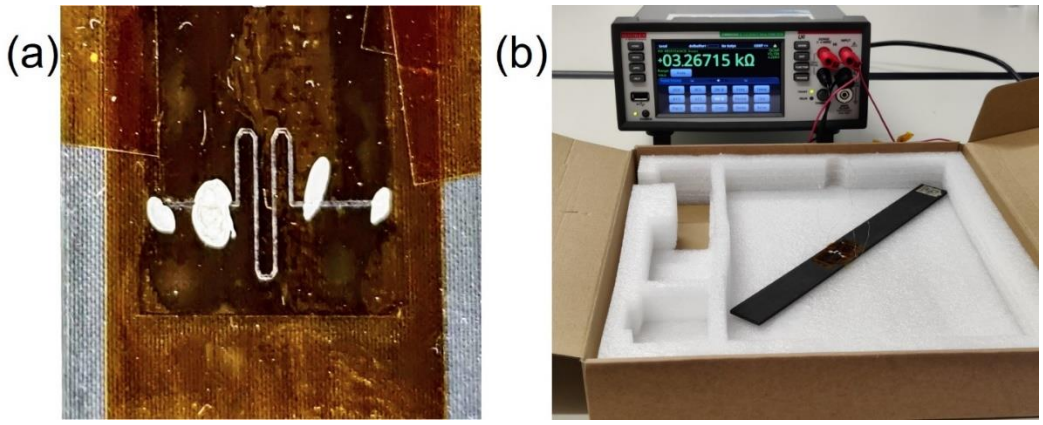

Figure 5.11. (a) Image of the serpentine LIG pattern with silver paste contacts; (b) LIG sensor on CFRP substrate connected to the multimeter in a four-wire setup.

In piezoresistive materials, the application of strain causes resistance to change. The relation between the applied strain and the resulting resistance variation is represented by gauge factor (GF) given by,

$$GF = \frac{\Delta \mathrm{R}/\mathrm{R}}{\varepsilon} \tag{1}$$

where $\Delta R/R$ represents the normalized resistance change, and ε represents the mechanical strain.

A standard three-point bend test was performed under flexure, as shown in Figure 5.12(a) to characterize the piezo resistivity and obtain the gauge factor of the sensor. The mechanical test was performed at an ambient temperature $(22 \pm 1\ °C)$ with a Zwick Roell Z100 machine. A load cell of $5\ kN$ was applied at a rate of $0.5\ mm/s$ and edge-to-edge spacing of $10\ mm$. The test was performed up to a maximum loading nose deformation at $1mm$. The copper contact leads of the LIG sensor were connected to the Keithley multimeter to record the change in resistance during the bending test.

The flexural strain during the bending test was calculated using the following formula,

$$\varepsilon_f = \frac{6Dd}{L^2} \tag{2}$$

where ε_f is the flexural strain, D is the deflection at the CFRP plate centre, d represents the plate thickness and L is the distance between the support spans.

The normalized resistance changes during the bend test exhibited a linear relationship up to a maximum test strain of 0.16%. As shown in Figure 5.12(b), a linear fit to the obtained data provides a GF value of 40.

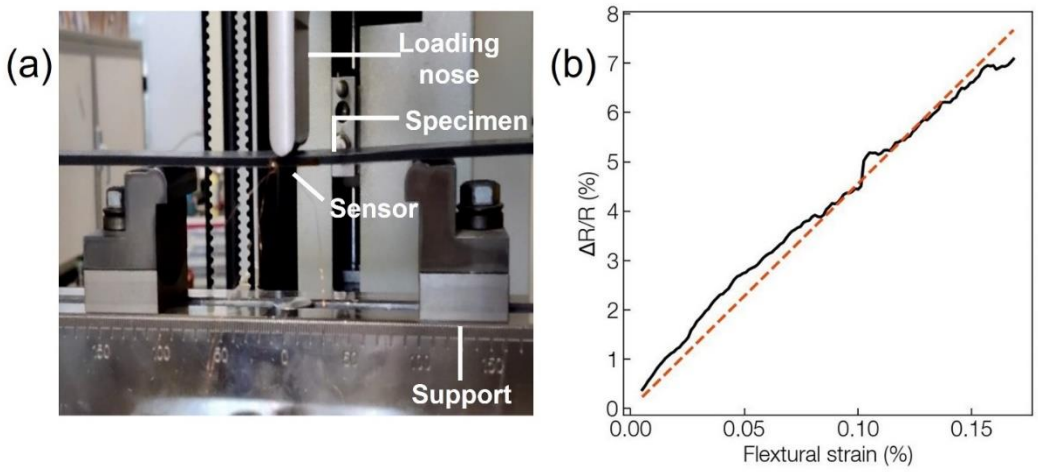

Figure 5.12. (a) Three-point bend test setup with the LIG sensor generated on CFRP substrate as the specimen; (b) Obtained normalized resistance change vs applied flexural strain.

The LIG strain sensor fabricated in this study displays good sensitivity with a GF of 40, in comparison to the commercial strain sensors with a GF < 5 [56]. Recent studies have fabricated strain sensors based on different carbonaceous materials, such as carbon nanotubes and graphene nanoplatelets [57]. However, in the above-mentioned studies, the fabrication process is relatively complex and involves multiple steps with chemical reagents. Zhen Pei et al. fabricated silver-coated carbon nanotubes based wearable strain sensor with a GF of 62.8 [58]. In comparison, the LIG based sensors offer a rapid fabrication and inexpensive alternative to large-scale production of piezoresistive sensors. Previous studies on LIG based strain sensors have demonstrated high GF > 100 [59,60]. As strain sensors have many outdoor applications, the sensor needs to maintain its functional stability under conditions such as high humidity or even complete immersion under water. Therefore, this study also demonstrates the

superhydrophobic property of the fabricated strain sensors. Also, the superhydrophobic LIG can be transferred to different substrates ranging from metals, glass, semiconductors, and polymers. Furthermore, the stability of the superhydrophobicity is assessed through complete immersion under water. The following sections provide results and discussions on the superhydrophobic property of the generated LIG.

5.3 Superhydrophobic LIG

The carbonaceous nature of graphene would naturally result in hydrophobic properties. However, in the case of LIG generation in an open atmosphere, oxygen could cause strong oxidation of the rGO, thereby rendering the surface hydrophilic [61]. Li et al. directly fabricated superhydrophobic LIG by performing the ablation in a controlled argon environment [62]. Few other studies have fabricated superhydrophobic (SH) LIG by laser ablation in open air followed by fluorosilane coating [63]. Alternatively, researchers have used tunability in laser parameters to minimize surface oxidation to result in SH surfaces [64,65].

The last-mentioned approach was followed in this study to generate SH-LIG directly. The laser parameters for the strain sensor fabrication were selected to result in superhydrophobic properties and piezo resistivity. In fact, the SH-LIG exhibited ultrahydrophobic properties with high contact angle $(165°)$ and low roll-off angle $(5°)$ for a $6\ \mu L$ droplet on the surface, as shown in Figure 5.13(a). Additionally, forceful impinging water droplets from a syringe needle are completely repelled due to the minimal surface interaction resulting in droplet bounce and exit, as shown in Figure 5.13(b). The above observations confirm single step fabrication of an extremely water-repellent surface. It is worth mentioning that the contact angle values obtained in this study remain greater than previously reported SH-LIG fabrication, with water contact angle values at about $155°$ [66,67].

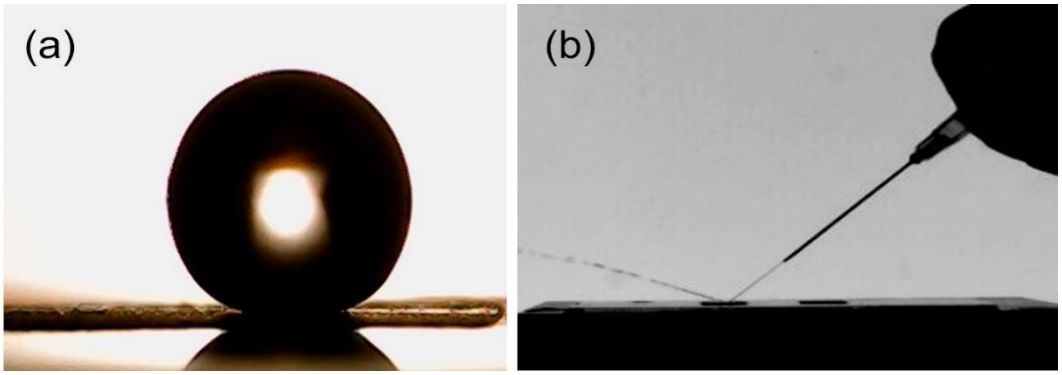

Figure 5.13. (a) 6 μL water droplet on the SH-LIG on a glass substrate; (b) Water jet bouncing off from the SH-LIG.

5.3.1 Substrate Independent SH-LIG

The laser ablation of the polyimide tape deposits the LIG well adhered to the substrate. The laser itself can then be used to create a sharp boundary cut between the modified and unmodified regions. Hence, after the modification, the unmodified tape can be simply peeled off as shown in Figure 5.14(a,b,c). Following the above method, the generated LIG was transferred to different substrates such as aluminum alloy Al6061, low-density polyethylene, soda-lime glass and silicon. Therefore, the possibility to combine complex patternability offered by the laser system with a simple transfer process onto different substrates makes the LIG fabrication process a truly large-scale fabrication technique.

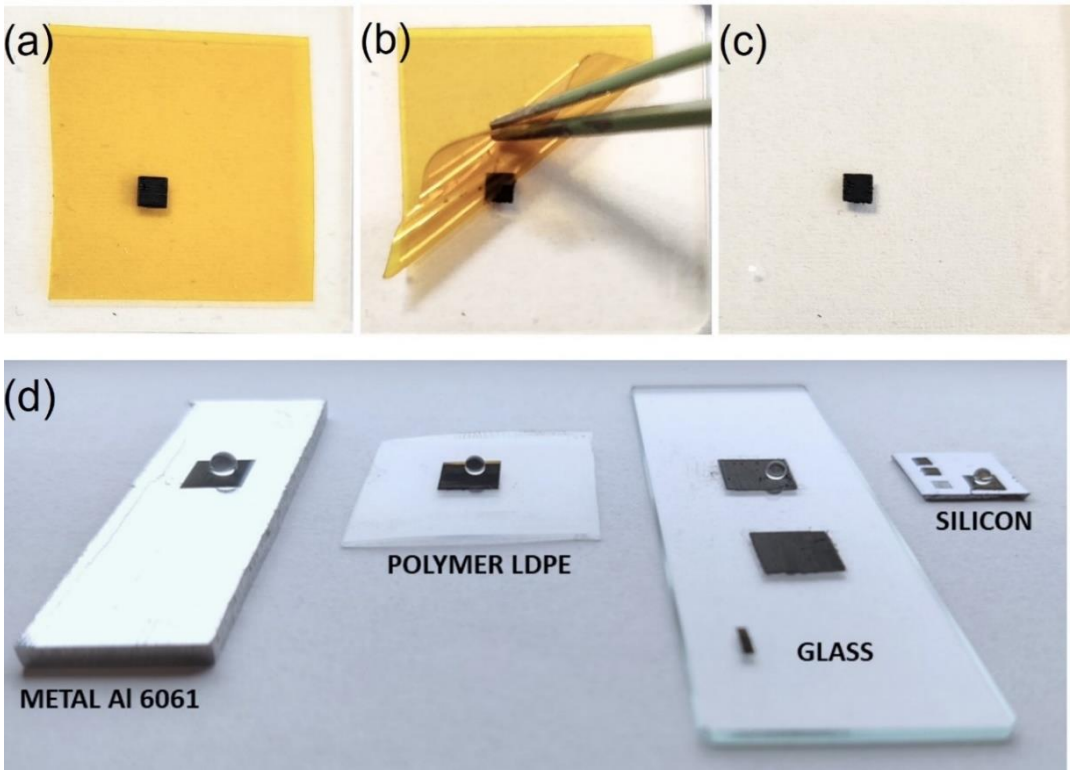

Figure 5.14. (a,b,c) Generated SH-LIG transfer from the Kapton tape to the glass substrate by tape peel-off in the corresponding sequence; (d)Water droplets on the SH-LIG fabricated on different substrates in a one-step laser ablation process.

The laser modification parameters for LIG fabrication on different materials were fixed as constant throughout this study. As shown in Figure 5.14(d), LIG exhibits superhydrophobic properties on all the substrates.

At this point, it becomes important to characterize the surface both chemically and topographically to support the claim of substrate-independent superhydrophobicity. The SEM images have already provided information regarding the nano-porous and fibrous nature of the LIG. However, ultrahydrophobic surfaces must have a hierarchical surface texture previously demonstrated by several studies on superhydrophobicity [68]. Therefore, it becomes important to analyze the micro-surface topography using the surface profilometer. Figure 5.15, presents the 3D surface map of the SH-LIG on glass surfaces whereas Table 5.1 shows the average surface roughness values (Sa) of the LIG obtained on different samples,

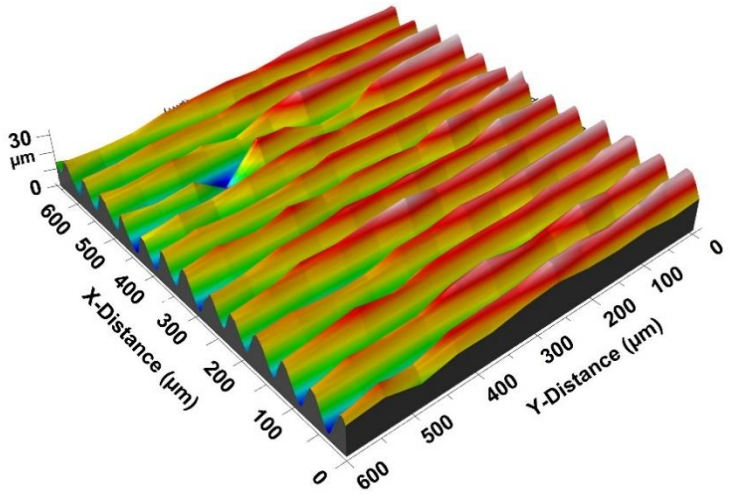

Figure 5.15. 3-D surface profile of the SH-LIG generated on soda lime glass substrate.

Table 5.1. Profilometer analysis results of average surface roughness of SH-LIG on different substrates

Substrate	Roughness [S_a (µm)]
Al 6061	6.22
Silicon	1.81
Glass	4.58

The above table shows that the average surface roughness varies drastically between samples. Nevertheless, the static contact angle and roll-off angle on all the SH-LIG substrates remained above 150° and below 5°, respectively. The above result confirms the contribution of hierarchical surface nature towards ultrahydrophobicity rather than micro or nano texture alone.

5.3.2 Surface Chemical Characterization

After the topographical characterization, the elemental composition of the SH-LIG surface was analyzed. Figure 5.16, shows the EDS spectra collected on

the SH-LIG generated on Al6061, silicon, and soda lime glass. Table 5.2 displays the corresponding quantitative values obtained from the EDS spectra. As expected, in all the cases, the carbon content was relatively high compared to below 8% (atomic) in pristine samples.

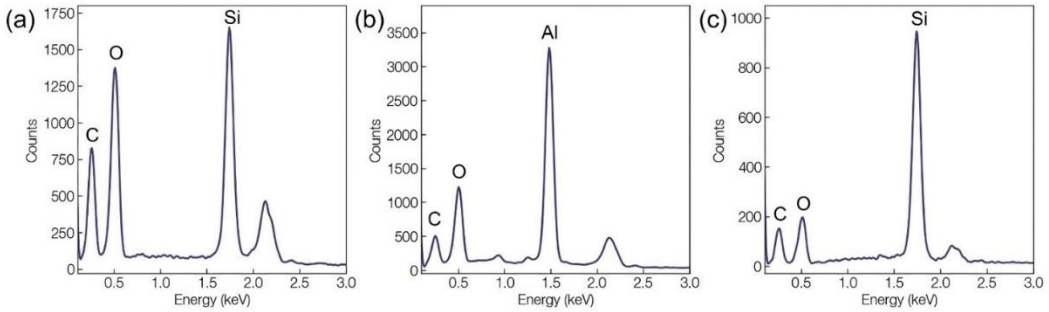

Figure 5.16. EDS spectra obtained from SH-LIG on the following substrates, (a) Sodalime glass; (b) Al 6061; (c) Silicon. Gold coating was used for the measured sample.

Table 5.2. EDS elemental composition analysis on different SH-LIG substrates in atomic %

Element	Al 6061	Silicon	Glass
Al	40.5	-	-
Si	-	69.2	18.7
C	28.5	23.3	45.9
O	29.1	7.4	35.5

The above EDS results confirm carbon as a major elemental component of all the SH-LIG samples. Hence, it can be concluded that the SH-LIG completely covers the surface and therefore, the superhydrophobicity is solely due to the LIG without any interference from the substrate.

To understand the chemical composition of the surface which contributes to the superhydrophobicity, FTIR spectroscopy was performed on the SH-LIG on a flat aluminium substrate in reflection mode. Furthermore, to compare the effect of

laser parameter on the resulting surface energy of the LIG, FTIR measurement was also performed on another sample with LIG formed at a higher average power $(16W)$, in comparison to the low power $(9W)$ used for SH-LIG fabrication. Figure 5.17 represents the FTIR spectra of the samples mentioned above.

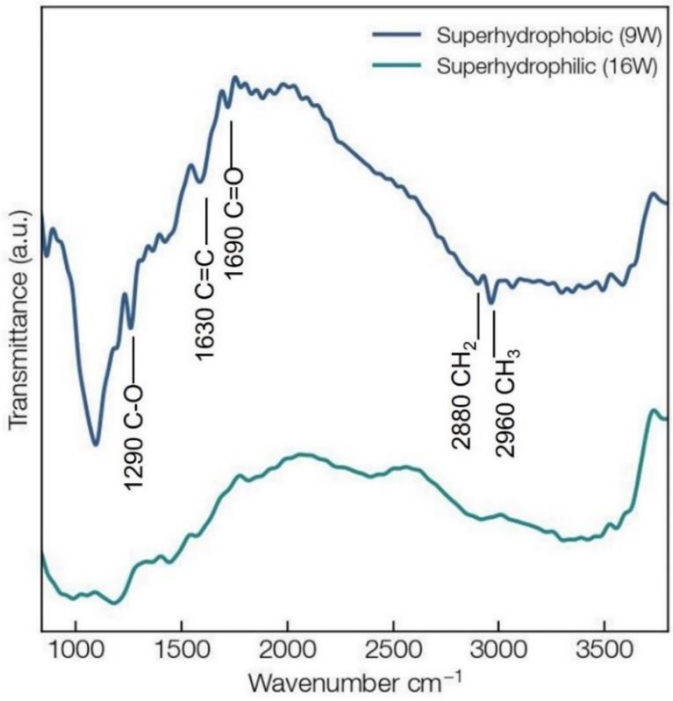

Figure 5.17. FTIR spectra comparison between superhydrophobic LIG (9W) and superhydrophilic LIG (16W).

Interestingly, the LIG modification performed at $16W$ was superhydrophilic in nature. For the SH-LIG, the spectrum shows an absorption peak centered at about $\sim 1290\ cm^{-1}$ which corresponds to the presence of $C-O$ bond of the alcohol groups or $C-O-C$ functional group [69]. The absorption at $\sim 1630 cm^{-1}$ could be attributed to the $C=C$ stretching of the aromatic ring members [70]. Another absorption peak located at $\sim 1690 cm^{-1}$ could be associated with $C=O$ carbonyl stretch [71]. Finally, the minor absorption peaks at $\sim 2880 cm^{-1}$ and $\sim 2960 cm^{-1}$ corresponds to the CH_2 and CH_3 stretching respectively [72]. Interestingly, the LIG modification performed at $16W$ does not show any significant peaks at the above-mentioned wavenumbers. As previously mentioned, the surface energy transition could be a result of relatively strong

photothermal ablation inducing greater oxidation and superhydrophilicity of the LIG.

The surface compositional analysis reveals the presence of carbonaceous material on all the substrates, contributing to the SH-LIG. The ability to transfer the SH-LIG on different substrates, along with the inherent hierarchical surface texture and reduced surface energy, proves to be an interesting alternative to toxic chemicals or complex fabrication processes.

5.3.3 Functional Stability

An important aspect of superhydrophobicity is the stability of the surface property while in use. However, previous studies on superhydrophobic LIG have seldom assessed the fabricated surface's functional stability. The stability proves to be an important factor for use in actual applications. As a comparison, the water repellence based on volatile organic compounds on laser textured metals loses its functional property by immersion under water for about two hours. On the other hand, the fluorosilane coatings remain stable even after immersion under water for days altogether [73,74]. Therefore, it becomes important to assess the stability to be fit for applications.

To test the stability of the SH-LIG, water immersion test was performed on the samples. The dynamic contact angles and the change in resistance was measured at regular intervals over a period of 24 hours. To measure the dynamic CA stability, $8\,mm \times 8\,mm$ area of SH-LIG was prepared on a glass substrate, whereas for the resistance measurement, a single LIG line was written on the CFRP material as the substrate. The laser parameters to fabricate the SH-LIG remained the same as before.

As shown in Figure 5.18, the variation in dynamic contact angle with immersion time demonstrates the stability of the SH-LIG surface. Both the advancing and receding contact angles (CA) are greater than $155°$. An important aspect of the dynamic contact angle measurements involves the CA hysteresis, defined as the difference between the advancing and receding contact angles [75]. Low contact angle hysteresis is necessary for the superhydrophobicity to be in a Cassie-Baxter state with very low adhesion to the surface.

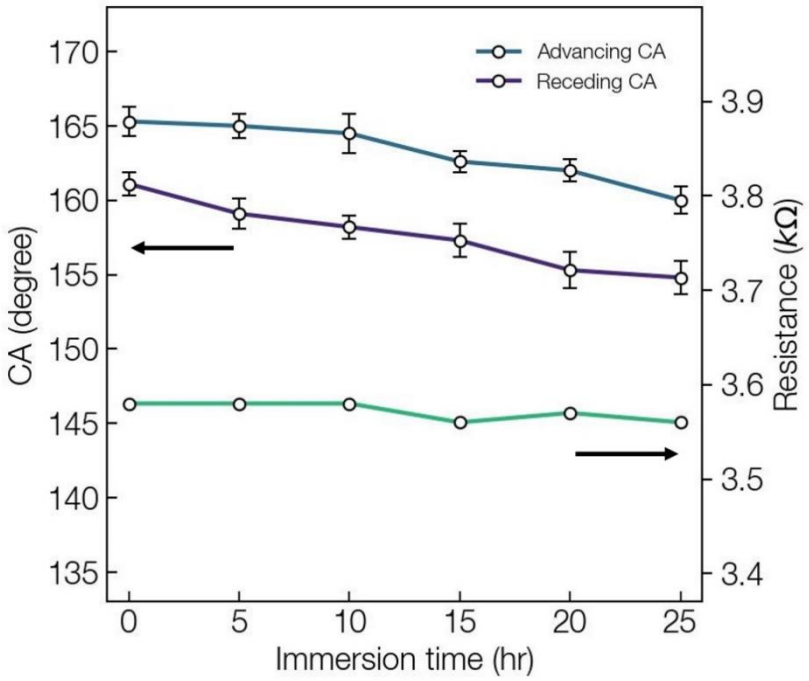

Figure 5.18. Measurements of dynamic contact angle for SH-LIG area on glass substrate and resistance of SH-LIG circuit line on CFRP substrate performed at different time intervals during complete immersion underwater upto 24 hours.

As shown in the Figure 5.18, even after continuous immersion for about 24 hours, the hysteresis remains ~ 6.8°, which confirms the excellent stability of the superhydrophobic surface. The stability of the superhydrophobic surface is a combined effect of the hydrophobic carbonaceous LIG and the hierarchical surface texture. Indeed, the hierarchical surface features provide an efficient air-trapping system that repels water penetration over time [76,77].

In coherence with the stability of the contact angle hysteresis measurements, the resistance of the LIG line ($1.5\ mm$) almost remained constant after the total duration of water immersion, also shown in Figure 5.18. The resistance measurement results of water immersion provides direct evidence of the applicability of the SH-LIG even under extreme conditions.

Superhydrophobic surfaces, especially in the Cassie-Baxter state, has trapped air layer within the hierarchical surface features. This thin air covering the superhydrophobic surface features, repelling water droplets, is termed a surface plastron [78]. This thin air layer is responsible for the shiny appearance of

superhydrophobic surfaces upon immersion underwater due to total internal reflection, as shown in Figure 5.19(b).

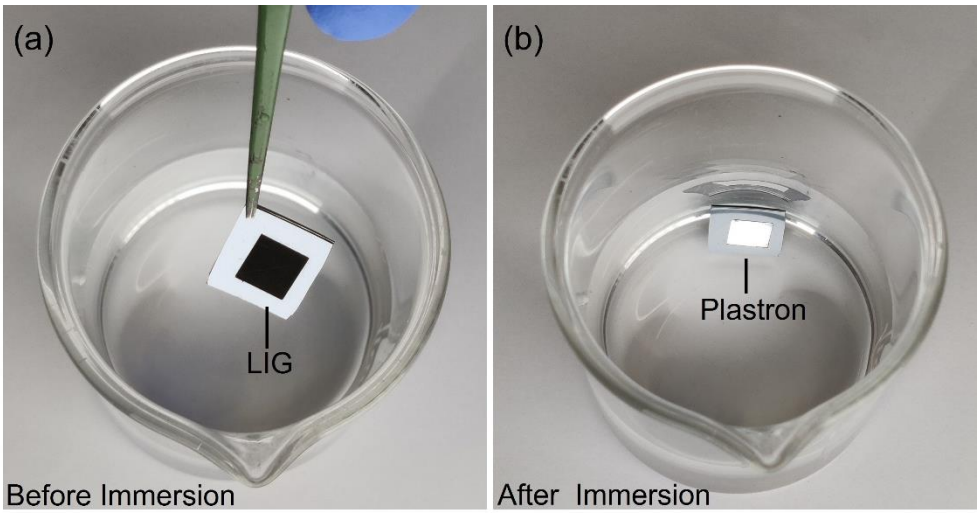

Figure 5.19. Depiction of total internal reflection of surface thin air film (plastron) for the SH-LIG on silicon surface (a) before immersion; (b) after immersion.

The water droplet bounce dynamics provides information about the superhydrophobic property of the surface. The droplet contact time with the surface decreases with an increase in superhydrophobicity due to the minimal energy exchange involved during the droplet-surface interaction. Especially for pagophobic applications, it is desirable for a water droplet to have minimal contact time with the surface to avoid droplet freezing [79]. As a result, the droplet dynamics can be used to study the superhydrophobic state. Figure 5.20(a,b) shows the high-speed camera images of the droplet ($6\mu L$) bounce on the SH-LIG surface before and after immersion in water for 24 hours. In both the cases, the droplet spreads like a thin sheet to a maximum diameter on surface contact, followed by recoil and surface exit, as usually observed on conventional biomimetic surfaces [80]. The freshly prepared SH-LIG has a contact time of $11.2\ ms$ whereas for the immersed SH-LIB, the contact time slightly increased to $12.1\ ms$. Indeed, this confirms the excellent stability of the superhydrophobicity on the LIG surface, bolstering the applicational prospects of a rapid, inexpensive, and eco-friendly approach to fabricate electronic sensors and functional surfaces.

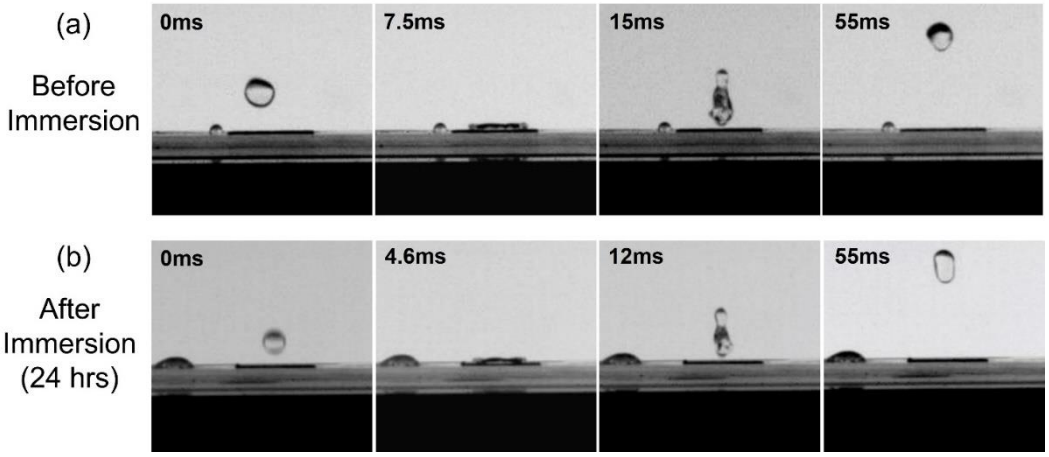

Figure 5.20. High speed camera images of impact, spread and bounce of 6 µL water droplet on the SH-LIG surface (a) before water immersion (b) after 24 hours of immersion in water.

5.3.4 Superhydrophobic LIG for Gas Sensing

Graphene-based materials are also of great interest for their gas sensing capability. The gas molecule adsorption on the graphene surface cause variation in the electrical conductivity due to a change in the local carrier concentration induced by the adsorbents taking the role of electron donors or acceptors. Unlike pristine monolayer graphene, graphene oxide has oxygen groups, defects, and vacancies. The density of the oxygen functional groups is expected to negatively affect the conductance response of the rGO. Hence, the response and recovery also improve with the increase in the reduction levels, i.e., reduced presence of oxygen functional groups. Robinson et al. [81] have demonstrated ppb level sensing of toxic gases such as hydrogen cyanide (HCN) and $2{,}4-dinitrotoluene$ using reduced graphene oxide.

These gas sensors, however, face difficulties in high humidity ($RH\ 50\% - 95\%$) environments due to water molecules occupying active sites of the gas sensor [82]. Several research works have sought to improve the sensing capabilities by using hydrophobic coatings based on self-assembled monolayer, heating elements or moisture barrier layers [83]. These methods, however, result in complex fabrication procedures and increased production cost.

The SH-LIG fabricated in this study can become an inexpensive alternative for gas sensing with stability under high humidity conditions. Figure 5.21(a) shows the gas sensing capability of the SH-LIG through the detection of human

breathe. The sensor exhibited good repeatability and recovered after each breathe, as shown in Figure 5.21(b). The breath analysis sensors are especially interesting for sensing nitric oxide (NO), varying from ten to hundreds of ppb between healthy and asthma patients [84,85]. The SH-LIB based sensor fabricated in this work could provide a simple and non-toxic approach towards reduced graphene oxide-based sensors.

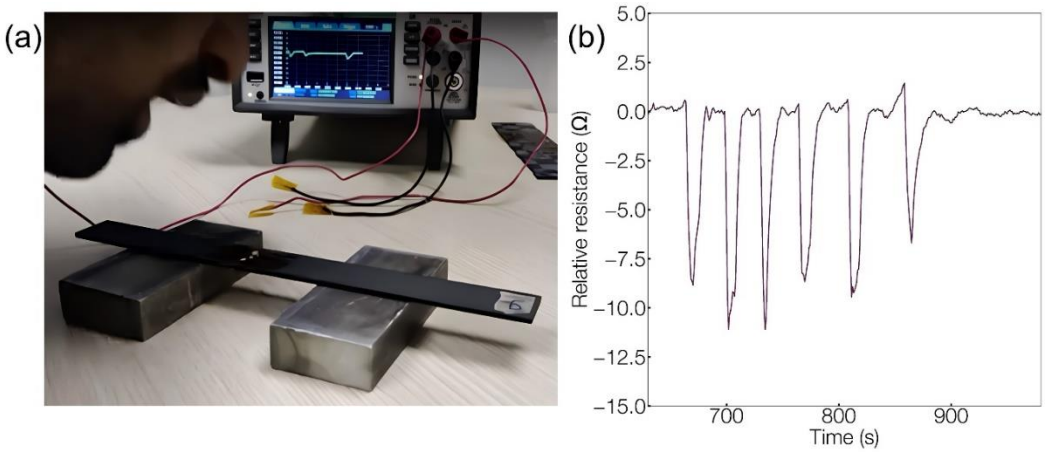

Figure 5.21. (a) SH-LIG on the CFRP substrate performing sensing of human breathe; (b) obtained relative resistance change for the performed six breathe cycles.

References

1. Mahmoudi, T.; Wang, Y.; Hahn, Y.-B. Graphene and Its Derivatives for Solar Cells Application. *Nano Energy* **2018**, *47*, 51–65, doi:10.1016/j.nanoen.2018.02.047.
2. Yoo, B.M.; Shin, H.J.; Yoon, H.W.; Park, H.B. Graphene and Graphene Oxide and Their Uses in Barrier Polymers: Review. *J. Appl. Polym. Sci.* **2014**, *131*, doi:10.1002/app.39628.
3. Abid; Sehrawat, P.; Islam, S.S.; Mishra, P.; Ahmad, S. Reduced Graphene Oxide (rGO) Based Wideband Optical Sensor and the Role of Temperature, Defect States and Quantum Efficiency. *Sci Rep* **2018**, *8*, 3537, doi:10.1038/s41598-018-21686-2.
4. Kim, E.H.; Lee, D.H.; Gu, T.J.; Yoo, H.; Jang, Y.; Jeong, J.; Kim, H.-W.; Kang, S.-G.; Kim, H.; Lee, H.; et al. Wafer-Scale Epitaxial Growth of an Atomically Thin Single-Crystal Insulator as a Substrate of Two-Dimensional Material Field-Effect Transistors. *Nano Lett.* **2023**, *23*, 3054–3061, doi:10.1021/acs.nanolett.3c00546.
5. Yang, G.; Yi, H.; Yao, Y.; Li, C.; Li, Z. Thermally Conductive Graphene Films for Heat Dissipation. *ACS Appl. Nano Mater.* **2020**, *3*, 2149–2155, doi:10.1021/acsanm.9b01955.
6. Kumar, N.; Wang, W.; Ortiz-Marquez, J.C.; Catalano, M.; Gray, M.; Biglari, N.; Hikari, K.; Ling, X.; Gao, J.; van Opijnen, T.; et al. Dielectrophoresis Assisted Rapid, Selective and Single Cell Detection of Antibiotic Resistant Bacteria with G-FETs.
7. Xie, T.; Wang, Q.; Wallace, R.M.; Gong, C. Understanding and Optimization of Graphene Gas Sensors. *Appl. Phys. Lett.* **2021**, *119*, 013104, doi:10.1063/5.0057066.
8. Alhazmi, H.A.; Ahsan, W.; Mangla, B.; Javed, S.; Hassan, Mohd.Z.; Asmari, M.; Al Bratty, M.; Najmi, A. Graphene-Based Biosensors for Disease Theranostics: Development, Applications, and Recent Advancements. *Nanotechnology Reviews* **2021**, *11*, 96–116, doi:10.1515/ntrev-2022-0009.
9. Perreault, F.; Fonseca De Faria, A.; Elimelech, M. Environmental Applications of Graphene-Based Nanomaterials. *Chem. Soc. Rev.* **2015**, *44*, 5861–5896, doi:10.1039/C5CS00021A.
10. Phiri, J.; Gane, P.; Maloney, T.C. General Overview of Graphene: Production, Properties and Application in Polymer Composites. *Materials*

Science and Engineering: B **2017**, *215*, 9–28, doi:10.1016/j.mseb.2016.10.004.

11. Yue, H.; Yao, L.; Gao, X.; Zhang, S.; Guo, E.; Zhang, H.; Lin, X.; Wang, B. Effect of Ball-Milling and Graphene Contents on the Mechanical Properties and Fracture Mechanisms of Graphene Nanosheets Reinforced Copper Matrix Composites. *Journal of Alloys and Compounds* **2017**, *691*, 755–762, doi:10.1016/j.jallcom.2016.08.303.
12. Amiri, A.; Naraghi, M.; Ahmadi, G.; Soleymaniha, M.; Shanbedi, M. A Review on Liquid-Phase Exfoliation for Scalable Production of Pure Graphene, Wrinkled, Crumpled and Functionalized Graphene and Challenges. *FlatChem* **2018**, *8*, 40–71, doi:10.1016/j.flatc.2018.03.004.
13. Mattevi, C.; Kim, H.; Chhowalla, M. A Review of Chemical Vapour Deposition of Graphene on Copper. *J. Mater. Chem.* **2011**, *21*, 3324–3334, doi:10.1039/C0JM02126A.
14. Bonaccorso, F.; Lombardo, A.; Hasan, T.; Sun, Z.; Colombo, L.; Ferrari, A.C. Production and Processing of Graphene and 2d Crystals. *Materials Today* **2012**, *15*, 564–589, doi:10.1016/S1369-7021(13)70014-2.
15. Agarwal, V.; Zetterlund, P.B. Strategies for Reduction of Graphene Oxide – A Comprehensive Review. *Chemical Engineering Journal* **2021**, *405*, 127018, doi:10.1016/j.cej.2020.127018.
16. Alotaibi, F.; Tung, T.T.; Nine, M.J.; Kabiri, S.; Moussa, M.; Tran, D.N.H.; Losic, D. Scanning Atmospheric Plasma for Ultrafast Reduction of Graphene Oxide and Fabrication of Highly Conductive Graphene Films and Patterns. *Carbon* **2018**, *127*, 113–121, doi:10.1016/j.carbon.2017.10.075.
17. Yang, C.; Gong, J.; Zeng, P.; Yang, X.; Liang, R.; Ou, Q.; Zhang, S. Fast Room-Temperature Reduction of Graphene Oxide by Methane/Argon Plasma for Flexible Electronics. *Applied Surface Science* **2018**, *452*, 481–486, doi:10.1016/j.apsusc.2018.04.272.
18. Hasani, A.; Sharifi Dehsari, H.; Amiri Zarandi, A.; Salehi, A.; Taromi, F.A.; Kazeroni, H. Visible Light-Assisted Photoreduction of Graphene Oxide Using CdS Nanoparticles and Gas Sensing Properties. *Journal of Nanomaterials* **2015**, *2015*, 1–11, doi:10.1155/2015/930306.
19. Sengupta, I.; Chakraborty, S.; Talukdar, M.; Pal, S.K.; Chakraborty, S. Thermal Reduction of Graphene Oxide: How Temperature Influences Purity. *J. Mater. Res.* **2018**, *33*, 4113–4122, doi:10.1557/jmr.2018.338.
20. Voiry, D.; Yang, J.; Kupferberg, J.; Fullon, R.; Lee, C.; Jeong, H.Y.; Shin, H.S.; Chhowalla, M. High-Quality Graphene via Microwave Reduction of Solution-Exfoliated Graphene Oxide. *Science* **2016**, *353*, 1413–1416, doi:10.1126/science.aah3398.

21. Lin, J.; Peng, Z.; Liu, Y.; Ruiz-Zepeda, F.; Ye, R.; Samuel, E.L.G.; Yacaman, M.J.; Yakobson, B.I.; Tour, J.M. Laser-Induced Porous Graphene Films from Commercial Polymers. *Nat Commun* **2014**, *5*, 5714, doi:10.1038/ncomms6714.

22. Cui, T.-R.; Li, D.; Hirtz, T.; Shao, W.-C.; Zhou, Z.-B.; Ji, S.-R.; Li, X.; Xu, J.-D.; Jian, J.-M.; Chen, Z.-K.; et al. Laser-Induced Graphene for Multifunctional and Intelligent Wearable Systems: For Health Care and Human–Computer Interaction. *Applied Sciences* **2023**, *13*, 4688, doi:10.3390/app13084688.

23. Zaccagnini, P.; Ballin, C.; Fontana, M.; Parmeggiani, M.; Bianco, S.; Stassi, S.; Pedico, A.; Ferrero, S.; Lamberti, A. Laser-Induced Graphenization of PDMS as Flexible Electrode for Microsupercapacitors. *Adv Materials Inter* **2021**, *8*, 2101046, doi:10.1002/admi.202101046.

24. Yan, W.; Yan, W.; Chen, T.; Xu, J.; Tian, Q.; Ho, D. Size-Tunable Flowerlike MoS $_2$ Nanospheres Combined with Laser-Induced Graphene Electrodes for NO $_2$ Sensing. *ACS Appl. Nano Mater.* **2020**, *3*, 2545–2553, doi:10.1021/acsanm.9b02614.

25. Vivaldi, F.M.; Dallinger, A.; Bonini, A.; Poma, N.; Sembranti, L.; Biagini, D.; Salvo, P.; Greco, F.; Di Francesco, F. Three-Dimensional (3D) Laser-Induced Graphene: Structure, Properties, and Application to Chemical Sensing. *ACS Appl. Mater. Interfaces* **2021**, *13*, 30245–30260, doi:10.1021/acsami.1c05614.

26. Wang, L.; Wang, Z.; Bakhtiyari, A.N.; Zheng, H. A Comparative Study of Laser-Induced Graphene by CO2 Infrared Laser and 355 Nm Ultraviolet (UV) Laser. *Micromachines* **2020**, *11*, 1094, doi:10.3390/mi11121094.

27. Gao, J.; He, S.; Nag, A. Electrochemical Detection of Glucose Molecules Using Laser-Induced Graphene Sensors: A Review. *Sensors* **2021**, *21*, 2818, doi:10.3390/s21082818.

28. Jeong, S.-Y.; Ma, Y.-W.; Lee, J.-U.; Je, G.-J.; Shin, B. Flexible and Highly Sensitive Strain Sensor Based on Laser-Induced Graphene Pattern Fabricated by 355 Nm Pulsed Laser. *Sensors* **2019**, *19*, 4867, doi:10.3390/s19224867.

29. Hristovski, I.R.; Herman, L.A.; Mitchell, M.E.; Lesack, N.I.; Reich, J.; Holzman, J.F. Manifestations of Laser-Induced Graphene under Ultraviolet Irradiation of Polyimide with Varied Optical Fluence. *Nanomaterials* **2022**, *12*, 1241, doi:10.3390/nano12081241.

30. Biswas, R.K.; Farid, N.; Bhatt, B.B.; Gupta, D.; O'Connor, G.M.; Scully, P. Femtosecond Infra-Red Laser Carbonization and Ablation of Polyimide for Fabrication of Kirigami Inspired Strain Sensor. *J. Phys. D: Appl. Phys.* **2023**, *56*, 085101, doi:10.1088/1361-6463/acb71e.

31. Dyer, P.E.; Pervolaraki, M.; Lippert, T. Experimental Studies and Thermal Modelling of 1064- and 532-Nm Nd:YVO4 Micro-Laser Ablation of Polyimide. *Appl. Phys. A* **2005**, *80*, 529–536, doi:10.1007/s00339-004-3085-0.

32. Sunderlal Singh, S.; Khare, A.; Joshi, S.N. Fabrication of Microchannel on Polycarbonate below the Laser Ablation Threshold by Repeated Scan via the Second Harmonic of Q-Switched Nd:YAG Laser. *Journal of Manufacturing Processes* **2020**, *55*, 359–372, doi:10.1016/j.jmapro.2020.04.006.

33. Ravi-Kumar, S.; Lies, B.; Zhang, X.; Lyu, H.; Qin, H. Laser Ablation of Polymers: A Review. *Polym. Int.* **2019**, *68*, 1391–1401, doi:10.1002/pi.5834.

34. Wu, C.; Rong, Y.; Li, M.; Zhang, G.; Huang, Y.; Zhang, T. High-Quality Cutting of Polypropylene (PP) Film by UV Nanosecond Laser Based on Thermal Ablation. *Optics & Laser Technology* **2022**, *147*, 107600, doi:10.1016/j.optlastec.2021.107600.

35. Malyshev, A.Y.; Bityurin, N.M. Laser Swelling Model for Polymers Irradiated by Nanosecond Pulses. *Quantum Electron.* **2005**, *35*, 825–830, doi:10.1070/QE2005v035n09ABEH008988.

36. Alam, S.N.; Sharma, N.; Kumar, L. Synthesis of Graphene Oxide (GO) by Modified Hummers Method and Its Thermal Reduction to Obtain Reduced Graphene Oxide (rGO)*. *Graphene* **2017**, *06*, 1–18, doi:10.4236/graphene.2017.61001.

37. Alamri, S.; Lasagni, A.F. Development of a General Model for Direct Laser Interference Patterning of Polymers. *Opt. Express* **2017**, *25*, 9603, doi:10.1364/OE.25.009603.

38. Du, Q.; Chen, T.; Liu, J.; Zeng, X. Surface Microstructure and Chemistry of Polyimide by Single Pulse Ablation of Picosecond Laser. *Applied Surface Science* **2018**, *434*, 588–595, doi:10.1016/j.apsusc.2017.10.200.

39. Selimis, A.; Tserevelakis, G.J.; Kogou, S.; Pouli, P.; Filippidis, G.; Sapogova, N.; Bityurin, N.; Fotakis, C. Nonlinear Microscopy Techniques for Assessing the UV Laser Polymer Interactions. *Opt. Express* **2012**, *20*, 3990, doi:10.1364/OE.20.003990.

40. Lee, Y.A.; Lim, J.; Cho, Y.; Lee, H.; Park, S.; Lee, G.-W.; Yoo, C.-Y.; Park, S.H.; Matham Murukeshan, V.; Kim, S.; et al. Attachable Micropseudocapacitors Using Highly Swollen Laser-Induced-Graphene Electrodes. *Chemical Engineering Journal* **2020**, *386*, 123972, doi:10.1016/j.cej.2019.123972.

41. Peng, Z.; Lin, J.; Ye, R.; Samuel, E.L.G.; Tour, J.M. Flexible and Stackable Laser-Induced Graphene Supercapacitors. *ACS Appl. Mater. Interfaces* **2015**, *7*, 3414–3419, doi:10.1021/am509065d.

42. Ma, W.; Zhu, J.; Wang, Z.; Song, W.; Cao, G. Recent Advances in Preparation and Application of Laser-Induced Graphene in Energy Storage Devices. *Materials Today Energy* **2020**.

43. Cardoso, A.R.; Marques, A.C.; Santos, L.; Carvalho, A.F.; Costa, F.M.; Martins, R.; Sales, M.G.F.; Fortunato, E. Molecularly-Imprinted Chloramphenicol Sensor with Laser-Induced Graphene Electrodes. *Biosensors and Bioelectronics* **2019**, *124–125*, 167–175, doi:10.1016/j.bios.2018.10.015.

44. Naseri, I.; Ziaee, M.; Nilsson, Z.N.; Lustig, D.R.; Yourdkhani, M. Electrothermal Performance of Heaters Based on Laser-Induced Graphene on Aramid Fabric. *ACS Omega* **2022**, *7*, 3746–3757, doi:10.1021/acsomega.1c06572.

45. Zhao, X.; Liu, Z.-B.; Yan, W.-B.; Wu, Y.; Zhang, X.-L.; Chen, Y.; Tian, J.-G. Ultrafast Carrier Dynamics and Saturable Absorption of Solution-Processable Few-Layered Graphene Oxide. *Appl. Phys. Lett.* **2011**, *98*, 121905, doi:10.1063/1.3570640.

46. Ghosh, A.; Miah, M.; Majumder, C.; Bag, S.; Chakravorty, D.; Saha, S.K. Synthesis of Multilayered Structure of Nano-Dimensional Silica Glass/Reduced Graphene Oxide for Advanced Electrochemical Applications. *Nanoscale* **2018**, *10*, 5539–5549, doi:10.1039/C8NR00852C.

47. Rawat, P.S.; Srivastava, R.C.; Dixit, G.; Asokan, K. Structural, Functional and Magnetic Ordering Modifications in Graphene Oxide and Graphite by 100 MeV Gold Ion Irradiation. *Vacuum* **2020**, *182*, 109700, doi:10.1016/j.vacuum.2020.109700.

48. Wahab, H.; Jain, V.; Tyrrell, A.S.; Seas, M.A.; Kotthoff, L.; Johnson, P.A. Machine-Learning-Assisted Fabrication: Bayesian Optimization of Laser-Induced Graphene Patterning Using in-Situ Raman Analysis. *Carbon* **2020**, *167*, 609–619, doi:10.1016/j.carbon.2020.05.087.

49. Hazra, K.S.; Rafiee, J.; Rafiee, M.A.; Mathur, A.; Roy, S.S.; McLauhglin, J.; Koratkar, N.; Misra, D.S. Thinning of Multilayer Graphene to Monolayer Graphene in a Plasma Environment. *Nanotechnology* **2011**, *22*, 025704, doi:10.1088/0957-4484/22/2/025704.

50. Soares, R.R.A.; Hjort, R.G.; Pola, C.C.; Parate, K.; Reis, E.L.; Soares, N.F.F.; McLamore, E.S.; Claussen, J.C.; Gomes, C.L. Laser-Induced Graphene Electrochemical Immunosensors for Rapid and Label-Free Monitoring of *Salmonella Enterica* in Chicken Broth. *ACS Sens.* **2020**, *5*, 1900–1911, doi:10.1021/acssensors.9b02345.

51. Scattareggia Marchese, S.; Epasto, G.; Crupi, V.; Garbatov, Y. Tensile Response of Fibre-Reinforced Plastics Produced by Additive Manufacturing for Marine Applications. *JMSE* **2023**, *11*, 334, doi:10.3390/jmse11020334.

52. Koumoulos, E.; Trompeta, A.-F.; Santos, R.-M.; Martins, M.; Santos, C.; Iglesias, V.; Böhm, R.; Gong, G.; Chiminelli, A.; Verpoest, I.; et al. Research and Development in Carbon Fibers and Advanced High-Performance Composites Supply Chain in Europe: A Roadmap for Challenges and the Industrial Uptake. *J. Compos. Sci.* **2019**, *3*, 86, doi:10.3390/jcs3030086.

53. Barile, C.; Casavola, C.; Pappalettera, G.; Paramsamy Kannan, V. Damage Monitoring of Carbon Fibre Reinforced Polymer Composites Using Acoustic Emission Technique and Deep Learning. *Composite Structures* **2022**, *292*, 115629, doi:10.1016/j.compstruct.2022.115629.

54. Sun, Q.; Zhou, G.; Meng, Z.; Jain, M.; Su, X. An Integrated Computational Materials Engineering Framework to Analyze the Failure Behaviors of Carbon Fiber Reinforced Polymer Composites for Lightweight Vehicle Applications. *Composites Science and Technology* **2021**, *202*, 108560, doi:10.1016/j.compscitech.2020.108560.

55. Forintos, N.; Sarkadi, T.; Czigany, T. Electric Resistance Measurement–Based Structural Health Monitoring with Multifunctional Carbon Fibers: Predicting, Sensing, and Measuring Overload. *Composites Communications* **2021**, *28*, 100913, doi:10.1016/j.coco.2021.100913.

56. Nguyen, T.; Dinh, T.; Foisal, A.R.M.; Phan, H.-P.; Nguyen, T.-K.; Nguyen, N.-T.; Dao, D.V. Giant Piezoresistive Effect by Optoelectronic Coupling in a Heterojunction. *Nat Commun* **2019**, *10*, 4139, doi:10.1038/s41467-019-11965-5.

57. Bragaglia, M.; Paleari, L.; Lamastra, F.R.; Puglia, D.; Fabbrocino, F.; Nanni, F. Graphene Nanoplatelet, Multiwall Carbon Nanotube, and Hybrid Multiwall Carbon Nanotube–Graphene Nanoplatelet Epoxy Nanocomposites as Strain Sensing Coatings. *Journal of Reinforced Plastics and Composites* **2021**, *40*, 632–643, doi:10.1177/0731684421994324.

58. Pei, Z.; Zhang, Q.; Liu, Y.; Zhao, Y.; Dong, X.; Zhang, Y.; Zhang, W.; Sang, S. A High Gauge-Factor Wearable Strain Sensor Array via 3D Printed Mold Fabrication and Size Optimization of Silver-Coated Carbon Nanotubes. *Nanotechnology* **2020**, *31*, 305501, doi:10.1088/1361-6528/ab8592.

59. Wang, W.; Lu, L.; Li, Z.; Lin, L.; Liang, Z.; Lu, X.; Xie, Y. Fingerprint-Inspired Strain Sensor with Balanced Sensitivity and Strain Range Using Laser-Induced Graphene. *ACS Appl. Mater. Interfaces* **2022**, *14*, 1315–1325, doi:10.1021/acsami.1c16646.

60. Li, Q.; Wu, T.; Zhao, W.; Ji, J.; Wang, G. Laser-Induced Corrugated Graphene Films for Integrated Multimodal Sensors. *ACS Appl. Mater. Interfaces* **2021**, *13*, 37433–37444, doi:10.1021/acsami.1c12686.

61. Wang, K.; Pang, J.; Li, L.; Zhou, S.; Li, Y.; Zhang, T. Synthesis of Hydrophobic Carbon Nanotubes/Reduced Graphene Oxide Composite Films by Flash Light Irradiation. *Front. Chem. Sci. Eng.* **2018**, *12*, 376–382, doi:10.1007/s11705-018-1705-z.

62. Li, Y.; Luong, D.X.; Zhang, J.; Tarkunde, Y.R.; Kittrell, C.; Sargunaraj, F.; Ji, Y.; Arnusch, C.J.; Tour, J.M. Laser-Induced Graphene in Controlled Atmospheres: From Superhydrophilic to Superhydrophobic Surfaces. *Adv. Mater.* **2017**, *29*, 1700496, doi:10.1002/adma.201700496.

63. Wang, L.; Li, J.; Chen, Z.; Song, Z.; Meng, X.; Chen, X. Porous Graphene-Based Photothermal Superhydrophobic Surface for Robust Anti-Icing and Efficient De-Icing. *Adv Materials Inter* **2022**, *9*, 2201758, doi:10.1002/admi.202201758.

64. Liu, F.; Wang, G.; Ding, X.; Luo, S. Multifunctional Laser-Induced Graphene Enabled Polymeric Composites. *Composites Communications* **2021**, *25*, 100714, doi:10.1016/j.coco.2021.100714.

65. Wakabayashi, S.; Arie, T.; Akita, S.; Nakajima, K.; Takei, K. A Multitasking Flexible Sensor via Reservoir Computing. *Advanced Materials* **2022**, *34*, 2201663, doi:10.1002/adma.202201663.

66. Liu, K.; Yang, C.; Zhang, S.; Wang, Y.; Zou, R.; Alamusi; Deng, Q.; Hu, N. Laser Direct Writing of a Multifunctional Superhydrophobic Composite Strain Sensor with Excellent Corrosion Resistance and Anti-Icing/Deicing Performance. *Materials & Design* **2022**, *218*, 110689, doi:10.1016/j.matdes.2022.110689.

67. Manderfeld, E.; Kleinberg, M.N.; Thamaraiselvan, C.; Koschitzki, F.; Gnutt, P.; Plumere, N.; Arnusch, C.J.; Rosenhahn, A. Electrochemically Activated Laser-Induced Graphene Coatings against Marine Biofouling. *Applied Surface Science* **2021**, *569*, 150853, doi:10.1016/j.apsusc.2021.150853.

68. Sharifikolouei, E.; Najmi, Z.; Cochis, A.; Scalia, A.C.; Aliabadi, M.; Perero, S.; Rimondini, L. Generation of Cytocompatible Superhydrophobic Zr–Cu–Ag Metallic Glass Coatings with Antifouling Properties for Medical Textiles. *Materials Today Bio* **2021**, *12*, 100148, doi:10.1016/j.mtbio.2021.100148.

69. Zelenková, G.; Zelenka, T.; Almáši, M.; Soldánová, M. Graphene as a Promising Additive to Hierarchically Porous Carbon Monoliths for Enhanced H2 and CO2 Sorption. *Journal of CO2 Utilization* **2023**, *68*, 102371, doi:10.1016/j.jcou.2022.102371.

70. Facile One-Step Preparation and Characterization of Graphene Quantum Dots Suspension via Electrochemical Exfoliation. *MJCHEM* **2021**, *23*, doi:10.55373/mjchem.v23i2.1007.

71. Barahuie, F.; Saifullah, B.; Dorniani, D.; Fakurazi, S.; Karthivashan, G.; Hussein, M.Z.; Elfghi, F.M. Graphene Oxide as a Nanocarrier for Controlled Release and Targeted Delivery of an Anticancer Active Agent, Chlorogenic Acid. *Materials Science and Engineering: C* **2017**, *74*, 177–185, doi:10.1016/j.msec.2016.11.114.

72. Gao, X.; Yokota, N.; Oda, H.; Tanaka, S.; Hokamoto, K.; Chen, P.; Xu, M. Preparation of Few-Layer Graphene by Pulsed Discharge in Graphite Micro-Flake Suspension. *Crystals* **2019**, *9*, 150, doi:10.3390/cryst9030150.

73. Jiao, X.; Li, M.; Yu, X.; Wong, W.S.Y.; Zhang, Y. Oil-Immersion Stable Superamphiphobic Coatings for Long-Term Super Liquid-Repellency. *Chemical Engineering Journal* **2021**, *420*, 127606, doi:10.1016/j.cej.2020.127606.

74. Zhang, D.; Liu, Z.; Wu, G.; Yang, Z.; Cui, Y.; Li, H.; Zhang, Y. Fluorinated Carbon Nanotube Superamphiphobic Coating for High-Efficiency and Long-Lasting Underwater Antibiofouling Surfaces. *ACS Appl. Bio Mater.* **2021**, *4*, 6351–6360, doi:10.1021/acsabm.1c00582.

75. Semprebon, C.; McHale, G.; Kusumaatmaja, H. Apparent Contact Angle and Contact Angle Hysteresis on Liquid Infused Surfaces. *Soft Matter* **2017**, *13*, 101–110, doi:10.1039/C6SM00920D.

76. Latthe, S.S.; Sutar, R.S.; Bhosale, A.K.; Nagappan, S.; Ha, C.-S.; Sadasivuni, K.K.; Liu, S.; Xing, R. Recent Developments in Air-Trapped Superhydrophobic and Liquid-Infused Slippery Surfaces for Anti-Icing Application. *Progress in Organic Coatings* **2019**, *137*, 105373, doi:10.1016/j.porgcoat.2019.105373.

77. Zhang, Y.; Wang, T.; Wu, M.; Wei, W. Durable Superhydrophobic Surface with Hierarchical Microstructures for Efficient Water Collection. *Surface and Coatings Technology* **2021**, *419*, 127279, doi:10.1016/j.surfcoat.2021.127279.

78. Vüllers, F.; Peppou-Chapman, S.; Kavalenka, M.N.; Hölscher, H.; Neto, C. Effect of Repeated Immersions and Contamination on Plastron Stability in Superhydrophobic Surfaces. *Physics of Fluids* **2019**, *31*, 012102, doi:10.1063/1.5064817.

79. Borrebæk, P.-O.A.; Jelle, B.P.; Zhang, Z. Avoiding Snow and Ice Accretion on Building Integrated Photovoltaics – Challenges, Strategies, and Opportunities. *Solar Energy Materials and Solar Cells* **2020**, *206*, 110306, doi:10.1016/j.solmat.2019.110306.

80. Fan, Y.; Wu, C.; Yang, J.; Wang, Y.; Zhou, Y.; Zhou, J.; Luo, J.; Zhang, J.; Huang, S.; Tian, X. Reducing the Contact Time of Impacting Water Drops on Superhydrophobic Surfaces by Liquid-like Coatings. *Chemical Engineering Journal* **2022**, *448*, 137638, doi:10.1016/j.cej.2022.137638.

81. Robinson, J.T.; Perkins, F.K.; Snow, E.S.; Wei, Z.; Sheehan, P.E. Reduced Graphene Oxide Molecular Sensors. *Nano Lett.* **2008**, *8*, 3137–3140, doi:10.1021/nl8013007.

82. Gao, W.-C.; Wu, W.; Chen, C.-Z.; Zhao, H.; Liu, Y.; Li, Q.; Huang, C.-X.; Hu, G.; Wang, S.-F.; Shi, D.; et al. Design of a Superhydrophobic Strain Sensor with a Multilayer Structure for Human Motion Monitoring. *ACS Appl. Mater. Interfaces* **2022**, *14*, 1874–1884, doi:10.1021/acsami.1c17565.

83. Tian, H.; Fan, H.; Li, M.; Ma, L. Zeolitic Imidazolate Framework Coated ZnO Nanorods as Molecular Sieving to Improve Selectivity of Formaldehyde Gas Sensor. *ACS Sens.* **2016**, *1*, 243–250, doi:10.1021/acssensors.5b00236.

84. Bos, L.D.; Sterk, P.J.; Fowler, S.J. Breathomics in the Setting of Asthma and Chronic Obstructive Pulmonary Disease. *Journal of Allergy and Clinical Immunology* **2016**, *138*, 970–976, doi:10.1016/j.jaci.2016.08.004.

85. Buszewski, B.; Kęsy, M.; Ligor, T.; Amann, A. Human Exhaled Air Analytics: Biomarkers of Diseases. *Biomed. Chromatogr.* **2007**, *21*, 553–566, doi:10.1002/bmc.835.

Chapter 6

Conclusion and Future Perspective

6.1 Contributions and Achievements

In this thesis, we have successfully investigated laser micromachining for surface modification of different material types: metals, glass, ceramics, and polymers. More importantly, the tunability of the laser parameters was appropriately used based on the material absorption characteristics to result in controlled surface modifications. Apart from the laser surface modification of the materials, further intermediate fabrication procedures such as chemical treatments were performed, and new techniques were proposed and demonstrated resulting in biomimetic functional surfaces from superomniphobic surfaces to laser induced graphene smart materials.

Therefore, this study provided a multidisciplinary approach based on the following techniques:

(i) Laser surface modification and following morphological-topography-chemical analysis to select ideal surface processing parameters for the corresponding material.
(ii) Perform appropriate chemical treatment, if needed, to result in desired surface functional properties.
(iii) Characterization of the fabricated functional surfaces and the demonstration for applications.

In the following sections, the achievements from this study are outlined based on the specific applications and a perspective on the outlook of the present research is envisaged.

6.1.1 Superhydrophobic Metal Surfaces

Superhydrophobicity in general is undergoing a major transitional phase. While the techniques to render the surface hierarchical or re-entrant are ever-improving, there is a rather sudden deficiency of appropriate coating techniques. Since the ban on toxic silane coatings that have been widely used to achieve superhydrophobicity, a renewed research is on for alternative eco-friendly and sustainable coating strategies.

This study proposes a simple and eco-friendly vegetable oil based treatment for achieving superhydrophobicity on metal surfaces. Apart from the chemical characterization to elucidate the involved hydrocarbon adsorption phenomenon, a complete static, dynamic and mechanical characterization was performed to compare the superhydrophobicity to that of a reference Fluorosilane coating. Indeed, the proposed approach combines fabrication speed, low cost, and a simple treatment procesdure when compared to the existing state-of-the-art eco-friendly superhydrophobic surfaces. This work has been presented in a conference (ICASS 2022), and later published in the journal Applied Surface Science [1].

Furthermore, the generally overlooked parameter of laser pulsewidth in the nanosecond regime is studied to demonstrate its importance to achieve superamphiphobicity. In fact, it was observed that if not for an ideal pulsewidth, the surface does not achieve superamphiphobicity even if other laser parameters such as scan spacing are varied. This study on superhydrophobicity on metal surfaces is expected to be a major step towards the transition to highly stable and eco-friendly superhydrophobicity, as a replacement to FAS coatings.

6.1.2 Laser Texturing for Joining Enhancement Applications

The chapter presents a study on laser modification of metal and ceramic surfaces to appropriately texture the surface for enhanced joining strength. The target substrate was a stainless steel (Crofer) for texturing a metal surface. The application of interest involves solid-oxide fuel cell (SOFC), for which an

efficient joining between the metallic interconnect and glass sealants is critical for the long-term functioning of the fuel cell stack. In this study, laser fluence is set as a variable parameter to control the surface roughness of the laser textured surface. Finally, two laser fluence parameters were selected to generate average surface roughness (S_a) values of 4.6 µm and 8.8 µm on an hourglass shaped Crofer samples. Following this, a torsion test was performed on the Crofer samples joined by the glass sealant. The test results confirmed a 30% increase in the torsional strength of laser processed sample (32 ± 5 MPa), as compared to as-received Crofer sample (27 ± 7 MPa), due to the mechanical interlocking effect as the glass infiltrates into the laser textured microfeatures [2].

In the second part, a silicon nitride (Si_3N_4) sample was laser modified to generate surface texture for joining applications. Post laser processing, the surface has high silica content, which could be detrimental to the joining applications. To remove the surface silica content an HF etching treatment was performed and surface elemental compositional analysis was performed to confirm the obtention of a textured silicon nitride surface. The reduced silica content is expected to enhance the joining performance and the work is still ongoing.

6.1.3 Laser Processing of a Bioresorbable Anti-bacterial Glass

This chapter demonstrates the precision fabrication of microfeatures on a bioresorbable glass substrate, in a single step fabrication process. The Cu doping of the bioresorbable cacium phosphate glass enables to absorb the infrared wavelength of the interacting nanosecond laser. Moreover, abnormal positive volume modifications are observed on the laser interaction zone attributed to the unusual positive temperature coefficient of surface tension, resulting in eliminating the typical HAZ associate with the long pulsed laser interaction on materials. A preliminary study has been conducted to select a suitablw range of laser parameters to result in modifications without micro-crack inititation on the glass surface. The ideal laser parameter regime was then selected to perform precision modification of complex microfeatures on the glass surface. This part of the study has been published in the journal Applied Sciences [3].

As a demonstration of a possible application, micro-optical features comprising of microlenses and diffraction gratings tunable in shape and size are fabricated on the Cu-doped CaPh glass surface in a single step process. The

fabricated micro-optics are characterized morphologically and optically. Interestingly, hyperbolic and spherical microlens profiles were obtained to demonstrate the shape tunability, and specifically the former is highly desired for applications to overcome spherical abberations and sharp focusing capabilitieS. Additionally, preferential etching is observed on the laser modified glass region in a PBS solution (7.4 pH), that eventually result in negative surface features demonstrating flexible surface modification capabilities of the laser micromachining [4]. Finally the ability to microstructure and generate optical features on the bioresorable glass substrate is expected to combine applications such as scaffolds fabrication for tissue engineering coupled with in-vivo optical diagnosis.

6.1.4 Laser Induced Graphene from Polymer Substrate

This part of the work involved the fabrication of the well-known laser induced graphene (LIG), which consists of reduced graphene oxide (rGO) obtained from a polyimide substrate (Kapton) through laser exposure. The contribution from this work regards the fabrication and characterization of a superhydrophobic form of LIG (SH-LIG) through a single laser fabrication process. The SH-LIG parameters are used to fabricate a strain sensor with a high gauge factor of ~40. Raman, FTIR and EDS spectroscopy techniques were used to characterize the generated reduced graphene oxide. Additionally, we demonstrated the ability to pattern transfer the SH-LIG on substrates of different materials including metals, polymers, and glasses, all in a single step transfer patterning. The stability of the SH-LIG was assessed by immersing the sample under water for 24 hours and measuring the dynamic contact angle, resistance, and droplet bounce at different time intervals [5].

6.2 Outlook and Perspective

In this section, based on the obtained results, we present the future research path that have the potential for impactful scientific and technological advancements. Once again, the section is divided, matching the achievements as reported above.

6.2.1 Superhydrophobic surfaces on metals

Stability and fabrication time are two critical features that define the functional attractiveness for the superhydrophobic surfaces. Therefore, the future work should address the points mentioned below regarding eco-friendly superhydrophobic surfaces. Taking cue from the vacuum based superhydrophobic fabrication technique, the presence of H_2O could strongly impact the hydrocarbon adsorption onto the metal substrates as the water molecules compete in the adsorption process on the metal-oxide substrates [6]. Possible research activity can be taken to further **reduce the fabrication time** as follows:

(i) Evading the cleaning procedure by sonication in water and alcohol solutions post laser processing could be a mean to remove possible residual water molecules prior to oil vapor treatment.
(ii) A high temperature thermal treatment (200°C - 300°C) could help to desorb the already present water molecules before the sample insertion into the oil container.

To be an ideal replacement to the fluorosilane coating for superhydrophobicity, it is of utmost importance to **increase the functional stability**, especially to be able to withstand greater impact and Laplace pressure from the droplet. To further improve the stability of the superhydrophobicity, laser induced periodic surface structures (LIPSS) could be generated during a second scan step with relevant laser parameters on the already present laser textured micro surface. Initial trials have already been conducted to generate LIPSS on polished stainless-steel substrates, as shown in Figure 6. 1. We should also underline hereby that the majority of studies on LIPSS generation has been performed with ultrafast lasers, whereas in this study the IR nanosecond fiber laser has been employed to generate LIPSS.

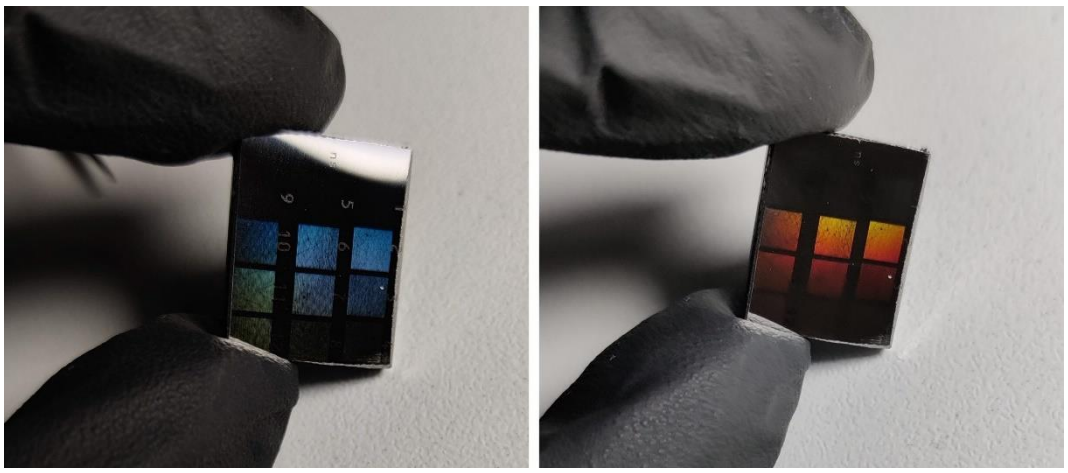

Figure 6. 1. Bright colours generated at different orientations of the stainless-steel sample with LIPSS generated using the IR nanosecond laser (1064 nm).

LIPSS has been well studied and reported to improve the stability of the superhydrophobicity through the uniform presence of a hierarchical nanostructure [7]. The further steps would be directed towards finding the suitable laser parameters to translate the LIPSS on even other metal substrates followed by stability analysis tests such as Laplace pressure and droplet bounce.

6.2.2 Laser Texturing for Joining Enhancement Applications

For this application, the possible future research directions are mentioned based on the substrate types. After selecting suitable laser parameters based on the torsional tests, the ideal parameters are used to process the final interconnect design to build the **SOFC stacks**. The stacks are then to be tested for long term performance to assess the functional enhancement provided by the glass sealant-laser textured crofer joining. Simultaneously, further laser texturing patterns are being explored to design laser generated microfeatures for improved joining strength. As mentioned previously in the chapter, the **laser textured silicon nitride** (Si_3N_4) with reduced silica content after the HF etching are to be tested for their joining strength to obtain conclusive remarks on the effect of surface microfeatures towards joining enhancement.

6.2.2 Laser Processing of Bioresorbable Glasses

Laser processing of the calcium-phosphate glass offers further interesting research steps to be explored. **Calcium-phosphate nanoparticles** are highly interesting for medical applications due to their promising ability to act as

efficient vaccine carriers and protein/peptide carriers [8]. They have been known to provide protection against undesirable premature enzymatic and proteolytic degradation [9]. Laser processing of the calcium-phosphate (CaPh) bioresorbable glass can be used as a means to generate CaPh nanoparticles. Depending on the ablation conditions, these nanoparticles could either be deposited onto another transparent substrate or be dispersed in a liquid solution and used for e.g. drug delivery.

Another research direction can be devoted to a **better understanding of the Inverse Marangoni dynamics** through simulation tools, especially to understand the influence of the Cu dopant in the corresponding effect. Also, it would be important to experimentally explore the possibility of the Inverse Marangoni flow occurrence in other glass compositions, especially commercial-grade glass compositions.

6.2.3 Pushing Laser Induced Graphene Forward

As a vibrant research topic with multifunctional applications, LIG offers various research pathways to pursue. The primary step in the following studies would be to fabricate an integrated multifunctional sensor platform, with the ability to perform liquid solution sensing, gas sensing, superhydrophobic/philic patterns, and joule heating. The final aim is to integrate the individual sensor elements onto a single substrate such as PDMS in a single fabrication step, thanks to selective laser patterning.

In essence, laser micromachining has emerged as one of the leading processing methods for functional materials, and it has revolutionized surface and volume material processing with an ease that was inconceivable a couple of decades ago. The field of laser-material interaction has a lot to offer with unexplored interaction mechanisms. It could also provide innovative solutions to solve current research problems that could be part of future technological advancements.

REFERENCES

1. Meena Narayana Menon, D.; Giardino, M.; Janner, D. Tunable Pulsewidth Nanosecond Laser Texturing: From Environment Friendly Superhydrophobic to Superamphiphobic Surfaces. *Applied Surface Science* **2023**, *610*, 155356, doi:10.1016/j.apsusc.2022.155356.
2. Smeacetto, F.; Zanchi, E.; Meena Narayana Menon, D.; Janner, D.; Lamnini, S.; Salvo, M.; De La Pierre, S.; Javed, H.; Ferraris, M. Torsional Behaviour of Glass-Joined, Laser-Processed Crofer 22 APU Interconnect: Unravelling the Effect of Surface Roughness on the Shear Strength. *Ceramics International* **2022**, *48*, 32837–32843, doi:10.1016/j.ceramint.2022.07.210.
3. Menon, D.M.N.; Pugliese, D.; Janner, D. Infrared Nanosecond Laser Texturing of Cu-Doped Bioresorbable Calcium Phosphate Glasses. *Applied Sciences* **2022**, *12*, 3516, doi:10.3390/app12073516.
4. Meena Narayana Menon, D.; Pugliese, D.; Giardino, M.; Janner, D. Laser-Induced Fabrication of Micro-Optics on Bioresorbable Calcium Phosphate Glass for Implantable Devices. *Materials* **2023**, *16*, 3899, doi:10.3390/ma16113899.
5. Menon, D.M.N.; Giardino, M.; Janner, D. Direct Fabrication of Ultrahydrophobic Laser-Induced Graphene for Strain Sensors. *Applied Sciences* **2023**, *13*, 4935, doi:10.3390/app13084935.
6. Kraus, M.; Trommler, U.; Holzer, F.; Kopinke, F.-D.; Roland, U. Competing Adsorption of Toluene and Water on Various Zeolites. *Chemical Engineering Journal* **2018**, *351*, 356–363, doi:10.1016/j.cej.2018.06.128.
7. Fan, P.; Pan, R.; Zhong, M. Ultrafast Laser Enabling Hierarchical Structures for Versatile Superhydrophobicity with Enhanced Cassie–Baxter Stability and Durability. *Langmuir* **2019**, *35*, 16693–16711, doi:10.1021/acs.langmuir.9b02986.
8. Habraken, W.; Habibovic, P.; Epple, M.; Bohner, M. Calcium Phosphates in Biomedical Applications: Materials for the Future? *Materials Today* **2016**, *19*, 69–87, doi:10.1016/j.mattod.2015.10.008.
9. Tsikourkitoudi, V.; Karlsson, J.; Merkl, P.; Loh, E.; Henriques-Normark, B.; Sotiriou, G.A. Flame-Made Calcium Phosphate Nanoparticles with High Drug Loading for Delivery of Biologics. *Molecules* **2020**, *25*, 1747, doi:10.3390/molecules25071747.

Appendix

Materials and Methods

A.1 Infrared Nanosecond Fiber Laser

The laser system used in this study is an industrial grade fiber laser (AREX 20MW, Datalogic, Bologna, Italy) with Neodymium-doped yttrium orthovanadate ($Nd:YVO_4$) as the gain medium with an emission wavelength of 1064 nm. The laser system has a master oscillator power amplifier configuration enabling it to achieve variable pulsewidth (4-250 ns) and high pulse repetition rate (20-500 kHz). The output laser beam is scanned along the substrate using a galvanometric scan system coupled to an F-Theta lens configuration providing a focal spot size of 60 µm and a maximum scan area of 10×10 cm, at a focal length of 16 cm.

To perform the modification, the appropriate design can be uploaded to the assigned software (LIGHTER MARVIS, Datalogic, Bologna, Italy) that controls the laser system marking. The galvanometric scan system enables complex pattern design in a designated order of laser modification.

A.2 Surface Contact Profilometry

The surface topographical information of the laser textured surfaces were obtained using a contact surface profilometer (Intra touch, Taylor Hobson, UK). In general, the average surface roughness (Sa), and the maximum peak to valley height (Sz) were analyzed to obtain information from the modified surface. The profilometer supports two different scan modes namely single line scan and 3D

surface map. For the majority of the study, the 3D map was used for more complete information of the surface. Specifically, for the line scan, the average roughness and the maximum peak to valley height were represented by Ra and Rz respectively. The obtained profilometer data were analyzed by the Talymap Analysis software(Taylor Hobson, UK).

A.3 Fourier Transform Infrared Spectroscopy

To investigate the surface composition of laser treated and chemically treated surfaces, Fourier transform infrared spectroscopy was performed in the reflection mode with a Shimadzu Tracer 100 FTIR Spectrophotometer coupled with a Shimadzu AIM-9000 Infrared Microscope. The atmospheric corrections are performed using the inbuilt software and are separately baseline corrected for better data representation.

A.4 Scanning Electron Microscopy and Energy Dispersive X-Ray Spectroscopy

The morphological analysis of all the samples were performed using the scanning electron microscope. Two different electron microscope systems were used during the doctoral studies. The first one is a tabletop SEM (JEOL-6000 Plus, Akishima, Japan) based on a thermionic emission source (Tungsten). For higher resolution surface analysis, a field emission source was used (FESEM; SupraTM 40, Zeiss, Germany). As required, the energy dispersive X-ray analysis system coupled to the SEM instrument was used for measurements (EDS, Bruker, Germany).

A.5 X-Ray Diffraction Analysis

The crystalline phase analysis of the laser processed samples were analyzed using PanAlytical X'Pert Pro (Netherlands) with Cu Kα from 10°-80°, with a step size of 0.02°, and a time per step of 18 s.

A.6 Surface Wettability Analysis

The surface wettability of the fabricated superhydrophobic surfaces were analyzed through the contact angle and roll-off angle measurements using a Drop

Shape Analyzer (DSA 100, KRÜSS Scientific, Germany). For the contact angle measurements, the droplet volume was set to 6 μL, unless specified otherwise. The recorded values are an average of three different measurements. For the roll-off angle measurements, the system has an in-built goniometer system for tilt until droplet roll-off. Finally, for all the laser treated samples, except for laser induced reduced graphene oxide (LIG), the processed samples are cleaned to remove debris by sonication in solutions of acetone, ethanol and water followed by drying using a nitrogen flush.